UNIVERSITÀ DEGLI STUDI ROMA TRE

Dipartimento di Matematica e Fisica

XXXVII Cycle of the Doctoral School in Physics

Ph.D. Thesis

Search for Higgs boson pair production in the two photons plus two bottom quarks final state using partial Run-3 proton-proton collision data with the ATLAS detector

---

Author
Federico Montereali
ID Number 627081

Supervisor
Prof. Biagio di Micco

Ph.D. Coordinator
Prof. Giorgio Matt

Accademic year 2024/2025

Introduction

The observation of the Higgs boson (H), announced by the ATLAS and CMS collaborations in July 2012, provided the last building brick for the Standard Model (SM) of particle physics, which currently provides the best description of fundamental interactions. Since its discovery, many properties of the Higgs boson, such as mass, spin, production cross-section, and its couplings to fermions and bosons, have been measured. However, the Higgs boson self-coupling, λ_{HHH}, is very far from being experimentally constrained. The Higgs boson self-coupling provides insight into the structure of the Higgs potential, and consequently into the spontaneous breaking of electroweak symmetry (EWSB) realized by the Higgs mechanism, which is responsible for generating the masses of elementary particles. This self-coupling can be probed directly by studying Higgs boson pair (HH) production, a rare process that has not yet been observed.

At the Large Hadron Collider (LHC), HH production occurs mainly via gluon-gluon fusion (ggF) and vector-boson fusion (VBF), both of which involve the trilinear self-interaction vertex. Any deviation from the Standard Model prediction of the self-coupling λ_{HHH}^{SM}, corresponding to a deviation of the coupling modifier $\kappa_\lambda = \lambda_{HHH}/\lambda_{HHH}^{SM}$ from unity, could indicate physics beyond the Standard Model (BSM).

This thesis presents the search for Higgs boson pair production in the final state with two bottom quarks and two photons using data from the 2015–2018 Run-II proton-proton collisions at $\sqrt{s} = 13$ TeV and the 2022–2023 Run-III data at $\sqrt{s} = 13.6$ TeV, collected with the ATLAS detector at the LHC, corresponding to integrated luminosities of 140 fb^{-1} and 59 fb^{-1}, respectively.

This final state, $HH \to b\bar{b}\gamma\gamma$, has a small branching ratio (0.26%) but benefits from a clear experimental signature due to the excellent di-photon invariant mass resolution ($\sim 2\%$), smooth background, and large $H \to b\bar{b}$ branching ratio (59%). This makes it one of the *golden channels* for HH searches. The final state is fully reconstructable, with no combinatorial issues in identifying the Higgs bosons.

As a reference, according to the SM, only 12 $HH \to b\bar{b}\gamma\gamma$ events are expected in the 140 fb^{-1} Run-II dataset, which corresponds to a suppression of six (three) orders of magnitude compared to di-photon production (single Higgs production in the di-photon channel), the primary background source for the $HH \to b\bar{b}\gamma\gamma$ search. Therefore, the analysis relies on selecting good candidates for $H \to b\bar{b}$ and $H \to \gamma\gamma$ decays to effectively separate signal from the dominant continuum and single Higgs backgrounds.

A signal region is defined by selecting events with two well-reconstructed and identified photons and exactly two hadronic jets consistent with originating from bottom quarks. These events are then divided into mutually exclusive categories to maximize the signal-to-background ratio and retain sensitivity to both the HH signal strength (the number of expected events for HH production normalized to its SM prediction) and variations of the trilinear Higgs self-coupling modifier κ_λ. Double Higgs production events would manifest

as an additional resonant contribution, overlaid on the narrow single Higgs peak and the smoothly falling continuum background in the di-photon invariant mass ($m_{\gamma\gamma}$) spectrum. To distinguish the HH signal from the background, particularly the single Higgs background, the kinematic variables of the b-jets play a crucial role. Specifically, the invariant mass of the two b-jets ($m_{b\bar{b}}$) shows, among the input variables of the Boosted Decision Tree (BDT) used to separate signal and background, the highest discriminating power.
In the $b\bar{b}\gamma\gamma$ channel, while the $H \to \gamma\gamma$ component is exceptionally well reconstructed with a few percent precision thanks to the ATLAS calorimeter, the $H \to b\bar{b}$ component suffers from a 15% invariant mass resolution.
A key part of this thesis is the exploration, development, and optimization of the Kinematic Fit Tool, which, by assuming a good transverse-plane balance between $H \to b\bar{b}$ and $H \to \gamma\gamma$, leverages the excellent reconstruction of the $H \to \gamma\gamma$ decay to improve the $H \to b\bar{b}$ resolution through maximization of an event-level likelihood function.
The thesis is completed by conducting the entire analysis workflow for the $b\bar{b}\gamma\gamma$ channel, using b-jets corrected by the implemented Kinematic Fit technique, to obtain the final statistical results.

This thesis is organized as follows. The first Chapter covers the most relevant theoretical aspects, offering an overview of the Standard Model of particle physics, with a focus on the scalar sector.
The second Chapter provides a technical description of the Large Hadron Collider and the ATLAS experiment, as well as the reconstruction of physics objects, with a particular attention on photons and b-jets.
The third Chapter summarizes the phenomenology of the Higgs boson at hadron colliders and recent measurements of its properties, followed by a discussion on double Higgs production and the latest results in the main analysis channels.
The fourth Chapter introduces the search for Higgs boson pair production in the $b\bar{b}\gamma\gamma$ decay channel using Run-II + partial Run-III data and presents preliminary considerations for the analysis workflow.
The fifth Chapter focuses on the implementation and optimization of the Kinematic Fit Tool, and, the final Chapter presents the complete analysis of the $HH \to b\bar{b}\gamma\gamma$ channel and the statistical results.

Contents

Chapter 1

The Standard Model of Particle Physics

The Standard Model (SM) of particle physics stands as the pinnacle of our understanding of the fundamental particles of nature and their interactions, excluding gravity. It summarizes our current comprehension of quantum mechanics and field theory, combining the Electroweak theory (Sect. 1.3) and Quantum Chromodynamics (Sect. 1.4), the fundamental theory of strong interactions, into a coherent model, classifying all known elementary particles, which include force carriers and matter particles (Sect. 1.1). Developed in the early 1970s as result of intensive research in experimental and theoretical particle physics [1], the SM has continually proven its merit, providing an extremely successful and predictive description of experimental data across a vast range of energies. Mathematically, its predictive power at different energy scales is thanks to its local gauge-invariant formulation [2] that ensures the renormalizability of the theory [3].
The success of the Standard Model culminated in the discovery of the Higgs boson in July 2012 by the ATLAS [4] and CMS [5] collaborations at CERN Large Hadron Collider (LHC) [6]. This new particle with mass around 125 GeV plays a fundamental role in actual physics because it can serve to quantify the accuracy of the Standard Model description of the world. Moreover, it confirmed the Brout-Englert-Higgs (BEH) mechanism (Sect. 1.5), which is a keystone of the SM, solving the crucial problem of incorporating mass terms for elementary particles.
Despite its powerful predictivity and accuracy, the Standard Model is unable to explain certain experimental evidence in particle physics, opening up the possibility of physics Beyond the Standard Model (BSM) requiring a transition to or extension with an even more complete theory (Sect. 1.6).

1.1 The main ingredients of the Standard Model

The Standard Model classifies all the elementary particles in two categories: bosons and fermions.
The fundamental interactions are mediated by gauge bosons, that are particles with integer spin obeying Bose-Einstein statistics [7, 8]. The photon, massless and chargeless spin-1 particle, is the mediator of electromagnetic force between electrically charged particles and it is described by the Quantum Electrodynamics. The charged W^+, W^- ($m_W = 80.4$

GeV) and neutral Z ($m_Z = 91.2$ GeV) spin-1 gauge bosons mediate the weak interactions between all fermions, responsible for processes like β-decay. Together with the photon they are responsible for electroweak interactions. The gluons are the massless spin-1 force carriers for the strong interactions and they are described in the Quantum Chromodynamics. Unlike photons, gluons being color charge carriers can interact with each other.
The Higgs boson (H), that is the only scalar spin-0 particle in the Standard Model, imparts mass to other particles (W, Z, quarks and leptons) through the spontaneous symmetry breaking mechanism described in Sect. 1.5.
Fermions, the fundamental particles with spin-1/2, are the building blocks of matter and are classified into quarks and leptons. They obey Fermi-Dirac statistics and the Pauli exclusion principle, which prevents two identical fermions from occupying the same quantum state simultaneously. Each fermion has a corresponding antiparticle with opposite charge. Quarks, which carry fractional electric charges, weak isospin and color charge, are influenced by all four fundamental forces, particularly the strong interaction mediated by gluons. Quarks and gluons are grouped together and called partons. There are six flavors of quarks: up (u), down (d), charm (c), strange (s), top (t), and bottom (b). Due to color confinement, quarks are never found in isolation but are always bound within color-neutral particles named hadrons, either as valence quark-antiquark ($q\bar{q}$) pairs, the so-called mesons, or as valence three-quark (qqq) combinations, the baryons, of which the lightest are the nucleons: the proton and the neutron. In addition to the valence quarks a hadron contains a population of other quarks. The color field is propagated by gluons with the creation of quark-antiquark pairs and subsequent annihilations, which leads to a floating population of quarks, called "sea quarks", that are essential to define their internal structure (Sect. 1.4.1).
Leptons, carry integer electric charges and interact primarily through electromagnetic and weak forces, not participating in the strong force by being colorless. The lepton family includes the electron (e), muon (μ), tau (τ), and their associated neutrinos (ν_e, ν_μ, and ν_τ), which are electrically neutral and interact via the weak force (and gravity), making them difficult to observe experimentally.
The 12 elementary fermions of the Standard Model are organized into three generations depending on their similar physical behavior. The lightest and most stable particles that compose the ordinary baryonic matter belong to the first generation, while the heavier particles that appear only in high-energy environments and decay rapidly make the second and third generations. The six quarks are arranged into three families: the $u - d$ quarks form the first generation, followed by the $c - s$, then the $t - b$. The six leptons are also divided into three families composed by the particle and its corresponding neutrino: $e - \nu_e$, $\mu - \nu_\mu$, and $\tau - \nu_\tau$.
All these particles with their properties are summarized in Figure (1.1). In the scheme the graviton, the theorized spin-2 boson mediator of gravitational interaction but not predicted by the SM, is also present.

1.2 Theoretical framework

The mathematical framework of the Standard Model is the relativistic Quantum Field Theory (QFT), in which the fundamental objects are the quantized field $\phi(x)$ that are functions of space-time coordinates $x^\mu = (x^0, x^1, x^2, x^3) \equiv (t, \boldsymbol{x})$ and particles correspond to excitation modes of these fields. The dynamics of a physical system involving a set of

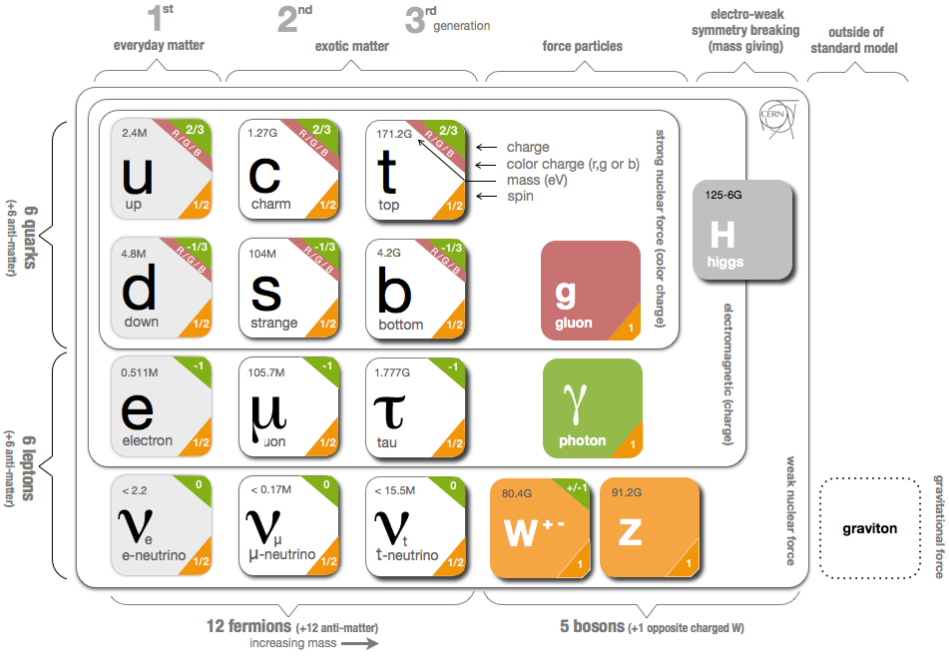

Figure 1.1: Summary of the interactions and particles with their properties composing the Standard Model [9].

fields is determined by a Lagrangian density $\mathcal{L}(\phi, \partial_\mu \phi)$, that is a functional of the field itself and its space-time derivative, yielding the action $S[\phi] = \int d^4x \mathcal{L}(\phi, \partial_\mu \phi)$. The equations of motion of classical fields are described by the *Euler-Lagrange* equations:

$$\frac{\partial \mathcal{L}}{\partial \phi_i} - \partial_\mu \left(\frac{\partial \mathcal{L}}{\partial(\partial_\mu \phi_i)} \right) = 0 \tag{1.1}$$

and they are obtained from the principle of stationary action $\delta S = 0$.
Imposing quantization conditions, in the form of equal-time (anti)commutation relations (*Heisenberg picture*), $\phi(x)$ and its conjugate momenta $\Pi(x) = \frac{\partial \mathcal{L}}{\partial(\partial_0 \phi(x))}$ are promoted to particle creation and annihilation operators acting on a quantum state[1]. The theory includes a state of minimum energy, invariant under translations, the vacuum state, from which creation operators produce states of a relativistic particle with a given mass, and with a spin defined by the transformation properties of the corresponding field.
The *spin-statistics theorem* [10] states that fields corresponding to quanta of integer spin (Bose–Einstein) must be quantized with commutation rules, while those with half-integer spin (Fermi–Dirac) with anticommutation rules.
In order to describe the particles of the Standard Model, three different type of fields are needed: spin-0 scalar field $\phi(x)$ (Higgs boson), spin-1/2 spinor fields, $\psi_\alpha(x)$ (fermions) and spin-1 vector fields, $A_\mu(x)$ (gauge bosons).
The free (non-interacting) scalar fields obey Klein-Gordon field equation $(\Box^2 + m^2)\phi(x) = 0$ where $\Box$ is the d'Alembert operator[2] and m is the mass of the field. This equation is derived

[1] The commutation rules are: $[\phi(x), \Pi(y)] = i\delta^{(3)}(\boldsymbol{x} - \boldsymbol{y})$, $[\phi(x), \phi(y)] = 0$, $[\Pi(x), \Pi(y)] = 0$.
The anticommution ones: $\{\psi_\alpha(x), \Pi_\beta(y)\} = i\delta_{\alpha\beta}\delta^{(3)}(\boldsymbol{x} - \boldsymbol{y})$, $\{\psi_\alpha(x), \psi_\beta(y)\} = 0$, $\{\Pi_\alpha(x), \Pi_\beta(y)\} = 0$
[2] $\Box = \frac{\partial^2}{\partial t^2} - \sum_{i=1}^{3} \frac{\partial^2}{\partial (x^i)^2}$

from the corresponding Klein-Gordon Lagrangian both in real and complex field case,

$$\mathcal{L}_{free}^{KG} = (\partial_\mu \phi^*)(\partial^\mu \phi) - m^2 \phi^* \phi, \tag{1.2}$$

where ϕ^* is the complex conjugate of ϕ.
The Dirac spinor field ψ_α has 4 complex components, thus incorporating both particle and antiparticle states and the kinematics is described by the free Dirac Lagrangian

$$\mathcal{L}_{free}^{Dirac} = \bar{\psi}(i\gamma^\mu \partial_\mu - m)\psi, \tag{1.3}$$

where $\bar{\psi} = \psi^\dagger \gamma^0$ and γ^0 is the first of the four 4×4 Dirac matrices γ^μ obtained from the three Pauli's matrices σ^i[3], yielding the equation for free fermions: $(i\gamma^\mu \partial_\mu - m)\psi = 0$.
The vector fields A^μ define the field strength $F_{\mu\nu} = \partial_\mu A_\nu - \partial_\nu A_\mu$ and in the massless case follow the *Maxwell* Lagrangian

$$\mathcal{L}_{free}^{Maxwell} = -\frac{1}{4} F_{\mu\nu} F^{\mu\nu} \tag{1.4}$$

that yields to equation of motion: $\partial^\nu F_{\mu\nu} = 0$. In the massive case, the equation of motion equation $\partial^\nu F_{\mu\nu} = m^2 A^\mu$ is derived from the more general *Proca* Lagrangian

$$\mathcal{L}_{free}^{Proca} = -\frac{1}{4} F_{\mu\nu} F^{\mu\nu} + \frac{1}{2} m^2 A^\mu A_\mu. \tag{1.5}$$

All free fields satisfying the respective equations allow plane-wave solutions

$$\propto \left(a_r(\boldsymbol{p}) u_r(\boldsymbol{p}) e^{-i(Et - \boldsymbol{p}\cdot\boldsymbol{x})} + b_r^\dagger(\boldsymbol{p}) v_r(\boldsymbol{p}) e^{+i(Et - \boldsymbol{p}\cdot\boldsymbol{x})} \right) \tag{1.6}$$

where $E = +\sqrt{|\boldsymbol{p}|^2 + m^2}$ and $a_r(\boldsymbol{p})$, $b_r^\dagger(\boldsymbol{p})$ are annihilation and creation operators for a general particle a and its antiparticle b of momentum $\boldsymbol{p}$. The spinor or vector features of the field, where needed, are encapsulated inside the non-operators $u_r(\boldsymbol{p})$, $v_r(\boldsymbol{p})$.
Particles are related to its antiparticle by the TCP transformation [11], a combination of time reversal ($t \to -t$), charge conjugation (particle/antiparticle charge interchange), and parity inversion ($\boldsymbol{x} \to -\boldsymbol{x}$), that guarantees that the mass, spin and, when applicable, their lifetime are exactly the same.
For a more comprehensive Lagrangian $\mathcal{L}$, the interactions between particles are needed. In general, $\mathcal{L}$ is the sum of the free part, already described and determined by fundamental particles' properties, mass and spin, and an interaction part, whose form is modelled on experimental data to compare them with the predictions resulting from the working hypotheses made about this specific part:

$$\mathcal{L} = \mathcal{L}_0 + \mathcal{L}_I. \tag{1.7}$$

In gauge theories, fundamental interactions are determined by requiring gauge invariance of the Lagrangian: the vector boson fields are introduced into the theory making it invariant under local transformations by interacting with the fundamental fields.
The Standard Model is a non-abelian Yang-Mills theory based on principle of local gauge symmetry with the symmetry group given by $SU(3)_C \times SU(2)_L \times U(1)_Y$.

[3]The γ^i matrices are defined as $\gamma^i = \begin{pmatrix} 0 & \gamma^i \\ -\gamma^i & 0 \end{pmatrix}$, $\gamma^0 = \begin{pmatrix} I & 0 \\ 0 & -I \end{pmatrix}$, where I is the 2x2 identity matrix and σ^i are the Pauli matrices: $\sigma^1 = \begin{pmatrix} 0 & 1 \\ 1 & 0 \end{pmatrix}$, $\sigma^2 = \begin{pmatrix} 0 & -i \\ i & 0 \end{pmatrix}$, $\sigma^3 = \begin{pmatrix} 1 & 0 \\ 0 & -1 \end{pmatrix}$.

According to the Noether's theorem [12], for each group symmetry, the associated charge and current are conserved. In the SM framework, the $SU(2)_L \times U(1)_Y$ group parametrizes the electroweak interaction and two charges are associated to this symmetry group: the electric charge and the weak hypercharge. The $SU(3)_C$ group describes the Quantum Chromodynamics, where three charges are present and they are named color charges.
The first gauge theory quantized was the Quantum Electrodynamics (QED) that is parametrized by the local abelian symmetry group $U(1)$. From the gauge invariance of the QED the electromagnetic interaction rises.
The Quantum Electrodynamics formalization as gauge theory can be seen as a prototype of the more complex electroweak and strong interaction theories that are characterized by non-abelian symmetry groups, and it is briefly discussed below. The starting point is the fermionic Lagrangian (Eq. (1.3)) and its invariance under $U(1)$ global transformations of the field $\psi(x)$:

$$\psi(x) \to e^{i\theta}\psi(x)\bar{\psi}(x) \to e^{-i\theta}\bar{\psi}(x), \tag{1.8}$$

and $\partial_\mu \theta = 0$ since θ is constant. By promoting global to *local* symmetry, that means transformations of the field with a location-dependent phase factor $\theta(x)$ are considered, it is not possible to obtain Lagrangian gauge invariance without introducing the electromagnetic field. In this case, if in the Dirac equation (1.3) the mass term continues to be invariant, the kinetic term does not

$$\partial_\mu \psi \to \partial_\mu \left[e^{i\theta(x)}\psi \right] = e^{i\theta(x)} \left[\partial_\mu \psi + i\partial_\mu \theta \right]. \tag{1.9}$$

The local gauge invariance is obtained by using the *covariant derivative* $D_\mu(x)$, that contains the gauge field $A_\mu(x)$, instead of the partial derivative. The vector field locally transforms as

$$A_\mu(x) \to A_\mu(x) - \frac{1}{q_0}\partial_\mu \theta(x), \tag{1.10}$$

where q_0 is a constant, and the $D_\mu(x)$ acts on the fermion field as

$$D_\mu(x)\psi(x) = \left[\partial_\mu + iq_0 A_\mu(x) \right] \psi(x), \tag{1.11}$$

recovering the local gauge invariance of the theory by cancelling exactly the undesired $\theta(x)$ partial derivative term.
The resulting quantum electrodynamics Lagrangian, considering also the gauge and Lorentz invariant kinematic term for A_μ (Eq. (1.4)), reads

$$\mathcal{L} = -\frac{1}{4}F^{\mu\nu}F_{\mu\nu} + i\bar{\psi}\gamma^\mu D_\mu \psi - m_0\bar{\psi}\psi = -\frac{1}{4}F^{\mu\nu}F_{\mu\nu} + i\bar{\psi}\gamma^\mu \partial_\mu \psi - m_0\bar{\psi}\psi - q_0 A_\mu \bar{\psi}\gamma^\mu \psi, \tag{1.12}$$

where the last term, shown in Fig. (1.2), is the interaction between the electron (fermionic field) and the electromagnetic force mediator, the photon (gauge field), that has not a mass term since it is forbidden by gauge invariance. It is important to note that m is not the physical mass of the electron, but the value that the mass would take in the absence of interactions, i.e. for $q_0 = 0$ that is the coupling constant. Typically, the interaction strength is expressed as the *fine structure constant* $\alpha = \frac{q_0^2}{4\pi} \backsimeq \frac{1}{137}$. In perturbation theory, that is allowed by the small size of α and it used to make predictions to compare with data by calculating the transition amplitudes associated with collision processes, the electron mass is indicated as $m = m_0 + \delta m$, where δm can be considered as the energy of the electric (and magnetic) field produced by the charge (and magnetic moment) of the electron. With this mass definition, $\mathcal{L}_0$ describes free electrons of mass m and the δm term is included

into interaction part $\mathcal{L}_I$. Even q_0 is not the measured electric charge of the electron, q, that is obtained by applyng the corrections which rise from the interactions. Neither m_0 nor q_0 are observables but Lagrangian parameters, and only through the renormalization procedure the theory results can be expressed in terms of the measurable quantites [13]. The QED manages to describe successfully the electromagnetic interactions up until very high energies and is predictive power is still unprecedented. Its evolution into the unified theory of the electroweak interactions is described in the next Section.

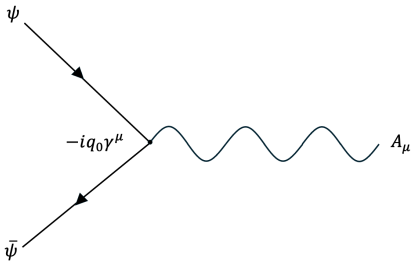

Figure 1.2: The Feynman diagram of the Quantum Electrodynamics vertex.

1.3 Electroweak (EW) interactions model

In 1934 Enrico Fermi formulated the theory of weak interactions to describe the β decay of the neutron [14]. In this theory Fermi encapsulated Pauli's intuition that to explain the continuous spectrum energy of electrons in beta decay, it is necessary to consider the emission of a massless neutral particle, later called neutrino, in addition to the electron. Analogously to the electromagnetic interaction between electron-photon, in Fig. (1.2), Fermi illustrated the weak interaction as the emission of an electron-neutrino pair during neutron decay into a proton: $n \to p + e^- + \bar{\nu_e}$ and, taking as model the QED vectorial current defined by the last term of Eq. (1.12), he made the hypothesis of a point-like vectorial current (V) interaction, $\frac{G_F}{\sqrt{2}}(\bar{p}\gamma^\mu n \bar{e}\gamma^\mu \nu)$. In this equation the particle symbols indicate the corresponding generalized field operators and $G_F \sim 1.17 \times 10^{-5} GeV^{-2}$ is the Fermi coupling constant and indicates the small strength of the weak interaction. The process is represented in Fig. (1.3).

Since in 1956 the parity violation in weak interaction was discovered by T. D. Lee, C. N.

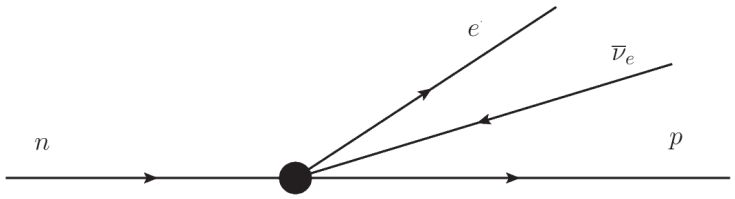

Figure 1.3: The Fermi four-point fermion interaction describing the β-decay.

Yang [15] and C. S. Wu [16], Fermi's theory was modified to include an axial vector current (A) that has $\bar{\psi}(x)\gamma^5\gamma^\mu\psi(x)$ form and does not change sign under parity transformation[4]. It is the conserved current associated to the chiral symmetry, that is the invariance of

[4] $\gamma^5 = i\gamma^0\gamma^1\gamma^2\gamma^3$

the theory under the field transformation $\psi_L(x) \to e^{i\theta_L}\psi_L(x)$ and $\psi_R(x) \to \psi_R(x)$, where $\psi_L(x) = \frac{1-\gamma^5}{2}\psi(x)$ denotes a left-handed fermionic field and $\psi_R(x) = \frac{1+\gamma^5}{2}\psi(x)$ a right-handed one. The violation of parity comes from a mixture of vectorial and axial currents with the 'V-A' form discovered by Sudarshan and Marshak [17], Feynman and Gell-Mann [18] and Sakurai [19] in 1957.

The electroweak theory was formulated by Weinberg [20] and Salam [21] in 1967 and it is a gauge theory based on the $SU(2)_L \times U(1)_Y$ symmetry group formulated by Glashow [22] in 1961. The subscript L denotes that the $SU(2)$ group acts only on the left-handed components of the lepton and quark fields that, consequently, are the only that interact with the three gauge fields $W^i_\mu(x)$ associated to the three generators $T^i = \frac{\sigma^i}{2}$ (*weak isospin operators*) of the symmetry group and corresponding to the γ, $W^\pm$ bosons. The $U(1)_Y$ generator is *weak hypercharge* Y acting on both left- and right-handed components of these fields and it is associated to a gauge boson B_μ corresponding to the Z boson. The electric charge arises as a combination of Y and T^3, that are invariant under gauge transformations:

$$Q = T^3 + \frac{1}{2}Y \tag{1.13}$$

Left-handed fermions behave as doublets under $SU(2)_L$ and they are written, conveniently and following the generations' classification, as

$$\begin{aligned} &\text{leptons: } \begin{pmatrix}\nu_e\\ e\end{pmatrix}_L, \begin{pmatrix}\nu_\mu\\ \mu\end{pmatrix}_L, \begin{pmatrix}\nu_\tau\\ \tau\end{pmatrix}_L \\ &\text{quarks: } \begin{pmatrix}u\\ d\end{pmatrix}_L, \begin{pmatrix}c\\ b\end{pmatrix}_L, \begin{pmatrix}t\\ b\end{pmatrix}_L. \end{aligned} \tag{1.14}$$

The right-handed field components transform as $SU(2)_L$ singlets: e_R, μ_R, τ_R and $u_R, c_R, t_R, d_R, s_R, b_R$.

The $U(1)_Y$ transformation does not perturb the $SU(2)_L$ structure, since both components of each doublets share the same weak hypercharge.

The electroweak Lagrangian can be written as

$$\mathcal{L} = -\frac{1}{4}B^{\mu\nu}B_{\mu\nu} - \frac{1}{4}\sum_{i=1}^{3} W_i^{\mu\nu}W^i_{\mu\nu} + i\bar{\psi}_L\gamma^\mu D_\mu\psi_L + \bar{\psi}_R\gamma^\mu D_\mu\psi_R \tag{1.15}$$

where the $\psi_{L,R}(x)$ terms encapsulate the sum over all the left-handed doublets and right-handed singlets. The $B_{\mu\nu}$ and $W^i_{\mu\nu}$ are the kinetic gauge tensors associated to their respective symmetry groups and can be expressed as

$$B_{\mu\nu} = \partial_\mu B_\nu - \partial_\nu B_\mu, \tag{1.16}$$

$$W^i_{\mu\nu} = \partial_\mu W^i_\nu - \partial_\nu W^i_\mu - g\epsilon^{ijk}W^j_\mu W^k_\nu \tag{1.17}$$

where ϵ^{ijk} is the Levi-Civita tensor whose components represent the structure constants of the $SU(2)_L$ group, while g its coupling constant.

The covariant derivative is defined according to the acting of the two symmetry groups on $\psi_L(x)$ and $\psi_R(x)$ as

$$D_\mu(x)\psi_L(x) = \left[\partial_\mu + ig'\frac{Y}{2}B_\mu(x) + ig\frac{\sigma_i}{2}W^i_\mu\right]\psi_L(x), \tag{1.18}$$

$$D_\mu(x)\psi_R(x) = \left[\partial_\mu + ig'\frac{Y}{2}B_\mu(x)\right]\psi_R(x), \tag{1.19}$$

respectively, with g' that is the $U(1)_Y$ coupling constant.
By linearly combining the two gauge fields $W_\mu^{1,2}(x)$ it is possible to obtain physical observable fields of the two charged $W^\pm$ bosons

$$W_\mu^\pm(x) = \frac{1}{\sqrt{2}}(W_\mu^1(x) \mp W_\mu^2(x)), \tag{1.20}$$

that mediate the electroweak charge interactions corresponding to a up and down weak isospin doublet components transition. By considering the terms of charge interaction by the EW Lagrangian (Eq. (1.15)) and using the gauge fields defined above, the form of the interaction-transition terms for leptons and quarks can be extrapolated: $(\bar{e}, \bar{\mu}, \bar{\tau})\gamma^\mu(1-\gamma^5)W_\mu^+(\nu_e, \nu_\mu, \nu_\tau)^T$ and $(\bar{d}, \bar{s}, \bar{b})\gamma^\mu(1-\gamma^5)W_\mu^+ V_{CKM}(u, c, t)^T$ (and their hermitian conjugate with W_μ^-), respectively. The V_{CKM} is the *Cabibbo-Kobayashi-Maskawa (CKM) unitary matrix* ([23, 24]) describing the quark mixing through

$$V_{CKM} = \begin{pmatrix} V_{ud} & V_{us} & V_{ub} \\ V_{cd} & V_{cs} & V_{cb} \\ V_{td} & V_{ts} & V_{tb} \end{pmatrix} \tag{1.21}$$

that is parametrized by three mixing angles and one complex phase, responsible for electroweak CP-violation. Every single element of this matrix indicates the coupling constant of a specific quark transition, and the universality of weak interactions is protected by requiring the unitarity of the matrix. Both V_{CKM} terms and its unitarity are tested at high precision, but further studies are ongoing at different experiments, such as general-purpose ATLAS and CMS, but especially Belle II [25] (SuperKEKB [26], Japan) and LHCb [27] (LHC, CERN), on the unitary violation due to new phenomena beyond the Standard Model.
The characterization of the neutral weak and electromagnetic interactions can be derived by rotating the two remaining gauge fields, $W_\mu^3(x)$ and $B_\mu(x)$, in a two-dimensional space by an angle θ_W:

$$Z_\mu(x) = -B_\mu(x)\sin(\theta_W) + W_\mu^3(x)\cos(\theta_W), \tag{1.22}$$

$$A_\mu(x) = B_\mu(x)\cos(\theta_W) + W_\mu^3(x)\sin(\theta_W), \tag{1.23}$$

where (θ_W) is the *Weinberg angle* (or *weak mixing angle*) and defined implicitly by the relation: $\cos(\theta_W) = \frac{g}{\sqrt{g^2+g'^2}}$. The $A_\mu(x)$ field is associated to photon as described by Quantum Electrodynamics, which is therefore incorporated into the EW theory, by requiring that the electron charge e and the weak coupling constants g and g' satisfy the relation: $e = g\sin\theta_W = g'\cos\theta_W$. The $Z_\mu(x)$ field identifies the weak neutral interaction mediator between fermions with the same *weak charge*, defined $Q_Z = \frac{1}{\sin\theta_W\cos\theta_W}(T^3 - Qsin^2\theta_W)$. The diagrams of the EW charged and neutral interaction vertices can be seen in Figure (1.4).

The gauge invariance of the theory implies the absence of any mass term associated to the gauge bosons, that is a correct description for the photon but not for the $W^\pm$ and Z weak bosons having large masses as confirmed by experimental evidence. The introduction of this mass terms into the Standard Model Lagrangian represents the consequence of the spontaneous electroweak breaking symmetry mechanism proposed by Brout, Englert and Higgs and described in Section 1.5.

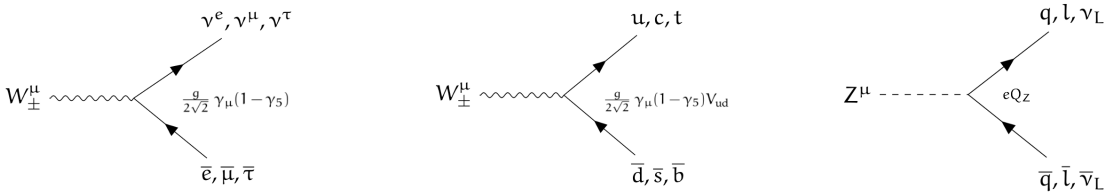

Figure 1.4: Electroweak charged interaction vertices for leptons (*left*) and quarks (*middle*). V_{ud} indicates the CKM matrix element related to the up- and down-type quarks. On the *right*, the EW neutral interaction term.

1.4 Quantum Chromodynamics theory

The Quantum chromodynamics (QCD) is the non-abelian gauge theory based on the $SU(3)_C$ symmetry group describing the strong interactions between quarks and gluons holding together in hadrons. The gluons are the gauge boson fields $G^\mu_a(x)$ with color index $a = 1, \ldots, 8$ associated to the 8 symmetry group generators $t^a = \frac{\lambda^a}{2}$, where λ^a are the Gell-Mann matrices[5]. By being the strong force mediators they are exchanged between quarks fields that are organized, following the group structure, in color triplets $q_f(x) = (q^1_f(x), q^2_f(x), q^3_f(x))$ for each flavor.
The QCD Lagrangian reads

$$\mathcal{L} = \sum_f i q_f D_\mu \gamma^\mu q_f - \frac{1}{4} G^a_{\mu\nu} G^{\mu\nu}_a. \tag{1.24}$$

The first term describes the free propagations of the quarks, for which mass term is ignored and as it will be introduced by Higgs mechanism, and their interaction with the theory gauge bosons delineated by the covariant derivative defined as

$$D_\mu(x) q_f(x) = \left[\partial_\mu + i g_s \sum_{a=1}^{8} G^a_\mu(x) t^a \right] q_f(x) \tag{1.25}$$

where g_s being the strong coupling constant equal for every quark flavour.
The gluons' kinematic is described by the Lagrangian second term through the field strength

$$G^{\mu\nu}_a(x) = \partial^\mu G^{\nu,a}(x) - \partial^\nu G^{\mu,a}(x) - g_s \sum_{b,c=1}^{8} f^{abc} G^{\mu,b}(x) G^{\nu,c}(x). \tag{1.26}$$

The last term, proportional to $SU(3)_C$ structure constants f^{abc}, represents the self-interaction of the gluons and it is implied by the non-Abelianity of the theory symmetry group. There is no equivalent term in QED as the chargeless photon interacts with electrically charged fermions while gluon carrying the color charge itself is coupled to both quarks and other gluons.

The Figure (1.5) depicts the Feynman diagrams related to the discussed QCD interaction terms. It is important to note that in strong interactions, a quark can change color charge by emitting or absorbing a gluon, but there is no mixing (flavour change) of quarks families which is allowed only by weak interaction.
For the strong interactions it is possible to identify an energy range in which the

[5]The eight Gell-Mann matrices naturally generalize the Pauli matrices for $SU(2)$ to $SU(3)$, on which Gell-Mann's quark model (*The Eightfold Way* [28]) is based.

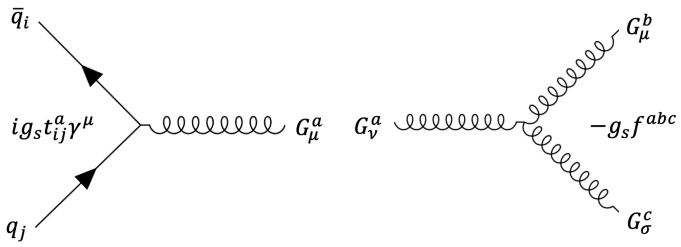

Figure 1.5: The Feynman diagrams of the QCD fundamental vertex qqg (left) and the gluon trilinear self-interaction (*right*).

perturbation theory can be applied and the related physical quantities expressed in series of strong coupling $\alpha_s = \frac{g_s^2}{4\pi}$, that is usually used instead of g_s. As direct consequence of QCD renormalization, α_s (*running* coupling) is a function of the momentum Q transferred during the interaction. At high Q, $\alpha_s \approx \frac{1}{\ln Q^2/\Lambda^2_{QCD}}$, where $\Lambda_{QCD} \sim 200$ MeV is the energy scale that sets the threshold between non-perturbative and perturbative regimes. In the limit of $Q^2 \to \infty$, the strong running coupling goes to zero, that physically means that partons behave as free particles. This property is known as *asymptotic freedom* [29, 30]. When $Q^2 \sim \Lambda^2_{QCD}$, the previous α_s expression is divergent and so not valid, $\alpha_s(\Lambda^2_{QCD})$ is large and the perturbative expansion does not provide reasonable predictions for strong processes. At this energy scale, the quarks and gluons cannot be observed in isolation but they must clump together to form colorless hadrons exhibiting another fundamental property of strong interactions: the *color confinement*. As a consequence, in the high-energy physics collisions produced in particle accelerators, partons can be detected only as *jets*, that are narrow cones of hadrons generated by the hadronization of gluons and quarks, except for the top quark that weak decays ($t \to Wb$) faster than the time scale of the process $\sim 1/\Lambda_{QCD}$.

1.4.1 Proton-Proton interactions

In proton-proton collisions induced by two beams of particles accelerated in opposite directions at hadron colliders, a parton a_1 inside the proton p_1 interacts with a parton a_2 inside the second proton p_2 realizing a partonic sub-process $\mathcal{P} \equiv (a_1 a_2 \to b_1 b_2 \dots b_n)$. The two partons carry only a fraction x_1 and x_2 of the total momentum of the respective protons and the sub-process energy is related to the center-of-mass $s = (\sum_i^2 E_i)^2 - (\sum_i^2 \boldsymbol{p}_i)^2$ of the two colliding protons through the relation $\hat{s} = (x_1 p_1 + x_2 p2)^2 \sim x_1 x_2 s$.
The total cross section for a specific hadronic process $pp \to X$ can be written as an incoherent sum of all partonic cross-sections

$$\sigma(p_1, p_2) = \int dx_1 dx_2 \sum_{\mathcal{P}_i} f_{a_1}(x_1, \mu_F^2) f_{a_2}(x_2, \mu_F^2) \hat{\sigma}_{\mathcal{P}_i}(\hat{s}, \alpha_s(\mu_R), Q^2; \mu_F, \mu_R) \tag{1.27}$$

where the $f_{a_i}(x_i, \mu_F^2)$ are the parton distribution functions (PDF), that indicate the probability that the parton involved in the interaction carries a fraction $x_i \in [0, 1]$ of the proton's momentum and they are convoluted with the $\hat{\sigma}(\hat{s})$, that is partonic cross-section for a given hard scattering process. The equation formalizes the QCD factorization theorem stating how an inclusive cross-section can be factorized into a *short distance* contribution computable in perturbative QCD as a power-series in α_s, $\hat{\sigma}$, and a *long distance* contribution, the PDFs, that is not perturbatively calculable but it can be extracted from data. The renormalization scale μ_R defines the scale for the strong coupling constant α_s calculation,

while μ_F is the factorization scale representing the scale that divides the short-distance physics from the long-distance one.
The Formula (1.27) is the result of many theoretical studies and experimental observations and its most important features are presented below.
The starting point is the *parton model* initially formulated by Feynman in 1969 for analyzing the high energy hadron collisions [31]. According to this model, any hadron is composed of point-like partons that in transverse scattering behave as quasi-free particles. In the naive quark model, the parton distribution functions $f_i(x)$ were introduced. The expected value of the fraction of proton momentum carried by the i-th parton is $\langle x \rangle_i = \int dx x f_i(x)$ and by summing on all partons of the proton the requirement is

$$\sum_i \int_0^1 dx x f_i(x) = 1. \tag{1.28}$$

If the proton is considered to be composed solely of valence quarks, *uud*, which is the constituent composition indicated by $SU(3)$, the parton distribution functions $f_i(x)$ would be peaked at $x = 1/3$. However, the quarks inside the proton are not completely free. Due to their mutual interactions, they can emit Bremsstrahlung gluons which in turn can produce quark-antiquark $q\bar{q}$ pairs, including $c\bar{c}$ and $s\bar{s}$ pairs. These quarks are named "sea quarks".
In the parton model, the parton distribution functions are directly related to the structure functions F_1 and F_2, which are a measure of the partonic structure of hadrons and are typically extracted from the deeply inelastic scattering processes:

$$F_2(x) = \sum_i e_i^2 x f_i(x) \quad , \quad F_1(x) = \frac{1}{2x} F_2(x), \tag{1.29}$$

where the second equation connecting the two structure functions is known as the *Callan-Gross relation*. In this equation, the x refers to Bjorken x_{Bj}, defined as $x \equiv \frac{Q^2}{2M\nu} \leqslant 1$, where M is the mass of the proton and ν is the energy exchanged between the lepton and the proton, which in deep inelastic scattering is so high that the proton structure is fragmented into a multi-hadronic state X with an invariant mass greater than that of the single proton (there is no conversion of kinetic energy into the formation of new hadrons). The Bjorken x, varying from 0 to 1, defines how much a scattering is elastic: the limit $x = 1$ corresponds to a totally elastic scattering and there is no proton fragmentation. If x is fixed, the structure functions do not depend on Q^2, and this phenomenon is known as *Bjorken scaling* [32], which has been observed in deeply inelastic collisions.
If the proton and neutron are considered as bound states of only up and down quarks, *uud* and *udd*, the sum rules, using the Equation (1.29), are

$$\int_0^1 dx F_2^{(p)}(x) = \frac{4}{9}\langle x \rangle_u + \frac{1}{9}\langle x \rangle_d \tag{1.30}$$

$$\int_0^1 dx F_2^{(n)}(x) = \frac{1}{9}\langle x \rangle_u + \frac{4}{9}\langle x \rangle_d. \tag{1.31}$$

The possibility of quarks to radiate gluons has consequences for Bjorken scaling, which is violated at high energy. The various emissions of soft and collinear gluons from a quark extracted from a proton in a deeply inelastic collision follow one another in a cascade of gluons that can, in turn, radiate other gluons and quark pairs, producing a *parton shower*. These emissions are perturbative, since α_s is small at the energy scales involved, and

as emissions proceed, α_s becomes larger until $\alpha_s \sim 1$, where the perturbative region is no longer valid, and the phenomenon of color confinement cannot be ignored. This is the *hadronization process*, and considering the formula in exam, (1.27), it is regulated by the μ_R renormalization scale: the transition from perturbative parton shower to non-perturbative hadron composition corresponds to the decrease of Q^2 below the value of μ_R.
Most of the radiation produced does not lead to the formation of a jet of hadrons different from the one forming around the initial quark. Hard gluons or those emitted at a large angle are very rare at high energy, but not suppressed, and their presence is important as it modifies the structure functions. Through a theoretical treatment of radiative corrections to the partonic cross-section, aimed at addressing the soft and collinear divergences that arise from the use of matrix element prescription, the structure functions (Eq. (1.29)) take the following form:

$$\frac{F_2(x,Q^2)}{x} = \sum_i e_i^2 \left[f_i(x,\mu_F^2) + \frac{\alpha_s}{2\pi} \int_x^1 \frac{dy}{y} f_i(y,\mu_F^2) P_{qq}\left(\frac{x}{y}\right) \ln \frac{Q^2}{\mu_F^2} \right] \tag{1.32}$$

where the first term in parenthesis corresponds to the renormalized naïve parton model quark distribution[6], and $x/y = z$ is the ratio of quark momentum before and after the emission of a gluon that carries a fraction of momentum $1 - z$ (soft divergence for $z \to 1$). $P_{qq}(z)$ is the splitting functions, that are proportional to the probability to find a daughter quark with momentum fraction z of the parent quark from which it is split.

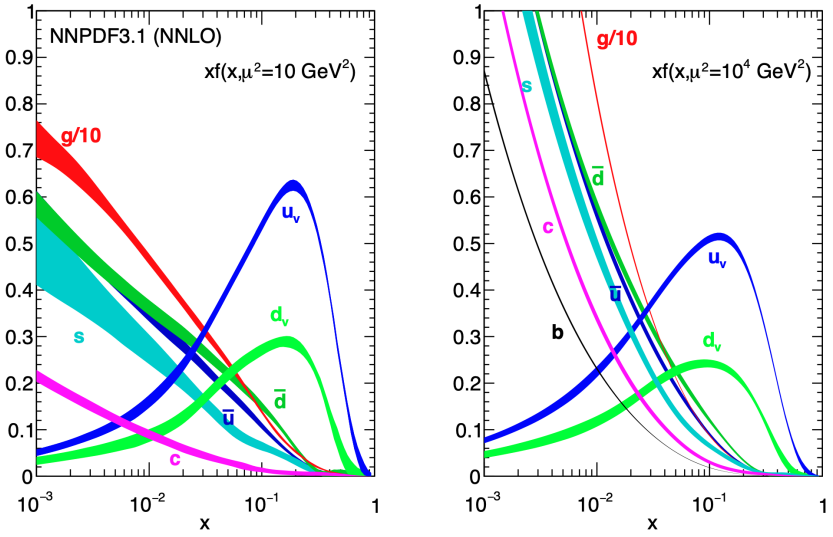

Figure 1.6: Evolution of the parton distribution functions for protons from a $\mu^2 = Q^2 = 10$ GeV^2 (*left*) scale up to 10^4 GeV^2 (*right*). It can also be noted the different contributions that sea and valence quarks have at low and high x.[33].

The formula (1.32) indicates that in QCD, F_2 and the quark PDFs are also functions of Q_2, contrary to the predictions of Bjorken scaling, whose violation is a trace of gluon radiation. By using a similar approach, an additional correction to the equation is given by the process of gluon annihilation into a $q\bar{q}$ pair from which the dependence of gluon's parton distribution function on Q^2 emerges. Moreover, an usual and consistent choice is

[6]Specifically, $f_i(x,\mu_F^2) = f_i(x) + \frac{\alpha_s}{2\pi}\int_x^1 \frac{dy}{y} f_i(y) P_{qq}\left(\frac{x}{y}\right) ln\frac{\mu_F^2}{\lambda}$, where λ is a lower transverse momentum cut-off to regularize the gluon collinear divergence.

to set $\mu_R^2 = \mu_F^2 \sim Q^2$, avoiding large logarithms in partonic cross-sections.
From (1.32) the *Dokshitzer-Gribov-Lipatov-Altarelli-Parisi* (DGLAP) equation [34, 35, 36], describing the PDF evolution from a Q^2 scale to any other Q^2 scale (Fig. (1.6)), is derived:

$$\mu_F^2 \frac{\partial f_i(x, \mu_F^2)}{\partial \mu_F^2} = \sum_j \int_x^1 \frac{dz}{z} P_{ij}(z) f_j(\frac{x}{z}, \mu_F^2). \tag{1.33}$$

It is a master equation of QCD, since even if the parton densities cannot be computed, it allows to extract PDFs at some energy scale (for example, $\sqrt{s} = 318$ GeV at HERA [37]) from experimental data and evolve upwards to make LHC ($\sqrt{s} = 13 - 13.6$ GeV) predictions.
In the modeling of proton-proton collisions, additional residual effects must be considered. Beyond the partons involved in the hard scattering process, the remnants of the colliding protons, known as 'spectator' partons, need to form color-neutral hadrons due to QCD color confinement. These spectators may interact with particles resulting from the hard interaction. Furthermore, multiple parton interactions (MPI) with significant momentum transfer can occur within a single proton-proton collision. These interactions can overlap and produce indistinguishable detector responses, creating a large QCD background (underlying event) that make the rare and interesting processes difficult to reveal. Lastly, there is the possibility for additional particle emissions, such as photons and gluons, both in the initial and final states. These processes, known as initial state radiation (ISR) and final state radiation (FSR), represent 'real' corrections to Standard Model processes, as these emitted particles are detectable in the event. An illustration of the *pp* collision is presented in Fig. (1.7).

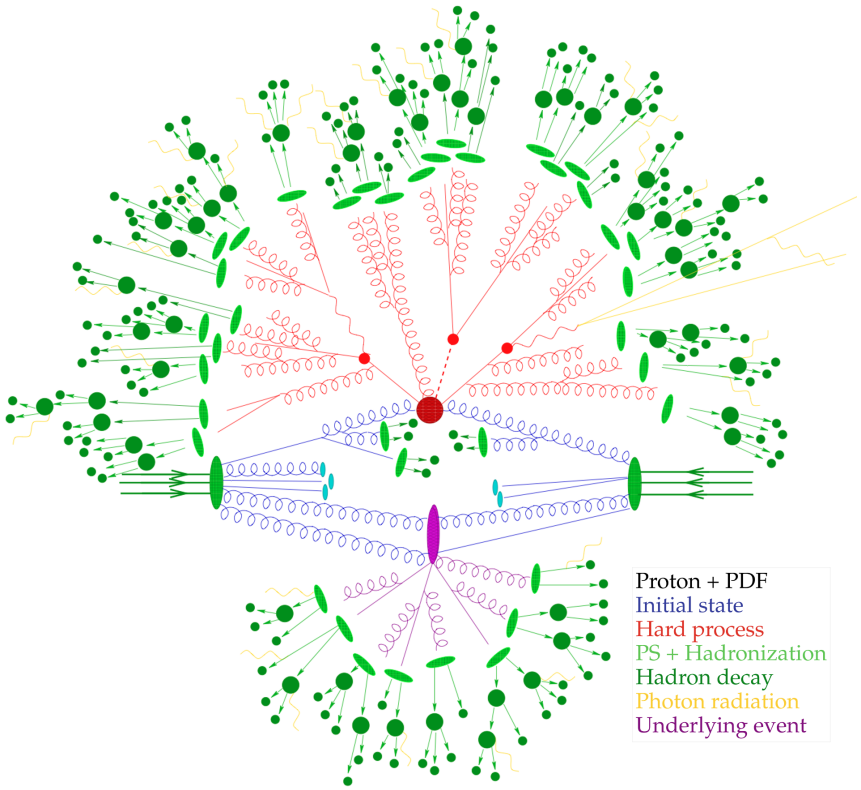

Figure 1.7: A picture of a *pp* collision with correlated processes [38].

1.5 Spontaneous Symmetry Breaking: The Brout-Englert-Higgs mechanism

The most important feature of the Standard Model is the mechanism of spontaneous electroweak breaking symmetry (EWBS) to the electromagnetic symmetry, $SU(2)_L \times U(1)_Y \rightarrow U(1)_Q$, by which the masses of weak vector bosons (and fermions) are generated preserving the gauge symmetry of the theory at high energy. This process was proposed about forty years ago by Higgs, Brout and Englert (BEH) [39, 40].
In order to cause the breaking of the symmetry, a new type of complex scalar spin-zero field called the Higgs field is introduced. In the SM scheme this new field is a $SU(2)_L$ doublet with nonzero $U(1)$ hypercharge, but a singlet in color space. The breaking is a consequence that the Higgs field, unlike the other fields, has a nonzero vacuum expectation value: it's supposed that the vacuum state, where usually there are no particles, is populated by massive Higgs bosons.
In the Standard Model the Higgs field reads

$$\Phi = \begin{pmatrix} \phi^+ \\ \phi^0 \end{pmatrix} = \frac{1}{\sqrt{2}} \begin{pmatrix} \phi_1 + i\phi_2 \\ \phi_3 + i\phi_4 \end{pmatrix}, \; Y_\phi = +1 \tag{1.34}$$

where ϕ_i with $i = 1, ..., 4$ are properly normalized real scalar fields. The Higgs Lagrangian can be written as an extension of that of the Klein-Gordon for a complex field (Eq. (1.2)) with the addition of a self-interaction term of strenght λ:

$$\mathcal{L} = (D_\mu \Phi)^\dagger D^\mu \Phi - \mu^2 \Phi^\dagger \Phi - \lambda (\Phi^\dagger \Phi)^2 = (D_\mu \Phi)^\dagger D^\mu \Phi - V(\Phi) \tag{1.35}$$

where the invariant product is $\Phi^\dagger \Phi = \frac{1}{2}(\phi_1^2 + \phi_2^2 + \phi_3^2 + \phi_4^2) = \frac{1}{2}\phi_i \phi^i$.
The first term of Eq. (1.35) contains the kinetic and gauge-interaction terms via the electroweak covariant derivative expressed in Eq. (1.18). The second term, $V(\Phi) = \mu^2 \Phi^\dagger \Phi + \lambda (\Phi^\dagger \Phi)^2$, is the scalar Higgs potential. By imposing $\lambda > 0$ to ensure that the potential is bounded below, two cases can be distinguished: for $\mu^2 \geq 0$, there is no spontaneous symmetry breaking since $V(\Phi)$ has an unique minimum at $\Phi_0 = 0$, while for $\mu^2 < 0$ it has a minimum at:

$$\Phi^\dagger \Phi = \frac{-\mu^2}{2\lambda} = \frac{v^2}{2}, \tag{1.36}$$

where v is the the vacuum expectation value (VEV) of the field, $\langle 0|\Phi|0\rangle$. In this case, $V(\Phi)$ minimization can be reached via infinite possible configurations of the field which is reflected in a degeneracy of equivalent minima along a circumference. The shape of the potential is shown in Fig. (1.8). The gauge transformations of $SU(2)_L \times U(1)_Y$ group correspond to rotations in a four-dimensional space: there are four independent transformations but only three independent rotation directions for a vector in a four-dimensional space. There is one combination of the $SU(2)_L$ and $U(1)_Y$ transformations that leaves the vacuum state invariant and it is not broken by the Higgs field and represents the gauge transformation of electromagnetism. The potential $V(\Phi)$ is invariant under these rotations [42].
The basis of states $\phi_1, ..., \phi_4$ is chosen to be oriented however we like relative to the local vacuum value and choose the VEVs of the four field to be

$$\langle \phi_3 \rangle \equiv \; v = \sqrt{\frac{\mu^2}{\lambda}}, \qquad \langle \phi_1 \rangle = \langle \phi_2 \rangle = \langle \phi_4 \rangle = 0 \tag{1.37}$$

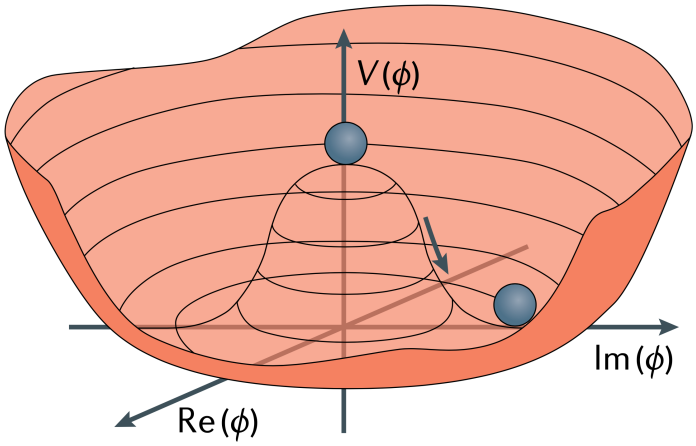

Figure 1.8: Higgs potential $V(\Phi)$ shape with $\mu^2 < 0$ in the Re(Φ)-Im(Φ) space [41].

with this choice, for $\mu^2 < 0$, the component that develops a nonzero vacuum value is the neutral one:

$$\Phi_0 = \langle 0|\Phi|0\rangle = \begin{pmatrix} 0 \\ \frac{v}{\sqrt{2}} \end{pmatrix}. \tag{1.38}$$

In this way, the conservation of electric charge is ensured. In fact the electric charge on the doublet in Eq. (1.34) is represented by the matrix:

$$Q = \begin{pmatrix} +1 & 0 \\ 0 & 0 \end{pmatrix} \tag{1.39}$$

so the Φ_0 is invariant under $U(1)_Q$ transformations:

$$e^{i\alpha Q}\Phi_0 = \begin{pmatrix} e^{i\alpha} & 0 \\ 0 & 1 \end{pmatrix} \begin{pmatrix} 0 \\ \frac{v}{\sqrt{2}} \end{pmatrix} = \Phi_0. \tag{1.40}$$

The breaking symmetry induced by $\Phi_0 \neq 0$ realizes the $SU(2)_L \times U(1)_Y \to U(1)_Q$ scheme. By defining a new real scalar field $H(x)$, with zero vacuum value, as $\phi_3(x) = v + H(x)$, the doublet becomes

$$\Phi = \frac{1}{\sqrt{2}} \begin{pmatrix} \phi_1 + i\phi_2 \\ v + H(x) + i\phi_4 \end{pmatrix}. \tag{1.41}$$

A two-dimensional spinor can be expressed to a spinor with the only *down and real* component through a transformation of the symmetry group, depending on the point (as shown in Ref. [43]). This is called the *non-linear realization*:

$$\Phi = \frac{1}{\sqrt{2}} \exp\left(\frac{i\xi^a(x)\sigma^a}{v}\right) \begin{pmatrix} 0 \\ v + H(x) \end{pmatrix} \tag{1.42}$$

where $H(x)$ and $\xi^a(x)$ are fields. This expression is equivalent to Eq. (1.34) up to first order in the fields, i.e., for infinitesimal fluctuations around the vacuum[7].
Consider the $SU(2)_L$ gauge transformations of Φ:

$$\Phi(x) \to \exp\left(i\lambda_L^a(x)\frac{\sigma^2}{2}\right)\Phi \tag{1.43}$$

[7]To linear order, $\xi^1 = \phi_2$, $\xi^2 = \phi_1$, $\xi^3 = -\phi_3$.

if we choose $\lambda_L^a(x) = -2\xi^2/v$ we arrive at a gauge, called *unitary gauge*, in which

$$\Phi = \frac{1}{\sqrt{2}}\begin{pmatrix} 0 \\ v + H(x) \end{pmatrix}. \tag{1.44}$$

By using this Φ expression inside the kinetic term of the Higgs Lagrangian (Eq. (1.35)),

$$\begin{aligned}(D^\mu\Phi)^\dagger(D_\mu\Phi) = &\frac{1}{2}(\partial_\mu H)^2 \\ &+\frac{g^2v^2}{4}W^{+,\mu}W^-_\mu + \frac{1}{2}\frac{g^2v^2}{4cos^2\theta_W}Z^\mu Z_\mu \\ &+\frac{g^2v}{2}W^{+,\mu}W^-_\mu H + \frac{g^2v}{4cos^2\theta_W}Z^\mu Z_\mu H^2 \\ &+\frac{g^2}{4}W^{+,\mu}W^-_\mu H^2 + \frac{g^2}{8cos^2\theta_W}Z^\mu Z_\mu H^2,\end{aligned} \tag{1.45}$$

the mass terms (second row of the previous equation) for the $W^\pm_\mu$ and Z_μ gauge fields emerge

$$m_W = m_Z \cos\theta_W = \frac{gv}{2}. \tag{1.46}$$

The last two rows of the Eq. (1.45) indicate the cubic (HVV) and quartic interactions ($VVHH$) between the Higgs field and the two gauge bosons, respectively. The couplings are proportional to the W and Z boson masses.
The potential term of the Higgs Lagrangian becomes

$$V = \frac{\mu^2}{2}(0, v+H)\begin{pmatrix} 0 \\ v+H \end{pmatrix} + \frac{\lambda}{4}\left|(0, v+H)\begin{pmatrix} 0 \\ v+H \end{pmatrix}\right|^2 \tag{1.47}$$

and using the relation $v^2 = -\mu^2/\lambda$, one obtains

$$V = -\frac{1}{2}\lambda v^2(v+H)^2 + \frac{1}{4}\lambda(v+H)^4. \tag{1.48}$$

Thus, V takes the usual form[8]:

$$V = \lambda v^2 H^2 + \lambda v H^3 + \frac{1}{4}\lambda H^4 \tag{1.49}$$

and from this potential, one can see that the Higgs boson mass reads

$$m_H^2 = 2\lambda v^2 = -2\mu^2 \tag{1.50}$$

here the Higgs vacuum expectation value $v \simeq 246$ GeV can be related to the Fermi constant, $v = (\sqrt{2}G_F)^{-\frac{1}{2}}$, and measured in muon decay. By indicating the Higgs trilinear and quartic self-couplings with $\lambda_3^{\rm SM}$ and $\lambda_4^{\rm SM}$, respectively, the scalar potential can be written as

$$V = \frac{1}{2}m_H^2 H^2 + \lambda_3^{\rm SM} v H^3 + \lambda_4^{\rm SM} H^4, \tag{1.51}$$

$$\lambda_3^{\rm SM} = \frac{m_H^2}{2v^2} \sim 0.13, \qquad \lambda_4^{\rm SM} = \frac{m_H^2}{8v^2}, \tag{1.52}$$

where $m_H \sim 125$ GeV. Since the leading-order contributions to double Higgs boson pair production *directly* cross section depend directly on the Higgs trilinear coupling, di-Higgs

[8] Doing the calculations another term comes out $-\frac{1}{4}\lambda v^4$ but it is not H dependent and contributes to the *vacuum energy*.

is the standard process for studying $\lambda^3_{\rm SM}$ at the LHC and its observation could precisely define the Higgs potential, finally probing in a satisfactory way the scalar sector of the Standard Model. Even the single Higgs production is sensitive to modifications of the Higgs trilinear self-coupling, but in this process such coupling affects only the higher-order corrections to cross section. However, manifestation of new physics could modify the Higgs potential at low energy, by altering the value of the Higgs self-interactions. A deviation from the SM predicted self-coupling value λ_3^{SM}, corresponding to a deviation of its modifier parameter

$$\kappa_\lambda = \frac{\lambda_3}{\lambda_3^{SM}} \tag{1.53}$$

from unity, may point to physics beyond the Standard Model (κ-framework [44]). In Chapter 3 the phenomenology of the Higgs boson at the hadron colliders will be discussed, with particular attention to the Higgs boson pair production.
Lastly, for the generation of the fermion masses through spontaneous symmetry breaking it is necessary to construct a new Lagrangian term. The gauge invariance of the theory forbids fermion mass terms due to its chiral structure, as the $SU(2)_L \times U(1)_Y$ group acts differently on left-handed and right-handed spinor components, making the mass term of Eq. (1.3), $m(\bar{\psi}_L\psi_R + \bar{\psi}_R\psi_L)$, not gauge invariant. The most general invariant Lagrangian terms involving the Higgs doublet and fermions are the *Yukawa interaction terms*

$$\mathcal{L}_{Yukawa} = -\sum_{f=l,q} y_f(\bar{\psi}_L\Phi\psi_R + \bar{\psi}_R\Phi\psi_L) \tag{1.54}$$

where y_f are the *Yukawa couplings* for leptons and quarks. In this case, the flavor-mixing for the quarks produced by EW charged interactions and expressed by V_{CKM} matrix is neglected[9].
By using the Φ field expression after symmetry breaking, Eq. (1.44), the Lagrangian terms take the forms

$$\mathcal{L}^{leptons}_{Yukawa} = -\frac{y_l}{\sqrt{2}}(v\bar{l}_L l_R + \bar{l}_L l_R H) + h.c \tag{1.55}$$

$$\mathcal{L}^{quarks}_{Yukawa} = -\frac{1}{\sqrt{2}}v(y_d\bar{d}_L d_R + \tilde{y_u}\bar{u}_L u_R) - \frac{1}{\sqrt{2}}(y_d\bar{d}_L d_R + \tilde{y_u}\bar{u}_L u_R)H + h.c \tag{1.56}$$

for leptons and quarks[10], respectively. The conjugate component of the scalar doublet $\tilde{\Phi} = i\sigma_2\Phi^*$ is necessary for the presence of right-handed down-type quarks and generates the $\tilde{y}$ couplings. The fermion masses corresponds to the terms proportional to the VEV and they are correlated to the Yukawa coupling through the relation

$$m_f = \frac{y_f v}{\sqrt{2}}, \tag{1.57}$$

that manifests how the dependence of interaction between the massive fermions and the Higgs field is proportional to the involved fermion mass ($-\frac{y_f}{\sqrt{2}}\bar{\psi}\psi H$): the larger the fermions mass, the larger the coupling to the Higgs.

[9] The results obtained under this assumption corresponds to those derived in the complete scheme after the rotation to the fermion eigenstate basis that diagonalizes the Higgs-fermion interaction mass matrix.
[10] $u_{L,R}$ indicates the up-type quarks (u, c, t), $d_{L,R}$ the down-type quarks (d, s, b).

1.6 Beyond the Standard Model

Despite its high predictivity and validation through numerous experimental measurements, the Standard Model (SM) is known to be an incomplete "effective" theory. It does not incorporate gravity and, while neutrino oscillations provide evidence for neutrino mass, the Standard Model requires a minimal extension to account for it, such as through the addition of three mass terms and a mixing matrix in the Pontecorvo-Maki-Nakagawa-Sakata (PMNS) formalism [45, 46], analogous to the CKM treatment of quarks (Eq. (1.21)). Furthermore, while the SM does not directly explain the nature of dark matter, and it does not offer a direct explanation for dark energy either, some hypotheses suggest that dark energy could be related to elements already within the Standard Model framework, such as the zero energy associated with the Higgs potential. These issues are significant given that dark matter and dark energy constitute most of the universe's energy ($\sim$75%) and matter ($\sim$95%). Additionally, it does not account for the observed matter-antimatter asymmetry. One of the main theoretical challenges suggesting the SM's incompleteness is the hierarchy problem. This problem arises from the large discrepancy between the electroweak scale ($\sim$100 GeV) and the Planck scale ($\sim 10^{19}$ GeV). The Higgs boson mass should naturally be much higher due to quantum corrections, which are proportional to the Plank energy scale. To match the observed Higgs mass of $\sim$125 GeV, these large corrections must cancel out almost perfectly, which seems highly improbable without fine-tuning. This implies theoretically, under the assumption of a fundamental theory at the Planck scale incorporating the SM, that new physics might be needed at the TeV scale to stabilize the Higgs mass and solve this problem.

These theoretical and experimental gaps suggest that the Standard Model needs to be extended or complemented with additional theories to provide a consistent description of all physical systems.

A theoretical framework addressing these issues is supersymmetry (SUSY), which posits that for every boson, there is a fermion partner, and vice versa. This theory could potentially unify general relativity and quantum mechanics through supergravity. However, no experimental evidence for SUSY particles has been found so far.

Another approach to extending the Standard Model is through the use of the Standard Model Effective Field Theory (SMEFT) by including higher-dimensional operators that respect the SM symmetries. These operators parameterize possible new physics effects at energy scales above the electroweak scale, providing a bridge between the observed physics at this low energy scale and the theoretical challenges posed by the Planck scale, offering insights into whether and how new physics might solve the hierarchy problem and address other fundamental issues of the Standard Model.

The new physics effects are included into the effective field theory (EFT) framework by adding new operators with canonical dimensions D larger than 4[11] to the SM Lagrangian:

$$\mathcal{L} = \mathcal{L}_{SM} + \sum_i \frac{c_i^{(6)}}{\Lambda^2} O_i^{(6)} + \sum_i \frac{c_i^{(8)}}{\Lambda^4} O_i^{(8)} + \cdots. \tag{1.58}$$

Here c_i are the *Wilson coefficients* and Λ is the SM cut-off, i.e. the scale at which the new dynamics is present and the Higgs self-coupling values deviate from all ones predicted by

[11] $\mathcal{L}_{SM}$ is defined dimension 4 since the action $S = \int d^4x \mathcal{L}_{SM}$ is always dimensionless and $\left[d^4x\right] = -4$. From the dimensional analysis of QFT Lagrangians: $[\phi] = [A_\mu] = 1$ and $[\psi] = 3/2$.

the Standard Model and it is typically set to 1 TeV[12]. The O_i^D are $SU(3)_C \times SU(2)_L \times U(1)_Y$ invariant operators and their contribution to amplitudes of physical processes at the energy scale of order v goes as $(v/\Lambda)^{D-4}$. Since $v/\Lambda < 1$ by construction, the EFT in its validity regime typically describes small deviations from the SM predictions.
The main motivation for using this framework is its model-independent nature that allows to interprete the constraints on the EFT parameters as bounds on masses and couplings of new particles in many beyond the Standard Model theories: translation of experimental data into a theoretical framework has to be done only once in the EFT context, rather than for each BSM model separately.
The leading new physics effects are associated with EFT operators with the lowest dimensionality, namely the dimension-6 ones. The contributions from $D \geq 8$ operators are suppressed by at least $(v/\Lambda)^4$ and they will be assumed negligible. In this simplified case, the new physics is considered CP-preserving and flavor universal and thanks to these restrictions, there are only 10 independent operators that influence Higgs physics at leading order.
A convenient choice for dimension-6 operators is provided by the *Higgs basis* in which the Higgs is assumed to be part of an $SU(2)_L$ doublet, as described in the previous Section, linearly realizing (the expansion in Higgs powers is valid) the EW simmetry. Otherwise, a more complex structure is necessary, considering that a much larger set of dimension-6 operators could, in principle, be relevant for Higgs physics. The advantage of this basis is that the operators connected to the LHC Higgs searches are separated from the others that can be estimated in observables not involving the Higgs. The 10 effective operators can be split into three class: the first one contains deformations of the Higgs couplings to the SM gauge bosons, parametrized by

$$\delta c_z, \quad c_{zz}, \quad c_{z\Box}, \quad \hat{c}_{z\gamma}, \quad \hat{c}_{\gamma\gamma}, \quad \hat{c}_{gg}, \tag{1.59}$$

the second class is related to modifications of the fermion Yukawa's couplings

$$\delta y_t, \quad \delta y_b, \quad \delta y_\tau, \tag{1.60}$$

and the last effect is a variation of the Higgs trilinear self coupling

$$\delta\lambda_3. \tag{1.61}$$

In the unitary gauge, the relative corrections to the Higgs boson interaction are given by

$$\begin{aligned}
\mathcal{L} \supset \frac{H}{v}\Bigg[& \delta c_w \frac{g^2 v^2}{2} W^+_\mu W^{-\mu} + \delta c_z \frac{(g^2+g'^2)v^2}{4} Z_\mu Z^\mu \\
& + c_{ww}\frac{g^2}{2} W^+_{\mu\nu} W^{-\mu\nu} + c_{w\Box} g^2 (W^-_\mu \partial_\nu W^{+\mu\nu} + h.c.) + \hat{c}_{\gamma\gamma}\frac{q^2}{4\pi^2} A_{\mu\nu}A^{\mu\nu} \\
& + c_{zz}\frac{g^2+g'^2}{4} Z_\mu Z^\mu + \hat{c}_{z\gamma}\frac{q\sqrt{g^2+g'^2}}{2\pi^2} Z_{\mu\nu}A^{\mu\nu} + c_{z\Box} g^2 Z_\mu \partial_\nu Z^{\mu\nu} + c_{\gamma\Box} g g' Z_\mu \partial_\nu A^{\mu\nu} \Bigg] \\
& + \frac{g_s^2}{48\pi^2}\left(\hat{c}_{gg}\frac{H}{v} + \hat{c}^{(2)}_{gg}\frac{H^2}{2v^2}\right) G_{\mu\nu}G^{\mu\nu} - \sum_f \left[m_f \left(\delta y_f \frac{H}{v} + \delta y_f^{(2)} \frac{H^2}{2v^2} \right) \bar{f}_R f_L + h.c. \right] \\
& - (\lambda_3^{SM} + \sigma\lambda_3) v H^3
\end{aligned} \tag{1.62}$$

[12]The odd energy dimension operators are excluded because they violate lepton number conservation, for D=5, and B-L invariance, for all odd D. However, these effects are very small and can be neglected.

where $\delta c_w = \delta c_z$, $\hat{c}_{gg}^{(2)} = \hat{c}_{gg}$ is the Higgs contact interaction with gluons, and the others parameters c_{ww}, $c_{w\Box}$, $c_{\gamma\Box}$, $\delta y_f^{(2)}$ are dependent quantities obtained by combining the 10 effective parameters. The variable $\delta\lambda_3$, used in Eq. (1.62), denotes the shift of the SM trilinear coupling due to new physics.
The Lagrangian (Eq. (1.62)) of this SMEFT minimal model as proposed in Ref. ([47]) describes the most important operators contributing to the single Higgs process, which is sensitive to self-coupling deformation but only indirectly at higher-order cross section corrections and it is overshadowed by other effects produced by new physics resulting in deviations of Higgs couplings with other gauge fields and fermions. In this case, a global analysis considering deviations in all Higgs couplings simultaneously is essential for accurate evaluation. The identification of a minimal set of effective operators describing the effects due to the modified Higgs self-coupling is easier for the di-Higgs processes, since being directly dependent by such coupling, suffer less than possible corrective contributions generated by the other interactions.
The goal of many analyses is to impose increasingly stringent constraints on the Wilson coefficients of operators of the EFT Lagrangians describing the anomalous Higgs interactions that can alter single-Higgs and di-Higgs production cross-sections, kinematics and decay rates.

Lastly, interesting considerations arise when exploring the relationship between the Higgs potential structure (Eq. (1.51)), its self-coupling, and the cosmological theory of inflation [48]. Inflation addresses key cosmological questions such as the universe's flatness, homogeneity, and isotropy, along with the origin of primordial density fluctuations that seeded structure formation.
Theories of cosmological inflation postulate a scalar field, the inflaton, that drives the rapid expansion of the universe during the inflationary epoch, which is hypothesized to have occurred shortly after the Big Bang. Although the inflaton remains unidentified, it could be any scalar field capable of mimicking a slow-moving field during the early universe. While most models treat the inflaton as an additional field beyond those found in the Standard Model of particle physics, some propose that the Higgs field itself could fulfill this role, thus linking particle physics and cosmology. This possibility, however, depends on the precise behavior of the Higgs potential at high energies.

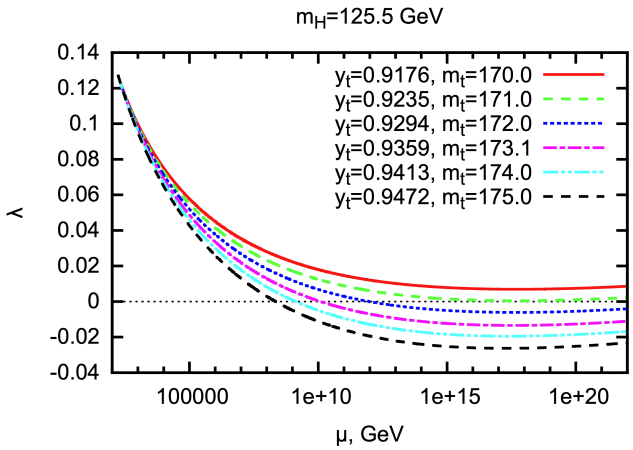

Figure 1.9: Higgs self-coupling running following from the SM renormalization group equations for several values of the top quark Yukawa coupling at the EW scale, with the Higgs boson mass fixed at 125.5 GeV [49].

As shown in Fig. (1.9), the Higgs self-coupling λ, following from the SM renormalization group equations, evolves with the energy scale μ, decreasing across configurations for various top quark Yukawa couplings (y_t). In some cases, it remains positive up to the Planck scale, while in others, it potentially turns negative, even before the inflationary scale of $\sim 10^{16}$ GeV, raising concerns about vacuum stability at high scales. The correlation between m_t (the top quark mass) and electroweak vacuum stability is crucial for discussing Higgs-driven inflation models, as variations in m_t impact whether the universe remains stable. Despite current data suggest stability, and the SM can be extended up to the inflationary scale, with the Higgs field coupled to gravity being responsible for inflation, future experiments may reveal metastability. This raises open questions regarding the feasibility of Higgs inflation and motivates further investigation into the connection between high-energy cosmology and particle physics [49, 50].

Chapter 2

The ATLAS experiment at the LHC

2.1 The Large Hadron Collider at CERN

Large Hadron Collider (LHC) [6] is the world's most powerful particle accelerator, and it was constructed by the European Organization for Nuclear Research (CERN) in the same 27-km circular tunnel that housed its Large Electron-Positron Collider (LEP) [51], situated 100 meters of depth underground on the France-Switzerland border.
Particle colliders accelerate two beams of particles in opposite directions to induce collisions for subsequent study in adjoining particle detector experiments. Lepton colliders initially demonstrated significant results, including the co-discovery of the J/Ψ particle in 1974 [52, 53] alongside fixed-target hadron machines, contributing to the understanding of charm physics. However, the necessity for higher center-of-mass energies to explore new physics phenomena posed challenges for lepton colliders.
Circular colliders, unlike linear variants, allow particles to pass through accelerating sections repeatedly during each revolution to gradually increase their energy up to desired nominal value. During the radial acceleration, to maintain circular trajectory, particles emit synchrotron radiation with an energy loss proportional to $\frac{E^4}{m^4 R}$. Large accelerators like LEP, where electrons collided with positrons at energies of 209 GeV travelling along a 27-km circumference, are favored by the inverse dependence of the energy loss on the bending radius R, but practical size constraints restrict achievable energies for circular lepton colliders. Moreover, the energy loss also goes with the inverse of the fourth power of the particle mass, indicating as the use of protons in colliders, like the LHC, is preferred for achieving higher collision energies, thanks to an energy loss reduction by a factor of $(m_p/m_e)^4 \sim 10^{13}$.
In two parallel beam pipes mantained at ultrahigh vacuum and temperature close to absolute zero, the LHC is designed to accelerate protons in a ring to energies up to 7 TeV and lead atoms up to 2.76 TeV per nucleon.
The LHC represents the final step of a multi-stage accelerator system illustrated in Fig. (2.1). Starting with a hydrogen source, a metal cylinder (duoplasmatron) surrounded by an electrical field is used to strip hydrogen gas of its electrons, creating a proton beam with an energy of 90 keV. The protons are then accelerated in four stages. First, a linear accelerator (LINAC 4), consisting of radio-frequency (RF) cavities, increases the protons' energy to 50 MeV. Next, the Proton Synchrotron Booster (PSB) pushes the energy up to 1.4 GeV. This is followed by the Proton Synchrotron (PS), a 628-meter-long synchrotron that further accelerates the protons to 25 GeV. The PS can also accelerate α particles, oxygen ions, electrons, positrons and antiprotons. Finally, the Super Proton Synchrotron

(SPS), a synchrotron with a circumference of about 7 Km, accelerates the proton beams up to 450 GeV before injecting them in the LHC's two beam pipes.

Upon entering in the LHC, the protons are separated into two beams travelling in opposite

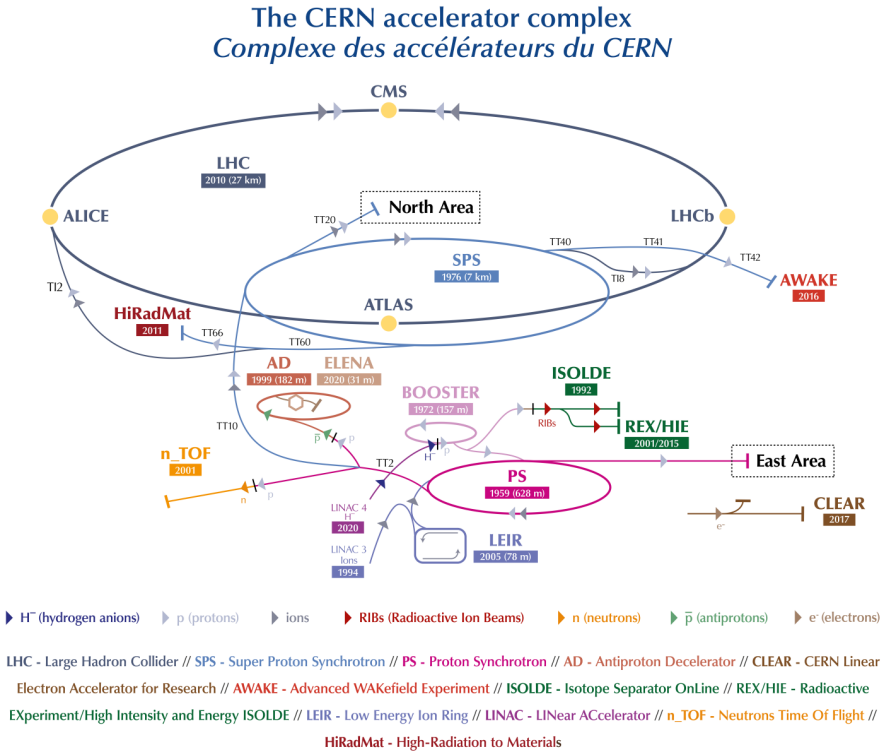

Figure 2.1: The CERN accelerator's complex. The LHC is the last ring (dark blue line) of this chain of particle accelerators and where the four largest experiments are located [54].

directions. In the LHC, counter-rotating particles are accelerated by resonant electromagnetic waves generated in eight radio-frequency cavities per beam. Each cavity operates in a superconducting state at a temperature of 4.5 K, maintaining an accelerating field of 2 MV per cavity at a frequency of $f_{RF} \sim 400$ MHz. The total theoretical energy gain per revolution is of 16 MeV per proton. The longitudinal acceleration provided is necessary to increase the beam energy to the maximum current energy of 6.8 TeV.

Bending magnets provide the transverse acceleration necessary to keep the particles on a circular trajectory. At the LHC, 1232 dipole superconducting magnets maintain the protons in orbit [55]. These magnets are cooled to a temperature of 1.9 K by superfluid helium, supplying a magnetic field of 8.33 T. To enhance the probability of pp interactions, quadrupole magnets focalize the accelerator beams that are confined to a diameter of approximately 10 μm.

Moreover, to further increase the possibility of having collision interactions, protons are grouped in bunches along their travel in the accelerators' chain. During the Proton Synchrotron acceleration, proton bunches are separated by a 25 ns interval and can contain up to $\sim 10^{11}$ protons. Once the protons reach their maximum energy, the two oppositely directed bunches are made to collide, resulting in the so-called Bunch Crossing (BC).

At four specific IPs the experiments are located to collect and analyze the collisions delivered by the LHC: the ATLAS and CMS experiments [4, 5] are multipurpose detectors located at the opposite LHC sides (Fig. (2.1)) and they focus primarily on proton-proton col-

lisions. Despite differing architectures and particle detection methodologies, both achieve comparable performance levels and serve as crucial cross-checks for physics measurements, yielding independent results. These experiments are designed to explore physics by exploiting the large energy and luminosity of the LHC, probing both the Standard Model of particle physics and potential new physics phenomena. Additionally, both experiments investigate collisions involving lead ions.
The Large Hadron Collider beauty (LHCb) experiment [27] is a single arm forward spectrometer and it specializes in precise particle tracking to analyze rare decays of long-lived b and c hadrons aiming at measuring with high accuracy the CP violation.
The Large Ion Collider Experiment (ALICE) is dedicated to studying collisions involving heavy lead ions to examine the properties of quark-gluon plasma [56]. In the CERN accelerator complex, several smaller experiments are also present. The Total Elastic and Diffractive Cross Section Measurement (TOTEM) experiment studies charged particles emitted near the beam line in the forward direction within the CMS detector to determine the total proton-proton cross section and an independent measurement of the instantaneous luminosity [57]. The Large Hadron Collider forward (LHCf) experiment, which consists of two detectors located on either side of the ATLAS experiment in a distance of 140 m to the interaction point, analyzes neutral forward particles to studies models of hadron interactions at very high energies [58]. The Monopole and Exotics Detector at the LHC (MoEDAL) experiment, an extension of LHCb, aims to discover particles carrying magnetic charge (magnetic monopoles) [59].

2.1.1 Luminosity and pile-up events

A collider is mainly characterized by two work parameters: the center of mass energy $\sqrt{s}$, that determines the type of particles that can be produced, detected and then studied, and the instantaneous luminosity $\mathcal{L}$, that is related to the discovery of rare events.
The instantaneous luminosity depending on the beam parameters of the particle accelerator provides the collider performance, and it can be written as

$$\mathcal{L} = \frac{n_{beam} N_{bunch}^2 f_{rev} \gamma}{4\pi \epsilon_n \beta^*} \tag{2.1}$$

where n_{beam} is the number of proton bunches inside the ring (2808 for 25 ns), N_{bunch} is the number of particles per bunch (nominal at 25 ns $1.15{\cdot}10^{11}$), f_{rev} is the revolution frequency of the bunches in the LHC tunnel(11.2 kHz for protons), γ is the proton beam energy in unit of rest mass ($\sim$7460), ϵ_n is the normalized transverse beam emittance (nominal design: 3.75 μm), β^* is the beta function (focal length) at the collision point (nominal design: 0.55 m) and F represents the geometric luminosity reduction factor due to the incidence angle of the beams (0.85 at $\beta^* = 0.55$) [60, 61]. The frequency of collisions is given by multiplying the frequency f_{rev} by the total number of filled bunches: $f_{collision} = 40$ MHz.
With these nominal parameters, the accelerator can operate with luminosity up to 10^{34} $\mathrm{cm}^{-2}\mathrm{s}^{-1}$. While ATLAS and CMS were designed to operate at this high luminosity, LHCb and ALICE at low luminosity, 10^{32} $\mathrm{cm}^{-2}\mathrm{s}^{-1}$ and 10^{27} $\mathrm{cm}^{-2}\mathrm{s}^{-1}$, respectively.
The rate of production of a particular process N_{event} with cross section σ_{event} is directly proportional to the instantaneous luminosity:

$$\frac{dN_{event}}{dt} = \mathcal{L} \cdot \sigma_{event}. \tag{2.2}$$

The total number of events produced and collected can be obtained by integrating the previous equation in a given time interval

$$N_{event} = \int \mathcal{L} \cdot \sigma_{event} dt = L \cdot \sigma_{event} \tag{2.3}$$

where L is the integrated luminosity that measures the size of the collected dataset. An increase of the accelerator luminosity results in a larger number of signal events. Moreover, the previous equation shows that the cross section of a certain event can be calculated by measuring the number of events produced and the accelerator luminosity: to produce events with very low cross sections, a very high luminosity is necessary.
Hence, maximizing luminosity is crucial for particle accelerators. Although it is very challenging to enhance luminosity by increasing the bunch revolution frequency f_{rev} and the number of colliding bunches N_{bunch}, because protons in the ring already travel near the speed of light, the LHC performance upgrades focus on increasing the number of protons in each bunch n_{beam} and reducing the total bunch collision area by squeezing the proton beams in the transverse plane.
Despite the advantages for physics of working with high luminosity, it can also result in a negative impact on the detectors' performance, primarily due to difficulty in distinguishing interesting hard interactions from the rest of the soft particle collisions. This effect is known as the *pile-up* contamination of the event, and it is usually treated as a background for the physics analyses performed by ATLAS. In addition to the general *in-time* pile-up, which refers to the contamination of signal events by multiple interactions occurring simultaneously within the same bunch crossing, there is also *out-of-time* pile-up, that indicates the contamination of the detector by collisions from previous and subsequent bunch crossings in the accelerator.
The pileup at the LHC is quantified by the mean number of interactions per crossing $\langle\mu\rangle$, calculated as the mean of the Poisson distribution of the number of interactions per bunch crossing μ. This quantity depends on the instantaneous luminosity of the beams

$$\langle\mu\rangle = \frac{\mathcal{L} \cdot \sigma_{inel}}{f_{rev}} \tag{2.4}$$

where σ_{inel} is the total inelastic cross-section. Although not precisely known, a reference value of $\sigma_{inel} = 80$ mb [62] is conventionally used by all LHC experiments for pp collisions. The pile-up contamination affects also the reconstruction of the event physics objects (jets, photons and leptons), that will be discussed in Section 2.3, degrading their energy resolution and creating a denser environment in the particle detector's tracker making the reconstruction of tracks and vertices more challenging.

2.1.2 LHC operational roadmap

Since the LHC first became operational in September 2008, albeit with initial testing delayed until November 2009 due to a magnet quench incident causing extensive mechanical damage, the accelerator at CERN has consistently increased its center-of-mass energy and luminosity to achieve the nominal design operational values of $\sqrt{s} = 14$ TeV and $\mathcal{L} = 1 \cdot 10^{34} cm^{-2} s^{-1}$. The entire operational history of the Large Hadron Collider can be divided into several alternating phases of data-taking and long shutdowns dedicated to upgrades of the LHC and experiments' detectors to gradually improve their performance. Even though the ATLAS detector was designed to perform optimally under the LHC nominal conditions for proton-proton collisions, and for a peak instantaneous luminosity of

$\mathcal{L} = 10^{27}$ cm^{-2}s^{-1} of heavy ion (p+Pb and Pb+Pb) collisions at 5.5 TeV per nucleon pair, it operated effectively despite the more demanding conditions reached by the LHC over the years. The performance, by upgrading the subsystems and their electronics, and analysis techniques were adjusted and improved to maintain the experiment's excellent physics. During the last data acquisition period (2015-2018), ATLAS has achieved a data-taking efficiency of approximately 95%, which represents the fraction of time during stable LHC collisions that ATLAS collects data. Additionally, $\sim$ 97.5% of the collected data is declared good for physics analysis [63].

The first phase is the **Run-I** (2009-2013), in which the LHC had its first recorded proton-proton collision in 2009 at an energy of 450 GeV per beam. In 2010 the proton beam energy had been increased up to 3.5 TeV making the LHC the highest energy particle collider ever built and starting the first period of data acquisition, which ended in 2013. In 2012, the center-of-mass energy was upgraded from its original $\sqrt{s} = 7$ GeV up to 8 GeV and a peak instantaneous luminosity of $7.7 \cdot 10^{33} cm^{-2} s^{-1}$ is reached, even if at double the design bunch-crossing separation, 50 ns instead of 25 ns. The total delivered luminosity was around 30 fb^{-1}. The discovery of the Higgs boson and the precise measurements of its properties were made possible by the data collected during this phase.

For ATLAS, it recorded 5 fb^{-1} of pp collision data at $\sqrt{s} = 7$ GeV and 21 fb^{-1} at $\sqrt{s} = 8$ GeV, 167 μb^{-1} of Pb+Pb collisions in 2010 and 2011 and 29.8 nb^{-1} of p+Pb collisions in 2013.

After Run-I, LHC underwent a two-year **Long Shutdown 1 (LS1)**, from 2013 to 2015, dedicated to upgrades and marking the beginning of the so-called *Phase-0*. This shutdown focused on consolidating LHC machine components to raise the center-of-mass energy and achieve the designed luminosity. Major repairs were carried out across the LHC and its injector chain. The improvements included repairing over 10,000 high-current splices in the superconducting magnets, replacing 18 dipole magnets, and implementing new safety systems to support higher beam energies. Upgrades to the collimation system, injection kicker magnets, and injection protection system were also made to handle longer bunch trains with 25 ns spacing and increased luminosity.

The data-taking period during Phase-0 is known as **Run-II** and it started in 2015. The LHC reached a peak instantaneous luminosity of $2.1 \cdot 10^{34} cm^{-2} s^{-1}$ in 2018 (Fig. (2.2a)), surpassing the designed value, and a $\sqrt{s}$ of 13 TeV close to the nominal one. The total luminosity certified to be good quality data for physics analysis is 139 fb^{-1} (Fig. (2.2b)). There were on average 33.7 interactions per bunch crossing during Run-II, with a peak value of over 60 interactions record in 2017-2018 as shown in Fig. (2.2c).

ATLAS recorded 147 fb^{-1} of proton-proton collision data at $\sqrt{s} = 13$ TeV; 179.8 nb^{-1} of p+Pb collisions were recorded in 2016 and 1.76 nb $^{-1}$ of Pb+Pb collisions were recorded in 2018. After the end of Run-II in 2018 a second upgrade period of **Long Shutdown (LS2)** began and the LHC *Phase-I* started.

During LS2 (2019-2022) [65], the current linear accelerator (LINAC 4) was installed into the injector complex taking the place of its predecessor (LINAC 2) [66], and the Proton Synchrotron Booster's injection beam energy was upgraded to reduce beam emittance. Moreover, new cryogenics plants were installed to improve the cooling systems of the superconducting RF cavities and magnets. All these upgrades and others allowed the LHC to handle beams up to 60% more intense in more safely condition.

The LHC is currently in the Phase-I data acquisition, the **Run-III**, started in 2022 and

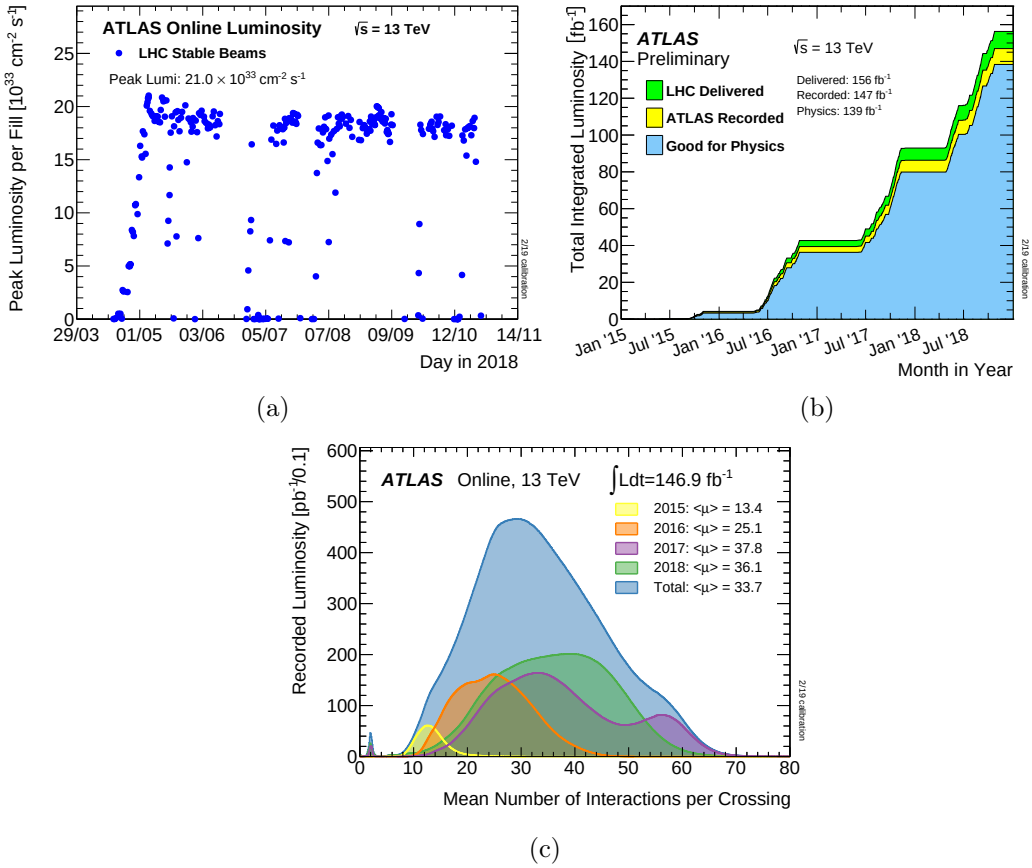

Figure 2.2: From Left to Right: the peak instantaneous luminosity delivered to ATLAS for each LHC fill versus time (2018), the total integrated delivered (green), recorded (yellow) and good quality for physics (blue) luminosity, and the average number of interactions per bunch crossing $\langle\mu\rangle$ during LHC Run-II 13 TeV pp collisions [64].

that will end in 2025. In this data-taking period the pp collision energy is increased to 13.6 TeV, while the peak instantaneous luminosity continues to be limited to approximately $2.2 \cdot 10^{34} cm^{-2} s^{-1}$ in ATLAS, primarily due to heat deposition affecting the inner triplet magnets, which are highly exposed to proton-proton collision debris, as they are responsible for the final beam focusing before the interaction point. The Run-III expected integrated luminosity is ~250 fb^{-1}, with an average of up to 60 interactions per bunch crossing. Figures (2.3) show the multi-year summary plots of the current Run-III data-taking including a comparison with the previous Runs.

The *Phase-II* will begin after the conclusion of Run-III and LHC will be shut down for the third two-year upgrade period (LS3) scheduled for 2026-2028. The significant enhancement of LHC components, such as low-β quadrupole triplets and crab cavities at the interaction regions, will result in its upgrade to the High-Luminosity LHC (HL-LHC), planned to be operative from 2029 with the starting of the Run-IV data-taking. In HL-LHC, the proton-proton center-of-mass energy will be of 14 TeV and the instantaneous luminosity will increase up to 5.0-7.5 times its original design value, with a predicted pile-up of $\langle\mu\rangle = 200$ [67].

The ATLAS detector is expected to collect an integrated luminosity of approximately 3000 fb^{-1} by the end of LHC operations, improving the sensitivity to rare new physics processes which are statistically limited. To address these HL-LHC conditions, the ATLAS trigger and data acquisition system will undergo significant upgrades to ensure better physics

object reconstruction, calibration, and pileup suppression, enabling the identification and discrimination of new physics events.

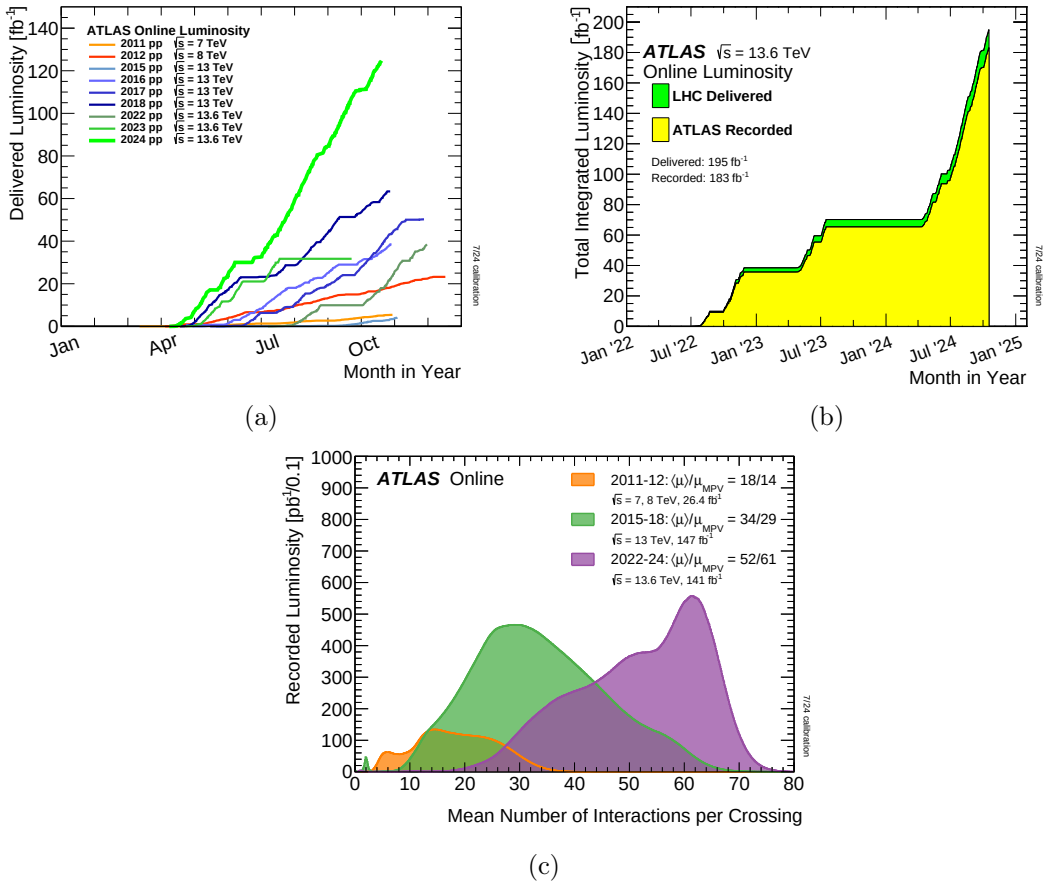

(a) (b)

(c)

Figure 2.3: From Left to Right: delivered luminosity to ATLAS per day for 2011-2024 *pp* collisions; total integrated luminosity as a function of time delivered to (green) and recorded by ATLAS (yellow) during LHC Run-III (2022-2024) 13.6 TeV *pp* collisions; comparison between interactions per crossing from all three Runs [68]. Updated to October 2024.

2.2 The ATLAS experiment

ATLAS (A Toroidal LHC ApparatuS) [4, 69] is a general-purpose particle detector at the Large Hadron Collider. It is the largest particle detector ever built, with a length of 44 m, a diameter of 25 m and a weight of 7000 tons. The detector is structured in three concentric cylindrical sub-detector systems at the centre of which lies the interaction point (IP), which is the intersection between two beam pipes, that contain beams of protons traveling at near light-speed in opposite directions. The protons collide with a center of mass energy of approximately 13.6 TeV in the current Run-III configuration.
Close to the beam line, there is the Inner Detector (ID), that allows to reconstruct the tracks and measure the momentum of the charged particles produced in collisions. It provides also the identification of the interaction vertices. The calorimeter system is placed around the ID and it is composed by an electromagnetic calorimeter (ECAL), dedicated to the identification of electromagnetic showers, and a hadronic calorimeter (HCAL), needed to identify and measure the energy of hadronic jets. Lastly, the Muon Spectrometer (MS), located in the outermost region of the detector, is dedicated to the identification and high

precision measurement of muons and their momentum.
These sub-detectors are divided longitudinally in three regions, the central part, called barrel and the two edges of the cylinder, called endcaps. The geometric acceptance is close to 4π sr in solid angle.
Two separate magnetic systems produce the magnetic fields that allow the measurement of the momentum of the charged particles by curving their trajectory: a 2 T solenoid magnet surrounds the Inner Detector, while a 8-coil toroidal magnetic system (0.1-3 T) plays the same role for the Muon Spectrometer.
The ATLAS detector system is shown in Fig. (2.4).

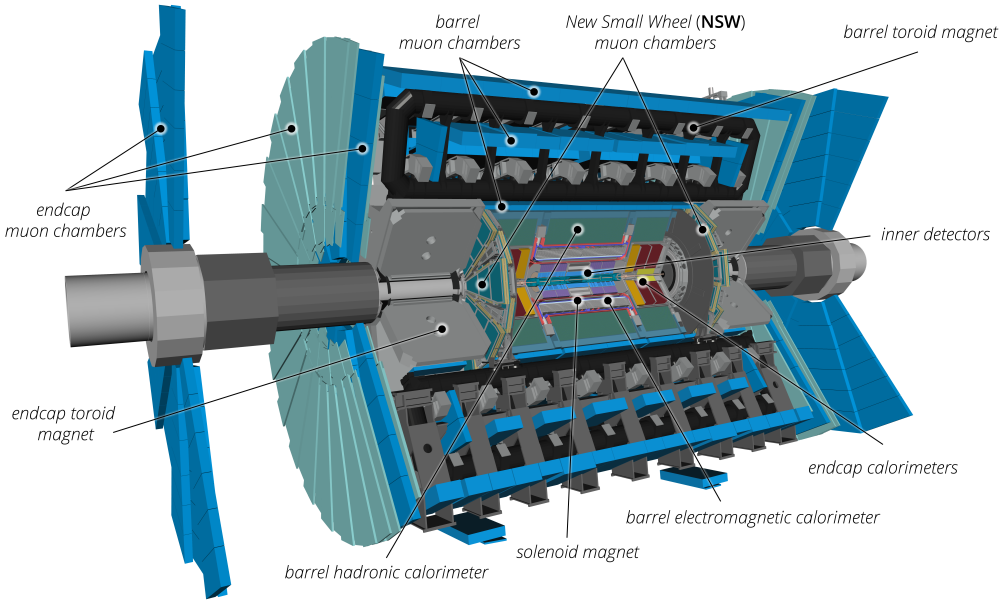

Figure 2.4: Section view of the ATLAS detector's Run-III configuration and the locations of the all sub-systems [69].

2.2.1 Coordinate system and kinematic variables

ATLAS uses a xyz right-handed coordinate system centered in the nominal interaction point of the beams, where the z-axis is defined along the beam direction, the x-axis points towards the center of the LHC ring and the y-axis is pointing upwards. The detector part in the positive z-direction is called side A, the part in the negative z-direction side C.
This reference system is usually defined by cylindrical coordinates: the radial coordinate R, the distance from the beam line in the $x-y$ plane, the azimuth angle ϕ, measured around the beam, and the polar angle θ, measured with respect to the beam axis. In this coordinate reference system, useful kinematic variables can be defined to be invariant for Lorentz boost along the longitudinal axis, which is important for hadron collisions as the interacting partons carry different longitudinal momenta whose spectrum is determined by the parton distribution functions as explained in Sect. 1.4.1. The rest frames of the parton-parton interactions will have different longitudinal boosts.
Since in the center of mass of the two protons the transverse momentum is zero and must remain so after the interaction for momentum conservation, it is useful to define the boost-invariant variables related to the projection on the transverse xy-plane.
For a particle of mass m and four-momentum $p^\mu = (E, p_x, p_y, p_z)$, two important longitu-

dinal boost invariant quantities are

$$p_T = \sqrt{p_x^2 + p_y^2} = |\boldsymbol{p}| \sin\theta, \;\; E_T = E \sin\theta \tag{2.5}$$

that define the transverse momentum and energy, respectively.
Instead of the polar angle θ to denote the directions, the *pseudorapidity* relative to the z-axis is usually used and defined as

$$\eta = -\ln \tan \frac{\theta}{2}. \tag{2.6}$$

The pseudorapidity is the approximation in the limit of negligible particle mass, or equivalently when the particle is travelling close to the speed of light, of another important quantity used to describe physics objects at hadron colliders known as *rapidity*:

$$y = \frac{1}{2} \ln \frac{E + p_z}{E - p_z} \; . \tag{2.7}$$

This choice of preferring rapidity (or pseudorapidity) over the polar angle θ is motivated precisely by the longitudinal Lorentz invariance of the difference between the rapidities Δy ($\Delta\eta$) of two particles. The ATLAS coordinate system and η distribution are illustrated in Fig. (2.5).

From the previous quantities, another important z-axis boost invariant variable can be

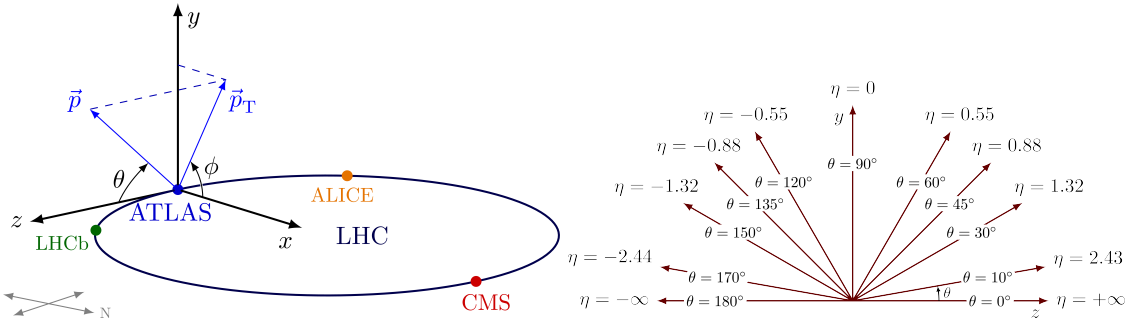

(a) (b)

Figure 2.5: The ATLAS coordinate system (a), including LHC and the other three large experiments, and the pseudorapidity η distribution (b) [70].

derived,

$$\Delta R = \sqrt{(\Delta\eta)^2 + (\Delta\phi)^2} \; , \tag{2.8}$$

that is the angular separation between two physics objects in the $\eta - \phi$ plane, which is useful for the reconstruction and definition of jets, as it will be discussed in Sect. 2.3.

2.2.2 Inner Detector

The Inner Detector system is the innermost sub-detector of the ATLAS experiment, and its layout is shown in Figure (2.6). Enveloped in the 2 T axial magnetic field produced by the central solenoid, the ID measures the momentum and the charge of the particles generated in the *pp* collisions from the curvature of their trajectory, which are defined through high-resolution position measurements, points typically known as *hits*. The information collected by the ID are then utilized to reconstruct the charged particles' tracks and identify the primary vertices from particle interactions and the possible secondary vertices generated

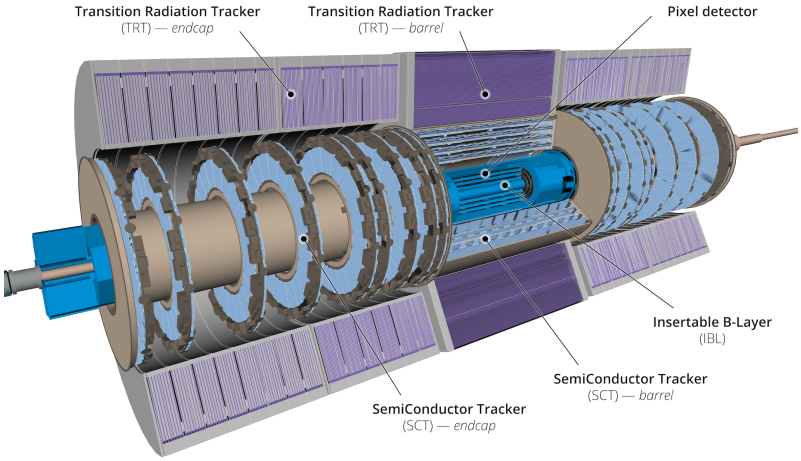

(a)

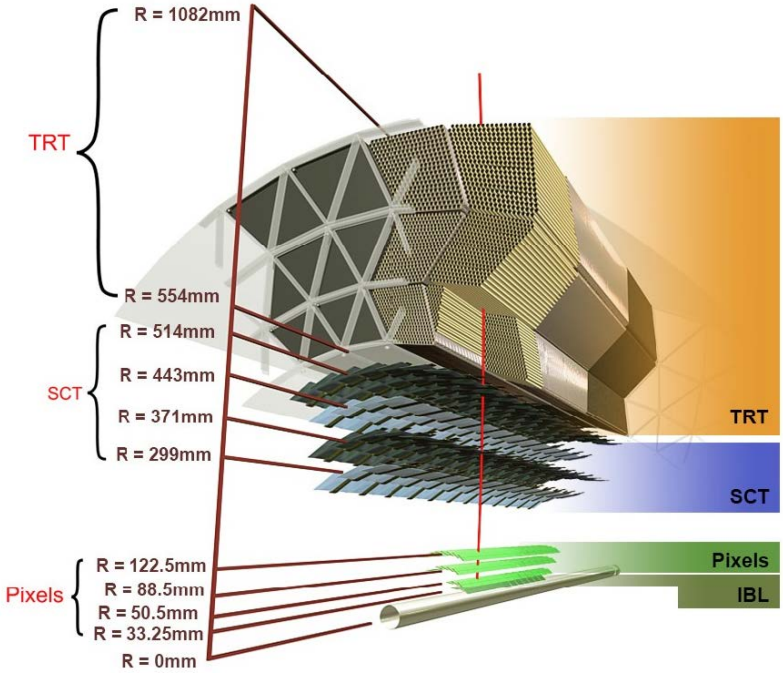

(b)

Figure 2.6: Cut-away view of the ATLAS Inner Detector (a) and its components (b) [69].

from the long-lived particles decay.
The inner detector provides an accurate and effective tracking for charged particles with transverse momentum $p_T > 0.5$ GeV in the pseudorapidity range of $|\eta| < 2.5$, achieving a transverse momentum resolution of:

$$\frac{\sigma_{p_T}}{p_T} \approx 0.05\% p_T \oplus 1\% \ , \tag{2.9}$$

where $\oplus$ indicates that the two contributions are summed in quadrature. In $|\eta| < 2.5$, two precision tracking detectors are present: the Pixel detector [71] and the Semiconductor Tracker (SCT) [72]. The ATLAS Pixel detector includes three-barrel concentric layers around the beam axis and three discs on each endcap side, comprising about 80 million readout channels. The silicon pixel detectors near the vertex region have highest granularity to resolve the primary and secondary interaction vertices. Each track crosses the

three layers segmented in $R-\phi$ and z and composed of identical pixel sensors with size of 50 μm×400 μm, furnishing an accuracy in the barrel region of 10 μm on $R-\phi$ and 115 μm on z, while of 10 μm ($R-\phi$) and 115 μm (R) in the endcaps.
An additional layer, the *Insertable b-layer* (IBL), was installed during LS1 in the inner detector's part and became operational at the start of Run-II data taking [73]. The IBL sensors characterized by 50 μm×250 μm pixels allow to add a further measurement point very close to the IP, enhancing the identification of secondary vertices and the detection of jets from b-quark hadronization.
The SCT comprises eight strip layers and approximately 6.3 million readout channels, providing four space points for each track. In the barrel region, the detector uses small-angle (40 mrad) stereo strips to measure both $R-\phi$ and z, with 80 μm-pitch strips in each layer parallel to the beam direction contributing to $R-\phi$ measurements. In the endcap region, there are both radial and 40 mrad stereo strips with a pitch roughly similar to that of barrel strips. The intrinsic accuracies per module in the barrel are 17 μm in the $R-\phi$ plane and 580 μm along z-axis, while in the discs are 17 μm ($R-\phi$) and 580 μm (R).
The Transition Radiation Tracker (TRT) [74], located at the outermost part of the ID, consists of several layers of gas-filled (70% Xe, 27% CO_2, and 3% O_2) straw tubes interleaved with transition radiation material. A resolution of 130 μm on $R-\phi$ is reached for charged particle tracks ($p_T > 0.5$ GeV) whose reconstruction is extended up to $|\eta| = 2$ thanks to this detector, that serves for tracking and electron identification by detecting transition radiation X-ray photons.

2.2.3 Calorimeter system

The ATLAS calorimeter system [75] is composed by two sub-systems: the electromagnetic calorimeter and the hadronic calorimeter. Designed to be hermetic with a fine segmentation, this system enables the reconstruction of photons, electrons, hadronic jets, and neutrinos via the measurement of the missing transverse energy (MET), determining the energies and positions of both charged and neutral particles that interact electromagnetically or strongly.
The calorimeter system is positioned outside the inner detector and the central solenoid, covering the pseudorapidity region $|\eta| < 4.9$. Over this η range, high-density absorbing materials, that degrades the energy of incoming particles creating a shower of secondary particles which are fully absorbed, are interleaved with active layers, that provide a measurable signal by collecting the deposited energy.
ATLAS utilizes two sampling calorimeter technologies: Liquid Argon (LAr) [76] for the electromagnetic calorimeters and all the endcap and forward calorimeters, and scintillating Tiles [77] for hadron calorimetry in the central region.
The LAr Calorimeter system includes several subsystems, namely the LAr Electromagnetic Barrel Calorimeter (EMB), the LAr Electromagnetic Endcap Calorimeter (EMEC), the LAr Hadronic Endcap Calorimeter (HEC) and the Forward Calorimeter (FCal).
The EMB and EMEC cover the $|\eta| < 3.2$ region and they are complemented by a high-granularity thin LAr presampler in $|\eta| < 1.8$ that corrects for energy loss in calorimeters' material upstream and can reconstruct neutral pions decaying to two photons and particles whose shower begins in the inner detector. After presampler, in the η region where the ID provides tracking, the fine granularity $\Delta\eta \times \Delta\phi$ of the electromagnetic calorimeter

allows for precision measurements of electrons and photons. The rougher granularity of the outer hadronic calorimeter suffices for detection of shower generated by hadrons and started inside the EM calorimeter, jet reconstruction and missing transverse momentum (E_T^{miss}) measurements.
In the barrel region, $|\eta| < 1.7$, the hadronic calorimetry is given by a steel/scintillator-Tile calorimeter.
The HEC consists of layers of copper absorber alternating with liquid Argon as active material. This subsystem comprises two wheels for each endcap, located next to the EM calorimeter endcaps, covering the region $1.5 < |\eta| < 3.2$, with a slight overlap with the Tile calorimeter. The FCal completes the solid angle coverage ($3.1 < |\eta| < 4.9$) with three modules: the first optimized for electromagnetic measurements using copper/LAr, and the other two modules for hadronic measurements using tungsten absorbers to minimize the hadronic shower lateral spread.
The energy resolution of the ATLAS ECAL is:

$$\frac{\sigma_E}{E} \approx \frac{10\% \div 17\%}{\sqrt{E}} \oplus 0.7\%, \tag{2.10}$$

while that of the ATLAS HCAL in the barrel region is:

$$\frac{\sigma_E}{E} \approx \frac{50\%}{\sqrt{E}} \oplus 3\%, \tag{2.11}$$

and in the forward region it is $\frac{\sigma_E}{E} \approx \frac{100\%}{\sqrt{E}} \oplus 10\%$. The ATLAS calorimeter detectors require minimal modifications to work at luminosities significantly higher than their original design since they were projected to operate both in LHC and HL-LHC. The main calorimeter upgrades involved the LAr calorimeter electronics, upgrading the trigger system to handle more efficiently the trigger rates by enhancing the selectivity and resolution of the trigger signatures of the physics objects, and the discrimination power against pileup background. The ATLAS calorimeter system is illustrated in Figure (2.7).

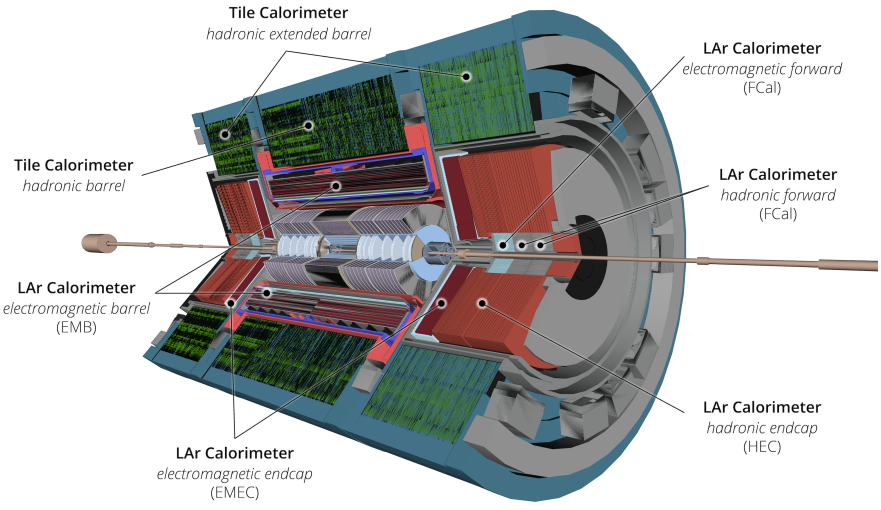

Figure 2.7: Schematic layout of the ATLAS calorimeters [69].

2.2.4 Muon Spectrometer

The Muon Spectrometer [78, 79] forms the large outer part of the ATLAS detector and it is designed to identify and measure the momentum of the charged particles that escape the barrel and endcap calorimeters in the pseudorapidity range $|\eta| < 2.7$. Its layout is presented in Figure (2.8).

The Muon Spectrometer (MS) is composed of trigger and high-precision tracking chambers

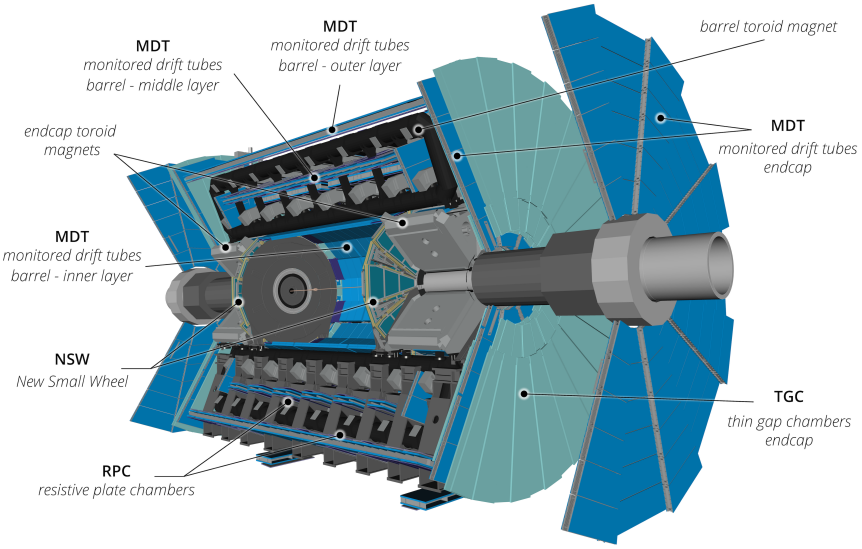

Figure 2.8: Section view of the ATLAS Muon System. The NSWs are visible.[69].

evaluating the deflection of muons in the magnetic field generated by the superconducting air-core toroidal magnets. The field integral of the toroids spans between 2.0 to 6.0 T·m throughout most of the detector.

In the barrel region, the MS comprises three concentric stations of chambers, each consisting of multilayered Monitored Drift Tubes (MDT), that are used for precise tracking of the magnetic bending coordinate η at a later stage of the muon trigger and in the offline analysis, providing an overall spatial resolution for a single chamber of 35 μm. The middle and outer stations ($-1.05 < \eta < 1.3$) are also equipped with Resistive Plate Chambers (RPC) for fast and high timing resolution (15-25 ns) triggering, allowing to identify the collision, and to measure the azimuthal coordinate ϕ of the tracks. Most of the barrel detectors remain the same as they were in the original Run-I configuration.

In the endcaps, the detectors are placed in three wheels orthogonal to the z-axis, the New Small Wheel (NSW) before the endcap toroid cryostats, the Big Wheel (BW) after them, and the Outer Wheel at ∼6 m after the Big Wheel. An "extended" endcap detectors' ring is located outside the radius of each endcap toroid cryostat providing a third measurement station between the NSW and BW for tracks with $1.05 < |\eta| < 1.3$, which are outside the Big Wheel acceptance. The outer wheels contain only MDTs, while the middle wheels have both MDTs and Thin Gap Chambers (TGC), in the range $1.05 < |\eta| < 2.7$ (2.4 for trigger), that play the same role of the RPC in the barrel.

If the middle and outer wheels are unchanged from Run-I, the NSWs were the main upgrade of the Long Shutdown 2 [80], replacing the previous inner wheels, known as Small Wheels, and providing tracking over the same polar angle range: $1.3 < |\eta| < 2.7$ (2.4 for trigger), to exploit the high luminosity performance expected in Run-3 and High Luminosity LHC. The huge increase of particle rates would have resulted in a loss in efficiency of the Small

Wheel, affecting the trigger and tracking performances due to the presence of many fake non-prompt muons and more background.
The ATLAS New Small Wheels utilize two innovative detector technologies: small-strip Thin Gap Chambers (sTGC) and Micromegas (MM) both for trigger and tracking, providing excellent performances thanks to the high spatial resolution, that for MM is < 100 μm for small angles and 72 μm for perpendicular tracks. This allows to confirm, at high expected rates, whether a particle originated from the interaction point and to reduce unwanted background events and thus a better efficiency.
The ATLAS muon system provides a momentum resolution between 2-3% and 10-15% in a p_T range between 10 GeV and 1 TeV.

2.2.5 Forward detectors

The ATLAS forward region is covered by four smaller detector systems. Positioned at $\pm$17 m from the IP, the Luminosity Cherenkov Integrating Detector (LUCID) detects inelastic proton-proton scattering in the forward direction and serves as the primary ATLAS online and offline luminosity monitor [81].
The Absolute Luminosity for ATLAS (ALFA) Roman Pot detector [82], located at $\pm$240 m from the collision point, uses scintillating fibre trackers within Roman pots that can approach within 1 mm of the beam, and it is employed in low luminosity and high β^* runs of the LHC, providing measurements of the total cross-section for proton-proton interactions.
The ATLAS Forward Proton (AFP) detector [83], situated at $\pm$210 m from the interaction point, studies soft, hard, and central diffractive events at low luminosities using a silicon-based tracker for momentum measurements and a time-of-flight system to correlate the interacting protons to a single vertex, minimizing background noise from multiple proton-proton collisions.
Lastly, the Zero Degree Calorimeters (ZDC) [84], placed at $\pm$140 m from the IP and composed of alternating layers of quartz rods and tungsten plates for measuring neutral particles at $|\eta| \geq 8.2$, are crucial for determining the centrality of heavy-ion collisions.

2.2.6 Trigger and Data Acquisition system

The Trigger and Data Acquisition (TDAQ) system [85] is crucial for the ATLAS experiment since it determines in real time whether to collect data from collisions, selecting events with distinguishing signatures of particles' presence. The TDAQ operations have an important impact on datasets used in offline physics analyses.
Due to data storage limitations and the extremely high event rate of LHC collisions, it's essential to reduce the recorded data: during Run-II, the LHC delivered an average of 33.7 proton-proton collisions per bunch crossing every 25 ns. Most data are produced by low-p_T inelastic and diffractive collisions that are not relevant to ATLAS physics goals. Therefore, the TDAQ system is designed to efficiently select interesting physics data and discard others.
The ATLAS TDAQ system operates on two online selection levels: the Level-1 Trigger (L1) and the High-Level Trigger (HLT). L1, which consists of custom-built electronics, performs an initial event rate reduction, accepting events from the 40 MHz bunch crossings at a rate below 100 kHz, utilizing reduced-granularity information from the calorimeters and muon system to identify events within 2.5 μs latency window. The spatial coordinates where the

Level-1 Trigger finds interesting features inside the detector are called Regions of Interest (ROIs).
The HLT, using software algorithms, makes the final event choice closely miming the offline selection. It analyzes and refines the ROIs' information, using full detector granularity and reconstruction algorithms to decide on event recording. The event rate is further reduced by HLT from 100 kHz, after the L1 selection, to approximately 3 kHz for offline analysis.
The Data Acquisition (DAQ) system transports data from custom subdetector electronics to offline processing, based on the two-level trigger decisions.
A diagram of the Run-III TDAQ system is depicted in Figure (2.9).

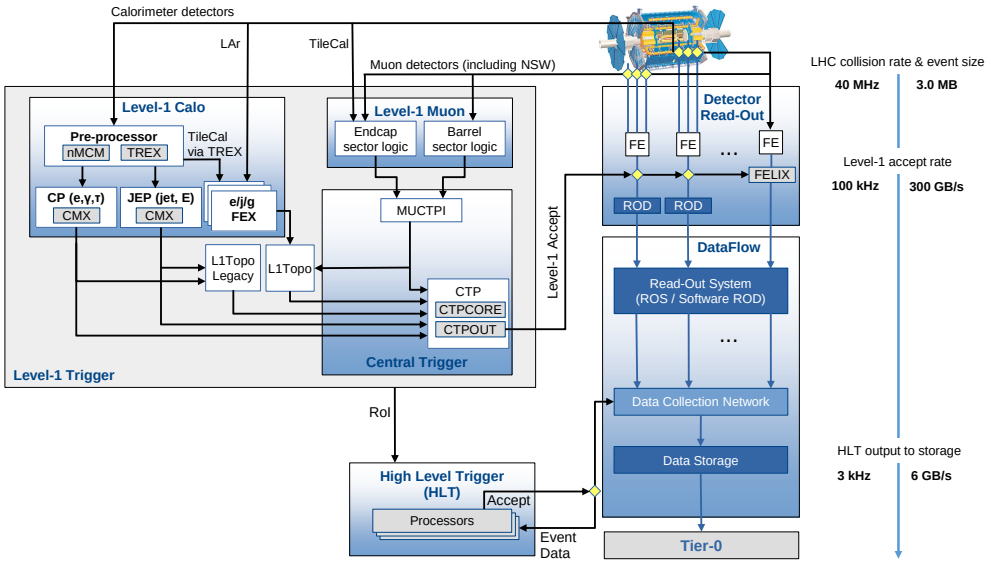

Figure 2.9: Overview of the Trigger and DAQ system [69].

2.3 Identification and reconstruction of physics objects in ATLAS

The previous Section introduced how the ATLAS detector identifies particles resulting from LHC *pp* collisions. To analyze high-energy physics, four-vectors suited for the interpreting these collisions rather than raw detector signals are necessary. These four-vectors, known as *physics objects*, represent the leptons, hadronic jets and photons resulting from the collisions.
This Section outlines the definitions recommended by the ATLAS collaboration for Run-II physics analyses and the reconstruction techniques for various physics objects in the detector, with a particular focus on jet reconstruction, and photon reconstruction and identification, as these are central to the analysis discussed in the last Chapters 4, 5 and 6.

2.3.1 Tracks and vertices

Reconstruction is a complex process aimed at identifying particles produced in the events by using track and cluster information built from all sub-detectors signals.
Tracking must be performed before constructing interaction vertices that ideally represent single proton-proton interactions. This step is crucial for accurately measuring charged particle momentum and minimizing mis-reconstruction effects from pileup interactions.
Tracks are reconstructed in the ID using a sequence of algorithms [86]. The inside-out algorithm starts from the track seeds in the SCT, defined by three space-points representing where the charged particle passed, created from the clusters of hits in the Pixel and SCT layers. A combinatorial Kalman filter, an iterative algorithm that estimates the state based on the projection of previous and current measurement [87], builds track candidates from these seeds by incorporating additional space-points from the remaining Pixel Detector and SCT layers compatible with the preliminary trajectory. Ambiguities due to possible sharing of space-points between track candidates are resolved by a stringent solver algorithm, which assigns a relative track score, via an artificial Neural Network (NN), based on the track quality, cluster multiplicity, and χ^2 of the track segment fit. The best candidates, with the highest scores, are selected and extended into the TRT. In the second stage, a back-tracking algorithm starts from TRT-reconstructed segments and extends inwards by adding silicon hits to reconstruct secondary particles.
The final reconstructed tracks, using full information from all three detectors, are described by five parameters: the impact parameter d_0, defined as the minimum distance in the $R-\phi$ transverse plane between the track and the primary vertex; the z coordinate of the point (z_0) where the track is closest to the interaction region; the pseudorapidity η and azimuthal angle ϕ of the outgoing particle, and the track momentum or curvature q/p_T, where q is the charge. Good track reconstruction is indicated by low resolution on these parameters, high reconstruction efficiency and low fake reconstruction rate.
Once tracks are created, primary vertices (PV) are reconstructed [86] using an iterative vertex finding algorithm to identify the hard-scatter (HS) interaction with the highest collision energy. Vertex seeds are derived from the z-position of the reconstructed tracks at the beam axis. An adaptive vertex χ^2 fitting algorithm [88] reconstructs the vertex position taking as inputs the seed position and the surrounding tracks. Tracks are weighted based on their χ^2 compatibility with the fitted vertex, and those incompatible seed new vertices. The procedure continues until all tracks are used, and vertices with at least two associated tracks are considered primary vertices. Vertices are matched to interactions by summing the weights of associated tracks.
The hard-scatter interaction, likely where significant physics occurs, is identified as the primary vertex with the largest sum of squared transverse track momenta, defined for each primary vertex PV_i as $\sum_{tracks \in PV_i} p_T^2$. All other vertices are considered as pile-up vertices.

2.3.2 Electrons and photons

Electrons and photons are reconstructed starting from similar energy deposits in the EM calorimeter due to their similar showers they produce. For electrons, one or more tracks in the Inner Detector identify an electron/positron candidate from an EM shower, while photons are identified solely by EM energy deposits. The process is complicated by bremsstrahlung photon emission from electron/positron particles or photon conversion into electron-positron pairs in the ID. Photons are defined as converted if their energy

deposits match converted vertices or tracks; otherwise, they are unconverted, having interacted upstream of the calorimeter to produce an electron-positron pair. Since 2017, ATLAS has improved electron/photon reconstruction with a dynamic, variable-size cluster type named *supercluster* [89], useful for recovering energy from bremsstrahlung photons or electrons from photon conversions.

The supercluster formation procedure consists of two stages. First, topoclusters, which are clusters of energy topologically connected with EM and hadronic calorimeter cells [1], employed indeed also for jet reconstruction, are evaluated one by one as seed clusters. An electron supercluster seed must have a minimum transverse energy E_T of 1 GeV with a matched track containing at least four hits in the silicon tracking detectors. For photon supercluster seeds, topoclusters are required to have a minimum E_T of 1.5 GeV, without any track requirements.

The second stage involves finding supercluster satellites within an $\eta \times \phi$ window centered on the seed barycenter. For both electrons and photons, a topocluster is considered a satellite if it falls within a $\eta \times \phi = 0.075 \times 0.125$ range, representing secondary showers from the same initial electron or photon. Only for electrons, a larger $\eta \times \phi = 0.125 \times 0.300$ window is applied, and its 'best-matched' track is also used for the seed cluster track. For photon conversion with a conversion vertex determined by silicon tracks, matching electron satellites are added to the supercluster. The different superclusters formed by all seed clusters with their associated satellites are depicted in Fig. (2.10).

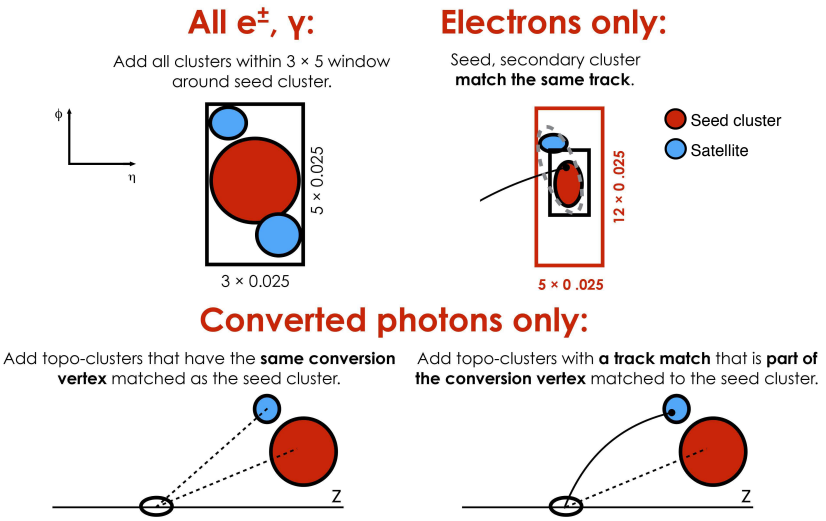

Figure 2.10: Schematic representation of the superclustering formation for photons and electrons: seed clusters are indicated in red, satellite clusters in blue [89].

The analysis-level electrons and photons are then created. Because superclusters are built independently for electrons and photons, a single seed cluster can produce both an electron and a photon. The easier scenario involves an physics object that can be easily identified only by a photon, or electron, supercluster whose seed is not also matched to

[1] Topoclusters are formed from seed calorimeter cells that have more than 4σ of energy, where σ is the expected noise. All cells adjacent to these spatial seed cells are grouped together iteratively. These topoclusters are then calibrated at both electromagnetically, treatin the isolated topo-cluster as the sum of the cell energies, and hadronically, which accounts for the differences between the electromagnetic and hadronic interaction in the ATLAS calorimeter.

an electron, or photon, then only a photon or an electron object is created for analysis. Otherwise, both an electron and a photon are reconstructed from the same initially object. For this ambiguity case, the object is flagged as ambiguous and each analysis is responsible for its final classification, depending on their specific requirements.
The electron and photon creation and ambiguity resolution procedures are presented in Figure (2.11).
After supercluster creation, a calibration procedure using multivariate (MVA) techniques trained on Monte Carlo (MC) simulation is employed to derive the electron and photon energy starting from the simple sum of the energy deposited in each ECAL cell. This calibration corrects for the longitudinal containment imperfections of the EM shower generated by electron or photon that can lose energy encountering inactive material before entering ECAL, for the lateral (along the η and ϕ directions) energy loss outside the reconstructed cluster, and for the energy deposited in the ECAL inactive layers.

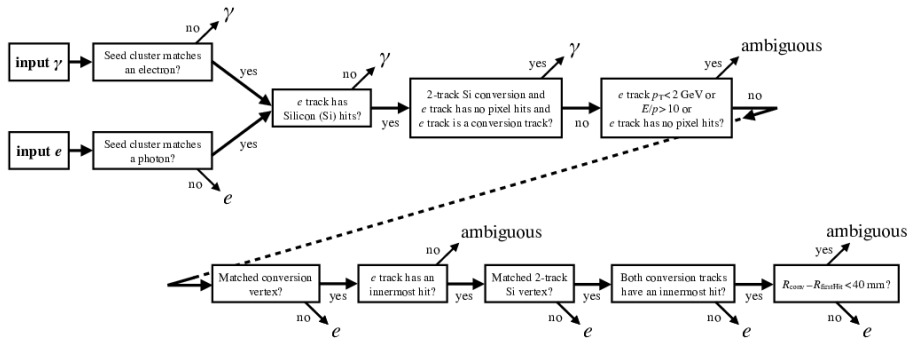

Figure 2.11: Workflow diagram of the logic for resolving ambiguities in particles initially identified both as photons and electrons. E/p represents the ratio of the supercluster energy to the momentum of the corresponding track, while R_{conv} and $R_{firstHit}$ indicate the radial position of the conversion vertex and initial hit of the track, respectively [89].

Additionally, EM shower energy leakage into the HCAL is accounted for. The above phenomena affect the linearity and the resolution of the photon (and electron) energy measurement: The energy calibration is crucial to address all these phenomena and ensure accurate photon and electron energy measurements.
A Boosted Decision Tree (BDT) regression algorithm corrects uncalibrated energy in different η and transverse momentum intervals, trained separately for electrons, converted photons, and unconverted photons using simulated single-particle events without pile-up. Input variables include energy deposits in different EM Calorimeter regions and cluster geometry.
Further corrections are applied to both data and simulated events to refine energy measurement precision. In data, scale factors derived from $Z \to e^+e^-$ events account for detector imperfections not modeled by simulations. The energy resolution from simulated events is adjusted to match data observations, validated using $J/\psi \to e^+e^-$ and $Z \to ll\gamma$ events [89]. A comparison of the di-electron invariant mass distribution between data and simulated $Z \to e^+e^-$ events, after applying the complete calibration procedure, is presented in Fig. (2.12).

Electron identification relies on a multivariate likelihood discriminant to distinguish prompt, isolated electrons from misidentified particles, based on ID track properties and longitudinal/lateral shower development in the EM calorimeter [89]. Three working points (WP), Loose, Medium and Tight, are defined by different likelihood discriminant

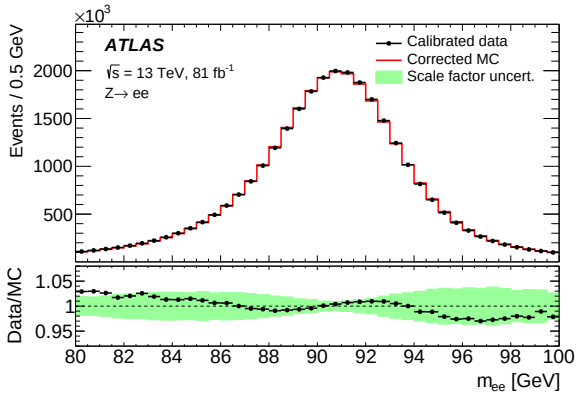

Figure 2.12: Comparison between $Z \to e^+e^-$ data and simulation of the electron pair invariant mass distribution after the calibration chain application. The simulation total number of events is normalized to the data. The green uncertainty band of the bottom panel shows the effects of the uncertainties in the calibration correction factors [89].

thresholds, providing average electron efficiencies of 98%, 90% and 80%, depending on whether the likelihood assigns a probability indicating the candidate particle is more electron-like or more background-like using a sample of simulated dijet, $Z \to e^+e^-$ and $W \to e\nu$ events binned in η and E_T. Additional and more stringent track quality and p_T requirements are applied for the Medium and Tight working point.

Photon identification criteria optimize the selection of prompt, isolated photons while suppressing background from misidentified hadronic jets. Three working points, Tight, Medium and Loose, like for electrons, are identified and optimized for photon identification separately in different pseudorapidity ranges to accommodate calorimeter geometry and upstream material effects on shower shape variables. The Tight working point's selection efficiency is E_T-dependent, ensuring a selection efficiency up to 20% for photons with $E_T > 30$ GeV with respect to E_T-independent strategy and simultaneously enhancing background rejection at high E_T as shown in Fig. (2.13).

The Tight identification distinguishes the converted and unconverted photons based on shower width in the ϕ direction that is wider when an electron-positron pair is generated by a converted photon inside the ID and its trajectory is curved due to the solenoidal magnetic field.

Photon isolation requirements further reduce fake photon backgrounds, mainly coming from high-energy $\pi^0 \to \gamma\gamma$ decays, measured by surrounding hadronic activity quantified through nearby energy deposits in the calorimeters or close-by tracks in the ID. Calorimetric isolation is defined by $E_T^{cone0.2}$ as the sum of the transverse energy of topoclusters within a cone of radius $\Delta R = \sqrt{(\Delta\eta)^2 + (\Delta\phi)^2} = 0.2$ centered on the photon supercluster barycenter, removing both the contribution of the photon energy itself by subtracting the energy deposited in a core window of size $\Delta\eta \times \Delta\phi = 0.125 \times 0.175$ and pile-up and underlying events. The calorimetric isolation variable is visualized in Fig. (2.14).

Track-based isolation is similarly defined by $p_T^{cone0.2}$ as the scalar sum of the transverse momentum of all selected tracks within a cone of radius $\Delta R = 0.2$, excluding tracks matched to photon conversion case of a converted photon candidate.

These procedures, exhaustively discussed in the aforementioned Ref. [89], ensure accurate reconstruction and identification of electrons and photons, critical for precise high-energy physics analyses.

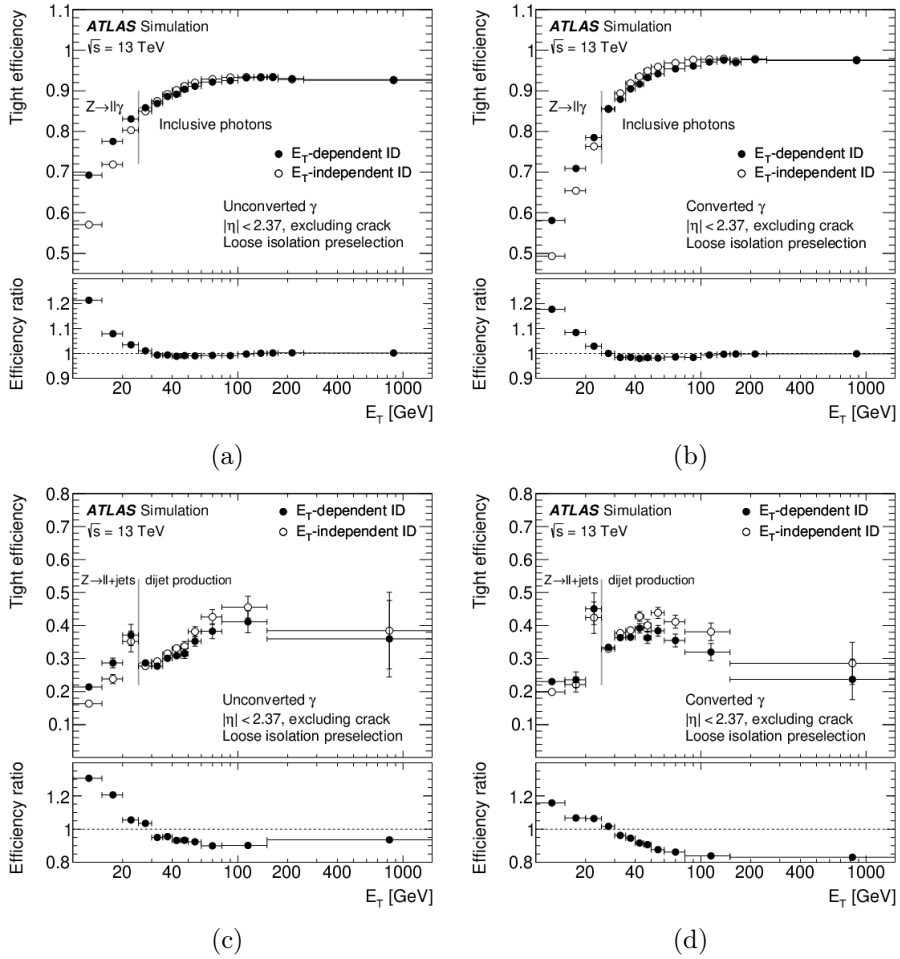

Figure 2.13: Tight photon identification efficiencies for unconverted (a) and converted (b) $Z \to ll\gamma$ *signal* photon, and for unconverted (c) and converted (d) $Z \to ll$+jets *background* photons, with $E_T < 25$ versus photon transverse energy. In each case, a comparison (and ratio) between E_T-independent and E_T-dependent approaches is present [69].

2.3.3 Jets

Jet reconstruction aims to combine quarks and gluons produced in the collisions, which hadronize into a physics object, the jet, that reveals information about the initial parton. The process involves two main steps: defining input objects and implementing the jet building algorithm.

Currently, for the first stage, ATLAS uses the ParticleFlow (PF) algorithm [90] for most analyses, including the $HH \to b\bar{b}\gamma\gamma$ analysis discussed in this Thesis (Section 4). This approach combines information from the ATLAS calorimeters and the Inner Detector to form signals representing all stable particles in the event. These identified and reconstructed ParticleFlow objects, ideally originating from the hadronization of the same parton, are the basis for jet clustering and reconstruction. The ParticleFlow method leverages the strengths of both the calorimeters and the Inner Detector, compensating for each other's limitations. For low-energy charged particles, the tracker provides better momentum resolution than the calorimeters. Conversely, calorimeters offer superior energy resolution at higher energies, have a larger pseudorapidity acceptance, and can detect neutral particles. The Inner Detector enhances the angular resolution for measuring charged particles' directions, captures low-energy tracks, and matches tracks to the primary interaction vertex,

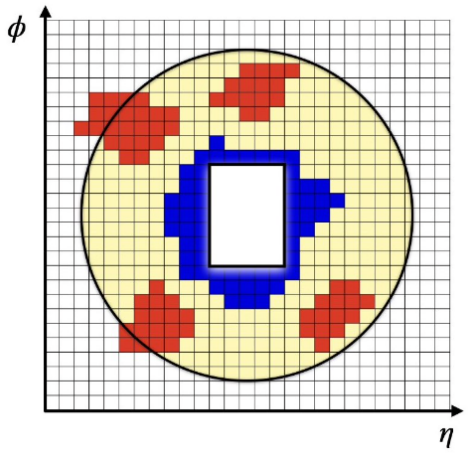

Figure 2.14: Cut of the cone with radius ΔR (shown in yellow) surrounding the photon energy cluster, that is excluded (the white rectangle) from the calculation of the $E_T^{cone0.2}$. The blue cells indicate corrections for out-of-core energy leakage, while the red cells represents the topoclusters within the cone, whose combined energy constitutes $E_T^{cone0.2}$.

which is crucial for pile-up rejection during jet clustering.
Both the hadronic jets and the soft activity reconstruction use this combination. Outside the geometrical ID acceptance, only the calorimeter information is used, with topoclusters as inputs for PF jet reconstruction. In the region $|\eta| < 2.5$, to avoid overlaps between the ID and calorimeter energy measurements, the charged track's calorimeter signal is identified and subtracted cell-by-cell, ideally leaving only a measurement of the electrically neutral particles. This is done only for well-reconstructed ID tracks meeting stringent track hits requirements. The main challenge of this technique is accurately subtracting all the energy of a single particle without affecting other particle energy deposits.
ParticleFlow objects are then used as inputs for the jet-bulding algorithm. An important feature of these algorithms is infrared and collinear (IRC) safety, meaning the final set of jets remains unchanged by arbitrary collinear or soft gluon emissions. At LHC, the current widely used *anti-k_t clustering algorithm* [91] sequentially combines PF inputs into larger objects based on the momentum-weighted distance between two clusters, given by:

$$d_{i,j} = min(k_{ti}^{2p}, k_{tj}^{2p}) \frac{\Delta R_{ij}^2}{R^2} \tag{2.12}$$

and the momentum-weighted distance between a cluster and the beam, given by:

$$d_{i,B} = k_{ti}^{2p} \tag{2.13}$$

where ΔR_{ij}^2 is the $\eta - \phi$ distance defined in Eq. (2.8), while k_{ti} is the transverse momentum. The parameter R is the jet radius. ATLAS typically uses two kinds of jets: the small-R jets ($R = 0.4$) for quark/gluon-initiated jets that are used by most of the physics analyses, and the large-R jets ($R = 1.0$) for reconstructing boosted particles decaying to quarks (e.g. top, W, Z).
The integer parameter p defines different sequential-recombination algorithms, with the anti-k_t algorithm specified by $p = -1$[2]. The algorithm identifies the minimum distance between d_{ij} and d_{iB}, starting from the highest momentum entity i. If $d_{ij} < d_{iB}$, i and j

[2] $p = 1$ indicates the k_t *algorithm*, while $p = 0$ represents the *Cambridge/Aachen* algorithm.

combine into a single pseudo-jet; otherwise, i is considered a final state and removed from the list of entities. The distances are then recalculated between the objects in the updated list, and the procedure is repeated until no entities remain. The anti-k_t algorithm tends to cluster soft particles with hard objects before combining soft particles among themselves, making it sensitive primarily to hard particles proximity and less to soft radiation, resulting in conical-shape jets (Fig. (2.15)).

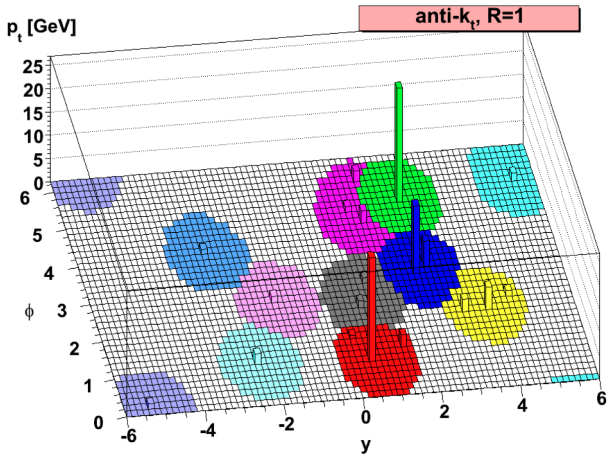

Figure 2.15: Visualization of the active catchment areas of the resulting hard jets clustered using the anti-k_t algorithm [91].

2.3.3.1 Jet calibration

While the calorimeters accurately measure the energy of electromagnetic particles (electrons, positrons, and photons), they underestimate the energy of hadronic particles due to undetectable energy losses from their interaction processes. Additionally, factors like pileup and energy leaks can cause further energy loss in the final jet measurement, which must be corrected for accurate reconstruction. Jet calibration involves adjusting the energy, momentum, and direction of reconstructed jets to match truth jets [92]. The stages of the ATLAS jet calibration for small-R jets are summarized in Fig. (2.16).

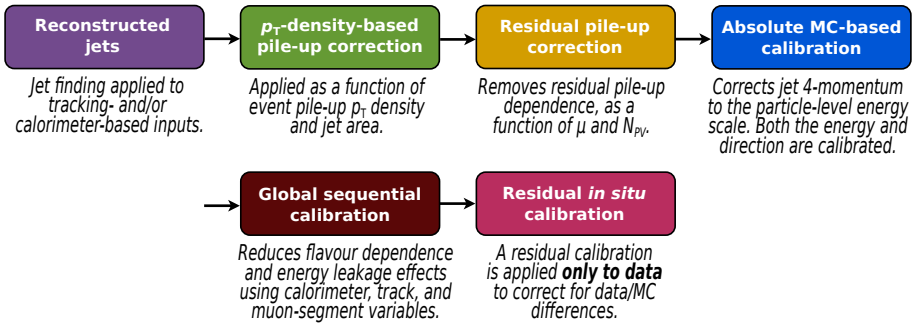

Figure 2.16: Steps of jet energy scale calibrations applied to the four-momentum of the jet [92].

The first relevant calibration step is removing pileup effects using two consecutive correction techniques: the *ρ-area subtraction*, where by using the jet area A and the jets' median

p_T density ρ in the $\eta - \phi$ plane an average pileup contribution is removed, and the *residual correction* which adds a further subtraction parametrized by the number of primary vertices N_{PV} and interaction per bunch crossing μ. The total area correction can be written as

$$p_T^{corr} = p_T^{reco} - \rho \cdot A - \alpha \cdot (N_{PV} - 1) - \beta \cdot \mu, \tag{2.14}$$

where p^{reco} refers to the EM-scale p_T of the reconstructed jet, and α, β are parameters of the residual correction.
The energy of the jet objects is then calibrated using truth simulated jets in a process known as *Jet Energy Scale* (JES) *calibration*, correcting for energy loss in inactive areas, mis-reconstruction, different HCAL and ECAL energy scales and biases in the jet η reconstruction. This relies on the jet energy response defined as $R = E_{jet}^{reco}/E_{jet}^{truth}$, where the reconstructed jets are anti-k_t matched to truth jets within $R = 0.3$, and utilized as correction factor for the jet four-momentum.
After the initial calibrations, residual dependencies of the JES on longitudinal and transverse features due to the jet's particle composition and its internal energy distribution are corrected, reducing flavor dependence and energy leakage effects, applying a series of six sub-calibrations known as Global Sequential (GSC) Calibration. It improves the jet p_T resolution and reduces the associated uncertainties by removing the reconstructed jets response dependencies on observables extracted from all sub-detector systems' information.
The above discussed calibrations are applied to both data and MC simulations. The final step of the calibration chain involves reducing discrepancies in jet response between data and MC simulations, that stem from detector material imperfect simulation, particle showering and pileup. To address this, the jet response is measured using data, but unlike MC simulations, the associated events lack generator information needed to estimate the true energy. Therefore, well-calibrated physics objects (such as photons, Z bosons, and multijets) recoiling against a jet are used to evaluate the correct jet energy. This calibration method, known as the *in-situ calibration*, uses the quantity $R_{in-situ} = p_T^{jet,reco}/p_T^{ref,reco}$, where $p^{ref,reco}$ is the transverse momentum of the reference object and $p^{jet,reco}$ the transverse momentum of the recoil jet, and it is applied via the double ratio $c = R_{in-situ}^{data}/R_{in-situ}^{MC}$, which is a valid measure of the jet energy scale difference between MC simulation and data being robust to well-modelled simulation secondary effects [92].
Different in-situ calibrations are applied in sequence and then statistical combined to correct the disagreement across a large p_T range (up to ~ 2 TeV).
Additionally, the Jet Vertex Tagger (JVT) tool is employed to further suppress pile-up [93]. This technique is based on a MVA analysis of pile-up sensitive track information, such as the transverse momentum associated to the track, to discriminate between pile-up jets and jets originating from the primary vertex. The MVA discriminant score ranges from 0 and 1, indicating the likelihood of a jet being due to pile-up, with 0 being the most probable. Cuts performed with this algorithm belong to one of three common working points, Loose, Medium and Tight, corresponding to a JVT score of 0.14, 0.64 and 0.92, respectively. For jets outside the Inner Detector acceptance ($|\eta| > 2.5$), where the JVT cannot be applied due to the lack of tracking information, the fJVT algorithm is used instead [94].

2.3.3.2 b-jets

The identification of jets originating from *bottom* quark hadronization, known as *b-jets*, is crucial for distinguishing these particular jets from the broader background of jets containing other quark flavors. This is an essential task for many physics processes of interest involving b-quarks in the final state, such as the decay of the Higgs boson into bottom quark pairs ($H \to b\bar{b}$) with a branching ratio (BR)[3] of approximately 59%, as detailed in the next Chapter, or the decay of a top quark into a W and bottom quark $t \to Wb$ (BR$\sim$100%). Additionally, decays of new particles into heavy quarks are prominent in many BMS models.
Particles composing bottom-initiated jets are characterized by the presence of a long-lived b-hadron, having a lifetime of the order of $\tau = 1.6$ ps [95], which allows the hadron to travel a small but significant distance in the detector before decaying. This length, for a B meson with a transverse momentum of 50 GeV, is of the order of 2-3 mm from the primary vertex. The (charged) decay products of B mesons are expected to produce tracks originating from a secondary vertex, distinct from the primary vertex where the B meson was produced. Key indicators for identifying b-jets include the distance between the secondary and the primary vertex, the mass of the daughter particles, that are much less massive than B mesons ($\geq$ 5 GeV)[4], the large impact parameter d_0 of the products' tracks, the presence of low energy, non-isolated leptons (typically a muons) inside the jet cone, and the hard fragmentation with B-hadrons carrying $\sim 3/4$ of jet's energy. A schematic illustration of a b-hadron decay into a jet is depicted in Figure (2.17).

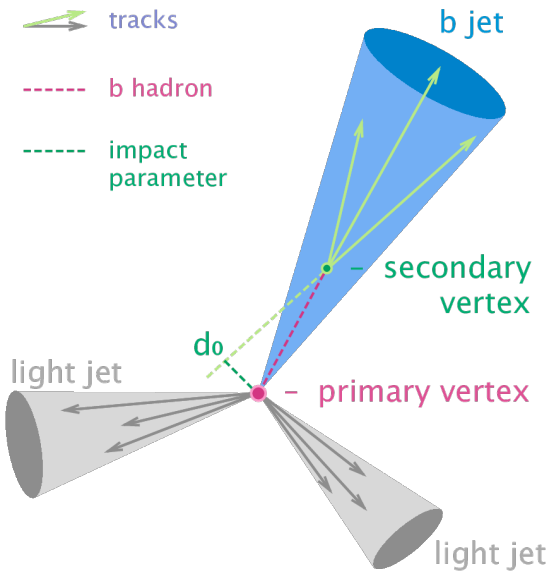

Figure 2.17: The typical features of b-hadron decay inside a jet, resulting in a secondary vertex with three charged particle tracks, are shown.

The ATLAS experiment employs various algorithms for b-jet identification, known as *b-tagging* algorithms, utilizing the features of B-hadron decays [96, 97]. The strategy has

[3]The branching ratio, also known as the branching fraction, of a final state is defined as the fraction of decays into this particular final state compared to all possible final states.
[4]They possess a momentum of a few GeV in the rest frame of the parent particle, with a substantial transverse component relative to the jet axis.

two stages. Firstly, detector specific low-level algorithms exploit the properties of b-jets. The two IP2D and IP3D algorithms [97] use the large impact parameters of tracks from b-hadron decays. ATLAS improved the flavor-tagging procedure by introducing a new Recurrent Neural Network based IP algorithm (RNNIP) [98] that explores correlations among tracks, treating track collections as sequences [99] and and addressing the assumption made by IP-based taggers that each track is independent of the others within the same jet, which fails to accurately represent the jet's characteristics. Displaced vertices indicative of b-hadron decays inside jets are formed starting from the ID tracks, that are constructed by a secondary-vertex-tagging SV1 algorithm [100]. Lastly, a topological multi-vertex finding algorithm, the JetFitter [101] uses the topological structure of the weak decays of heavy flavour hadrons to reconstruct the full b-hadron decay chain.
In the second stage, the low-level algorithms' outputs are combined using multivariate techniques into a single output to enhance the b-jet identification performance. There are mainly two high-level algorithm series, MV2 and DL1, that differ for their architecture. MV2 algorithms are based on a Boosted Decision Tree [96], while DL1, introduced at the beginning of Run-II, on a deep feed-forward neural network (DFNN), providing a continuous variable output with three different probabilities (p_b, p_c and p_{light}) combined into a final discriminant:

$$D_{DL1} = \ln\left(\frac{p_b}{f_c \cdot p_c + (1 - f_c) \cdot p_{light}}\right). \tag{2.15}$$

Here, f_c is the effective c-jet fraction in the background hypothesis and it is optimized for performance improvement for both light and c-jets rejection.
An improved version of the DL1 algorithm is the DL1r [102], used in most Run-II searches including the legacy $HH \to b\bar{b}\gamma\gamma$ analysis [103], which significantly enhances light-and charm rejection by optimizing the network architecture and including kinematic jet variables, as jet p_T and η, and RNNIP output probabilities.
Several working points, defined by the efficiency of b-jet identification, are provided for each b-tagging algorithm. Typically, these working points are set to achieve b-tagging efficiencies of 60%, 70%, 77%, and 85%. Jets that meet the criteria of the chosen b-tagging algorithm are referred to as *b-tagged jets*. The Fig. (2.18) illustrate a comparison of the performance of the MV2 and DL1 algorithms from 2018, alongside the DL1r algorithm, which was optimized in 2019. The DL1r from 2019 demonstrates a significant improvement over the other algorithms
In 2022 DL1r evolutes in DL1d [104] developed for Run-III. The RNNIP is replaced by Deep Impact Parameter Sets (DIPS) algorithm [105], which treats tracks in the jet as an unordered, variable-sized sets rather than sequences, significantly reducing training and evaluation time. DIPS is based on the Deep Sets architecture [106], which features a permutation-invariant and highly parallelizable design. Since the decay products of b-hadrons do not have an inherent sequential order, the Deep Sets architecture is more physically appropriate.
From 2023, the b-jet trigger relies on a new algorithm GN1 [107], based on a single and sophisticated Graph Neural Network (GNNs) [108], which predicts the jet flavour by directly taking tracks and jet information as inputs. This means that this technique is independent of low-level flavour tagging algorithms. The GN1 combines a GNN with the two auxiliary training objectives for common vertex track grouping and underlying physics process prediction, providing a better performance and adaptability through a greater understating of the jet's internal structure.

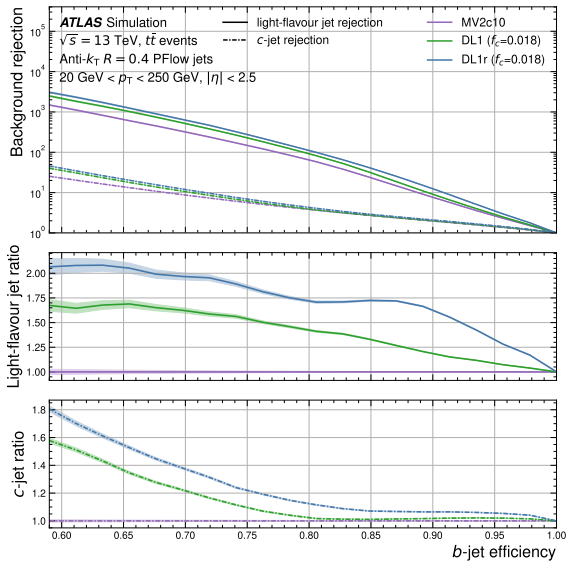

Figure 2.18: The rejection factors for light-flavour jets and c-jets as a function of b-jet efficiency are examined for the high-level b-tagging algorithms MV2(c10), DL1, and DL1r. In the two bottom panels the comparison between the rejection of light-flavour jets and c-jets by these algorithms relative to MV2c10 is illustrated. The colored bands represent the statistical binomial uncertainties of the rejection factors [102].

The best performance is achieved by updating GN1 to GN2 [109], adopting the transformer architecture [110] and optimizing for the model hyper parameters. The expected trigger rate as a function of the b-tagging efficiency for the DL1d, GN1 and GN2 algorithms is presented in Figure (2.19). The performance of the GN1 and GN2 taggers surpasses that of DL1d, which was the main tagger in 2022.

Thanks to a 4x improvement in background rejection compared to DL1 and the expect strong benefit on ATLAS physics program at Run-III LHC and HL-LHC, GN2 is the currently ATLAS recommended b-tagging algorithm. The $HH \to b\bar{b}\gamma\gamma$ analysis presented in this thesis adopts this algorithm. There is also the potential to incorporate additional information on leptons and neutral particles into the jets for possible future improvements.

2.3.3.3 b-jet energy corrections

The standard JES calibration described in Section 2.3.3.1, applied to all jets, is optimized for multi-jet events, which predominantly consist of light-quarks jets. This correction is not ideal for b-jets due to the complications introduced by the frequent production of muons and neutrinos in B meson decays, whose energy escapes the ATLAS calorimeters, and the large mass of the b-quark which reduces the jet's boost resulting in a large fraction of particles outside the usual jet cone (out-of-cone radiation).
The previously discussed calibration chain (see Figure (2.16)) is integrated with an additional calibration specific to b-jets. Two corrections, μ-in-jet and p_T-Reco, are combined in a decoupled method denoted b-jet energy calibration, implemented via a *BJetCalibration* (BCal) Tool adopted as the standard b-jet calibration across all di-Higgs boson channels involving b-jets in their final states ($HH \to b\bar{b}\gamma\gamma$, $HH \to b\bar{b}b\bar{b}$, $HH \to b\bar{b}\tau\tau$, $HH \to b\bar{b}ll$+MET and $HH \to b\bar{b}VV$. More details in Sect. 3.4.1.
The leptonic and semileptonic b-hadrons branching ratio is approximately 42%, including

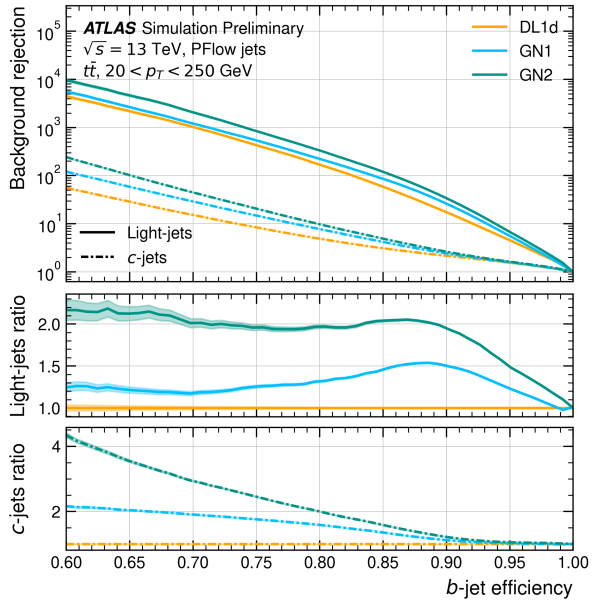

(a)

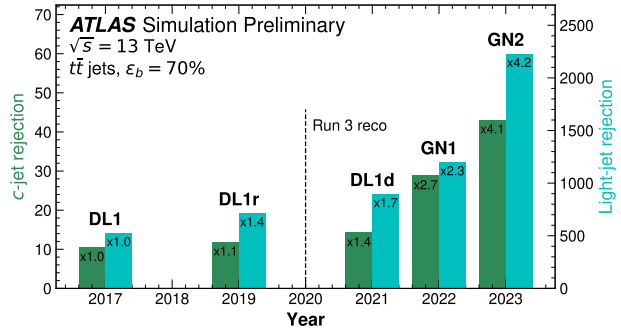

(b)

Figure 2.19: In (a), the c-jet and light-jet rejections of versus the b-jet efficiency for jets in a $t\bar{t}$ sample with $20 < p_T < 250$ GeV for DL1d, GN1, GN2 algorithms are shown, with their ratio compared to the DL1d performance in the bottom panels. Binomial errors are denoted by the colored shaded bands. In (b), the improvement of different ATLAS flavour tagging algorithms with respect to the DL1d $c-jet$ (green) and light-jet (turquoise) rejection (77% WP) over time in $t\bar{t}$ MC simulation is shown [109].

electron and muon contributions. Therefore, b-jets are expected to contain a muon about 20% of the times.

Default jet energy calibrations do not account for these events, as muons are generally not excluded from jet reconstruction algorithms because they are minimum ionizing particles that deposit a small amount of energy, typically a few GeV, in the calorimeter, degrading the mass resolution for the signal processes in the case of semileptonic B meson decays. The μ-in-jet correction addresses this issue. When a non-isolated *medium* muon with $p_T > 5$ GeV is found within a distance

$$\Delta R = min(0.4, 0.04 + \frac{10}{p_T\,[\text{GeV}]}) \tag{2.16}$$

from the jet axis. Its 4-momentum is added to that of the jet and the small fraction of energy deposited by the muon in the calorimeters is subtracted. Rather than applying a fixed ΔR cut of 0.4, a variable cut is used to account for the fact that jet boost decreases the angular muon separation. If multiple muons are identified, only the one with the highest

transverse momentum is considered. Jets that include a muon are labelled as *semileptonic*, while those without are are labelled as *hadronic*.
In addition to the muon-in-jet correction, a global p_T-dependent scale factor is applied to the jet four-vector to account for the presence of neutrino in semileptonic decays and out-of-cone radiation. The p_T-Reco correction is based on Monte Carlo simulations, which model the expected response of reconstructed b-jets in comparison to a scenario where jet clustering includes all stable hadrons, non-isolated muons, and neutrinos, i.e., truth information from the simulations. This correction adjusts the reconstructed b-jets to correct for energy leakage outside the b-jet cone and by the energy carried away by undetected neutrinos. Corrections are calculated separately for b-jets from B mesons undergoing either semi-leptonic or fully hadronic decays. To be applicable for any analysis involving b-jets in the final state, the correction factor is derived from $t\bar{t}$ samples and covers a wide p_T range up to 400 GeV.
As will be detailed in the following Chapters, the di-Higgs channel of interest of this Thesis, the Higgs $HH \to b\bar{b}\gamma\gamma$, benefits from the $H \to \gamma\gamma$ part which features a very narrow peak in the $m_{\gamma\gamma}$ spectrum. This narrow peak aids in rejecting a significant amount of background by allowing the definition of precise $m_{\gamma\gamma}$-spectrum window to select the Higgs boson signal. Conversely, the $H \to b\bar{b}$ suffers from the b-jet miscalibration and has a larger resolution in $m_{b\bar{b}}$ compared to $m_{\gamma\gamma}$. Any $m_{b\bar{b}}$ improvement is advantageous for background rejection. The enhancement in b-jet energy resolution achieved through the BCal decoupled method results in approximately 22% improvement in $m_{b\bar{b}}$ invariant mass resolution, as shown in Figure (2.20).

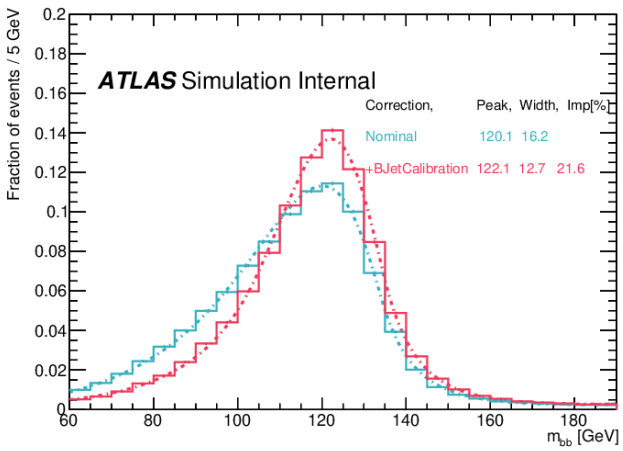

Figure 2.20: Comparison between the di-jet invariant mass $m_{b\bar{b}}$ distribution constructed using the conventional ket energy calibration (turquoise) and after implementing the specific b-jet energy calibrations (pink) for simulated $HH \to b\bar{b}\gamma\gamma$ events [103]. The distributions are fitted using the Bukin function, with the peak, resolution, and relative improvement detailed in the legend.

The main focus of this Thesis, discussed in Section 5, is the implementation and optimization of a new tool for the correction of b-jets through a Kinematic Fit, which constrains the HH system to be balanced on the transverse plane via a negative log likelihood minimization. This is applied after BCalibration to further improve $m_{b\bar{b}}$ by exploiting the high precision on the $H \to \gamma\gamma$ component.

2.3.4 Muons

Muons are reconstructed using independent information from the Inner Detector, Muon Spectrometer tracking detectors, and calorimeters, which help determine track parameters and quantify energy loss [111].
The combination of each sub-detector information allows to reconstruct the muon track by fitting together segments, that are short straight-line tracks made by hits found in each layer within the muon chambers. A track candidate is accepted only if its fit χ^2 meets specific selection criteria. Hits with large contributions to the χ^2 are removed, and the track fit is repeated. Four types of candidate muons are defined based on the dominant sub-system involved in their reconstruction.
A *Combined Muon* is formed by performing a global fit taking all the hits correlated to tracks reconstructed in ID and MS.
A *Segment-Tagged Muon* is reconstructed when an ID track is extrapoleted to a precision-plane track segment in the MS.
A *Calorimeter-Tagged Muon* is identified from an ID track matched with an energy deposit in the calorimeters compatible with the passage of a minimum ionizing particle. This recovers the muon reconstruction acceptance in detector's regions where the MS is only partially instrumented to allow cabling and services for the ID and the calorimeters.
An *Extrapolated Muon* is reconstructed only from MS hits with its track loosely matched to the primary interaction vertex.
To suppress contamination from muons originating from hadron decays, prompt muons must meet specific identification criteria, similarly to electrons and photons. Muon identification is based on variables quantifying the fit quality of the muon track. Background muons from charged meson decays typically result in poorer-quality track fits compared to prompt muons. Five identification working points are defined: Tight, Medium, Loose, High-p_T, and Low-p_T. The Medium WP provides a good balance for many analyses, maintaining low systematic uncertainties in prompt muon reconstruction efficiency and background rejection. The Loose WP offers higher efficiency at the cost of reduced purity and increased systematic uncertainties. The Tight WP delivers the highest purity and improved background rejection, with a slight efficiency loss for prompt muons compared to Medium WP. Lastly, The High-p_T WP and Low-p_T WP are designed to enhance momentum resolution for muon tracks above 100 GeV and below 3 GeV, respectively.
The efficiency of a selected WP indicates the probability that a prompt muon is reconstructed and meets the WP criteria, while the purity of a WP is one minus the hadron misidentification rate, reflecting the fraction of light hadrons reconstructed as muons that meet the WP criteria.

2.3.5 Taus

Tau leptons, with a mean lifetime of approximately 290 fs, decay before reaching the ATLAS detector. They can decay leptonically, $\tau \to l\nu_l\nu_\tau$, $l = e, \mu$, or hadronically, $\tau \to \nu_\tau$+hadrons, with branching ratios of 34% and 66%, respectively.
Hadronic visible tau candidates (τ_{had}^{vis}) are seeded by jets formed using the anti-k_t algorithm, with a distance parameter of 0.4. These candidates are required to have $p_T > 10$ GeV and $|\eta| < 2.5$. In tau reconstruction, track selection is performed via BDTs that categorize tracks based on their p_T, the number of tracking detector hits and their transverse and longitudinal impact parameters relative to the tau vertex. The primary class, intended to

collect the charged tracks (mostly $\pi^{\pm}$) from tau decay, is defined by the core cone region, $\Delta R < 0.2$, and specific track quality criteria.
Dedicated algorithms identify the hadronic tau decays' visible products. Depending on cuts on a Recurrent Neural Network score, four working points with increasing background rejection (Very loose, Loose, Medium and Tight) are defined for use in physics analyses. The τ_{had}^{vis} reconstruction process is detailed in Ref. [112].

2.3.6 Missing Transverse Energy

Since neutrinos and other invisible particles produced in pp collisions cannot be directly detected, their presence is revealed from an imbalance in transverse momentum, known as missing transverse momentum (MET, or E_T^{miss}). As mentioned in [113], the total transverse momentum of a pp collision is expected to be zero. By imposing its conservation:

$$\sum_{i \in particles} p_T^i = \sum_{i \in \text{visible particles}} p_T^i + \sum_{j \in \text{invisible particles}} p_T^j = 0, \tag{2.17}$$

the event-based quantity E^{miss} can be defined as the total transverse momentum carried by invisible particles:

$$\begin{aligned} E_T^{miss} = \sum_{i \in \text{invisible particles}} p_T^i = - \sum_{i \in \text{visible particles}} p_T^i \\ = \sum p_T^e + \sum p_T^\mu + \sum p_T^\gamma + \sum p_T^\tau + \sum p_T^{jet} + \sum p_T^{soft}. \end{aligned} \tag{2.18}$$

The magnitude E_T^{miss} is used to detect invisible particles produced in pp collisions by examining all the fully calibrated visible physics objects in the event. These objects are combined with the MET soft-term, which is the soft hadronic activity associated with tracks that have $p_T > 0.5$ GeV and $|\eta| < 2.5$, matched to the primary vertex and not related to any reconstructed physics object.

Chapter 3

Phenomenology of the Higgs boson at the LHC

The existence of the Higgs boson was predicted with the formulation of the Higgs mechanism in 1964. Nearly half a century later, following significant theoretical developments and extensive searches at LEP and Tevatron [114], the ATLAS and CMS experiments observed a particle consistent with the Standard Model Higgs boson, with a mass of approximately 125 GeV, in July 2012 [115, 116].
This landmark discovery confirmed the existence of a spinless quantum field that permeates the universe and gives mass to massive elementary particles. It initiated a new era of research at the LHC focused on detailed and precise measurements of the Higgs boson's properties, that are crucial for testing the predictions of the Standard Model and potentially invalidating certain beyond-the-Standard-Model theories or even uncovering new physics, directly or indirectly.
Within the Standard Model, the interaction strength, or 'coupling', between the Higgs boson and other particles is determined entirely by the particle's mass and type. The initial measurements during the LHC Run-I were primarily accessible via production and decay channels associated with the Higgs boson's couplings to the vector gauge bosons (W, Z), thereby validating the presence of gauge couplings as a fundamental test of the spontaneous electroweak symmetry breaking mechanism. Additionally, precise analyses of the proton–proton collision data from this period provided evidence that, unlike all other known fundamental particles, the properties of the observed particle were consistent with the hypothesis that it has no spin [117].
The exceptional performance of the LHC during Run-II, offering 30 times more events than at the time of the Higgs discovery due to the higher collision rate of collisions and an increase in collision energy from 8 to 13 TeV, enabled ATLAS and CMS to independently confirm the couplings of the Higgs boson to the third-generation charged (the top quark, the bottom quark, and the τ lepton). In high mass resolution decay channels, such as those involving four leptons (electrons or muons) or diphoton final states, the mass of the Higgs boson m_H has been measured with permille precision. Furthermore, there is compelling experimental evidence for the Yukawa interactions of the Higgs boson with second-generation fermions from the search for Higgs decays to muons. Nonetheless, several Higgs decay channels present significant experimental challenges at the LHC. The expected Standard Model couplings of the Higgs boson to first-generation fermions remain beyond the current experimental reach. Finally, the Higgs boson can interact with itself. The self-coupling is one of the Higgs key properties still to be measured, which is directly

accessible through the Higgs boson pair production, the focus of this thesis.
In this section, an overview of the production and decay modes of a single Higgs (H) boson is presented, along with the latest measurements from ATLAS and CMS regarding its mass, width, and couplings. Following this, Higgs boson pair (HH) production is discussed, with a summary of the most recent results obtained by the two Collaborations.

3.1 Single Higgs production channels and decay modes

The Feynman diagrams depicting the main production mechanisms of the Standard Model Higgs bosons are shown in Figure (3.1). These include gluon-gluon Fusion (ggF), Vector Boson Fusion (VBF), associated production with a vector boson (VH), also referred to as *Higgs-strahlung*, and associated production with a pair of top quarks (ttH) or b-quarks (bbH). Other qqH processes contribute minimally and are experimentally inaccessible. Only about 0.05% of Higgs bosons are produced in association with a single top quark (tH). Figure (3.2a) illustrates the cross sections for each production mode of a SM Higgs boson as a function of the center-of-mass energy of the pp collision.

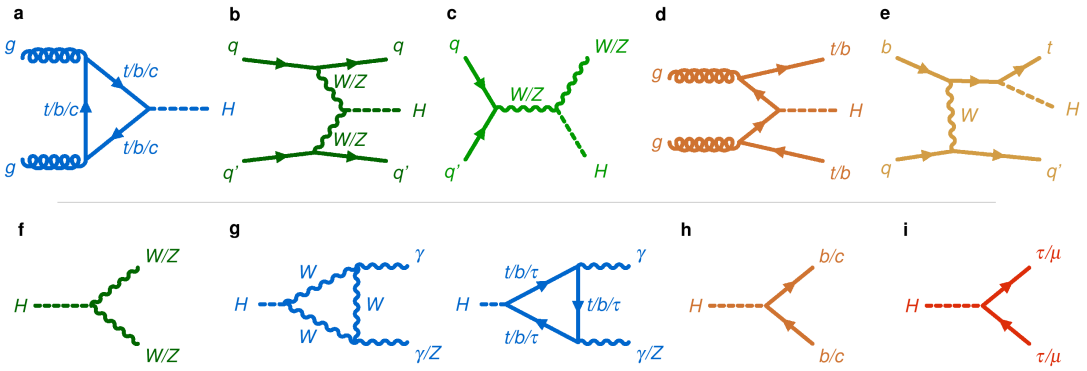

Figure 3.1: The Feynman diagrams for the main Higgs boson production and decay processes are illustrated. The Higgs boson can be produced through ggF (a), VBF (b), Higgs-strahlung (c), top or bottom quark pairs (d), or a single top quark (e). Bottom panels depict the Higgs boson decaying into a pair of vector bosons (f), photons or a Z boson and a photon (g), quarks (h), or charged leptons (i). [118].

The most probable production mechanism for a Higgs boson is gluon-gluon Fusion $gg \to H + X$, accounting for approximately 87% of the total production rate. This dominance is due to the abundance of gluon-gluon interactions during proton-proton collisions at the Large Hadron Collider's energies. In this process, two gluons interact through a loop of quarks, producing a Higgs boson emerging from the third vertex of the triangular loop. Since the Higgs boson's coupling to quarks depends on the quark mass, the loop predominantly consists of the heaviest quark, the top quark.
Vector Boson Fusion is the second most significant SM Higgs production mode at the LHC, with a cross section at the LHC (7%). Higgs boson production via VBF, $qq \to qqH$, occurs through the scattering of two (anti-)quarks, mediated by the exchange of a W or Z boson, with the Higgs boson radiated off the exchanged weak-boson. The scattered quarks generate two energetic jets in the forward and backward regions of the detector with a large rapidity gap. Due to the color-singlet nature of the weak-gauge boson exchange, gluon radiation from the central-rapidity regions is significantly suppressed. These distinctive features of VBF processes can be exploited to differentiate them from overwhelming QCD

backgrounds, providing a clean environment for Higgs boson searches.
Higgs-strahlung, with a 4% cross section, ranks third among Higgs production modes. In this process, $pp \to VH + X$, the Higgs boson is emitted by a W or Z boson produced by quark-antiquark annihilation, resulting in the Higgs boson and the decay products of the vector boson in the final state. Providing complete kinematic information for the decay products can further aid in suppressing large QCD backgrounds. The WH and ZH production modes offer a relatively clean environment for studying Higgs decays into bottom quarks.
Lastly, associated production with top quarks has the smallest cross section among these production modes (1%). This process yields two top quarks, $pp \to t\bar{t}H$, which can be identified by their decays, alongside the Higgs boson decay products.

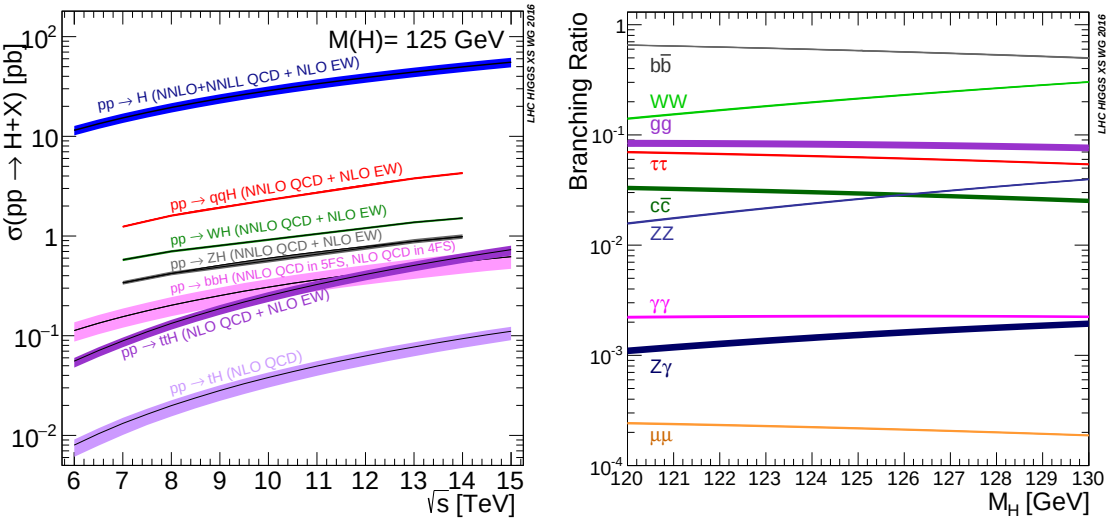

(a) (b)

Figure 3.2: (Left) The cross sections for H production as a function of the center of mass energy ($\sqrt{s}$) for proton-proton collisions. Here, the VBF process is denoted as qqH. (Right) The BRs for different decays of the SM Higgs boson near $m_H = 125$ GeV [119, 120].

Once produced, the Higgs boson is predicted to decay almost instantaneously, with a lifetime of 1.6×10^{-22} seconds. The branching ratios (BRs) of various final states are crucial since experiments often specialize in detecting a single final state to minimize background events. Therefore, it is essential to identify final states that not only have high BRs but are also clearly and precisely identifiable. An interesting aspect of the Higgs BR is its dependence on the masses of the particles it decays into. Specifically, the decay probability is proportional to the square of the final particles' masses for decays into vector bosons ($\lambda_{H,Boson} \propto m^2_{Boson}$), while for decays into fermions, it is directly proportional to the particles' masses ($\lambda_{H,Fermion} \propto m_{Fermion}$).
Although it might seem preferable to prioritize massive vector boson final states due to their favorable coupling scaling and high masses, these processes are not kinematically feasible because the Higgs boson mass of ∼125 GeV, that, for instance, is insufficient to physically create two WW bosons, whose production has a kinematic threshold of ∼160 GeV. Consequently, for the process to occur, one particle must be virtual. This results in a rich theoretical landscape for Higgs decays, with numerous accessible decay modes, allowing the measurement of its couplings to several particles. In Fig. (3.2b) the branching ratios for the most relevant decay modes of the SM Higgs boson as a function of m_H are

depicted.
More than 90% of these decays occur through eight decay modes (see bottom diagrams in Figure (3.1)): decays into gauge boson pairs, W bosons with a branching fraction of 22%, Z bosons 3%, photons 0.23%, Z boson and photon 0.2%, as well as decays into fermion pairs, i.e., b-quarks 58.9%, which is the dominant decay mode, c-quarks 3%, τ-leptons 6%, and muons 0.02%. Decays into massless gauge bosons, such as gluons and photons, are possible via a loop of heavy quarks or even W bosons in the case of photons. The decay into gluons has a larger BR (9%) but is indistinguishable from the vast QCD background produced in a hadron collider. Conversely, despite its tiny BR, the decay into a photon pair offers an extremely clear signature.
The Higgs boson may also decay into invisible particles, with a rate exceeding the SM prediction of 0.1%, which is an area of active investigation. Such decays are conceivable in theories that extend beyond the Standard Model, proposing, for instance, the existence of dark matter particles that do not interact with the detector.

3.2 Higgs mass and width measurements

The mass of the Higgs boson is a fundamental and free parameter within the Standard Model. Its precise measurement is critical since the Higgs boson's mass influences key properties, including production cross-sections and decay branching fractions.
The ATLAS and CMS experiments exploit mainly two decay channels, the $H \to \gamma\gamma$ [121, 122] and $H \to ZZ^* \to 4l$, $(l = e, \mu)$ [123, 124]. Together with $H \to WW^* \to l\nu l\nu$ channel, these are considered the golden-channels that contributed to the discovery of the Higgs boson in 2012. Additionally, other decays channels, such as $H \to b\bar{b}$ and $H \to \tau^+\tau^-$, are also utilized. Although the two primary $H \to \gamma\gamma$ and $H \to ZZ$ decay modes have low branching fractions, they are characterized by final states with exceptionally clean signatures in the detector and an excellent mass resolution (1-2%), allowing for a more precise measurement of the Higgs boson mass compared to other leading channels.

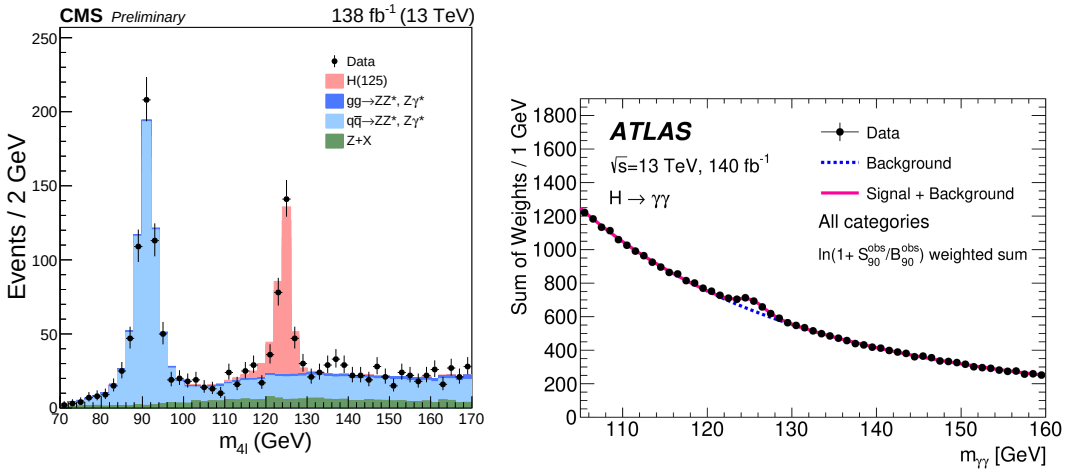

(a) (b)

Figure 3.3: CMS [124] observed data and the expected pre-fit m_{4l} distributions and ATLAS [121] post-fit $m_{\gamma\gamma}$ distribution, targeting the $H \to ZZ^* \to 4l$ and $H \to \gamma\gamma$ channels.

In Figure (3.3), the distributions of the two most significant variables for the two golden

channels are shown: the four-lepton invariant mass (CMS) and the diphoton mass (ATLAS) in their respective full Run-II analyses.
ATLAS [125] has performed a full Run-I and Run-II combination for the $H \to ZZ^* \to 4l$ and $H \to \gamma\gamma$ channels, while CMS [122] conducted a full Run-I and partial Run-II combination:

$$m_H(\text{ATLAS}) = 125.11 \pm 0.09_{\text{stat.}} \pm 0.06_{\text{syst.}} \text{ GeV}, \tag{3.1}$$

$$m_H(\text{CMS}) = 125.38 \pm 0.11_{\text{stat.}} \pm 0.08_{\text{syst.}} \text{ GeV}. \tag{3.2}$$

The Higgs width is predicted to be tiny by the SM, $\Gamma_H = 4.07$ MeV [119], since the boson couples to Standard Model particles via their masses, which leads to very small couplings for accessible final states for a 125 GeV Higgs boson. Consequently, Beyond SM decays could significantly enhance this width. Measuring the Higgs width directly is impossible since Γ_H^{SM} is much narrower than the experimental precision ($\sim$0.1 GeV) of ATLAS and CMS, which is far smaller than the experimental resolution for diphoton or four-lepton masses. An indirect measurement, however, is possible. Exploiting $gg \to H \to ZZ^*$ events, and targeting $4l$ and $2l2\nu$ decays, ATLAS [126] and CMS [124] measured Higgs widths consistent with the SM prediction:

$$\Gamma_H(ATLAS) = 4.5^{+3.3}_{-2.5} \text{ MeV}, \quad \Gamma_H(CMS) = 2.9^{+1.9}_{-1.4} \text{ MeV}. \tag{3.3}$$

3.3 Higgs coupling measurements

In the Standard Model, fermions acquire mass through gauge-invariant interactions with the Higgs field, encoded in the Yukawa couplings. The Higgs is also responsible for the electroweak symmetry breaking, thereby generating the masses of gauge bosons, as discussed in Sect. 1.5. Although this straightforward solution is elegant, Investigating the couplings of the Higgs boson to both vector bosons and fermions is thus crucial, as Beyond Standard Model physics could significantly alter the predictions of the SM.
Beyond-the-SM physics is expected to influence production modes and decay channels in a correlated manner if governed by similar interactions. For instance, any change in the Higgs boson's interaction with W bosons and top quarks would not only impact the $H \to WW$ or $H \to \gamma\gamma$ decay rates but also alter the production cross sections for ggH, WH, and VBF modes. To probe such deviations from SM predictions, a set of parameters κ_i, which normalize the couplings relative to their SM predicted values, is employed. These parameters modify the Higgs boson coupling strengths without affecting the kinematic distributions of a given process. To determine the value of a specific Higgs boson coupling, a simultaneous fit of multiple production times branching fraction measurements, parameterized by the multiplicative coupling strength modifiers κ, is required.
Various scenarios have been explored. A simplified approach to fitting Higgs boson couplings introduces two parameters, κ_V and κ_F, which scale the Higgs boson's couplings to massive gauge bosons and fermions, respectively. With the limited data available at the time of discovery, this fit provided initial indications of the existence of both types of couplings. With the current dataset, the sensitivity has significantly improved, and both coupling modifiers are now measured with considerable consistency with the Standard Model predictions, as shown in the left plot of Fig. (3.4).
In a more detailed model, the coupling modifiers for heavy gauge bosons (κ_W, κ_Z) and

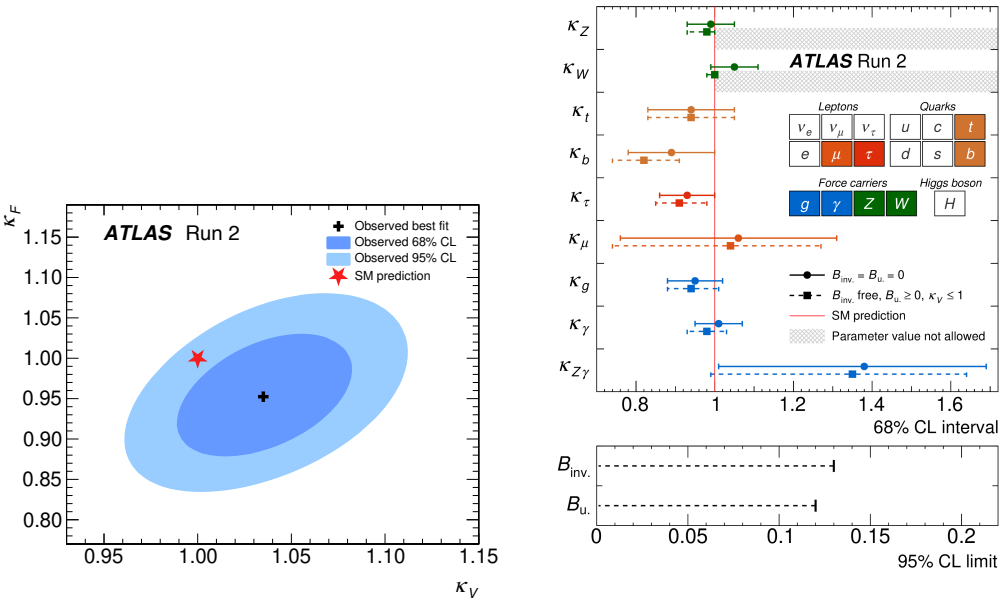

(a) (b)

Figure 3.4: ATLAS Higgs-to-fermion versus Higgs to heavy gauge boson coupling measurement for the full Run-II dataset. (Right) ATLAS reduced coupling strength modifiers per particle type with effective photon, $Z\gamma$ and gluon couplings. $B_{inv.}$ and $B_{u.}$ are the branching fractions corresponding to decays to invisible and undetected non-SM particles, respectively [118].

fermions (κ_t, κ_b, κ_τ, κ_μ) are treated independently and assumed to be positive[1]. Processes that occur via loops of intermediate virtual particles in the SM, such as Higgs boson production via ggH or decay to a pair of gluons, photons, or $Z\gamma$, are parameterized in terms of these κ_i. In extensions of the SM where invisible or undetected (due to large backgrounds) non-SM Higgs boson decays are considered, loop-induced processes may receive additional contributions. A more comprehensive fit for deviations in Higgs boson couplings can be defined by introducing additional modifiers for the effective coupling to gluons (κ_g), photons (κ_γ), and $Z\gamma$ ($\kappa_{Z\gamma}$). ATLAS results for this fit are shown in Fig. (3.4b).
All measured coupling strength modifiers are compatible with their Standard Model predictions, with no evidence of new physics or deviations detected.

Higgs self-coupling via single Higgs production Although the trilinear Higgs self-coupling can be directly probed through Higgs pair production processes, as detailed in the next Section, it can also be explored indirectly via single-Higgs production: it does not depend on λ_3 at Leading Order (LO), but it is affected by λ_3 at Next-to-Leading Order (NLO), where loop-level contributions make the measurements sensitive to variations in the Higgs trilinear self-coupling. The relevant Feynman diagrams are depicted in Fig. (3.5). Unlike a scenario typically considered to study the self-coupling modifier, where only the trilinear Higgs coupling is assumed to vary, large corrections to the Higgs self-couplings

[1]The coupling to c-quarks is usually constrained by $\kappa_c = \kappa_t$ to address the low sensitivity to this coupling, though in some studies it is treated as free parameter.

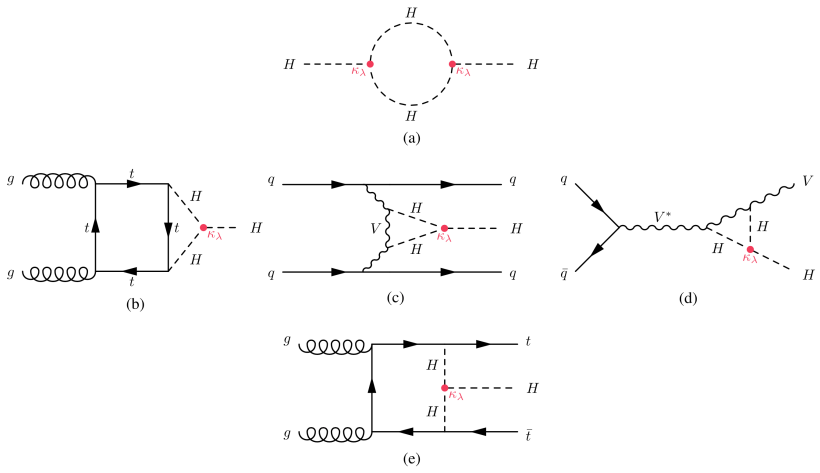

Figure 3.5: Illustrations of one-loop Feynman diagrams that depend on the λ_3 parameter are shown for (a) the Higgs boson self-energy, and for single-Higgs production in the (b) ggF, (c) VBF, (d) VH, and (e) ttH channels [127].

are rarely isolated and are usually accompanied by changes in other Higgs interactions. These corrections modify single-Higgs processes at tree level, producing effects comparable to those induced at loop level by deviations in the Higgs self-coupling.
Therefore, a precise determination of κ_λ necessitates a global fit that also accounts for distortions in single-Higgs couplings. While the expected sensitivity from such global fit is not as strong as when only the Higgs boson self-coupling is allowed to deviate from its SM value, this approach is less model-dependent.
The results and constraints on self-coupling obtained through this indirect single-Higgs approach are less precise than those derived from double Higgs analyses. However, they could become more competitive in the future, even though HH measurements are currently dominated by statistical uncertainties and are expected to improve more rapidly than the precision of H measurements.
The most stringent constraints on Higgs boson self-interactions to date are provided by combining di-Higgs and single-Higgs boson production analyses, as performed by the ATLAS collaboration using its full Run-II dataset, detailed in Ref. [127].

3.4 Higgs boson pair production

In the Standard Model, the Higgs field potential is assumed to be a quartic potential, which is the minimal level required to construct a gauge-invariant Lagrangian. Following electroweak symmetry breaking, this leads to both trilinear and quartic self-interactions for the Higgs boson, as outlined by Equation (1.51).
If the Higgs boson potential that induces EWSB precisely matches that of the Standard Model, the $\lambda_3^{SM} \sim 0.13$ with sub-percent accuracy. Any alterations to this potential would affect this relation. Direct measurement of the Higgs boson self-coupling is the only method to determine the exact form of the BEH potential.
The lowest-order Higgs boson self-interaction is the trilinear one. The most effective and straightforward approach to measuring this coupling is by detecting pairs of Higgs bosons in the final state. However, the production rate of such events is approximately 1000 times less than that for single Higgs bosons, making their measurement difficult at the current LHC capabilities. In the same way that Higgs pair production is essential for studying

the trilinear self-coupling, triple Higgs production via gluon fusion, $gg \to HHH$, is crucial for investigating the quartic self-coupling. The cross-sections for these processes, which are suppressed by a factor of v compared to the trilinear self-coupling (Eq. (1.51)), are significantly smaller than those for HH production, suggesting that λ_4 is likely to remain elusive and challenging to access for a long time.

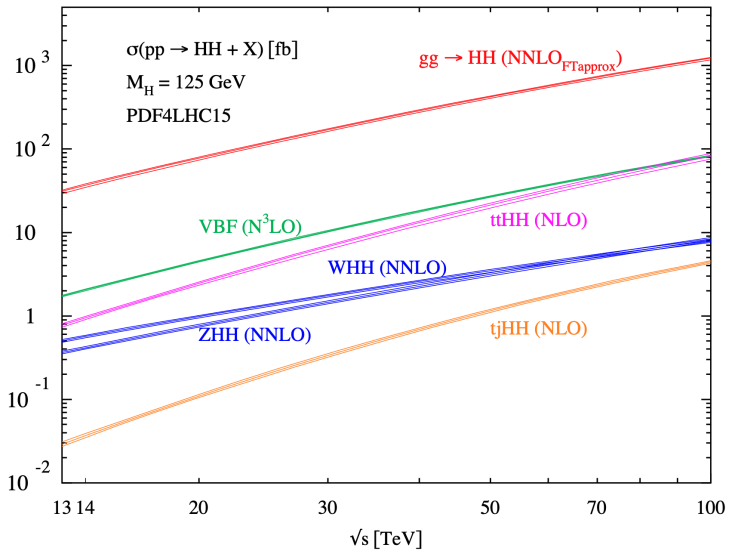

Figure 3.6: Total cross sections for double Higgs production at hadron colliders in SM via gluon-gluon Fusion, Vector-Boson Fusion, double Higgs-strahlung and double Higgs bremsstrahlung off top quarks [128].

Searches for double Higgs production at the LHC focus on the two main production mechanisms: gluon-gluon fusion and vector-boson fusion, similar to single Higgs production processes. Their cross-sections, along with those for less dominant production modes with such small cross-sections that are not experimentally accessible at present, are illustrated as a function of the center-of-mass energy of the pp collision in Fig. (3.6).

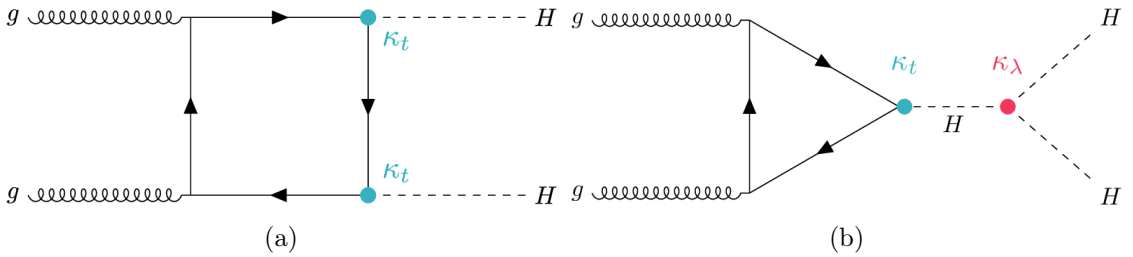

Figure 3.7: The two Feynman diagrams for the dominant gluon–gluon fusion HHproduction processes [127].

The dominant loop-induced ggF mechanism is characterized by destructive interference between the Leading Order (LO) box diagram (Fig. (3.7a)) and the triangle diagram (Fig. (3.7b)), the latter of which involves the trilinear Higgs coupling. The box diagram does not contribute to the Higgs boson self-couplings and is solely driven by the Higgs-top quark Yukawa interaction, with the coupling modifier $\kappa_t = y_t/y_t^{SM}$. The relative contributions of these two amplitudes, as well as their interference, can be observed in the Higgs pair invariant mass distribution m_{HH} shown in Fig. (3.8).

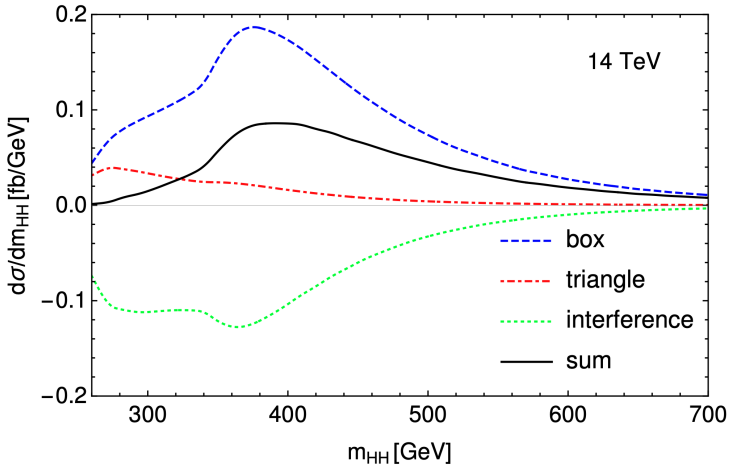

Figure 3.8: Leading-order distribution of the Higgs pair invariant mass for the various contributions to the gluon fusion production process and their interference [128].

The m_{HH} variable is crucial in experimental analyses for characterizing the properties of the HH system: higher values of m_{HH} are associated with increased transverse momentum of the Higgs bosons and more energetic event kinematics. The box diagram has an invariant mass spectrum peaking around $2m_t \approx 350$ GeV. The effect of the trilinear Higgs self-coupling in the LO total cross section results in a reduction of approximately half compared to the box-only contribution, and the invariant mass spectrum becomes generally softer as the triangle contribution increases. Changes in the m_{HH} distribution due to anomalous values of κ_λ are depicted in Figure (3.9).

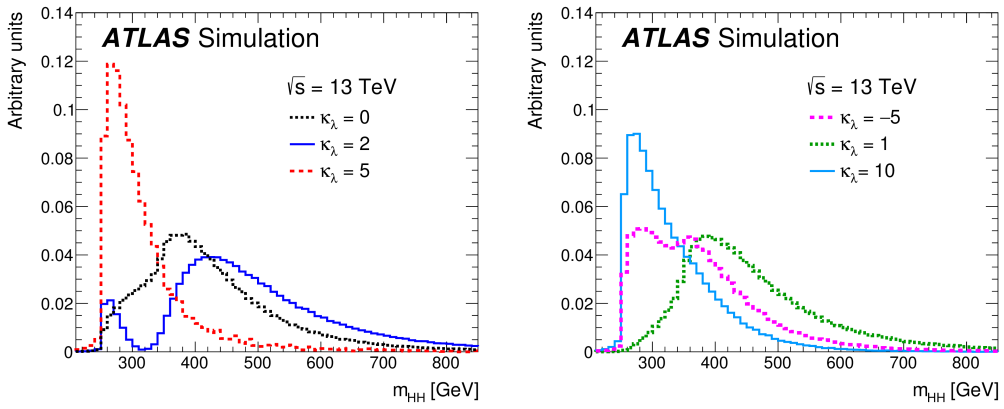

(a) (b)

Figure 3.9: HH invariant-mass distribution in ggF for various values of κ_λ assuming $\kappa_t = 1$. For $\kappa_\lambda = 0$, i.e. no triangle contribution, the distribution shows a cross-section increase for $m_{HH} > 2m_t$ and a large high-m_{HH} tail. For $\kappa_\lambda = 10$, the triangle diagram dominates. At $\kappa_\lambda = 2$, maximum destructive interference occurs between the box and triangle diagrams. Since the interference is destructive when κ_λ is positive, a deficit is observed between $2m_H$ and $2m_t$. Although the deficit is less pronounced when $\kappa_\lambda = 5$, interference still occurs at high m_{HH} values, resulting in a narrower distribution compared to the case when $\kappa_\lambda = 10$ [129].

The ggF cross section can be expressed as a second-order polynomial in κ_t and κ_λ:

$$\sigma(\kappa_t, \kappa_\lambda) \sim \kappa_t^4 |\mathcal{M}_B|^2 + \kappa_t^3 \kappa_\lambda (\mathcal{M}_T \mathcal{M}_B + \mathcal{M}_B \mathcal{M}_T) + \kappa_\lambda^2 \kappa_t^2 |\mathcal{M}_T|^2 \tag{3.4}$$

where the $\mathcal{M}_B$ and $\mathcal{M}_T$ denote the amplitudes of the box and triangle diagrams, respectively. Their destructive interference results in a very small cross section [130, 131],

$$\sigma_{ggF}^{SM}(HH) = 30.77(34.13)^{+6\%}_{-23\%}(\text{scale} + m_{top}) \pm 2.3\%(\text{PDF} + \alpha_s)\ \text{fb} \tag{3.5}$$

calculated at next-to-next-to-leading-order (NNLO) in α_s for pp collisions at a center-of-mass energy of 13 (13.6) TeV and a Higgs boson mass equal to $m_H = 125$ GeV. The "scale" uncertainty accounts for missing higher-order perturbative QCD calculations, the "PDF+α_s" uncertainty addresses the variations in the strong coupling constant and parton distribution functions, and "m_{top}" covers missing finite top-quark mass effects. This value is a three order of magnitude smaller than the corresponding production rate for a single Higgs boson via ggF ($\sigma_{ggF}^{SM}(H) = 48.6$ pb [95]).
The sub-dominant VBF production mode, similar to single Higgs production, is dominated by W and Z exchange. At $\sqrt{s} = 13$ (13.6) TeV, it accounts for a double Higgs production rate about 18 times smaller than ggF HH, according to SM predictions at next-to-next-to-next-to-leading-order (N3LO) in QCD: $\sigma_{SM}(HH) = 1.687(1.874)^{+0.05\%}_{-0.04(-0.03)\%}(\text{scale}) \pm 2.7\%(\text{PDF} + \alpha_s)$ fb [132, 133].

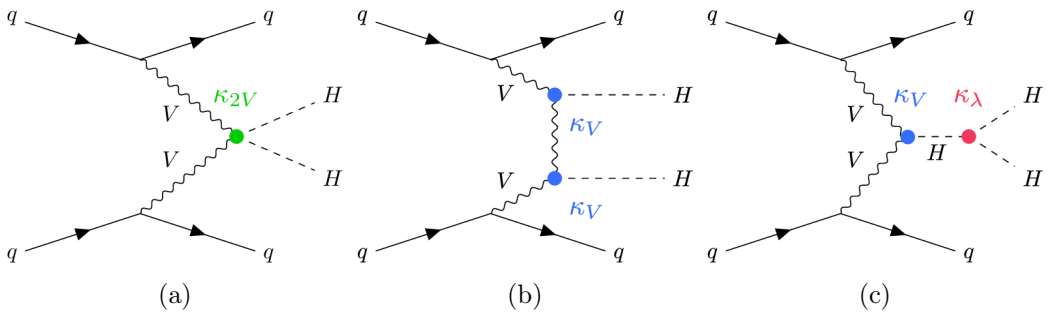

Figure 3.10: Leading-order diagrams contributing to Higgs boson pair production via Vector Boson Fusion [127].

This involves diagrams from two Higgs radiations off virtual W or Z bosons (Fig. (3.10a-b)), and diagrams where a single off-shell Higgs boson decays into a Higgs pair (Fig. (3.10c)), which scale with κ_{2V}, κ_V^2, and $\kappa_\lambda\kappa_V$, respectively. κ_V and κ_{2V} describe the coupling strengths of the HVV and $HHVV$ interaction vertices, normalized to their SM predictions. Thus, double Higgs production via VBF depends on the trilinear Higgs boson self-coupling modifier κ_λ and provides a unique probe of the quartic interaction vertex between two vector bosons and a Higgs boson pair (namely, κ_{2V}). While κ_V is currently well constrained by searches for single Higgs boson production via VBF, the other two couplings remain far from measurement. Deviations from unity for κ_λ and κ_{2V} strongly enhance double Higgs production via VBF, leading to a quadratic dependence of the VBF HH cross-section on the two coupling modifiers:

$$\begin{aligned}\sigma(\kappa_{2V}, \kappa_V, \kappa_\lambda) \sim\ & \kappa_{2V}^2|\mathcal{M}_a|^2 + \kappa_V^4|\mathcal{M}_b|^2 + \kappa_V^2\kappa_\lambda^2|\mathcal{M}_c|^2 \\ & + \kappa_{2V}\kappa_V^2|\mathcal{M}_a\mathcal{M}_b + \mathcal{M}_b\mathcal{M}_a| + \kappa_{2V}\kappa_V\kappa_\lambda|\mathcal{M}_a\mathcal{M}_c + \mathcal{M}_c\mathcal{M}_a| \\ & + \kappa_V^3\kappa_\lambda|\mathcal{M}_b\mathcal{M}_c + \mathcal{M}_c\mathcal{M}_b|,\end{aligned} \tag{3.6}$$

where $\mathcal{M}_a$, $\mathcal{M}_b$ and $\mathcal{M}_c$ are the amplitudes of the diagrams in Fig. (3.10). The defining feature of the final state in the VBF HH production mode, the presence of two forward and highly energetic hadronic jets, in addition to the double Higgs final state, aids in efficiently distinguishing the signal from competing background processes, making the investigation

of HH produced via VBF particularly compelling.
Given the extensive range of Higgs boson decay modes described in Sect 3.1, numerous signatures can be leveraged when searching for Higgs boson pair production. The branching ratios associated with each final state are summarized in Fig. (3.11).

	bb	WW	ττ	ZZ	γγ
bb	34%				
WW	25%	4.6%			
ττ	7.3%	2.7%	0.39%		
ZZ	3.1%	1.1%	0.33%	0.069%	
γγ	0.26%	0.10%	0.028%	0.012%	0.0005%

Figure 3.11: Branching fractions for different final states in di-Higgs decay processes.

Searches in multiple HH decay modes are performed and combined in order to obtain the best sensitivity. All channels have trade-offs between BR and the final state signal purity. Complementarity of research in different decay channels reflects the complementary sensitivity to couplings' variations. Due to the large Higgs boson Branching Ratio (BR) to bottom quarks (59%), most searches require at least one $H \to b\bar{b}$ decay while different decay modes of the second Higgs boson are considered.

3.4.1 State-of-the-art of HH searches in ATLAS and CMS

ATLAS and CMS have dedicated a significant effort to HH searches with full Run-II data collected in pp collisions at $\sqrt{s} = 13$ TeV with an integrated luminosity of about 140 fb^{-1} in different channels and interesting results are released by the two Collaborations' analyses: $HH \to b\bar{b}VV$ (CMS [134, 135]), $HH \to bbll + E_T^{miss}$ (ATLAS [136]), $HH \to WW\gamma\gamma$ (CMS [137]), and $HH \to Multileptons$ (ATLAS [138] and CMS [139]). In the following, the HH non-resonant searches with full Run-II data by the ATLAS and CMS experiments in the three most sensitive (*golden*) channels, $b\bar{b}b\bar{b}$, $b\bar{b}\tau\tau$ and $b\bar{b}\gamma\gamma$ are discussed. The combinations of the different analyses from the two Collaborations and a brief overview of the resonant searches and the HL-LHC projections are also presented.
In all three ATLAS and CMS analyses, the jets are reconstructed using the anti-κ_t jet clustering algorithm with a radius parameter of 0.4 and those originating from b quarks are identified through specific multivariate classification techniques, the ATLAS DL1r algorithm, examined in Sect. 2.3.3.2, and the CMS *DeepJet* [140] model, that is also a Deep Neural Network (DNN) combining information from ParticleFlow jet constituents, track-based variables and secondary vertex properties. Different thresholds on the DeepJet algorithm output define working points based on b-tagging accuracy: *Loose* with 94% efficiency (10% misidentification for light-flavor and charm jets), *Medium* with 84% efficiency (1% misidentification), and *Tight* with 58% efficiency (0.1-0.2% misidentification).

3.4.1.1 Nonresonant $HH \to b\bar{b}b\bar{b}$ process

The fully hadronic final state is characterized by the largest BR of 34% and the challenging multi-jet background. Both in ATLAS [141] and in CMS [142] the events selection requires exactly four reconstructed jets b-tagged using the DL1r working point that gives 77% efficiency (1/170 and 1/5 misidentification for light-flavor and c-jets, respectively) for jets associated with true b-hadrons and the Tight DeepJet working point. The jets then paired, according to the increasing distance between highest-p_T jets, to form the two Higgs boson candidates H_1, H_2 ($> 90\%$ correct $H \to b\bar{b}$ matching).
In ATLAS, the ggF and VBF signal regions are cathegorized by the pseudorapidity separation $|\Delta\eta|$ and the discriminant $X_{HH} = \sqrt{(\frac{m_{H_1} - 124\ \text{GeV}}{0.1 m_{H_1}})^2 + (\frac{m_{H_2} - 117\ \text{GeV}}{0.1 m_{H_2}})^2}$, in order to improve the HH analysis sensitivity. The invariant mass of the Higgs boson candidate pair, m_{HH}, is used as the signal-background discriminating variable. In CMS, the signal is extracted via a multivariate BDT score and the m_{HH} in the ggF and VBF subcategories, respectively. There is no deviation from a background-only hypothesis and the observed (expected) upper limits at 95% confidence level (CL) are set on HH production cross section compared to the SM expectation σ/σ_{SM} to 5.4 (8.1) and on the coupling modifiers $-3.9 < \kappa_\lambda < 11.1$ ($-4.6 < \kappa_\lambda < 10.8$) and $-0.03 < \kappa_{2V} < 2.11$ ($-0.05 < \kappa_{2V} < 2.12$) for ATLAS, while to $\sigma/\sigma_{SM} < 3.9$ (7.8), $-2.3 < \kappa_\lambda < 9.4$ ($-5.0 < \kappa_\lambda < 12.0$) and $-0.1 < \kappa_{2V} < 2.2$ ($-0.4 < \kappa_{2V} < 2.5$) for CMS.

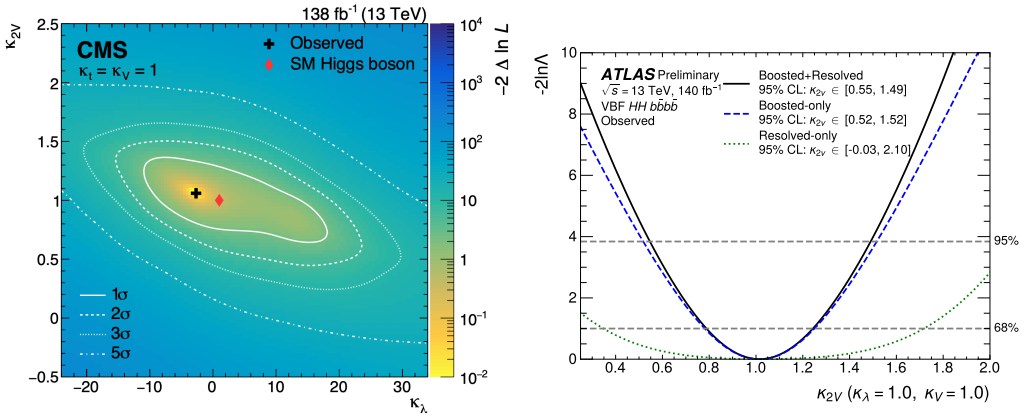

(a) (b)

Figure 3.12: The CMS profile likelihood test statistic scan on data as function of κ_λ, κ_{2V} [143] (a) and the ATLAS Observed values of $-2\ln\Lambda$ versus κ_{2V} for the boosted (dashed blue), resolved (dotted green) analyses, and their combination (solid black) are shown in (b) [144].

The most interesting results about the κ_{2V} is produced from the CMS boosted regime analysis, [143]: $0.62 < \kappa_{2V} < 1.41$ ($0.66 < \kappa_{2V} < 1.37$) at 95% CL. This is the more stringent limit excluding $\kappa_{2V} = 0$ at 6.3σ. In this analysis, only events with both Higgs bosons in the highly Lorentz-boosted regime, i.e. with sufficiently large transverse momentum ($p_T > 300$ GeV) for the decay products of each Higgs boson to become merged into a single large-radius ($\Delta R = 0.8$) jet, are selected and reconstructed via a graph neural network algorithm, *ParticleNet* [145].
ATLAS has recently performed a boosted $HH \to b\bar{b}b\bar{b}$ analysis in VBF topology [144], constraining the κ_{2V} coupling to be within $0.55 < \kappa_{2V} < 1.49$ ($0.37 < \kappa_{2V} < 1.67$) at 95% CL. The $\kappa_{2V} = 0$ exclusion observed (expected) significance is 3.8 (3.3). The two required (+2

VBF jets) Higgs boson candidates $H \to b\bar{b}$ are reconstructed as large-R jets with $R = 1.0$ and $p_T \in [250 - 3000]$ GeV. They are identified by applying a double b-tagging algorithm based on a deep neural network [146]. To enhance sensitivity to the κ_{2V} parameter, the boosted analysis is combined with the resolved analysis (Fig. (3.12b)).

3.4.1.2 Nonresonant $HH \to b\bar{b}\tau\tau$ process

The decay channel has a moderate branching fraction (7.3%), the cleaner final state thanks to a good compromise between background and final state reconstruction but electroweak and top backgrounds can mimic signal. The events are selected in three separate signal categories characterized by the presence of exactly two b-tagged jets and two oppositely charged τ leptons that can both decay hadronically, $\tau_{had}\tau_{had}$, or one decays hadronically and the other leptonically (electron or muon), $\tau_{lep}\tau_{had}$. In ATLAS [147], the main backgrounds including the production of top-quark pairs ($t\bar{t}$), single top quarks, W/Z+jets and fake-τ, are estimated by both MC simulation-based and data-driven methods.
After a careful preselection for each of the three signal regions using a combination of multiple trigger cuts based on the fundamental properties of the involved taus and leptons, the selected events are divided into three mutually exclusive categories.
A set of multivariate BDT discriminants is used to extract the signal from background. The statistical analysis allows to set an observed (expected) upper limit at the 95% CL on ggF+VBF σ/σ_{SM} corresponding to 5.9 (3.3), while the coupling parameters are constrained to a 95% confidence interval of $-3.1 < \kappa_\lambda < 9.0$ ($-2.5 < \kappa_\lambda < 9.3$) and $-0.5 < \kappa_{2V} < 2.7$ ($-0.2 < \kappa_{2V} < 2.4$).
In CMS [148], hadronic τ leptons are identified using a convolutional neural network, the *DeepTau* algorithm. The main background sources are $t\bar{t}$ production, $Z/\gamma^* \to ll$ production and QCD multijet events: the first two contributions are modeled using simulation methods, the third using data-driven approach. A binned maximum likelihood fit of a DNN discriminant is performed in all the ggF and VBF categories. Upper limits at 95% CL are set both on σ/σ_{SM} to 3.3 (5.2) and on $-1.7 < \kappa_\lambda < 8.7$ ($-2.9 < \kappa_\lambda < 9.8$) and $-0.4 < \kappa_{2V} < 2.6$ ($-0.6 < \kappa_{2V} < 2.8$).

3.4.1.3 Nonresonant $HH \to b\bar{b}\gamma\gamma$ process

This final state is characterized by a small branching ratio (0.26%), but also by a clear experimental signature, thanks to the excellent di-photon invariant mass resolution ($\sim 2\%$), and a smooth background, mainly di-photon continuum ($\gamma\gamma$+jets) and single Higgs boson, that is estimated using data-driven methods in CMS [149] and in combination with MC simulation in ATLAS legacy analysis [103]. The final state is fully reconstructable and there are not combinatoric issues for H identification.
A signal region is defined looking for events with two well reconstructed and identified photons and exactly two hadronic jets compatible with originating from the hadronization of bottom quarks.
The reduced invariant mass of the diphoton plus b-tagged jets system is defined as

$$m^*_{b\bar{b}\gamma\gamma} = m_{b\bar{b}\gamma\gamma} - (m_{b\bar{b}} - 125 \text{ GeV}) - (m_{\gamma\gamma} - 125 \text{ GeV}) \,, \tag{3.7}$$

and it is used in ATLAS to divide the selected events into two regions, targeting the SM signal, $m^*_{b\bar{b}\gamma\gamma} > 350$ GeV, and the BSM one, $m^*_{b\bar{b}\gamma\gamma} \leq 350$ GeV. This corrected invariant mass is designed to improve the resolution of the four-object mass $m_{b\bar{b}\gamma\gamma}$ by reducing

the effects of detector resolution. In each region, a dedicated BDT is trained to isolate HH signals from backgrounds relying on ggF-targeting and VBF-targeting input variables. Among the BDT input variables, the dijet mass shows the highest discriminating power. The diphoton invariant mass is used as the final discriminant variable to obtain the statistical results via a maximum likelihood fit to its distribution in the range $[105, 160]$ GeV, performed simultaneously over all the five categories defined by $m^*_{b\bar{b}\gamma\gamma}$ and BDT score.
No significant excess of events is observed in the data with respect to the expected background and observed (expected) upper limits at 95% CL are set on the HH cross-section, $\sigma/\sigma_{SM} < 4.0$ (5.0). The 95% confidence intervals for the coupling modifiers are $-1.4 < \kappa_\lambda < 6.9$ ($-2.8 < \kappa_\lambda < 7.8$) and $-0.5 < \kappa_{2V} < 2.7$ ($-1.1 < \kappa_{2V} < 3.3$).
In the CMS analysis, a particular attention is reserved to the ttH background and in order to reduce it, a DNN, *ttHScore*, is used. A 2D fit in the ($m_{\gamma\gamma}$, m_{jj}) plane, in the mass range $100 < m_{\gamma\gamma} < 180$ GeV and $70 < m_{jj} < 190$ GeV, is performed for the signal extraction simultaneously in all the 14 mutually exclusive categories (14 ggF, 2 VBF) categories defined by the outputs of two MVA classifiers used separately for ggF and VBF events to discriminate signal and background and Higgs boson pair system mass expressed similarly to the ATLAS analysis (Eq. (3.7)).
The observed (expected) 95% CL limits on σ/σ_{SM} is 7.7 (5.2) and on coupling modifiers are $-1.7 < \kappa_\lambda < 8.7$ ($-2.9 < \kappa_\lambda < 9.8$), and $-1.3 < \kappa_{2V} < 3.5$ ($-0.9 < \kappa_{2V} < 3.1$).

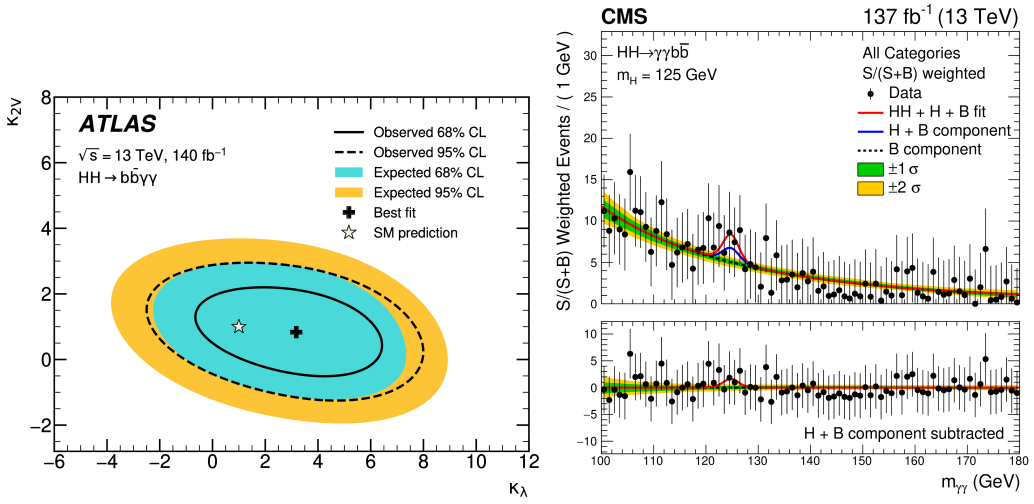

(a) (b)

Figure 3.13: (Left) The ATLAS profile likelihood test statistic scan on data as function of κ_λ, κ_{2V}. All other coupling modifiers are fixed to 1 [103]. (Right) The $m_{\gamma\gamma}$ distribution for the selected events in the data (black points) weighted by S/(S+B), where S and B represent the signal and background events, respectively, derived from a signal-plus-background fit. The lower panel displays the residual signal yield after subtracting the background [149].

3.4.1.4 Analyses combinations

The three discussed analyses, $b\bar{b}b\bar{b}$, $b\bar{b}\gamma\gamma$, and $b\bar{b}\tau\tau$, are combined to improve the HH sensitivity. In ATLAS, the combination includes the $bbll + E_T^{miss}$ and Multilepton decay modes [150], whereas CMS considers the $b\bar{b}ZZ$, $b\bar{b}WW$, $WW\gamma\gamma$, and Multilepton analyses [151], providing complementary ways to investigate Higgs boson pair production for a more comprehensive analysis and an improved sensitivity.

In both collaborations, the assumption in performing a statistical combination, a global likelihood function as the product of the individual analysis likelihoods in ATLAS and Poisson probability functions in CMS, that the analyses are statistically independent. In absence of HH signal, the statistical analysis of ATLAS combination sets observed (expected) limits at 95% CL of ggF+VBF $\sigma/\sigma_{SM} < 2.9$ (2.4), while CMS of $\sigma/\sigma_{SM} < 3.4$ (2.5). The ATLAS upper limits on modifier couplings are $-1.2 < \kappa_\lambda < 7.2$ $(-1.6 < \kappa_\lambda < 7.2)$ and $0.6 < \kappa_{2V} < 1.5$ $(0.4 < \kappa_{2V} < 1.6)$, while the corresponding CMS limits are $-1.24 < \kappa_\lambda < 6.49$ $(-2.28 < \kappa_\lambda < 7.94)$ and $0.67 < \kappa_{2V} < 1.38$ $(0.61 < \kappa_{2V} < 1.42)$ excluding $\kappa_{2V} = 0$ with a significance of 6.6σ (mainly thanks to the $b\bar{b}b\bar{b}$ boosted channel), that establishes existence of the quartic coupling g_{VVHH}.

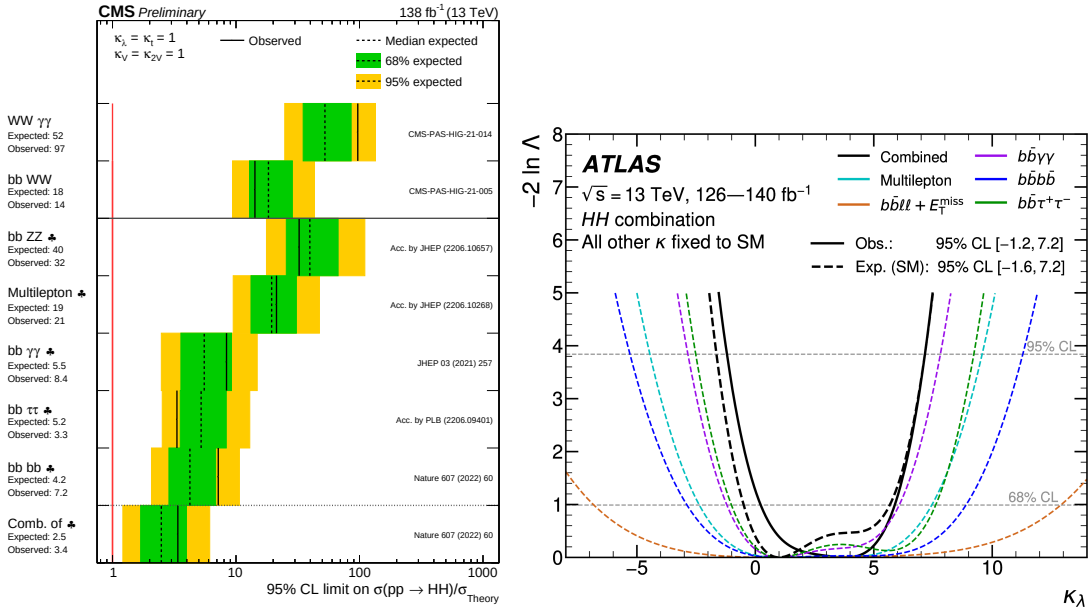

(a) (b)

Figure 3.14: CMS observed and expected upper limits on the SM $\sigma_{HH}/\sigma_{HH}^{SM}$ in different final state searches and their combination. The green band and yellow bands represents the regions containing 68% and 95%, respectively, of the limits under the background-only hypothesis [152]. The ATLAS expected values (dashed lines) of the profile-likelihood-ratio test statistic $(-2\ln\Lambda)$ obtained for different values of κ_λ for the different decay channels and their combination are shown in (b). The solid black line indicates the combination observed values [150].

3.4.1.5 Resonant di-Higgs processes

Searches for resonant HH production rely on many beyond the Standard Model theories predicting new heavy scalar particles that can decay into pairs of Higgs bosons. Models as *two-Higgs-doublets* (2HDM), that is the natural choice for beyond-SM model containing two Higgs doublets instead of just one, *Minimal Supersimmetric Standard Model* (MSSM), that realizes the supersimmetry in which the Higgs has a symmetric fermionic superpartner (the Higgsino), or *Composite Higgs model* (CHM), where the Higgs boson is a bound state of new strong interactions, contain spin-0 resonances motivating the searches to probe the existence of these particles in the mass range between 250 GeV and 5 TeV. Another possibility is that the Higgs boson pair is produced resonantly via the decay of a spin-2

Kaluza–Klein (KK) graviton, as suggested by the Randall–Sundrum (RS) model of warped extra dimensions. The corresponding Feynman diagrams are depicted in Fig. (3.15).

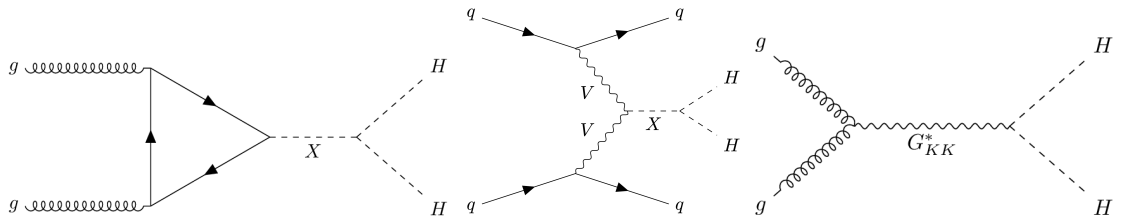

(a) (b) (c)

Figure 3.15: Feynman diagrams for resonant Higgs boson pair production via gluon–gluon fusion (a) and VBF (b) for a generic spin-0 boson, and ggF (c) for a Kaluza-Klein graviton [153].

The analysis strategies adopted for the HH resonant processes are similar to nonresonant ones in both the collaborations searches. Focusing on spin-0 resonance, the complementarity of the ATLAS (CMS) analyses permits to explore the existence of scalar particle (X) in the mass range $251 < m_X < 5000$ ($280 < m_X < 4500$) GeV produced via gluon-gluon fusion. For the $b\bar{b}\gamma\gamma$ channel, that is the most sensitive at low mass $m_X \lesssim 350$ GeV (entire resonant search mass range: $251 < m_X < 1300$ GeV), ATLAS [154] extracts the signal from background, that includes SM HH, by using a BDT score obtained as combinations of two separated BDT outputs, one for $\gamma\gamma$ and $t\bar{t}\gamma\gamma$ and the other for single H backgrounds. The diphoton invariant mass reconstructed with a 1% resolution is used as final discriminating variable. CMS [155] performs, as in nonresonant case, a 2D fit on $(m_{\gamma\gamma}, m_{b\bar{b}})$ resulting in the largest deviation from the only background hypothesis, that is observed at 650 GeV with a local (global) significativity of 3.8σ (2.8σ), Fig. (3.16a).

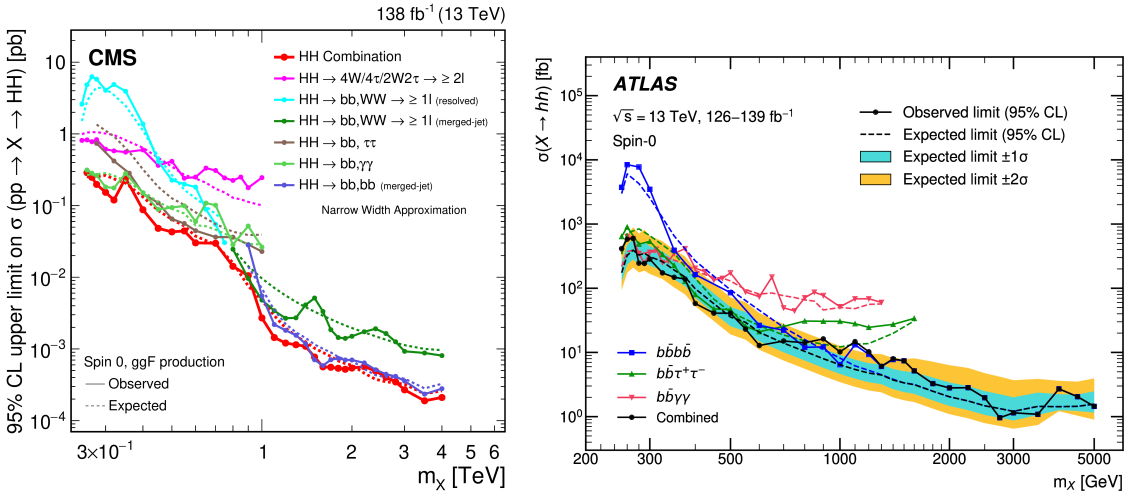

(a) (b)

Figure 3.16: CMS (a) and ATLAS (b) observed(expected) 95% CL upper limits on $\sigma(X \to HH)$ for a spin-0 resonance as a function of its mass m_X in the $b\bar{b}b\bar{b}$, $b\bar{b}\gamma\gamma$, and $b\bar{b}\tau\tau$ (plus $b\bar{b}WW$ and $Multileptons$ for CMS) searches and their combination. For ATLAS the upper limits observed (expected) are in the range 0.96-600 fb (1.2-390 fb), varying with m_X [154, 155].

In the ATLAS $b\bar{b}\tau\tau$ search, that exhibits the greatest sensitivity in the intermediate resonance mass range $350 \lesssim m_X \lesssim 800$ GeV (total mass range: $251 < m_X < 1600$ GeV),

the HH signal is estimated using a fit to Parametrized Neural Network (PNN) output distribution, that is performed on m_X. As visible in Fig. (3.16b), the largest deviation from the Standard Model is observed at 1.1 TeV with a local (global) significativity of 3.3σ (2.1σ), and it is mainly due to $b\bar{b}\tau\tau$ channel.
The $b\bar{b}b\bar{b}$ decay channel dominates for high $m_X > 0.8$ TeV and both the Collaborations' analyses focus mainly on the boosted regime that, being characterized by two high-energy Higgs bosons each form a large-R jet identified as described in nonresonant analyses, allows to extend the resonant searches up to 5 TeV.
CMS performs resonant searches in three other analyses covering a larger number of HH signatures and combining them with the three golden decay modes: the $HH \to b\bar{b}WW \to b\bar{b}l\nu qq, b\bar{b}2l2\nu$ in resolved and merged regimes, sensitive at low-intermediate and high mass resonance ranges respectively, and the $HH \to Multileptons$ ($WWWW, WW\tau\tau, \tau\tau\tau\tau$), which differs from other typical channels that require at least one $H \to b\bar{b}$ and produces a small local excess, 1.5-2σ, in the observed limits for masses above 600 GeV, as shown in Figure (3.16a).

3.4.1.6 HL-LHC projections

As highlighted in Sect. 2.1.2, the High-Luminosity LHC project is scheduled to start in 2029, after the upgrades of the ATLAS and CMS detectors and trigger systems taking place during the LS3, delivering a total integrated luminosity of 3000 fb^{-1} and a predicted number of pile-up events of approximately 200 at a center-of-mass energy $\sqrt{s} = 14$ TeV. The statistics will increase by a factor of 10 compared to combining Run-II+Run-III data and a significantly improved sensitivity on HH production is expected, allowing a concrete aim to discover and measure the Higgs self-coupling.
The ATLAS projections [156] rely on a extrapolation of the different HH analyses based on the most recent results obtained with the full Run-II dataset and scaled by multiplicative factors to take into account the increase in integrated luminosity and center-of-mass energy from Run-II (126 fb^{-1}, 13 TeV) to the HL-LHC (3000 fb^{-1}, 14 TeV). The performance of the detector and trigger are assumed to be the same.
The systematic uncertainties (such as those related to the jet energy scale and resolution, flavor tagging, theoretical quantities, and background estimation) are treated with particular attention due to the difficulty to predict their changes at HL-LHC. Four scenarios are outlined: the first, where only statistical uncertainties are considered, excluding systematics (*No syst. unc.*); the second, the *baseline* scenario, where systematic uncertainties are scaled down based on the expected improvements thanks to HL-LHC dataset; the third (*Theoretical unc. halved*) is characterized by Run-II experimental uncertainties while theoretical uncertainties are divided by two; and the last scenario, where uncertainties are taken exactly as those of Run-II (*Run-II syst. unc.*).
At the end of HL-LHC running (3000 fb^{-1}), in the first scenario without uncertainties, the discovery significance combining the results of the three most sensitive HH channels ($b\bar{b}b\bar{b} + b\bar{b}\gamma\gamma + b\bar{b}\tau\tau$) is calculated to be 4.9σ, while in the baseline scenario it is 3.4σ. In Fig. (3.17a), the confidence intervals on κ_λ obtained for all scenarios through the combined statistical analysis are presented. For the baseline (No syst. unc.) case, the κ_λ 95% CI is $[0.0, 2.5]$ ($[0.3, 1.9]$) .
The CMS prospects [151] are based on parametric simulation performed with the DELPHES software [157] of the detector to model its response in the HL-LHC conditions, taking in consideration the pile-up effects. The performance of the reconstruction and

identification algorithms are parametrized through the simulation, while the statistical and experimental uncertainties are scaled by $1/\sqrt{L}$, the theoretical ones by $1/2$.
Assuming the absence of HH production, both the ATLAS and the CMS collaboration expect an 95% CL upper limit ggF+VBF $\sigma/\sigma_{SM} < 1.0$ (0.55 for the ATLAS baseline condition and 0.75-0.8 for CMS Fig. (3.17b)) after the combination of $b\bar{b}b\bar{b}$, $b\bar{b}\gamma\gamma$ and $b\bar{b}\tau\tau$ channels, indicating that the sensitivity is sufficient to confirm the existence of the SM HH production.

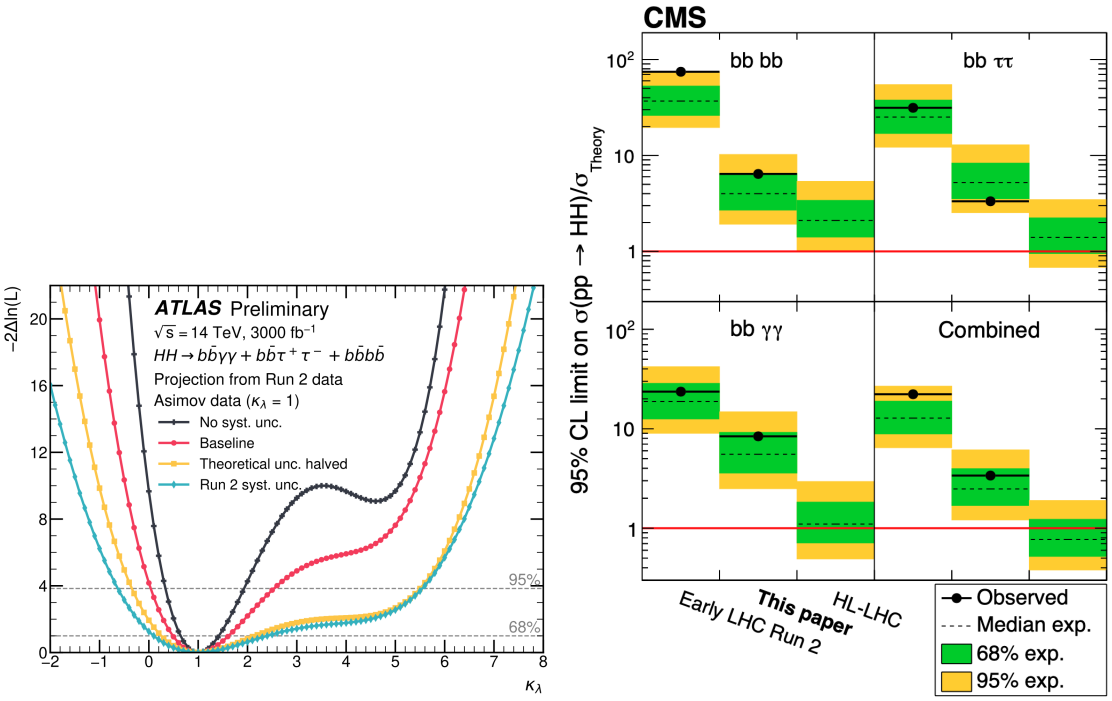

(a) (b)

Figure 3.17: (Left) ATLAS projected negative log-profile-likelihood versus κ_λ for combined $HH \to b\bar{b}b\bar{b} + b\bar{b}\gamma\gamma + b\bar{b}\tau\tau$ at $\sqrt{s}$=14 TeV and 3000 fb−1 is shown in the four different uncertainty scenarios [156]. The 68% and 95% confidence intervals are defined by the intersections of the four curves with the dashed horizontal lines. (Right) CMS comparison of observed and expected limits on HH production for $b\bar{b}b\bar{b}$, $b\bar{b}\gamma\gamma$, and $b\bar{b}\tau\tau$ channels using early LHC Run-II data (35.9 fb^{-1}), full Run-II data (138 fb^{-1}) and projected HL-LHC data (3000 fb^{-1}) [151].

Chapter 4

Search for Higgs boson pair production in the $b\bar{b}\gamma\gamma$ decay channel

This Chapter presents the search for nonresonant Higgs boson pair production in the two bottom plus two photons final state is performed using 140 fb^{-1} of proton-proton collision data at a center-of-mass energy of 13 TeV recorded by the ATLAS detector at the CERN Large Hadron Collider. As outlined in Sect. 3.4, SM double Higgs production is an extremely rare process. The $b\bar{b}\gamma\gamma$ state benefits from the high branching ratio for the $H \to b\bar{b}$ decay (59% for a SM Higgs boson), while the low branching ratio for the $H \to \gamma\gamma$ decay (0.23%) is offset by the excellent trigger and reconstruction efficiency for photons with the ATLAS detector. Additionally, the invariant mass of the photon pair can be measured with a resolution of 1-2 GeV, leading to a very distinct and clear signature. The branching fraction for the $b\bar{b}\gamma\gamma$ channel, 0.26%, is the lowest among the *"golden channels"* for the di-Higgs searches (Fig. (3.11)).
To improve the signal-to-background ratio, which is crucial for this analysis, all competing SM processes that could mimic the $b\bar{b}\gamma\gamma$ signature must be thoroughly understood and accurately modeled. The $HH \to b\bar{b}\gamma\gamma$ search includes Higgs boson pairs produced via Vector Boson Fusion as signal, in addition to the dominant ggF production mode. As discussed in Sect. 3.4, the VBF HH production mechanism depends on the trilinear Higgs boson self-coupling modifier κ_λ, providing additional information that impacts the allowed range of κ_λ by up to $\sim 7\%$. Moreover, it probes the cubic and quartic vertices HVV and $HHVV$, which define the couplings of a single Higgs boson and a Higgs boson pair, respectively, to two vector bosons.
In di-photon production, the invariant mass of the photon pair $m_{\gamma\gamma}$ is expected to follow a smoothly decreasing distribution, leading to the $\gamma\gamma$+jets background being classified as non-resonant, or continuum, background. The production of a single Higgs boson decaying into two photons constitutes a subdominant background for the $HH \to b\bar{b}\gamma\gamma$ search. The largest contributions are provided by ggF, Z boson-associated production, and $t\bar{t}H$. The two photons from H decay will appear as a narrow resonant peak centered around $m_H \approx 125$ GeV in the $m_{\gamma\gamma}$ spectrum, forming the resonant background.
Although the $b\bar{b}\gamma\gamma$ final state has an expected BR significantly lower than those of $b\bar{b}b\bar{b}$ (34%) and $b\bar{b}\tau\tau$ (7.3%), it achieves a higher expected signal-to-background (S/B) ratio and greater trigger efficiency, mainly due to the $H \to \gamma\gamma$ component, which in ATLAS has a much higher efficiency ($> 95\%$, Fig. (4.2)) compared to $H \to b\bar{b}$ or $H \to \tau\tau$. This results in a larger acceptance in phase-space regions, such as at small HH invariant mass, where potential deviations from the Standard Model might be more pronounced. These factors

compensate for the lower expected event yield and provides a sensitivity comparable to that of the other two decay modes.
In Fig. (4.1), the signal acceptance times efficiency, which depends on κ_λ, is shown for the three golden channels. Generally, it is lower for BSM signals with variations in κ_λ, mainly due to reduced trigger selection efficiency. This occurs because the softer spectrum results in lower p_T objects that fail to meet the trigger thresholds. Unlike $b\bar{b}\gamma\gamma$, other HH analyses experience a more significant drop in the low m_{HH} regions, where the self-coupling modifier differs from 1.

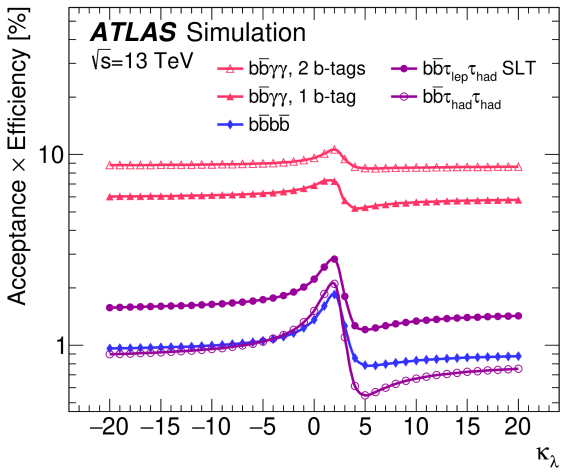

Figure 4.1: Acceptance, defined as the fraction of signal events that are geometrically detected, multiplied by efficiency, which is the fraction of signal events that pass the selection cuts, as a function of κ_λ for the $HH \to b\bar{b}b\bar{b}$, $b\bar{b}\tau\tau$ and $b\bar{b}\gamma\gamma$ analyses [129].

In this introductory section to the $HH \to b\bar{b}\gamma\gamma$ channel, following the description of the data and Monte Carlo samples used in the analysis discussed in Chapter 6, the reconstruction of the relevant physical objects is detailed, along with the event selection criteria applied to retain only those events exhibiting a good $b\bar{b}\gamma\gamma$ signature.

4.1 Data and simulation samples

The analysis is based on LHC full Run-II data from pp collisions at a center-of-mass energy of 13 TeV collected by the ATLAS detector between 2015 and 2018, and partial Run-III pp collision data for $\sqrt{s} = 13.6$ TeV between 2022 and 2023. After applying data-quality requirements [63] to ensure optimal performance of the detector subsystems, the total integrated luminosity amounts to 140 fb^{-1} for Run-II [62] and 59 fb^{-1} for partial Run-III, with an uncertainty of 0.83% and 2%, respectively.

Simulated events are essential for accurately modeling both signal and background processes, including the ATLAS detector's response. Monte Carlo (MC) samples are widely used in ATLAS physics analyses to estimate selection efficiencies, construct distributions for key discriminating variables, and build expected statistical models under background-only or signal-plus-background hypotheses.
The production of MC samples begins with the generation of physics events using process amplitudes calculated at a specific order in perturbation theory. This step is carried out

by an event generator. The subsequent emission of quarks and gluons (parton showering) and their hadronization is also simulated by an event generator, which may differ from the one simulating the hard scattering event. This generator typically also handles the decays of unstable particles produced in the hard-scattering interaction. Underlying and pile-up events are included in the MC samples (see Fig. (1.7)). The next step involves simulating the interaction of stable particles in the final state with the ATLAS detector and its response, achieved through a detailed simulation based on Geant4 [158]. Finally, the reconstruction algorithms applied to both simulated and real data are identical.
The simulated event samples used in this analysis are summarized in Table (4.1). The simulated $HH \to b\bar{b}\gamma\gamma$ samples are generated for both ggF and VBF HH production modes. Events from ggF HH production were generated at next-to-leading order (NLO) in QCD using the Powheg-Box v2 generator [159, 160] in the finite top-quark mass approximation. The parton distribution functions from the PDF4LHC21 set [161] are used in the matrix element. Parton showering, hadronization, and the underlying event are simulated using Pythia 8.309 [162]. Four samples were generated for $\kappa_\lambda = 1$ and $\kappa_\lambda = 0, 5, 10$. Events from VBF HH production are generated at leading order (LO)

Process	**Generator**	**PDF set**	**Showering**	**Tune**	**Accuracy**
ggF HH	Powheg Box v2	PDF4LHC21	Pythia 8.3	A14NNPDF23LO [163]	NLO
VBF HH	MadGraph5_aMC@NLO	NNPDF30NLO	Pythia 8.3	A14NNPDF23LO	LO
ggF H	Powheg Box v2	NNPDF30NNLO (Run-II)	Pythia 8.3	AZNLO (Run-II)[164]	NNLO
		PDF4LHC21 (Run-III)		A14NNPDF23LO (Run-III)	
VBF H	Powheg Box v2	NNPDF30 (Run-II)	Pythia 8.3	AZNLO (Run-II)	NLO
		PDF4LHC21 (Run-III)		A14NNPDF23LO (Run-III)	
WH	Powheg MiNLO [165]	NNPDF30 (Run-II)	Pythia 8.3	AZNLO	NLO
		PDF4LHC21 (Run-III)		A14NNPDF23LO (Run-III)	
$qq \to ZH$	Powheg MiNLO	NNPDF30 (Run-II)	Pythia 8.3	AZNLO	NLO
		PDF4LHC21 (Run-III)		A14NNPDF23LO (Run-III)	
$gg \to ZH$	Powheg MiNLO	NNPDF30 (Run-II)	Pythia 8.3	AZNLO	NLO
		PDF4LHC21 (Run-III)		A14NNPDF23LO (Run-III)	
ttH	Powheg Box v2	NNPDF30 (Run-II)	Pythia 8.3	A14NNPDF23LO (Run-II)	NLO
		PDF4LHC21 (Run-III)		A14NNPDF23LO (Run-III)	
bbH	Powheg Box v2	NNPDF30 (Run-II)	Pythia 8.3	A14NNPDF23LO (Run-II)	NLO
		PDF4LHC21 (Run-III)		A14NNPDF23LO (Run-III)	
$tHjb$	MadGraph5_aMC@NLO	NNPDF30	Pythia 8.3	A14NNPDF23LO	NLO
tHW	MadGraph5_aMC@NLO	NNPDF30	Pythia 8.3	A14NNPDF23LO	NLO
$\gamma\gamma$+jets	Sherpa 2.2.14	NNPDF30NNLO	–	–	$\gamma\gamma$+0,1(NLO),2,3(LO)
$t\bar{t}\gamma\gamma$ (nonallhad)	MadGraph5_aMC@NLO	NNPDF30NLO	Pythia 8.3	A14NNPDF23LO	–

Table 4.1: List of the nominal event samples for the HH signal, H background, and continuum background for Run-II and Run-III. The Table includes the simulation generator, the PDF and applied tuning parameters' sets, with the QCD accuracy level of the event generator.

using MadGraph5_aMC@NLO [166], with the NNPDF3.0NNLO PDF set [167] interfaced to Pythia 8.309 for parton showering. The VBF HH samples are normalized using cross sections evaluated at next-to-next-to-next-leading order (N3LO) in QCD. Twelve more VBF HH samples were produced and simulated in addition to the SM sample, but with varying values of κ_{2V}, κ_λ, and κ_V as shown in Table (4.2), allowing for the construction of signal regions sensitive to deviations from the Standard Model prediction.

The background samples include simulated events of single Higgs bosons decaying into $\gamma\gamma$, produced via ggF, VBF, and in association with a W or Z boson, a $t\bar{t}$ or $b\bar{b}$ pair, or a single top-quark. Simulated event samples of continuum diphoton production in association with top quark pairs ($t\bar{t}\gamma\gamma$) or with jets from quarks of other flavors ($\gamma\gamma$+jets)

κ_λ	κ_{2V}	κ_V
1	1	1
1	1	0.5
10	1	1
1	1.5	1
2	1	1
-5	1	0.5
1	2	1
1	0	1
1	0.5	1
1	3	1
0	1	1
1	1	1.5
0	0	1

Table 4.2: Grid of coupling modifier values used for producing the VBF HH samples. The SM sample corresponds to (1,1,1).

were generated and utilized to optimize the event classification described in Sect. 6.1. These samples were simulated using MadGraph5_aMC@NLO, with the NNPDF30NLO PDF set interfaced to Pythia 8.309 for parton showering, and the Sherpa v2.2.14 generator [168], respectively.

Starting from the AOD (Analysis Object Data) format[1] of the samples in Table (4.1), which contain essential information about the reconstructed events for common analyses, such as tracks, Particle Flow objects, and a limited amount of calorimeter cell data, a derivation framework implemented in *Athena* [169], the ATLAS software framework, is used to generate a reduced AOD model, termed Derived-AOD (DAOD). The DAOD format retains only data relevant to specific physics groups, including object and trigger information, a thinned track collection, generator-level (*truth*) information, and any additional data required for calibration tools (known as *Combined Performance (CP)* algorithms). Although the primary purpose of the framework is data reduction, it also includes the reconstruction of secondary physics objects when only their inputs were stored in the AOD. For instance, jets are reconstructed during the derivation process using PF objects stored in the AOD; similarly, heavy-flavor tagging is performed based on these jets and associated tracks stored in the AOD [170].
From Run-III, a common framework among HH analyses is adopted to produce from DAODs[2] the final flat ntuples, containing calibrated objects and user-level variables for analysis: the *Easyjet* framework [171].

A specific weight is assigned to each event and calculated for each MC sample and for each data period i, based on the corresponding luminosity L_i reported in Table (4.3), as

$$w_i = \frac{\sigma_{generated} \cdot FilterEff \cdot kFactor \cdot w_{MC} \cdot w_{pileup} \cdot SF}{\sum_{N_{gen.}} w_{MC}} \cdot L_i \ . \tag{4.1}$$

[1]The AOD are created from the Raw Data Objects (RDOs), which are C++ object representations of the byte-stream information obtained from MC simulations or trigger data.
[2]Specifically, the DAOD_PHYS, that is the derivation format for ∼80% of all physics analyses, and its future lightweight version DAOD_PHYSLITE, which already includes applied calibrations and contains all necessary information for running systematics. This new format will be the default for the HL-LHC.

Year	Luminosity [fb^{-1}]
2015-2016	36.6467
2017	44.6306
2018	58.7916
2022	31.3985
2023	27.7667

Table 4.3: Integrated luminosity recorded by ATLAS in Run-II and partial Run-III per year of data taking.

Here, the $\sigma_{generated}$ represents the theoretical cross-section for the generated processes. The $FilterEff$ accounts for the efficiency of event selections applied at the generator level, while the $kFactor$ adjusts the leading-order cross-section to account for next-to-leading order (NLO) corrections. The term w_{MC} is an event-specific weight assigned by the generator, and w_{pileup} adjusts the event weights to account for variations in the number of vertices, compensating for differences in pileup conditions across data periods relative to the fixed pileup configuration used during event generation. The denominator, $\sum_{N_{gen.}} w_{MC}$, represents the total sum of weights for all generated events, ensuring proper normalization. Finally, SF encapsulates the scale factors applied to account for simulation-to-data corrections for JVT, fJVT, b-tagging jet efficiencies, as well as photon reconstruction and trigger efficiencies. The data events are unweighted.

4.2 Object reconstruction and event selection

The $HH \to b\bar{b}\gamma\gamma$ analysis, similar to the $H \to \gamma\gamma$ analysis, employs different sets of di-photon triggers for each data-taking year. All triggers require at least two photons, calibrated for energy scale and resolution as described in Section 2.3.2, with transverse momentum thresholds of 35 GeV for the leading- photon and 25 GeV for the subleading-p_T photon, both satisfying the Loose identification criteria for 2015-2016 and Medium for other years to mitigate fake rates.

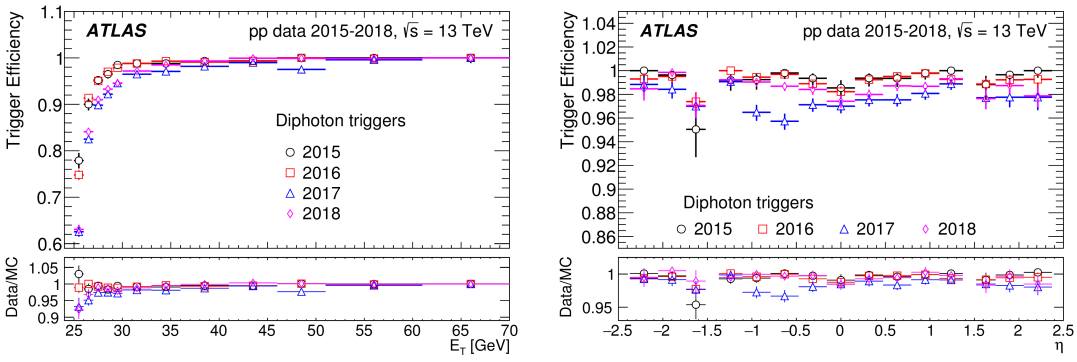

(a) (b)

Figure 4.2: Efficiencies of the diphoton triggers in 2015-2018 varying with the offline photon (a) E_T and (b) η. The ratios of data to MC simulation are shown in the bottom panel. Photons in the calorimeter transition region ($1.37 < |\eta| < 1.52$) are not included [172]. Equivalent plots for Run-III are in production.

Figures (4.2a-b) present the di-photon trigger efficiencies for each Run-II year as a function of photon E_T and η. Slightly lower efficiencies are observed in 2017–2018 due to the more stringent photon identification criteria and there is no significant η-dependence in the trigger efficiency, which remains close to 100%.
Selected events are required to include two photon candidates ($N_{\text{photons}} \geq 2$) within the acceptance region of the finely segmented electromagnetic calorimeter ($|\eta| < 1.37$ or $1.52 < |\eta| < 2.37$) and which satisfy the Tight identification criteria.
Among all potential collision vertices, the primary diphoton vertex is identified as the hardest vertex, i.e. the vertex with the highest sum of squares of transverse momenta of contributing tracks. Photon candidates must also meet a Loose isolation criterion, $E_T^{\text{cone0.2}} < 0.065 \cdot p_T$ and $E_T^{\text{cone0.2}} < 0.05 \cdot p_T$. The two leading photons that pass these selection cuts are then required to have $|\eta| < 1.37$ or $1.52 < |\eta| < 2.37$, an invariant mass $m_{\gamma\gamma}$ between 105 and 160 GeV, and transverse momenta with $p_T/m_{\gamma\gamma} > 0.35$ and $p_T/m_{\gamma\gamma} > 0.25$.

Following the discussion of Sect. 2.3.3, jets are reconstructed from particle-flow objects using the anti-k_t clustering algorithm with a radius parameter of $R = 0.4$. Jet candidates must have $p_T > 25$ GeV. A tight Jet Vertex Tagger (JVT) is applied to distinguish jets from the hard scatter from those originating from pile-up. The selected jets are calibrated using the calibration chain shown in Fig. (2.16).
To target $H \to b\bar{b}$ decays, events are required to contain exactly two b-tagged jets ($N_{b-\text{jet}}^{77\%} = 2$), which are central jets within the acceptance of the inner detector ($|\eta| < 2.5$) and satisfy the GN2 b-tagging algorithm with a nominal efficiency of 77%. This requirement ensures orthogonality with the $HH \to b\bar{b}b\bar{b}$ channel, which requires more than two b-jets. The two b-jets are then identified as leading or subleading, based on their pseudo-continuous binned b-tagging score ($pcbt$). If both the selected b-jets have the same b-tagging score, they are ordered according to their p_T. The *BCal* correction (Section 2.3.3.3) is applied to the energy of the two b-tagged jets. The specific PtReco correction factor has been updated to use the new GN2 b-tagging algorithm and it results in an improvement of approximately 22% in the $m_{b\bar{b}}$ invariant mass resolution, similar to what was observed in the legacy analysis that employed the DL1r algorithm, as shown in Fig. (2.20) that translated to an approximately 7% enhancement in the expected signal significance.
Jets that fail the b-tagging condition are ranked based on a discrete b-tagging score, divided into three bins: central jets with GN2 efficiencies of 77%–85%, 85%–100%, and non-central jets. As for the two Higgs candidate b-jets, jets with the same score are further ranked by p_T.
Events with six or more central jets are rejected to reduce background from $t\bar{t}H$, where the top quarks decay hadronically ($qq, gg \to (t\bar{t}H) \to bW^+bW^-H \to bq\bar{q}bq\bar{q}\gamma\gamma$). No requirements are imposed on the number of non-central jets.
The selection of the forward and highly energetic VBF jets in this analysis is based on a BDT (the *VBF jet tagger*), trained exclusively on SM VBF HH events, since the key variables related to the VBF topology, such as the di-jet invariant mass m_{jj} and the angular separation between the two VBF jets $\Delta\eta(j_1, j_2)$, show minimal dependence on the coupling modifiers κ_λ and κ_{2V}. The BDT is used to distinguish VBF jet pairs from other di-jet systems. Specifically, the signal corresponds to jet pairs where both reconstructed jets have an angular distance from a true VBF quark of $\Delta R < 0.3$, otherwise they are

classified as background. Reconstructed jets already classified as candidate b-jets cannot be considered as VBF signals.
The VBF jet tagger model is applied to all possible jet combinations, excluding the two candidate b-jets, and the jet pair with the highest BDT score is selected as the VBF jet pair for each event.

Electron candidates are reconstructed from energy deposits measured in the electromagnetic calorimeter and matched to ID tracks. They must have $p_T > 10$ GeV and $|\eta| < 2.47$, excluding the region $1.37 < |\eta| < 1.52$ corresponding to the EM calorimeter crack. Additionally, they must pass Medium identification and Tight isolation criteria. Muons are reconstructed from high-quality tracks in the Muon Spectrometer and are required to have $|\eta| < 2.7$ and $p_T > 10$ GeV, with a matching of these tracks to Inner Detector tracks. Muons, like electrons, must satisfy Medium identification requirements.
Both electrons and muons are matched to the primary vertex by constraints on the tracks' longitudinal and transverse impact parameters, $|z_0|$ and $|d_0|$, respectively. These requirements are $|z_0| \sin\theta < 0.5$ mm (where θ is the polar angle of the track) for both electrons and muons, and $|d_0|/\sigma_{d_0} < 5$ (3) for electrons (muons).
Events are required to contain exactly zero electrons and muons to reduce background from single Higgs events produced via the $t\bar{t}H$ mechanism, where the top quark decay chain creates leptons in the final state.

The missing transverse momentum E_T^{miss} is computed as the magnitude of the negative vector sum of the transverse momenta of all selected and calibrated physics objects that are matched to the primary vertex, as explained in Section 2.3.6.

To avoid double-counting the same detector signals within a single event, an overlap removal procedure is applied. In this analysis, priority is given to photons, which requires removing electrons, muons, and jets within $\Delta R = 0.4$ of any selected photon. Subsequently, jets within $\Delta R = 0.2$ of electrons are removed. Finally, electrons and muons within $\Delta R = 0.4$ of any jet are also eliminated.

The efficiency of the event preselection for SM ggF (VBF) HH events is 13% (9%) for both Runs, corresponding to expected yields of 1.537 (0.054) and 0.719 (0.0248) for Run-II and Run-III, respectively, as shown in Table (4.4), which presents the yields for all samples. The lower efficiency for VBF HH production compared to ggF HH is due to the larger pseudorapidity of the two Higgs bosons in VBF production. Consequently, true b-jets in VBF HH events are more likely to fail the $|\eta| < 2.5$ requirement, and photons from $H \to \gamma\gamma$ decays tend to have lower transverse momentum.
As the $b\bar{b}\gamma\gamma$ group is aiming for a Run-II + partial Run-III publication by mid-2025, the analysis is currently still blinded. Consequently, only data in the sideband regions are considered, excluding the signal region $120 < m_{\gamma\gamma} < 130$ GeV.
Lastly, Figures (4.3) show the level of agreement between data and MC prediction in $m_{\gamma\gamma}$ distributions for Run-II and Run-III.
The $m_{\gamma\gamma}$ distribution in Run-II data exhibits a surplus near ∼115 GeV, which is absent in the MC predictions. To quantify this excess, the local significance in the corresponding bin is calculated as $(S - B)/\sqrt{S}$, resulting in 3.11σ. Localized fluctuations in data may appear less significant when considered within the broader statistical context (commonly

referred to as the look-elsewhere effect [173]). A simplified correction is applied to account this effect, by multiplying the p-value (corresponding to the 3.11σ local significance) by the number of bins in the $m_{\gamma\gamma}$ distribution. This correction reduces the global significance of the excess to 2.035σ, which suggests that the observed surplus is not strong enough to indicate a significant incompatibility between data and MC predictions.
The background is estimated from MC samples, and the continuous $\gamma\gamma$+jets component is normalized to the data sideband.

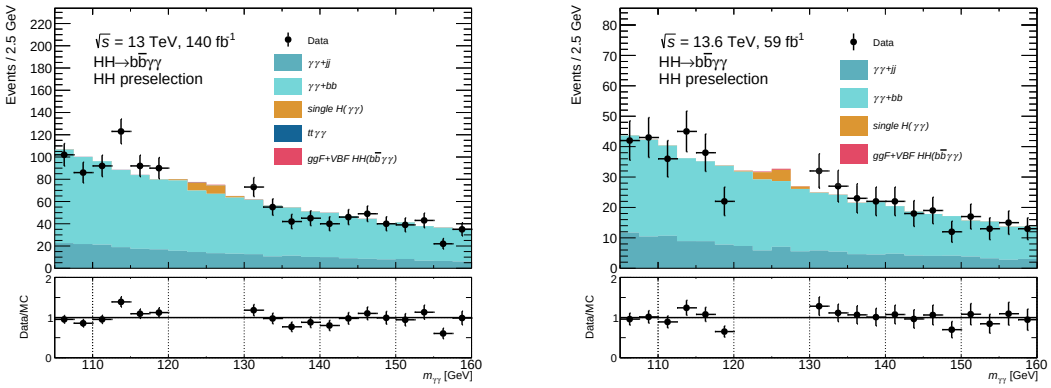

(a) (b)

Figure 4.3: Comparison of the $m_{\gamma\gamma}$ distributions between data and simulations for events after preselection for Run-II (a) and Run-III (b). Background scale factors, calculated as $\text{yield}^{data}_{sideband}/\text{yield}^{\gamma\gamma+\text{jets}}_{sideband}$, are applied to the $\gamma\gamma$+jets component. The bottom panels display the ratio of data to simulation in each bin.

Yields after preselection		
Process	**Run-II**	**Run-III**
ggF HH SM	1.537	0.719
ggF HH ($\kappa_\lambda = 0$)	3.189	1.466
ggF HH ($\kappa_\lambda = 5$)	3.399	1.553
ggF HH ($\kappa_\lambda = 10$)	24.613	11.201
VBF HH SM	0.054	0.0248
VBF HH (0,1,1)	0.171	0.076
VBF HH (1,1.5,1)	0.214	0.103
VBF HH (1,3,1)	4.193	2.009
VBF HH (10,1,1)	4.038	1.800
VBF HH (-5,1,0.5)	0.361	0.173
VBF HH (0,0,1)	1.953	0.937
VBF HH (1,0,1)	1.501	0.704
VBF HH (1,0.5,1)	0.485	0.225
VBF HH (1,1,0.5)	0.677	0.322
VBF HH (1,1,1.5)	3.339	1.538
VBF HH (1,2,1)	0.954	0.464
VBF HH (2,1,1)	0.052	0.023
ggF H	4.631	2.145
VBF H	0.499	0.217
W^-H	0.038	0.019
W^+H	0.057	0.028
bbH	0.595	0.265
$gg \to ZH$	0.764	0.357
$qq \to ZH$	2.408	1.039
tHjb	0.878	–
tWH	0.079	–
ttH	7.915	3.857
$tt\gamma\gamma$ *(nonallhad)*	1.657	–
$\gamma\gamma$*-jets*	735.031	328.377
data sideband	1114	459

Table 4.4: Yields of ggF and VBF, with various combinations of $(\kappa_\lambda, \kappa_{2V}, \kappa_V)$ listed in Table (4.2), $HH \to b\bar{b}\gamma\gamma$ and background events passing the pre-selections defined in Sect. 4.2. Here, WH is divided into W^+H and W^-H. At the time of this work, the $tHjb$, tWH, $tt\gamma\gamma$ Run-III samples are not available as they are still undergoing validation.

Chapter 5

$HH \to b\bar{b}\gamma\gamma$: Kinematic Fit Tool

The ongoing Run-III of the LHC presents a critical opportunity for the search for Higgs boson pair production. The full dataset expected from Run-III offers the potential for a first indication of HH production. In this thesis partial Run-III data collected in 2022-2023 are used, which hold significant promise. For context, the sensitivity to HH production improved by a factor of 3.5 between the full Run-II analysis and partial Run-III data. The data gathered during Run-III is expected to yield even greater sensitivity enhancement.
Several improvements are expected in the reconstruction, identification, and calibration of physics objects relevant for HH searches. Among these, the kinematic variables of b-jets play a crucial role in distinguishing HH signals from backgrounds, particularly in the $b\bar{b}\gamma\gamma$ channel studied in this work, where the background from single $H \to \gamma\gamma$ has the same shape as the HH signal in the $m_{\gamma\gamma}$ spectrum (the final discriminant variable), requiring to explore with attention the $H \to b\bar{b}$ features. Among the input variables of the BDT used for separating signal and background, $m_{b\bar{b}}$ shows the highest discriminating power.
In the $HH \to b\bar{b}\gamma\gamma$ channel, the 4-momenta of the $H \to \gamma\gamma$ component are reconstructed with excellent precision, within a few percent, but in contrast, the $H \to b\bar{b}$ part suffers from a 15% invariant mass resolution. This is due to the imperfect nature of particle detectors, such as finite segmentation, material impurities, and technological readout limitations. Each recorded event contains variations in reconstruction effects, meaning the relative contribution of these effects may vary on an event-by-event basis. Additionally, contributions from initial and final state radiation effects further complicate the reconstruction of the $H \to b\bar{b}$ system.
To improve the $m_{b\bar{b}}$ resolution, and consequently enhance the sensitivity to HH production and the coupling modifier κ_λ, beyond what is achieved with the current analysis that uses b-jets corrected via the BCalibration (Sect. 2.3.3.3), an event-level Kinematic Fit (KF) is developed and implemented in this work as an additional correction for the b-jets.
The primary objective of the Kinematic Fit Tool is to improve the resolution of reconstructed physical observables by imposing appropriate kinematic constraints. In the context of the $b\bar{b}\gamma\gamma$ channel, this approach is particularly valuable. Assuming a good balance in the transverse plane between $H \to b\bar{b}$ and $H \to \gamma\gamma$, as shown in Fig. (5.1), it allows for calibrating the HH system in this plane by exploiting the excellent reconstruction of the $H \to \gamma\gamma$ decay to achieve an additional improvement in the $H \to b\bar{b}$ resolution through the maximization of an event-level likelihood function.
In this chapter, after introducing the basic concepts and fundamental components that express both the resolution of physics objects and the constraint conditions in the Kinematic Fit Likelihood, its evaluation and optimization are discussed. Various configurations of its

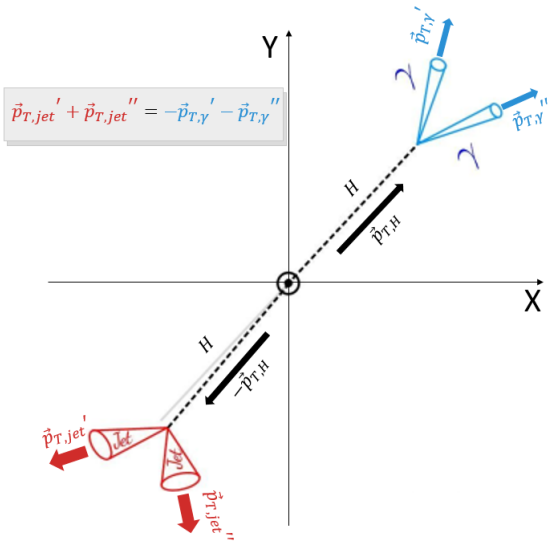

Figure 5.1: p_T balance diagram.

application, including different versions of the likelihood expression, the impact of different constraint parameterizations, and potential biases introduced by other simultaneous corrections, are all tested. This is done while keeping in mind the integration of the algorithm into the analysis framework and its computational time and resource consumption. Since the Kinematic Fit Tool is first implemented, extensively explored, and optimized in the previous Run-II analysis, nearly all the tests are conducted within the Run-II *HGamCore* analysis framework [175]. Although this framework has a processing structure quite similar to Run-III Easyjet [171], it presents differences compared to the current framework, which incorporates the latest calibrations and analysis properties. A relevant example for the proposed study is the use of a different b-tagging algorithm for jets, transitioning from the Dl1r model to the more recent GN2. The results obtained in the transition between the two frameworks are nonetheless comparable, as discussed in Sect. 5.5.

5.1 Kinematic Fit Likelihood Construction

The likelihood estimation at the event level is based on the *maximum likelihood estimation* method [176]. This approach maximizes the probability density of observing a measurement y^{obs} (e.g., the reconstructed b-jet momentum from a Higgs boson candidate) given a corresponding prediction y^{pred} from a likelihood model, subject to constraints associated with y^i for a given event. The reconstructed event variables serve as inputs, and the method returns the likelihood that these specific values represent the actual event. By maximizing this likelihood through adjustments to these variables, a more precise set of reconstructed events is expected.

The specific likelihood model, derived from Monte Carlo simulations, is based on the expected $HH \to b\bar{b}\gamma\gamma$ kinematics. Inputs include the basic properties of the four-vectors of the detected signatures, jets and photons, and their combinations. Specifically, the model ensures that the reconstructed $b\bar{b}\gamma\gamma$ system is balanced in the transverse plane. It is optimized for events with two b-jet candidates and two photons, as well as for events with up to three additional central jets (maximum number required by the analysis to reject the $t\bar{t}H$ background), whether b-tagged or not, which must be accounted for in the transverse momentum balance. This is particularly relevant for events with contributions

from final state and initial state radiations.
The model includes a set of characteristic probability density functions (PDFs), $f(y_i^{obs}|y_i^{pred})$ representing both the kinematic constraint conditions and the resolution of the observables. The latter distributions are referred to as transfer functions (TFs) and will be discussed in more detail in next Section 5.1.1. These PDFs are then combined into a single likelihood function:

$$\mathcal{L}(y_1^{obs}, ..., y_N^{obs}|y_1^{pred}, ..., y_N^{pred}) = \prod_i^N f(y_i^{obs}|y_i^{pred}) \ . \tag{5.1}$$

From this likelihood, the corresponding negative log-likelihood (NLL) $-2\ln\mathcal{L}$ is extracted. This quantity can be minimized by simultaneously varying the parameters of the likelihood model using numerical minimization techniques. The reason of this conversion is that maximizing the likelihood is computationally challenging for several reasons (for example, likelihood functions are products of probabilities, which can result in very small values) and the optimization algorithms typically perform better when working with sums rather than products, as sums are more easily manipulated. To address these issues, the logarithm of the likelihood function is taken, transforming the product of probabilities into a sum. This makes it computationally more efficient to maximize the log-likelihood (LL) with respect to the likelihood itself. Additionally, most optimization algorithms are designed to minimize functions instead of maximize them and consequently, the maximization problems are typically converted into minimization ones. This is done by negating the log-likelihood.
Finally, from all these considerations, the following general form for the negative log-likelihood function can be defined:

$$-2\ln(\mathcal{L}) = \sum_{v=E,\eta,\phi} \sum_{j=jets,\gamma} \left[-2\ln\left[\mathrm{TF}_v^j(v_{Fit}^j, v_{Reco}^j)\right]\right] - 2\ln(f_{Constr}) \tag{5.2}$$

where v represents the variables whose resolution is targeted for improvement, while the indices j refer to the relevant objects in the analysis, such as jets and photons. The term TF_v^j denotes the transfer function corresponding to a specific observable of v for a given object j, while f_{Constr} represents the constraint applied in the likelihood function.
The effectiveness of the individual terms in the likelihood function is evaluated to select the optimal components. These terms are then combined into a final likelihood function, which will be presented in Section 5.2.

5.1.1 Transfer Functions

The likelihood function requires terms that encapsulate the resolution of reconstructed variables, i.e., the uncertainty associated with a reconstructed observable measured with suboptimal detector accuracy. Ignoring this information would lead to arbitrary reordering of event objects to satisfy constraints, without regard to their original values. This information is embedded in PDFs, referred to here as transfer functions aimed to restore reconstructed observables as closely as possible to their true values, accounting for potential detector-induced degradation and smearing.
These distributions are extracted from simulations, specifically from Monte Carlo Standard Model gluon-gluon fusion signal sample, mc16a, corresponding to data from the 2015 and 2016 periods, comprising approximately 400,000 events.
In this study, TFs are evaluated only for jet observables, precisely the transverse momentum p_T, energy E, and both the azimuthal angle ϕ and pseudo-rapidity η. The TFs are

calculated at jet-level, as the kinematic quantities of the reconstructed jets are directly compared to those of the true jets. It is important to note that energy and transverse momentum are considered independent variables because they are calibrated independently and cannot be derived from each other without additional information, such as the jet mass and flight angle.

Given the excellent resolution of photon energies and angles, these quantities are assumed to follow a Gaussian distribution with a 1% resolution, in line with earlier and preliminary versions of this work [177]. All the studied transfer functions exhibit strong similarities, with many general properties applicable across different distributions. In fact, they are all well approximated by the same custom distribution function, created specifically for this analysis using a step-function approach. This method is adopted due to the difficulty in finding a continuous and analytical function capable of accurately representing the asymmetric bell-shaped distributions seen in simulated data and influenced by various complex effects, such as detector performance and reconstruction algorithms. The step-function approach involves multiplying transient or step functions (which range from 0 to 1) with opposite orientations. This process yields analytical and normalizable functions, making them suitable candidates for PDFs, as they are positive definite and have a finite integral. Additionally, multiplying these functions by other bell-shaped curves, such as a Gaussian, can produce asymmetric variations. A comprehensive study is reported in [178].

The specific function developed for this analysis is referred to as $TaOGaTa$[1], and its mathematical expression is given by:

$$\begin{aligned} TaOGaTa(x) = N \times & \big(\frac{1}{\pi}\big(\tan^{-1}(a(x-m)) + \frac{\pi}{2}\big)\big)^{\alpha} \\ & \times\ e^{\frac{(x-\mu)^2}{2\sigma^2}} \times \\ & \times \big(\frac{1}{\pi}\big(\tan^{-1}(-b(x-n)) + \frac{\pi}{2}\big)\big)^{\beta} \end{aligned} \tag{5.3}$$

where a, b, α and β are positive parameters, and N is a normalization factor. The distributions are produced by comparing the quantities of interest of the reconstructed jets, with the BCalibration applied if they are DL1r b-tagged, to those of the true jets associated within a distance $\Delta R(j_{Reco}, j_{True}) < 0.1$. A notable difference among the various distributions is that, while for angles the transfer function is computed as the absolute difference between the true and reconstructed values ($TF_{angles} = \theta_{True} - \theta_{Reco}$), in the case of energy and transverse momentum, the difference is relative to the true value ($TF_{Energy} = \frac{E_{True} - E_{Reco}}{E_{True}}$). This approach provides more stable transfer functions with respect to changes in energy scales. Nevertheless, there is still a strong energy dependence, so the energy and p_T transfer functions are divided into six regions based on their energy. Additionally, they are subdivided into four categories depending on the value of pseudo-rapidity (η), as different detector regions exhibit varying resolutions (see Section 2.2).

In total, 50 transfer functions were analyzed (24 each for energy and p_T and one for each angle). These distributions and their parameterizations will be discussed in the following sections.

[1] The name is derived from syllables reminiscent of the components of the final result, where "Ta" represents rising and descending arctangent step-functions, and "Ga" represents the Gaussian core, separated by a capital "O".

5.1.1.1 Energy Transfer Functions

Energy resolution varies depending on the detector region in which particles are detected. The data is divided into the following four regions:

- **Barrel:** $-1.37 < \eta < 1.37$
  the central lateral component of the detector.
- **Crack:** $1.37 \leq |\eta| < 1.52$
  the region between Barrel and End-cap, characterized by poor resolution.
- **End-cap:** $1.52 \leq |\eta| < 2.5$
  the forward region of the detector.
- **No-track:** $2.5 \leq |\eta| < 4.4$
  the region closest to the beam pipe. Particles detected here do not pass through the ID so their tracks cannot be reconstructed.

The energy transfer functions are analyzed as a function of $\ln(p_T)$, to address the wide energy range. The results are depicted in the 2D plots shown in Figure (5.2).

The transfer function distribution changes significantly, particularly at low energies,

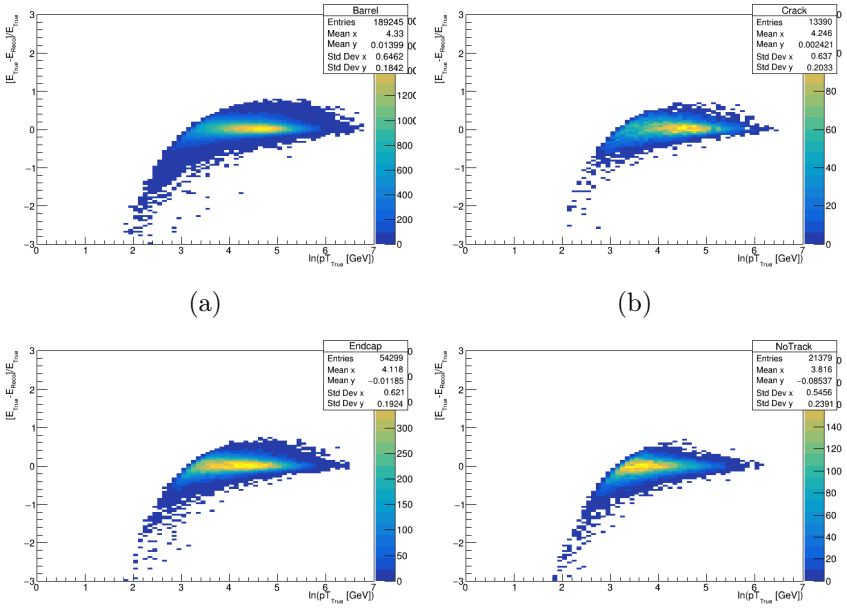

(a) (b)

(c) (d)

Figure 5.2: Energy TFs as function of $\ln(p_T)$ in the Barrel (a), Crack (b), End-cap (c) and No-Track (d) regions. The colour scheme represents the concentration of events in the specific points of the graph.

where the reconstruction algorithms tend to overestimate energy due to the noise suppression cuts applied during reconstruction. The energy measurement is an average of several contributions, and less energetic measurements are excluded when they fall below the noise threshold, leading to a higher mean energy.

Better results of the Kinematic Fit application are expected by treating different energy ranges as separate cases. Despite the evident differences among various detector regions, the shapes of the plots presented in Figure (5.2) are approximately consistent. This consistency allows to divide the data into energy regions based on $\ln(p_T)$ intervals, ensuring

comparable statistics across adjacent bins, across all spatial parts. The chosen intervals are:

$$\ln(p_T[GeV]) \in [2.0, 3.7], [3.7, 4.0], [4.0, 4.5], [4.5, 5.0], [5.0, 5.3], [5.3, 6.0]$$

Some examples of the resulting energy transfer functions, fitted with the *TaOGaTa* distribution (Eq. (5.3)), are shown in Figure (5.3).

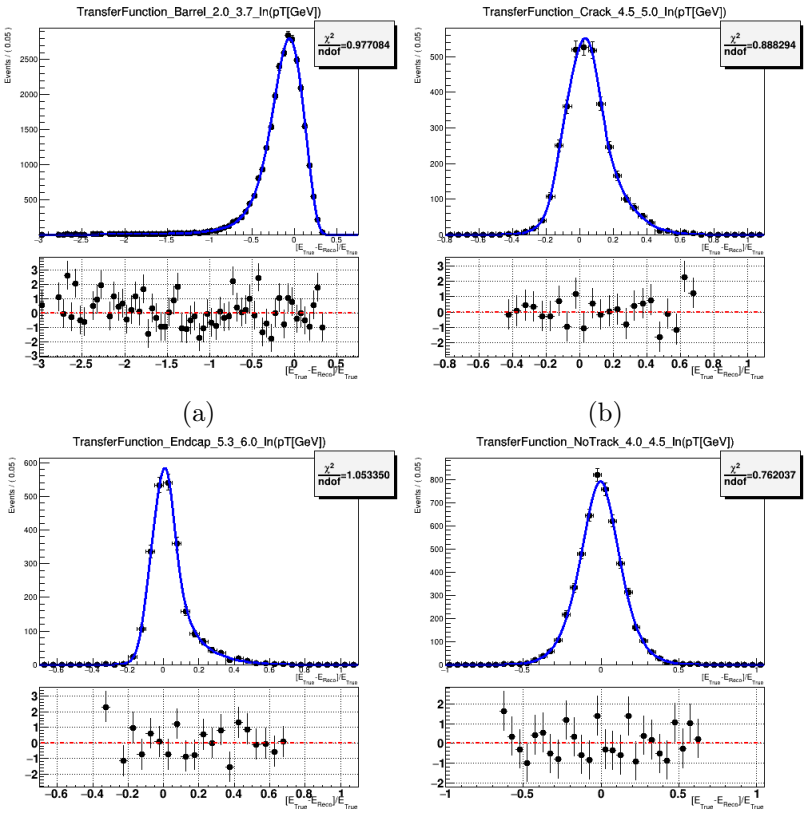

Figure 5.3: Energy transfer functions fitted with a TaOGaTa distribution (Equation (5.3)) for some η-ln(p_T) regions. The pulls on these plots are computed as $\frac{x-\lambda}{\sqrt{\lambda}}$ where x is the data value and λ is the fit value while their errors are fixed to 1.

5.1.1.2 Momentum Transfer Functions

The behavior of the transverse momentum (p_T) transfer functions closely resembles that of the energy functions. As shown in the 2D plots in Figure (5.4), the distributions are similar to those observed for energy. Thus, the same division of events into η-ln(p_T) regions is employed for momentum. The *TaOGaTa* distribution is again used for parameterization, and examples of the fitted transfer functions are shown in Figure (5.5).

5.1.1.3 Angular Transfer Functions

Unlike the previous distributions, the angular transfer functions for jets are determined by the absolute difference between the reconstructed and true values of the corresponding quantities. The distributions are independent of the energy scale and are therefore characterized by a single function.
Since the distribution is expected to be symmetric, a double Gaussian fit (the sum of two Gaussians, one for the core and another for the tails) is initially attempted. However, the

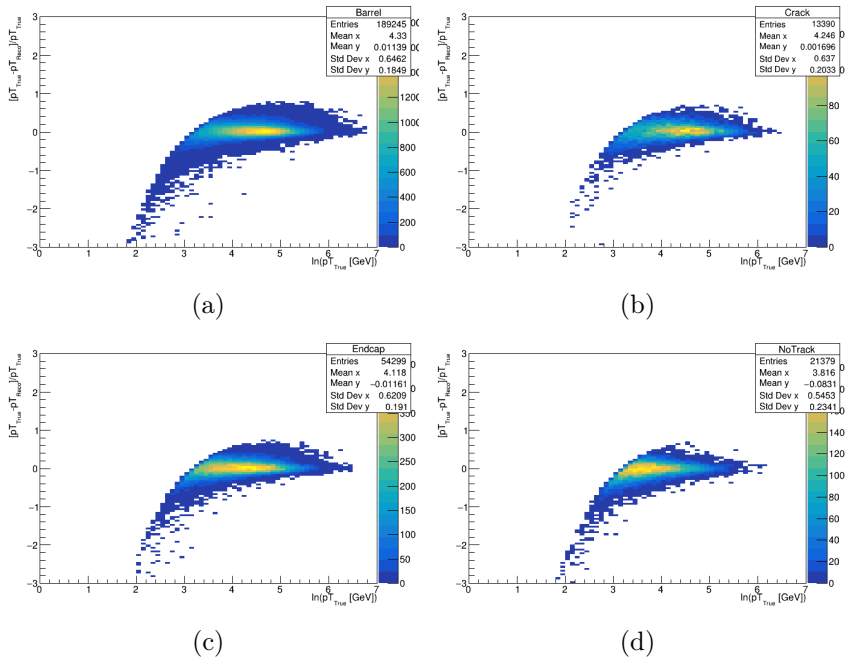

Figure 5.4: 2D graphs of the p_T function plotted against the value of $\ln(p_T)$ in the Barrel (a), Crack (b), End-cap (c) and No-Track (d) regions. The colour scheme represents the concentration of events in the specific points of the graph.

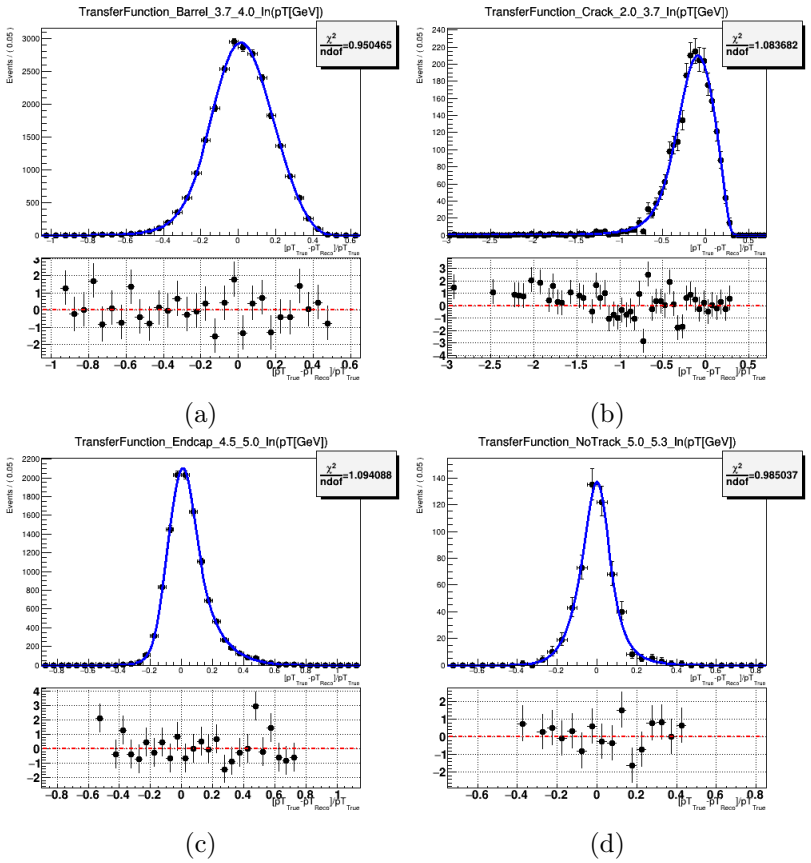

Figure 5.5: Transverse momentum transfer functions fitted with a TaOGaTa distribution (Eq. (5.3)) for some η-$\ln(p_T)$ regions. The pulls on these plots are computed as $\frac{x-\lambda}{\sqrt{\lambda}}$ where x is the data value and λ is the fit value while their errors are fixed to 1.

fit does not optimally represent the data, particularly in the tails, which do not overlap as well with the data as the *TaOGaTa* distribution (Eq.(5.3)). The resulting fits, shown in Figure (5.6), indicate the strong adaptability of the proposed function.

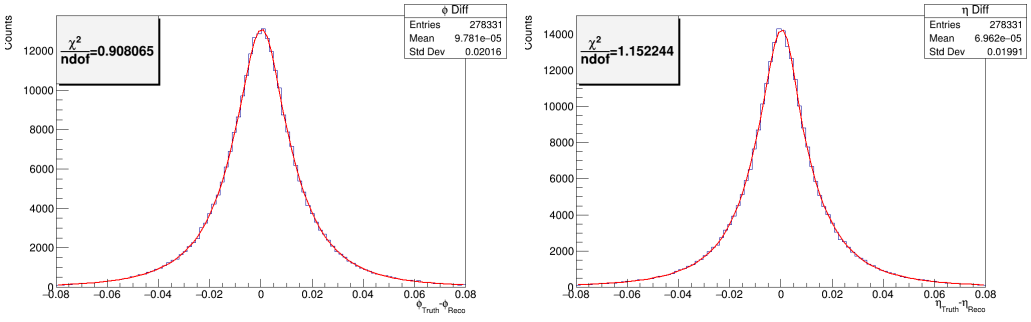

(a) (b)

Figure 5.6: Histograms representing the fitted simulated angular distributions, ϕ (Left) and η (Right). In graph (a) the x axis is expressed in radians. The function used to fit the data is the TaOGaTa (see equation (5.3).

5.1.2 Constraints

In complex processes like $HH \to b\bar{b}\gamma\gamma$, multiple constraints are usually applicable. Aside from the different conditions that may be selected as a focus, the manner in which the same constraint is expressed can convey varying information to the analysis, potentially affecting its performance. In the context of a collider experiment, one of the simplest and most significant constraints is the total transverse momentum ($\vec{p_T}$). It is expected that the total transverse momentum, i.e. the sum of all generated particles' momentum perpendicular to the beam direction, should be negligible for each event, as outlined in Sect. 2.2.1. Since linear momentum is a vector, conservation implies that each component along any axis should also be conserved.
By enforcing this condition, it is possible to leverage the highly precise measurement of the photons' transverse momentum to enhance the resolution of the jets' momentum. Using the same simulated Standard Model ggF signal sample employed for the transfer functions, the probability that the total $\vec{p_T}$ differs from zero, both for its two independent transverse components (p_X and p_Y) and its scalar magnitude (p_T), is evaluated by fitting the relevant distributions.

5.1.2.1 Transverse Momentum Components

To thoroughly analyze the total transverse momentum along the x-axis (p_X) and y-axis (p_Y) for each event, the simulated data are categorized based on the number of jets present in the event, as this significantly affects the resolution. The analysis is optimized for up to three additional central jets, the maximum considered by this analysis to reject the $t\bar{t}H$ background. As a result, eight distributions are fitted: one pair for p_X and p_Y in each jet configuration. These p_X and p_Y distributions are calculated using the momentum of jets and photons at the truth level. As an example, the data for events with no additional central jets (only the two required b-jets are present) are shown in Figure (5.7) for both p_X and p_Y. In cases where there are additional jets, the distributions exhibit a broader spread as the number of jets increases.

As with the angular distributions, rather than using the general Gaussian distribution,

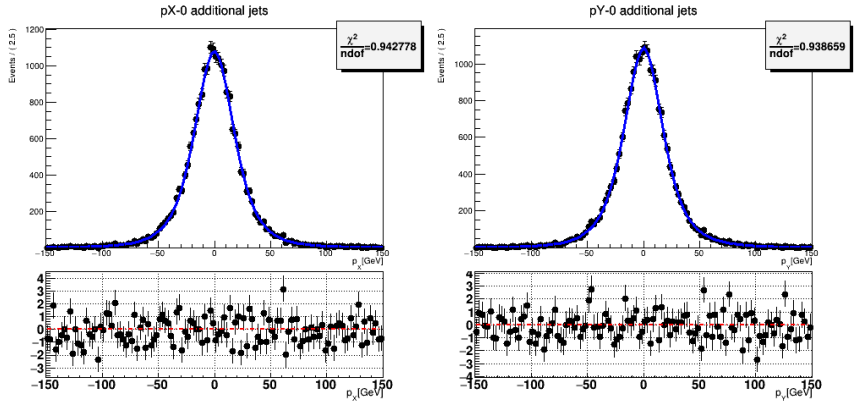

(a) (b)

Figure 5.7: The p_X (left) and p_Y (right) distributions of the $b\bar{b}\gamma\gamma$ system for simulated events with no additional jets. The function used to fit the data is the TaOTa (Eq. (5.4)). The pulls on these plots are calculated as $\frac{x-\lambda}{\sqrt{\lambda}}$ where x is the data value and λ is the fit value while their errors are fixed to 1.

which does not optimally fit the data, the constraints have been modeled using a custom function, represented in Fig. (5.7), namely:

$$\begin{aligned} TaOTa(x) = N \times \big(\frac{1}{\pi}\big(\tan^{-1}(a(x-m)) + \frac{\pi}{2}\big)\big)^{\alpha} \times \\ \times \big(\frac{1}{\pi}\big(\tan^{-1}(-b(x-n)) + \frac{\pi}{2}\big)\big)^{\beta} \end{aligned} \tag{5.4}$$

where a, b, α, and β are positive parameters, and N the normalization factor.

5.1.2.2 Scalar Transverse Momentum

An alternative approach to imposing momentum conservation on the transverse axis is to combine p_X and p_Y into a single quantity representing the total scalar transverse momentum: $p_T = \sqrt{p_X^2 + p_Y^2}$. The resulting distribution is depicted in Figure (5.8).

It is important to note that this scalar quantity does not carry all the information provided by the two independent components. This is because p_T is a scalar, which means directional information is lost. However, given the symmetry of the experiment around the beam axis, it may be assumed that this loss of information would not significantly impact the final results. On the other hand, even the independent components p_X and p_Y do not capture all the possible information about the $\vec{p_T}$ resolution, as they are treated as uncorrelated variables in the likelihood function. This could lead to cases where the reconstructed total $\vec{p_T}$ is unrealistically large more frequently than expected.

The data is again fitted with a custom function:

$$ExOTa(x) = e^{-e^{-a(x-m)}} \times \big(\frac{1}{\pi}\big(\tan^{-1}(-b(x-n)) + \frac{\pi}{2}\big)\big)^{\beta} \tag{5.5}$$

where a, b, and β are positive parameters, and N is the normalization factor.

After these considerations, the optimal approach seems to involve using all of these conditions simultaneously. Although considering correlated conditions is typically avoided, as it reduces the unique information added by each term, it is reasonable to assume that each condition provides some independent information that can improve the analysis.

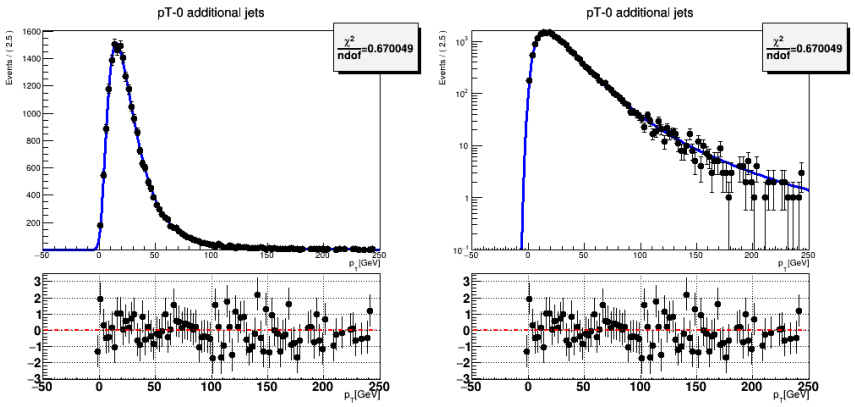

(a) (b)

Figure 5.8: The p_T distribution for events with no additional jets both in linear (left) and logarithmic (right) scale. The function used to fit the data is the ExOTa (equation (5.5)). The logarithmic scale demonstrates how the custom function appropriately handles the asymmetric distribution tails. The pulls on these plots are calculated as $\frac{x-\lambda}{\sqrt{\lambda}}$ where x is the data value and λ is the fit value while their errors are fixed to 1.

With this framework, different constraints will be employed in the next section to evaluate their performance and determine the optimal configuration for this channel.

5.2 Tests, Optimizations and Results

The effectiveness of the Kinematic Fit (KF) technique is determined by its impact on the invariant mass resolution of jets in signal simulations. This evaluation is typically performed by processing a portion of 30,000 events of the same SM ggF sample used in the previous section to derive the transfer functions and constraints employed in the KF algorithm. The processed data are then utilized to calculate the jets' invariant masses, which are plotted as a histogram fitted using a Bukin function. The σ parameter of the Bukin distribution (whose expression is provided in Appendix A) is generally used to quantify improvements in resolution.
As previously indicated, this process has been repeated numerous times to test various KF configurations and identify the most optimal one. The primary distribution discussed in this section corresponds to the most inclusive case, which considers all the events with 0, 1, 2, and 3 additional central jets. This allows for a comprehensive discussion of the different configurations. However, during the study, attention is also given to the behavior of all non-inclusive distributions (and other inclusive cases, such as 0+1 and 0+1+2 additional jets) to optimize the analysis, but these distributions are presented here only when they are relevant to the discussion.
The shown distributions include events that pass the preselection criteria described in Sect. 4.2 and that are appropriately weighted according to the analysis (Eq. (4.1)).

5.2.1 Jet Energy and Momentum Resolutions

The first test performed involves the application of the KF as described in its initial implementation [177], but with the new distribution functions for jet energy and transverse momentum, that replace the original Gaussian distributions used for energy and

p_T-dependent response likelihood[2].
At this stage, the jet angular distributions are fixed to their reconstructed values to investigate the impact of these terms separately. For photons, the angles follow a normal distribution with a resolution of 1% (as in previous studies [177]).
Regarding the constraints, they are initially applied to p_X and p_Y as Gaussian distributions with a standard deviation ($\sigma_{bb\gamma\gamma}$) of 14 GeV for 0 additional jets and 16 GeV for cases with ≥ 1 additional jet. These standard deviations were empirically determined to result in optimal performance when using a Gaussian distribution to describe the constraint conditions [177]. However, as mentioned in Sect. 5.1.2, these constraints do not follow a normal distribution. The corresponding likelihood function is:

$$\begin{aligned} -2\ln(\mathcal{L}) = \sum_{j=jets} \Big[-2\ln\Big[\mathrm{TF}_E\Big(\frac{E^j_{Fit} - E^j_{Reco}}{E^j_{Fit}}\Big)\Big] - 2\ln\Big[\mathrm{TF}_{p_T}\Big(\frac{p^j_{T,Fit} - p^j_{T,Reco}}{p^j_{T,Fit}}\Big)\Big]\Big] + \\ + \sum_{j=\gamma} \sum_{v=E,\eta,\phi} \Big[\Big(\frac{v^j_{Fit} - v^j_{Reco}}{\sigma_v}\Big)^2\Big] + \Big(\frac{\sum_{j=jets,\gamma} p^j_X}{\sigma_{bb\gamma\gamma}}\Big)^2 + \Big(\frac{\sum_{j=jets,\gamma} p^j_Y}{\sigma_{bb\gamma\gamma}}\Big)^2 \end{aligned} \tag{5.6}$$

The results are presented in Figure (5.9).

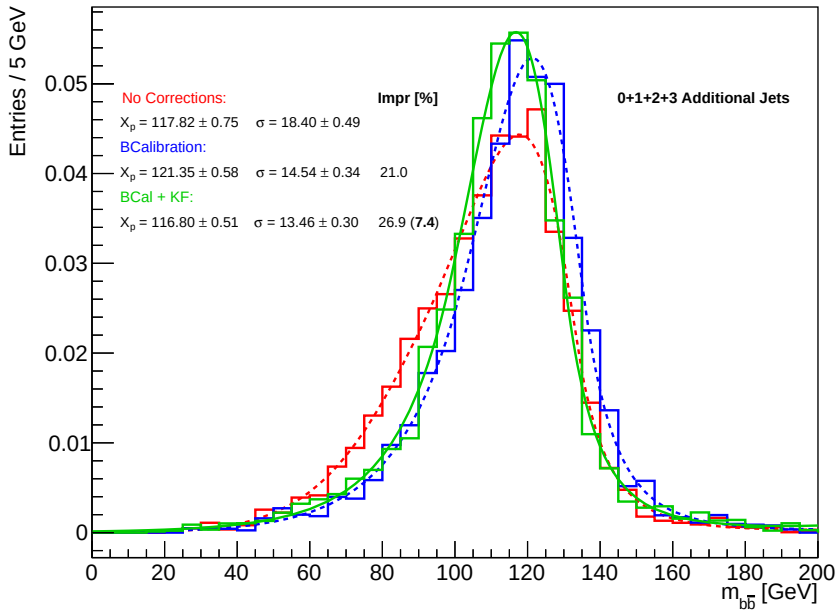

Figure 5.9: Comparison of the di-jet invariant masses for jets reconstructed using nominal correction (red), BCalibration (blue), and the Kinematic Fit (green) implemented with the new transfer functions on E and p_T. The solid (KF) and dashed (no corrections, BCal) lines represent the fitted Bukin distributions. The best-fit parameters are determined using the RooFit MLE method, with relative errors corrected for weighted datasets via the SumW2Error option, ensuring accurate error estimates that account for the sum of squared event weights.

[2]Specifically, the mean (E_μ) and standard deviation (E_σ) of the Gaussian distribution $(E_{True} - E_{Reco} \cdot E_\mu)^2/(E_{True} \cdot E_\sigma)^2$ are extracted directly by taking the mean and root mean square from histograms of energy obtained by binning $t\bar{t}$ MC samples in b-jets' p_T^{Reco}. Similarly, the jet p_T response was interpolated from $(p_T^{Reco} \cdot E_\mu)/p_T^{True}$ on transverse momentum histograms.

	No Corrections	BCal	Kinematic Fit
X_p	117.82 ± 0.75	121.35 ± 0.58	116.80 ± 0.51
σ	18.40 ± 0.49	14.54 ± 0.34	13.46 ± 0.30
χ	-0.30 ± 0.03	-0.18 ± 0.02	-0.15 ± 0.02
ρ_1	-0.41 ± 0.09	-0.02 ± 0.03	0.04 ± 0.02
ρ_2	0.21 ± 0.03	0.16 ± 0.02	0.18 ± 0.01

Table 5.1: Table with Bukin fit parameters for each of the corrections shown in Fig. (5.9): X_p is the peak position, σ the peak width, χ the peak asymmetry, ρ_1 and ρ_2 the left and right tails respectively.

The Kinematic Fit shows a higher peak and narrower width compared to cases with either nominal correction or BCal correction. The differences in resolution between these distributions are quantified by the relative percentage change in the σ parameter of the fitted Bukin functions. In this test, the KF yields a σ_{KF} of approximately 13.46 GeV, showing an improvement of 7.4% relative to the σ_{BCal} and 26.9% relative to the σ_{NoCorr} case where no corrections are applied.

A previous attempt using a similar likelihood, but with a Bukin distribution for the transfer functions, produced similar results. However, the new parameterization is preferred for several reasons. Firstly, the Bukin function has certain undesirable properties, such as its complexity and the lack of continuity in its derivatives. Secondly, a distribution better suited to describe the transfer functions (such as the TaOGaTa distribution) is expected to scale more effectively with increasing data sample sizes.

5.2.2 Angular Resolutions

The next aspect examined is the performance of the Kinematic Fit when angular resolutions of the jets are introduced, resulting in the jet angles no longer being fixed to their reconstructed values. The following results pertain to the inclusion of photon and jet angles in the likelihood function. For photons, the angle transfer functions continue to follow a normal distribution with a resolution of 1%. The jet angle transfer functions are derived from the fit of simulated data, as detailed in Sect. 5.1.1.
The corresponding likelihood function is expressed as follows:

$$
\begin{aligned}
-2\ln(\mathcal{L}) = \sum_{j=jets} \Big[&-2\ln\big[\mathrm{TF}_E\big(\frac{E^j_{Fit}-E^j_{Reco}}{E^j_{Fit}}\big)\big] - 2\ln\big[\mathrm{TF}_{p_T}\big(\frac{p^j_{T,Fit}-p^j_{T,Reco}}{p^j_{T,Fit}}\big)\big] + \\
&+ \sum_{\Omega=\eta,\phi} -2\ln\big[\mathrm{TF}^j_{Angles}(\Omega^j_{Fit}-\Omega^j_{Reco})\big]\Big] + \sum_{j=\gamma}\sum_{v=E,\eta,\phi}\Big[\big(\frac{v^j_{Fit}-v^j_{Reco}}{\sigma_v}\big)^2\Big] + \\
&+ \Big(\frac{\sum_{j=jet,\gamma} p^j_X}{\sigma_{bb\gamma\gamma}}\Big)^2 + \Big(\frac{\sum_{j=jet,\gamma} p^j_Y}{\sigma_{bb\gamma\gamma}}\Big)^2
\end{aligned}
\tag{5.7}
$$

Despite this version of the KF outperforming both the nominal and BCal correction cases, its resolution (σ_{KF} = 13.55 GeV) is slightly worse than the previous attempt with fixed angles (σ_{KF} = 13.46 GeV). The difference is small enough to suggest that the observed

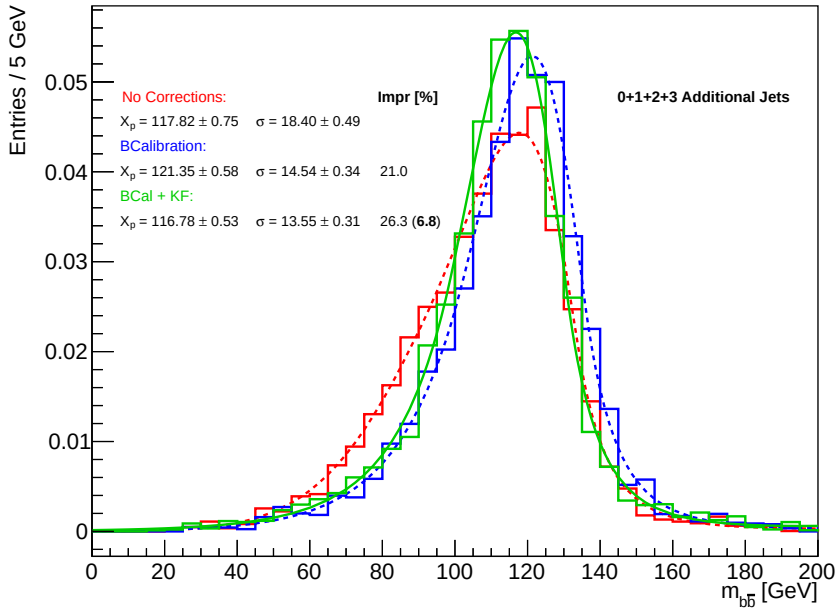

Figure 5.10: Comparison of the di-jet invariant masses for jets reconstructed using nominal correction (red), BCalibration (blue), and the Kinematic Fit (green), in which the jets angles resolution are implemented. The solid (KF) and dashed (no corrections, BCal) lines represent the fitted Bukin distributions. Best-fit parameters: Roofit MLE method.

variations are likely due to statistical fluctuations rather than a real performance change. Therefore, the introduction of angular resolutions does not provide any significant improvement over the previous method. This is expected, as the angular transfer functions are represented by very narrow distributions (Fig. (5.6)).
Consequently, after confirming that the angular normal distributions of the photons also do not have a significant impact on performance, all angular values are fixed for subsequent tests, and no further investigations are conducted regarding this aspect.

5.2.3 Removal of PtReco Correction

The initial implementation of the Kinematic Fit technique for the $HH \to b\bar{b}\gamma\gamma$ analysis [177] aimed to improve the $m_{b\bar{b}}$ resolution was based on studies from single Higgs analyses, particularly the VH(bb) analysis [179], where this method is utilized. In that analysis, the precise energy resolution of the $Z \to ll$ decay is used to constrain the $H \to b\bar{b}$ decay through a log-likelihood fit balancing the VH system, thereby enhancing the resolution of the two b-jets invariant mass.
In the single Higgs tests, the KF tool is applied only to events with two leptons, two b-jets, and at most one additional jet, as no improvement is observed for events with four or more jets. Specifically, the tool is used after the muon-in-jet correction application, without the PtReco correction.
To evaluate the impact of the PtReco correction in the $HH \to b\bar{b}\gamma\gamma$ case, a test is conducted by removing it while maintaining the muon-in-jet correction, replicating the conditions from the single Higgs analysis.
Consequently, both the energy and momentum transfer functions are recalibrated on the uncorrected samples before applying the Kinematic Fit. The results of this test are assessed

for events with 0, 1, 2, and 3 additional jets. The specific case of 0 additional jets, analogous to the $2l + 2$ b-jets scenario from the single Higgs analysis, is shown in Figure (5.11), with detailed results for all additional jets cases summarized in Table (5.2).

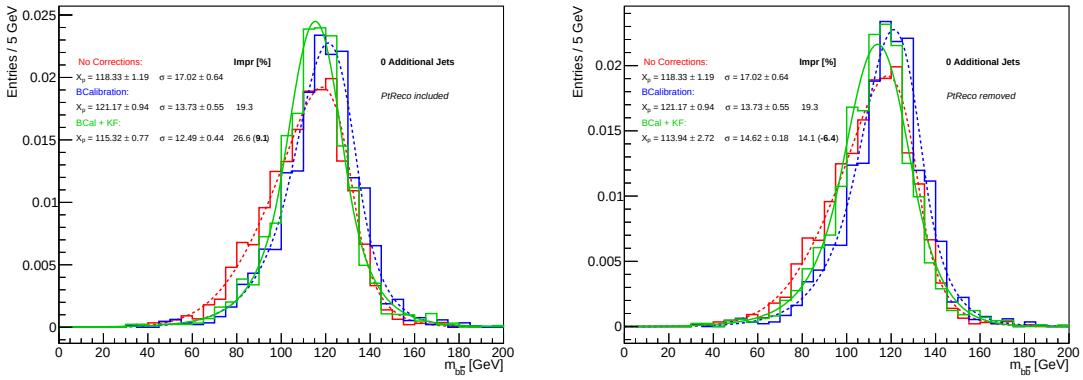

(a) (b)

Figure 5.11: Di-jet invariant mass in the 0 additional jets case: red, blue and green lines represent the samples with no correction, BCal correction and KF application, respectively. The two plots show the different behavior of the KF when PtReco correction is included (left) and removed (right). Best-fit parameters: Roofit MLE method.

		X_{peak} [GeV]	σ	σ-**Improv** [%]
0 Add jets	BCal	121.17	13.73	
	KF$_{wPtReco}$	115.32	12.49	9.03
	KF$_{NoPtReco}$	113.90	14.62	-6.50
1 Add jets	BCal	122.52	15.28	
	KF$_{wPtReco}$	116.79	14.29	6.50
	KF$_{NoPtReco}$	116.20	16.46	-7.70
2 Add jets	BCal	118.80	17.50	
	KF$_{wPtReco}$	115.60	15.90	9.14
	KF$_{NoPtReco}$	115.30	17.40	0.60
3 Add jets	BCal	120.80	14.10	
	KF$_{wPtReco}$	116.30	12.60	10.60
	KF$_{NoPtReco}$	115.90	16.80	-2.20

Table 5.2: Comparison of the peak position (X_{peak}) and resolution (σ) for all (no inclusive) additional jets cases, with and without the PtReco correction before KF application.

The results indicate that the KF performs significantly better on fully BCal corrected events. Removing the PtReco correction leads to a noticeable reduction in the resolution of the di-jet invariant mass, particularly in the 0 and 1 additional jet categories, which contribute most significantly to the final result. Therefore, in subsequent studies, the kinematic fit algorithm will always be applied after the complete BCalibration.

5.2.4 Constraint Parametrization

The next aspect to consider is the parametrization of the constraint. Previously, the constraint was modeled as a Gaussian term with a resolution dependent on the number of jets, and this approach was evaluated empirically as explained in Sect. 5.2.1. From Section 5.1.2, it is clear that the transverse momentum distributions do not follow Gaussian distributions, making it appropriate to explore a more suitable parametrization for the constraint condition.
The first constraint tested was a scalar momentum conservation term, following the ExOTa distribution shown in Figure (5.8a) and expressed by the Eq. (5.5).
The likelihood function is thus formulated as:

$$-2\ln(\mathcal{L}) = \sum_{j=jets}\Big[-2\ln\big[\mathrm{TF}_E\big(\frac{E^j_{Fit}-E^j_{Reco}}{E^j_{Fit}}\big)\big] - 2\ln\big[\mathrm{TF}_{p_T}\big(\frac{p^j_{T,Fit}-p^j_{T,Reco}}{p^j_{T,Fit}}\big)\big]\Big] + \\ + \sum_{j=\gamma}\Big[\big(\frac{E^j_{Fit}-E^j_{Reco}}{\sigma_E}\big)^2\Big] - 2\ln\big[f_{p_T}(p_T)\big] \tag{5.8}$$

where f_{p_T} is the aforementioned distribution.
The typical results for the jet invariant mass resolutions are reported in Figure (5.12).

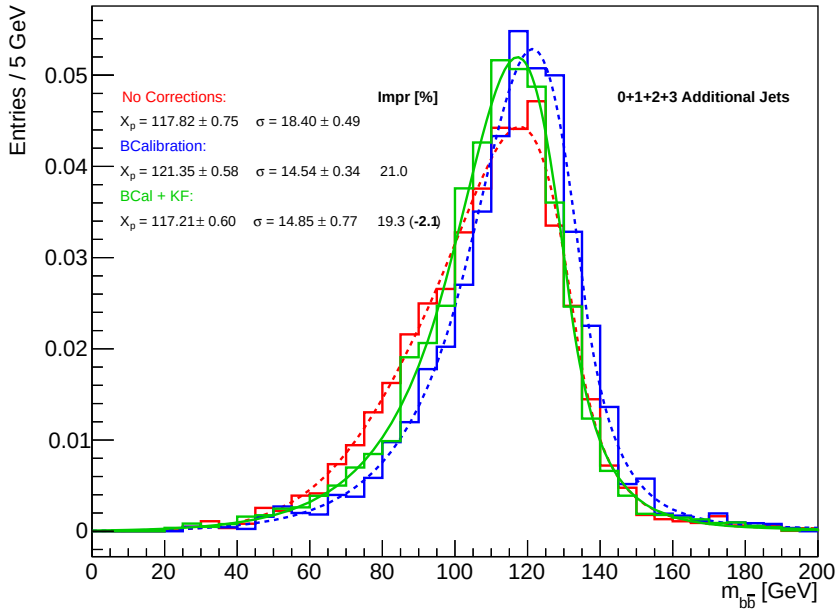

Figure 5.12: Comparison of the di-jet invariant masses for jets reconstructed using nominal correction (red), BCalibration (blue), and the Kinematic Fit (green) with only the p_T constraint. The solid (KF) and dashed (no corrections, BCal) lines represent the fitted Bukin distributions. Best-fit parameters: Roofit MLE method.

This parametrization performs worse than the previous one, with a σ_{KF} of around 14.85 GeV, compared to the earlier best value of 13.46 GeV. In fact, this attempt even underperforms relative to the BCal correction by 2%.
Next, the momentum constraint in the $x-$direction (p_X) is added in addition to the scalar

momentum constraint. The resulting likelihood is:

$$-2\ln(\mathcal{L}) = \sum_{j=jets}\Big[-2\ln\Big[\mathrm{TF}_E\Big(\frac{E^j_{Fit}-E^j_{Reco}}{E^j_{Fit}}\Big)\Big]-2\ln\Big[\mathrm{TF}_{p_T}\Big(\frac{p^j_{T,Fit}-p^j_{T,Reco}}{p^j_{T,Fit}}\Big)\Big]\Big]+ \\ +\sum_{j=\gamma}\Big[\Big(\frac{E^j_{Fit}-E^j_{Reco}}{\sigma_E}\Big)^2\Big]-2\ln\big[f_{p_T}(p_T)\big]-2\ln\big[f_{p_X}(p_X)\big] \tag{5.9}$$

where f_{p_X} is the TaOTa distribution of Eq. (5.4) and used in Figure (5.8). Results from this updated parametrization are shown in Fig. (5.13).

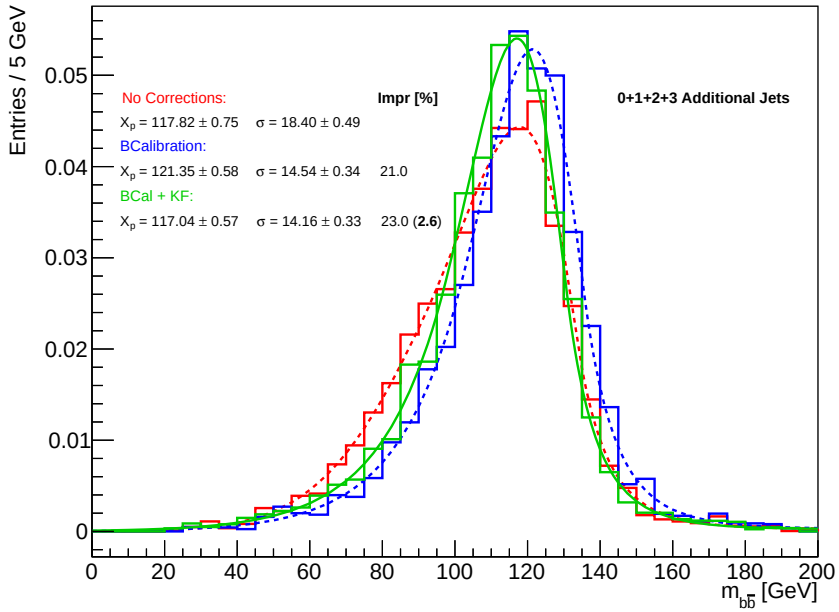

Figure 5.13: Comparison of the di-jet invariant masses for jets reconstructed using nominal correction (red), BCalibration (blue), and the Kinematic Fit (green) with the p_T and p_X constraints. The solid (KF) and dashed (no corrections, BCal) lines represent the fitted Bukin distributions. Best-fit parameters: Roofit MLE method.

This approach shows improvement over the previous iteration, with a new σ_{KF} value of 14.16 GeV, slightly better than the BCal correction ($\sigma_{BCal} = 14.54$ GeV) but still worse than the original parametrization.
The addition of the p_Y constraint resulted in further minor improvements, but the performance remains inferior to that of the originally proposed parametrization, as summarized in Table (5.3). This suggests that the standard Gaussian assumption for the constraint may encapsulate an additional optimization factor that adjusts the strength of the constraint. This strength factor, which is a scalar multiplier applied to the constraint, is not yet considered in previous tests.

5.2.5 Scan of the Constraint Strength Parameter (λ)

A new parameter, λ, is introduced into the likelihood function to control the strength of the applied constraint. To ensure comparability with previous results, only the p_X and p_Y constraints are imposed in this analysis.

		X_{peak}	σ	σ-**Improv [%]**
0+1+2+3 Add jets	BCal	121.35	14.54	
	Kinematic Fit	p_T **constraint**		
		117.21	14.85	-2.13
		$p_T - p_X$ **constraint**		
		117.04	14.16	2.61
		$p_T - p_X + p_Y$ **constraint**		
		117.21	13.85	4.75
		Gaussian constraint		
		116.80	13.46	7.43

Table 5.3: Comparison of the peak position (X_{peak}), resolution (σ_{KF}) and its relative improvement over σ_{BCal}, for all tested constraint configurations.

The likelihood function thus takes the following form:

$$-2\ln(\mathcal{L}) = \sum_{j=jets}\Big[-2\ln\big[\mathrm{TF}_E\big(\frac{E^j_{Fit}-E^j_{Reco}}{E^j_{Fit}}\big)\big] - 2\ln\big[\mathrm{TF}_{p_T}\big(\frac{p^j_{T,Fit}-p^j_{T,Reco}}{p^j_{T,Fit}}\big)\big]\Big] + \\ + \sum_{j=\gamma}\Big[\big(\frac{E^j_{Fit}-E^j_{Reco}}{\sigma_E}\big)^2\Big] - 2\boldsymbol{\lambda}\ln\big[f_{p_X}(p_X)\big] - 2\boldsymbol{\lambda}\ln\big[f_{p_Y}(p_Y)\big] \tag{5.10}$$

A scan over different values of λ was conducted to determine the value that provides the optimal di-jet mass resolution.

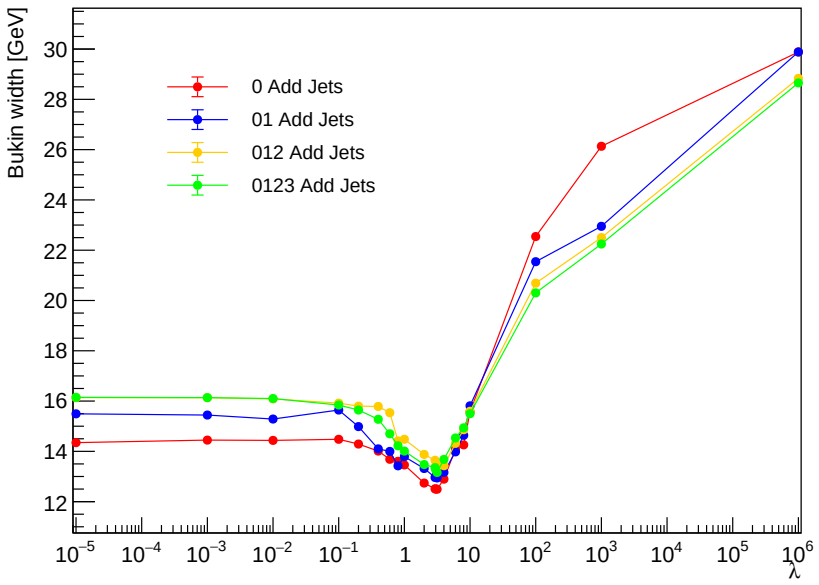

Figure 5.14: Scan of λ values plotted against the Bukin width of the di-jet invariant mass resulting from the KF application. The different lines represent the cumulative addition of events with more additional jets.

As shown in Figure (5.14), the scan successfully identifies a minimum value for λ different from the previously assumed value of $\lambda = 1$. The optimal value of λ is approximately 3.05.

The results for parameter values close to this minimum are largely comparable; however, the choice of $\lambda = 3.05$ offers a slightly improved resolution, particularly for cases with fewer additional jets, which are the primary contributors to the final result.
Detailed results of the kinematic fit using this optimized parameter are shown in Figure (5.15).

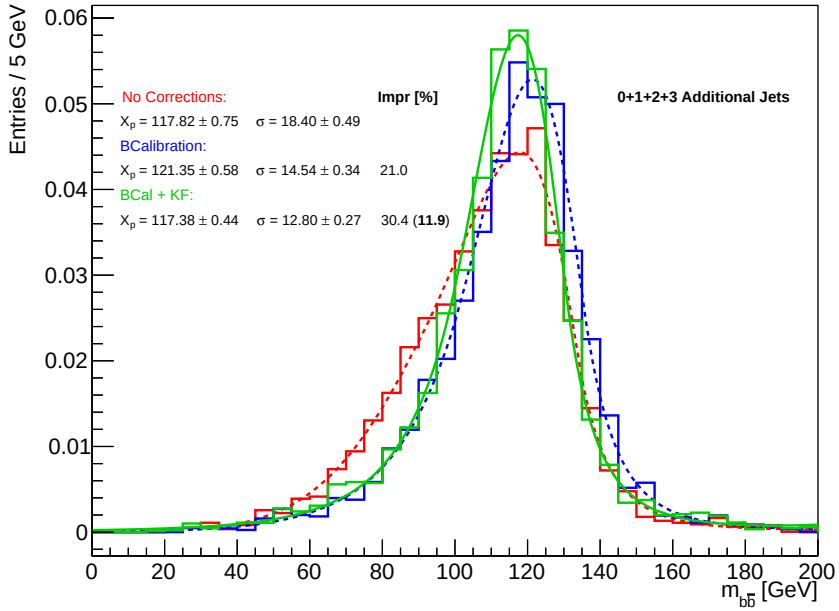

Figure 5.15: Comparison of the di-jet invariant masses for jets reconstructed using nominal correction (red), BCalibration (blue), and the Kinematic Fit (green) with both the p_X and p_Y constraints weighted by a λ factor of 3.05. The solid (KF) and dashed (no corrections, BCal) lines represent the fitted Bukin distributions. Best-fit parameters: Roofit MLE method.

This result represents the best outcome achieved using the Kinematic Fit, yielding a σ_{KF} value of 12.80 GeV. This corresponds to a 5% improvement over the previous parameterization, a 12% improvement relative to the BCalibration (σ_{BCal}), and a substantial 30% improvement relative to the nominal correction (σ_{NoCorr}).
Interestingly, the addition of the p_T constraint (with its own strength factor, λ_{p_T}) in the new likelihood does not result in any noticeable improvements. This is demonstrated by a scan of λ_{p_T}, shown in Figure (5.16). The plot clearly shows that all values of λ_{p_T} lead to a higher or equal width in the $m_{b\bar{b}}$ distribution compared to the case without applying the p_T constraint (dashed lines), indicating that, in this parametrization, the scalar p_T distribution does not contribute significant information regarding the transverse momentum of individual events. Instead, it introduces additional noise, weakening the p_X and p_Y constraints. Therefore, this term is not included.

5.2.6 Latest Considerations on Transfer Functions

To ensure that the kinematic fit is correctly implemented and that its application does not distort the $m_{b\bar{b}}$ distribution of the background, tests are performed on two background samples (30,000 events): the dominant continuum $\gamma\gamma$+jets and the most relevant single Higgs process, $t\bar{t}H$. The $m_{b\bar{b}}$ distributions for the two b-jets are shown in Figures (5.17a)

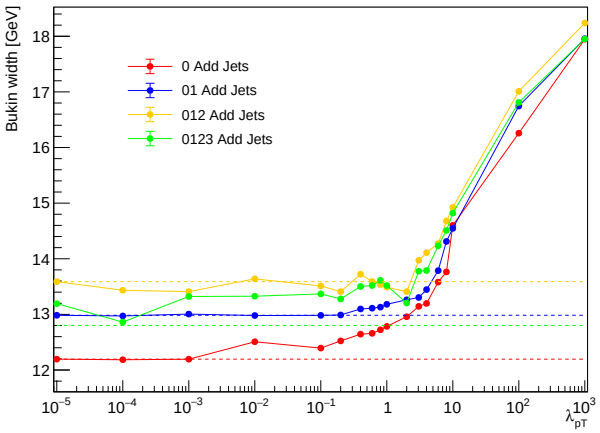

Figure 5.16: Scan of λ_{p_T} values plotted against the Bukin width of the di-jet invariant mass resulting from the KF application, including the weighted p_X-p_Y constraint. The different color lines represent the cumulative addition of events with more additional jets. The dotted lines represent the Bukin width without the p_T constraint term.

and (5.17c). The Kinematic Fit improves the resolution in processes where the transverse momentum is conserved, such as $\gamma\gamma$+jets. In contrast, for $t\bar{t}H$, where part of the momentum is carried away by neutrinos, no improvement is expected over the nominal and BCal corrections. This behavior can be seen in both samples and it is confirmed by comparing the reconstructed and true jet masses, as illustrated in Figures (5.17b) and (5.17d), indicating that the TFs operate correctly. The full-event $m_{b\bar{b}}$ distributions, discussed in the next chapter, further support these observations.

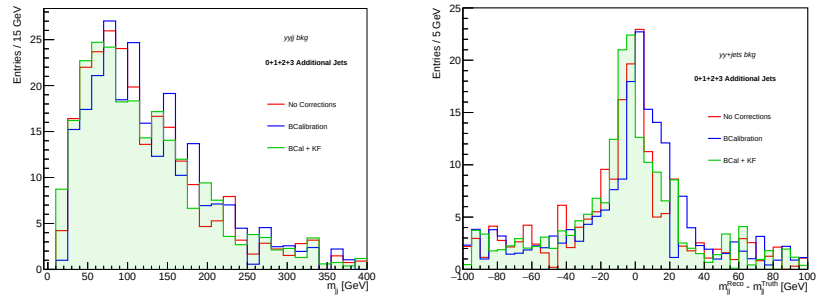

(a) (b)

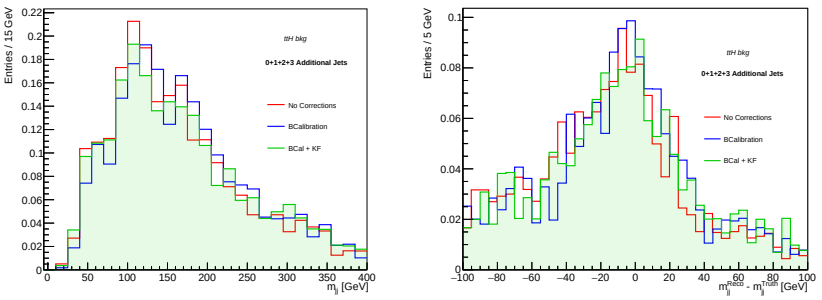

(c) (d)

Figure 5.17: Di-jet invariant mass distributions for jets reconstructed using nominal correction (red), BCalibration (blue), and the Kinematic Fit (green), for the $\gamma\gamma$+jets (a) and $t\bar{t}H$ (c) backgrounds. The plots (b) and (d) show a comparison between these distributions and their corresponding true values to better understand the KF impact.

A test is also conducted using different binning schemes for $\ln(p_T)$ to evaluate their impact on the results. A wider binning,

$$\ln\left(p_T[GeV]\right) \in [2.0, 3.0], [3.0, 4.0], [4.0, 5.0], [5.0, 6.0] \ ,$$

and a finer binning,

$$\ln\left(p_T[GeV]\right) \in [2.0, 2.3], [2.3, 2.7], [2.7, 3.0], [3.0, 3.3], [3.3, 3.7], [3.7, 4.0], ..., [5.7, 6.0] \ ,$$

are tested. In the two plots (5.18a)-(5.18b), and when compared to Fig. (5.15), it can be observed that both an excessively wider or finer p_T-binning slightly worsen the mass distribution resolution of the two jets. In particular, this may be due to a reduced robustness of the fitting function, which, as can be seen, struggles to accurately reach the peak height. This can be attributed to the shape of the peak, which, unlike the more regular standard case, is defined less consistently, characterized by a single $m_{b\bar{b}}$ bin that stands out compared to the others in both tests. In the case of overly wide binning, this configuration could be explained by a reduced precision in characterizing the distribution. The fact that a single bin represents a wide range of jet $ln(p_T)$ implies that subtler variations in the distribution's behavior are not properly captured, resulting in a less smooth $m_{b\bar{b}}$ distribution peak shape. In the plot on the right, with finer binning, it is possible that some p_T-bins contain an insufficient number of events, leading to greater statistical fluctuations and providing a more accurate description only for those jets that kinematically fall into the more populated bins. This results in a misregularization of the more frequent events that comprise the $m_{b\bar{b}}$-peak and the adjacent bins.
The "standard binning" is confirmed as the optimal compromise.

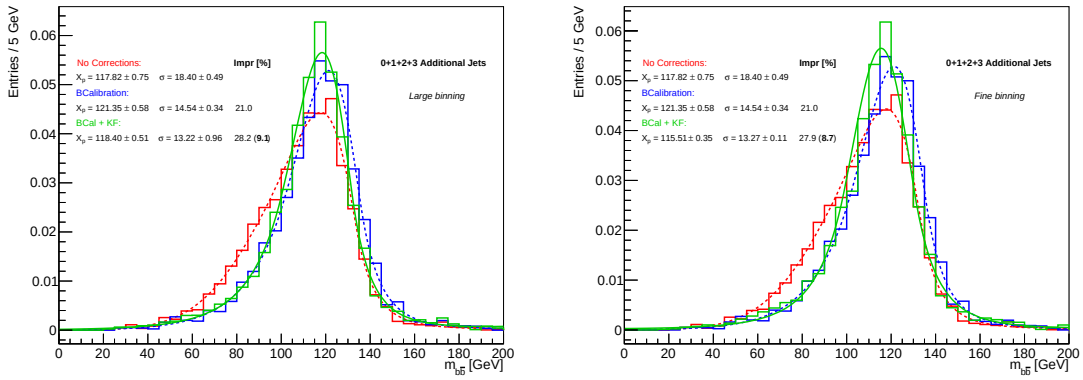

(a) (b)

Figure 5.18: Comparison of the di-jet invariant masses for jets reconstructed using nominal correction (red), BCalibration (blue), and the Kinematic Fit (green) that uses TFs with a wider (Left) and finer (Right) p_T binning compared to the standard configuration (Fig. (5.15)). The solid (KF) and dashed (no corrections, BCal) lines represent the fitted Bukin distributions. Best-fit parameters: Roofit MLE method.

A final test is conducted using the hadronic and semileptonic transfer functions separately (see Sect. 2.3.3.3 for definitions of the two categories), to confirm that no information is lost when using only the inclusive ones, which consider semileptonic (around 20%) and hadronic events together. For the semileptonic case, there are only two "detector (η) bins", Endcap ($1.52 < |\eta| \leq 4.4$) and Barrel ($-1.37 \leq \eta < 1.52$), as there are not

enough events in the 'NoTrack' and 'Crack' zones (using the usual 400,000-event SM ggF sample). In both cases, the distributions are fitted with a TaOGata function. The p_T transfer functions for the same bin are shown in Fig. (5.19), where it can be noted that the semileptonic TF is broader. These considerations are analogous for the E transfer functions.

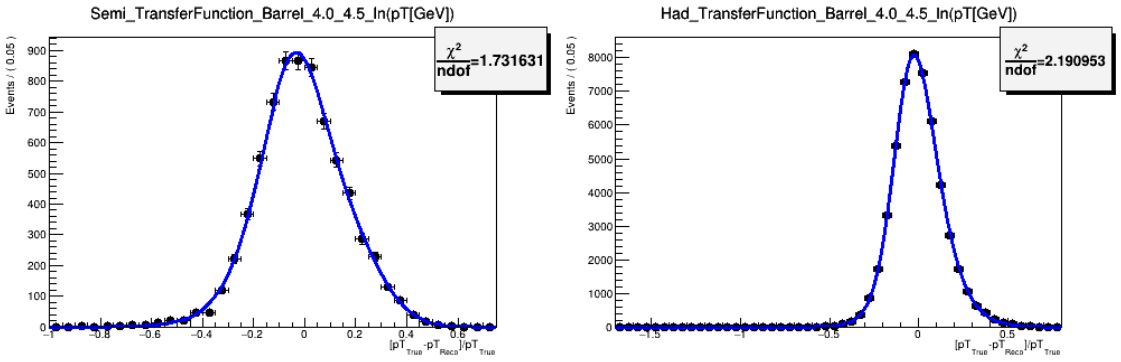

(a) (b)

Figure 5.19: Transverse momentum transfer functions fitted with a TaOGaTa distribution (Equation (5.3)) for a specific η-ln(p_T) bin in the semileptonic (Left) and hadronic (Right) cases.

		X_{peak} [GeV]	σ	**σ-Improv [%]**
0 Add jets	BCal	121.17	13.73	
	KF$_{Hadr/Semilep}$	118.46	12.39	9.76
	KF$_{Incluive}$	117.75	12.19	11.22
0+1 Add jets	BCal	121.99	13.90	
	KF$_{Hadr/Semilep}$	117.76	13.00	6.47
	KF$_{Inclusive}$	117.56	12.98	6.62
0+1+2 Add jets	BCal	121.55	14.84	
	KF$_{Hadr/Semilep}$	117.93	13.64	8.09
	KF$_{Inclusive}$	117.76	13.59	8.42
0+1+2+3 Add jets	BCal	121.35	14.54	
	KF$_{Hadr/Semilep}$	117.86	13.37	8.04
	KF$_{Inclusive}$	117.38	12.80	11.97

Table 5.4: Comparison of the Bukin $m_{b\bar{b}}$ fit peak position (X_{peak}), resolution (σ_{KF}), and its relative improvement over σ_{BCal}, for the cases where hadronic and semileptonic TFs are used separately or inclusively.

Although the results are acceptable (see Table (5.4)), they are slightly worse than the inclusive case, which, together with considerations about code complexity, confirms the choice of using the inclusive transfer functions for final use.

Finally, to describe the $H \to \gamma\gamma$ component more accurately and realistically, the photon energy, which in previous tests is modeled by a Gaussian distribution with a fixed 1% resolution, is characterized by a transfer function similar to that used for jets,

but using the TaOTa function, which is already employed for the $p_X - p_Y$ constraint. The results are nonetheless very similar, and no further details are necessary, especially considering the points discussed in the following Section 5.5.

5.3 Kinematic Fit second iteration: $m^*_{b\bar{b}\gamma\gamma}$ improvement

Following the exploration of potential improvements to the $m_{b\bar{b}}$ mass resolution, a new term is introduced in the likelihood function (Eq. (5.10)) to further enhance the precision of the four-object reduced invariant mass distribution, $m^*_{b\bar{b}\gamma\gamma}$, as previously discussed in Sect. 3.4.1.3. This term enforces the invariant mass of the jets to match the mass of the Higgs boson, expressed as: $\mathcal{L}^{Higgs}_{Constraint} = -(m_{b\bar{b}} - m_H)^2$.
The $m^*_{b\bar{b}\gamma\gamma}$ variable is critical for event selection in the analysis and it is used as an input to the BDT to enhance signal-background discrimination. While this constraint has a substantial effect on the $m_{b\bar{b}}$ invariant mass, essentially rendering it unsuitable for evaluating the Kinematic Fit effects due to the mass being forced toward the Higgs mass, it remains a reasonable approach when considered in the broader context. The primary goal of the Kinematic Fit is not just to reconstruct the most accurate event observables but to distinguish di-Higgs signal from the background more effectively.

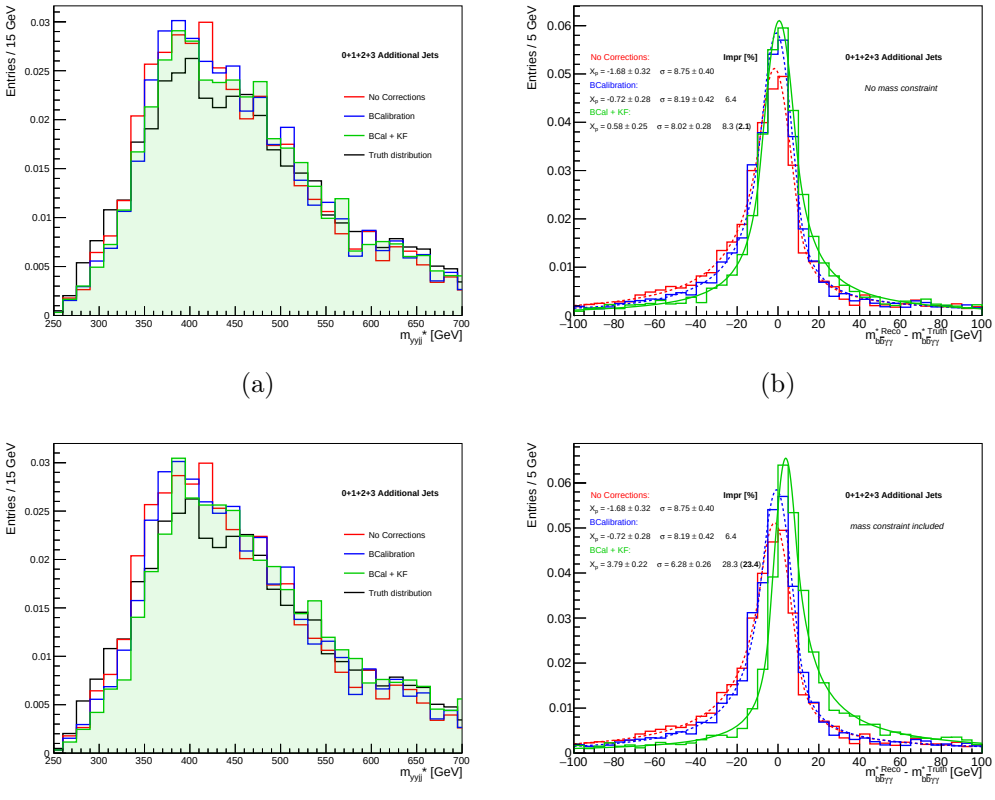

Figure 5.20: On the left, the four-object reduced invariant mass ($m^*_{b\bar{b}\gamma\gamma}$) distributions for jets reconstructed using nominal correction (red), BCalibration (blue), Kinematic Fit (green) without (a) and with (c) the mass constraint. The Truth distribution of the quantity is also present (black). The plots (b) and (d) show a comparison, as difference, between the reconstructed and truth distributions o better understand the KF impact. The DSCB is the fit function. Best-fit parameters: Roofit MLE method.

Therefore, the Kinematic Fit algorithm is applied twice per event, in two separate and independent configurations, to optimize both $m_{b\bar{b}}$ and $m^{*}_{b\bar{b}\gamma\gamma}$. The outcome of the second configuration, incorporating the mass constraint, provides the modified KF jets to use to calculate $b\bar{b}\gamma\gamma$ kinematics and relevant quantities, while from the first configuration only the $m_{b\bar{b}}$ variable is extracted.
To evaluate the impact of this new constraint, simply plotting the $m^{*}_{b\bar{b}\gamma\gamma}$ distribution (Fig. (5.20a) and (5.20c)) is insufficient, as the improvements are not visually distinguishable. Therefore, the evaluation focuses on comparing the resolutions obtained from a Double-Sided Crystal Ball (DSCB) fit (detailed in Eq. (6.6)) of the $m^{*,Reco}_{b\bar{b}\gamma\gamma} - m^{*,True}_{b\bar{b}\gamma\gamma}$ distributions (Fig. (5.20b)) and (5.20d)).
The shift from zero is likely due to a mismatch between the dijet mass constraint set at exactly 125 GeV and the true di-jets mass, which does not have its mean precisely at this value. The right-tail asymmetry arises from this discrepancy and the shape of the $m^{True}_{b\bar{b}}$ distribution, which exhibits typical asymmetry of $m_{b\bar{b}}$ distribution largely discussed in this chapter.

5.3.1 Optimization of the invariant mass constraint (λ_m-scan)

Following the optimization procedure used for the $p_X + p_Y$ constraint, a new parameter λ_m is introduced in the mass constraint term:

$$\mathcal{L}^{Higgs}_{Constraint} = -\boldsymbol{\lambda_m}(m_{b\bar{b}} - m_H)^2 \ . \tag{5.11}$$

This parameter is scanned to properly weight the new constraint and identify the optimal configuration for the best resolution of $m^{*,Reco}_{b\bar{b}\gamma\gamma} - m^{*,True}_{b\bar{b}\gamma\gamma}$. Although the scan (Fig. (5.21)) suffers from instabilities in the DSCB fitting, a general trend is discernible, and a minimum is found at $\lambda_m = 0.1$.

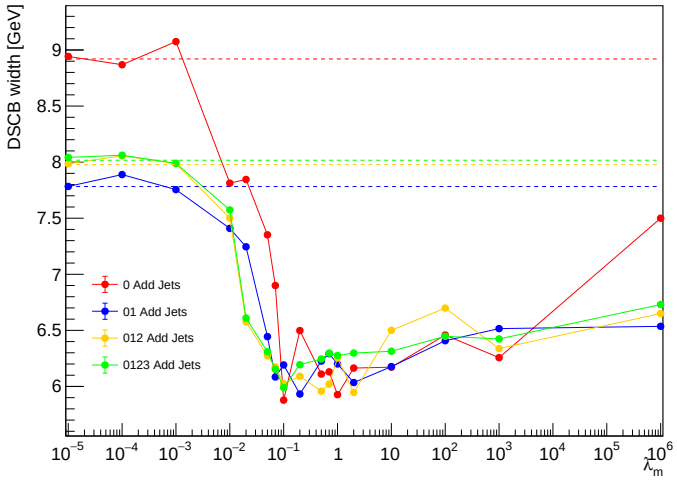

Figure 5.21: Scan of λ_m values plotted against the DSCB width of the $m^{*,Reco}_{b\bar{b}\gamma\gamma} - m^{*,True}_{b\bar{b}\gamma\gamma}$ resulting from the KF application. The different lines represent the cumulative addition of events with more additional jets. The dotted lines represent the DSCB width with $\lambda_m = 0$.

The final result, represented in Fig. (5.22), demonstrates an additional 26% improvement in the $m^{*,Reco}_{b\bar{b}\gamma\gamma} - m^{*,True}_{b\bar{b}\gamma\gamma}$ resolution compared to the BCal correction. This improvement is over 30% relative to the nominal jet calibration, and 25% better than the Kinematic Fit configuration with $\lambda_m = 0$.

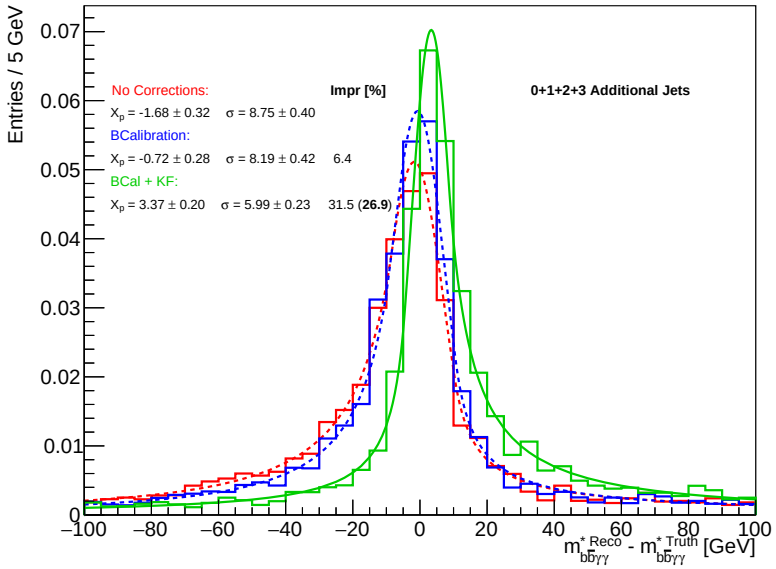

Figure 5.22: The difference between $m^{*,Reco}_{b\bar{b}\gamma\gamma}$ and $m^{*,True}_{b\bar{b}\gamma\gamma}$ distributions for jets reconstructed using nominal correction (red), BCalibration (blue), Kinematic Fit (green) using the mass constraint weighted by a λ_m factor of 0.1. The solid (KF) and dashed (no corrections, BCal) lines represent the fitted DSCB distributions. Best-fit parameters: Roofit MLE method.

$m^*_{b\bar{b}\gamma\gamma}$ background tests Analogously to the first iteration of the fit, where tests discussed in Section (5.2.6) assess possible distortions of the $m_{b\bar{b}}$ distribution in the background due to the tool, the same validation is performed for the second iteration but focusing on the $m^*_{b\bar{b}\gamma\gamma}$ distribution using the same 30,000-event background samples.
Figures (5.23a)-(5.23b) illustrate that, as in the $m_{b\bar{b}}$-tests of the first KF iteration, no significant sculpting is observed for either the continuum $\gamma\gamma$+jets or the single-Higgs $t\bar{t}H$ background. The deviations from the truth distribution are expected and consistent with the inclusion of the mass constraint term (Eq. (5.11)).

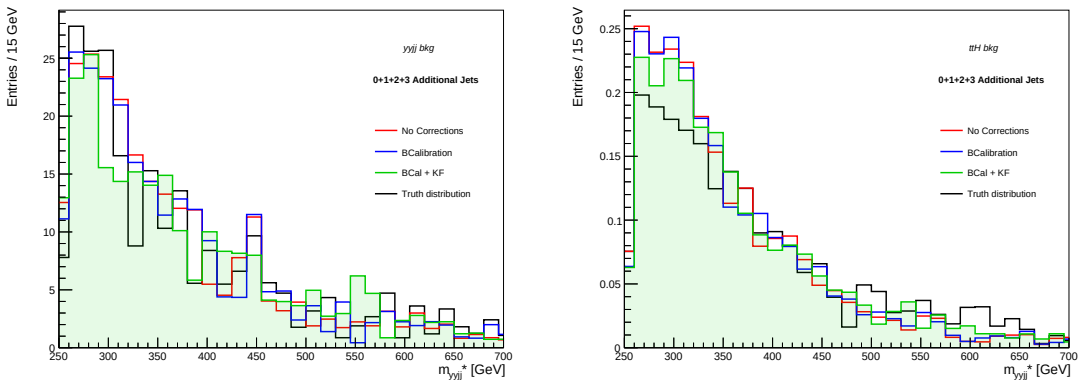

(a) (b)

Figure 5.23: The $m^*_{b\bar{b}\gamma\gamma}$ distributions for jets reconstructed using nominal corrections (red), BCalibration (blue), and the Kinematic Fit with the mass constraint (green), for the $\gamma\gamma$+jets (a) and $t\bar{t}H$ (b) backgrounds. The truth distribution is also included (black).

5.4 Implementation and Integration of the Kinematic Fit Tool

The Kinematic Fit algorithm is developed in C++ and fully integrated with the CERN ROOT data analysis framework, allowing for flexible compatibility with the associated analysis frameworks. Up until the legacy analysis, the framework used to produce and provide the final ntuples for statistical analysis was HGamCore, but starting from Run-III, it is Easyjet, as briefly discussed at the beginning of this Chapter.
The Kinematic Fit Tool is integrated directly into the event loop process, immediately after the BCalibration step. It is implemented as an optional component that can be easily enabled or disabled with a simple flag, without requiring changes to other parts of the framework's code. This approach is essential for maintaining a clean and clear code structure, and it is also extremely beneficial for R&D studies.
The Tool receives all reconstructed four-vectors of the jets and photons and performs minimization of the custom negative log-likelihood using MIGRAD, a minimization algorithm implemented in ROOT's Minuit class. MIGRAD searches for the function's minimum using its gradient. The post-fit four-vectors are then returned to the analysis framework for further processing, such as $HH \to b\bar{b}\gamma\gamma$ kinematics calculations, and they are directly saved into the final ntuples.

Computational Time and Resource considerations During various tests and optimizations, as previously discussed, careful attention was paid to ensuring that the computational time and resources required by the Kinematic Fit process were not excessive and remained within the acceptable limits set by the analysis group for the final ntuple production. In an experiment of the scale of ATLAS, even minor performance costs can lead to significant delays in the analysis process. It is thus necessary to balance the improvement in precision with the associated computational resources, as minimal gains may not justify the increased cost.
In addition to considerations about the form of the different likelihoods tested -clearly, those with more terms require more resources, as explicitly noted in studies on angular variables and their subsequent removal (Sect. 5.2.2)- many studies were conducted at the code structure level. For instance, the Kinematic Fit is not performed if more than 3 additional central jets are present in the event, since such events are anyway excluded during preselection for statistical analysis. On the C++/ROOT side, a lot of optimizations were made, for example in handling input files containing Transfer Function parameters for each event and implementing of these TFs via RooFit, TF1, or C functions, with this latter method chosen for balancing code clarity and simplicity while maintaining performance and $m_{b\bar{b}}$ resolution results.
Thanks to the analysis of CPU time consumption (performed using the <chrono> C++ standard library) on the usual SM HH ggF sample with 30,000 events, the Kinematic Fit is found to have an overall time performance impact of about $\sim 3\%$ on the processing and production of the final ntuples.
Finally, it was verified that the Kinematic Fit did not lead to excessive memory consumption or cause excessive memory swapping during sample processing. Metrics such as Resident Set Size (RSS), which measures non-swapped physical memory used by a process, Virtual Memory Size (VMM), which is the total virtual memory allocated, and swap memory usage were closely monitored. Comparisons with cases where the KF tool was

not included confirm that there is no significant additional memory usage when the Tool is used.

5.5 Porting the Kinematic Fit Tool from HGamCore to Easyjet Framework

During the migration of the algorithm from the HGamCore[3] to the Easyjet framework[4], the structure of the Kinematic Fit code is adjusted to better interface with the new, more Python-like Easyjet environment. The performance is verified to be comparable with the results achieved in the previous framework, despite the differences between the two analysis approaches.
As described in Section 4.2, the two candidate b-jets are now selected using a 77% GN2 b-tagging working point.
To improve both code structure and CPU computation time -intuitively, it is no longer necessary to update, save, the four-vectors for photons as well as jets- the energy terms for photons are excluded from the Kinematic Fit. This change effectively treats the photon excellent four-momentum as a true-level quantity, and the di-photon system $H \to \gamma\gamma$ is only included in the transverse momentum constraint of the $b\bar{b}\gamma\gamma$ system.
This modification is applied only after confirming that the overall results of the Kinematic Fit Tool are not significantly impacted by the removal of these terms.
The final form of the likelihood function is

$$-2\ln(\mathcal{L}) = \sum_{j=jets}\Big[-2\ln\big[\mathrm{TF}_E\big(\frac{E^j_{Fit}-E^j_{Reco}}{E^j_{Fit}}\big)\big] - 2\ln\big[\mathrm{TF}_{p_T}\big(\frac{p^j_{T,Fit}-p^j_{T,Reco}}{p^j_{T,Fit}}\big)\big]\Big] + \\ -2\lambda\ln\big[f_{p_X}(p_X)\big] - 2\lambda\ln\big[f_{p_Y}(p_Y)\big] \quad \underbrace{-\lambda_m(m_{b\bar{b}}-m_H)^2}_{\text{included in KF 2nd iteration}} \tag{5.12}$$

and the relative results are shown in Fig. (5.24)-(5.25), considering all events from the ggF Run-II mc20a sample[5] (see more plots in Appendix B). An additional improvement of 12.7% (32.2%) in $m_{b\bar{b}}$ ($m^*_{b\bar{b}\gamma\gamma}$) resolution is achieved compared to BCalibration correction. This corresponds to a 28.7% (34.2%) improvement over the nominal jet calibration.
These results are comparable to those obtained with the previous HGamCore framework (Figures (5.14)-(5.22)).

[3]HGamCore Kinematic Fit repository: https://gitlab.cern.ch/jdevivi/KinematicFit
[4]Easyjet Kinematic Fit repository: https://gitlab.cern.ch/r3hh-public/KinematicFit
[5]The difference between the previously mentioned mc16a and mc20a is in the version of the ATLAS software, Release 21 and Release 22, respectively.

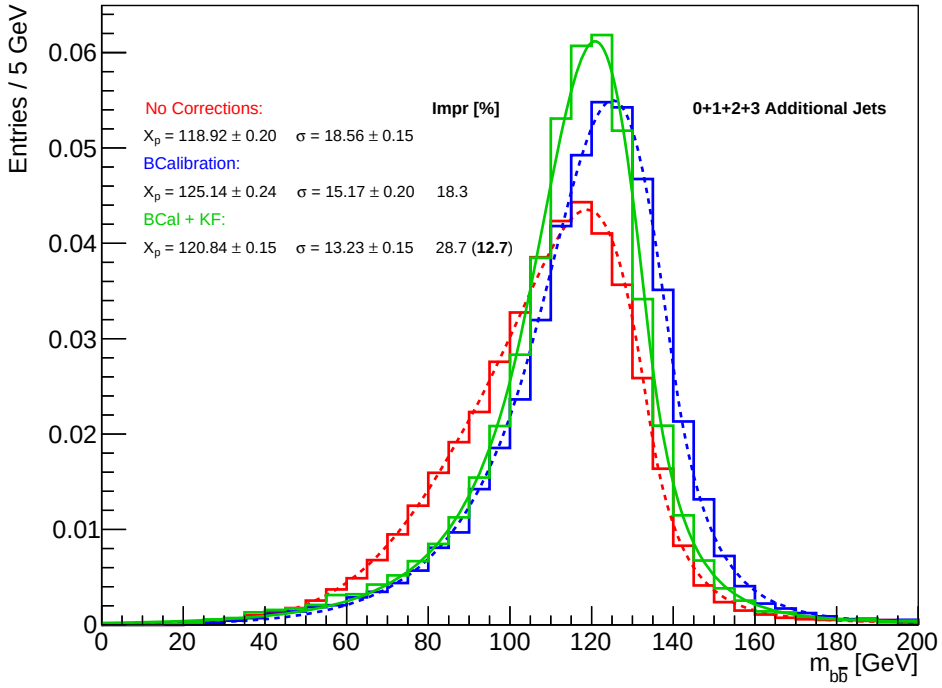

Figure 5.24: Di-jet invariant mass plot in Run-III easyjet framework: red line indicates the nominal correction case, blue and green lines the BCal correction and the Kinematic Fit ones, respectively. Best-fit parameters: Roofit MLE method.

	No Corrections	BCal	Kinematic Fit
X_p	118.92 ± 0.20	125.14 ± 0.24	120.84 ± 0.15
σ	18.56 ± 0.15	15.17 ± 0.20	13.23 ± 0.15
χ	-0.32 ± 0.01	-0.18 ± 0.01	-0.16 ± 0.01
ρ_1	-0.45 ± 0.03	-0.03 ± 0.01	0.05 ± 0.01
ρ_2	0.22 ± 0.01	0.13 ± 0.01	0.15 ± 0.01

Table 5.5: Table with Bukin fit parameters for each of the corrections shown in Fig. (5.24): X_p is the peak position, σ the peak width, χ the peak asymmetry, ρ_1 and ρ_2 the left and right tails respectively.

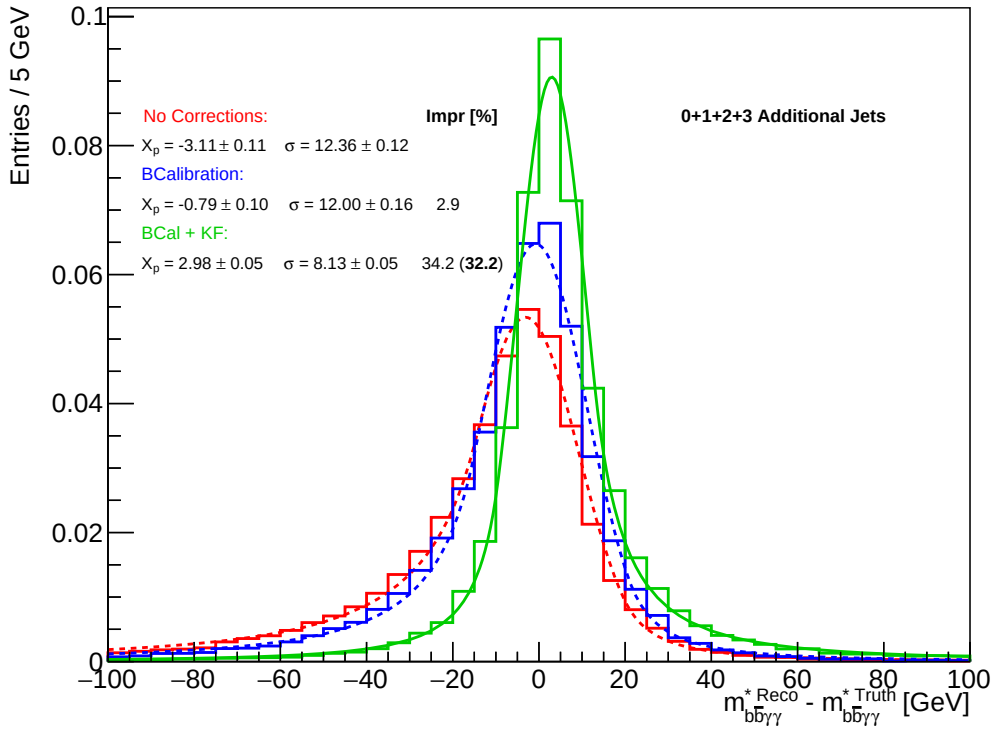

Figure 5.25: Plot of the difference between $m^{*,Reco}_{b\bar{b}\gamma\gamma}$ and $m^{*,True}_{b\bar{b}\gamma\gamma}$ in Run-III easyjet framework: red line indicates the nominal correction case, blue and green lines the BCal correction and the Kinematic Fit ones, respectively. Best-fit parameters: Roofit MLE method.

	No Corrections	BCal	Kinematic Fit
μ_{CB}	-3.07 ± 0.11	-0.95 ± 0.08	2.55 ± 0.06
σ_{CB}	12.20 ± 0.11	11.40 ± 0.20	0.09 ± 0.07
α_{Lo}	0.94 ± 0.01	1.17 ± 0.01	1.46 ± 0.01
α_{Hi}	1.78 ± 0.02	1.71 ± 0.01	1.12 ± 0.01
n_{Lo}	1.99 ± 0.01	1.91 ± 0.03	1.82 ± 0.03
n_{Hi}	1.99 ± 0.01	1.91 ± 0.03	1.99 ± 0.01

Table 5.6: Table with Double-Side Crystal Ball fit parameters (Eq. (6.6)) for each of the corrections shown in Fig. (5.25).

Chapter 6

$HH \to b\bar{b}\gamma\gamma$ analysis

Following the introduction to the $HH \to b\bar{b}\gamma\gamma$ decay channel, the description of the dataset, as well as all the simulated samples for the signal and background processes used in the analysis, and the definition of the physics objects and the signal region (Sect. 4), which aims to select events containing a pair of high-quality photons and two b-jets -corrected using the kinematic fit technique described in the previous section- this Chapter first outlines the event categorization for those passing the preselection. Subsequently, the modeling of the di-photon invariant mass spectrum for both signal and background processes is described, along with a detailed account of all systematic uncertainties affecting the analysis results. All these components are combined to construct the statistical model, which ultimately leads to the final results presented in Sect. 6.4. As the $b\bar{b}\gamma\gamma$ group is targeting a Run-II+partial Run-III publication for the half of 2025, the analysis is currently still blinded, so only expected results can be provided in this thesis. The blinded region is $120 < m_{\gamma\gamma} < 130$ GeV.

6.1 Event categorization

The events that pass the initial selection criteria are further classified into mutually exclusive categories based on the reduced four-object invariant mass $m^*_{b\bar{b}\gamma\gamma}$, already introduced in Sect. 3.4.1.3 and defined by Equation (3.7), and the outputs of a Boosted Decision Tree, resulting in 5 different regions.
This corrected invariant mass was designed in the previous analysis [180] to improve the resolution of the four-object mass $m_{b\bar{b}\gamma\gamma}$ by reducing the effects of detector resolution. The application of the Kinematic Fit enables a more accurate description of this distribution, bringing it closer to its true shape (Sect. 5.3).
A *High Mass* region is defined by $m_{b\bar{b}\gamma\gamma^*} > 350$ GeV to target Standard Model ggF and VBF HH production, both in a Standard Model-like scenario and for values of κ_{2V} deviating from 1. Conversely, a *Low Mass* region, characterized by $m_{b\bar{b}\gamma\gamma^*} \leq 350$ GeV, is used to retain sensitivity to ggF and VBF HH production with Beyond Standard Model κ_λ values. The 350 GeV threshold was chosen as a compromise to impose stringent constraints on κ_λ mainly from the Low Mass region, while still maintaining significant sensitivity to SM HH production and larger κ_{2V} values via the High Mass region.
Figure (6.1) illustrates the dependence of ggF and VBF HH production on the coupling modifiers κ_λ and κ_{2V}.
Two separate BDTs, trained with XGBoost [181] and only simulated event samples, are used for each mass region to discriminate HH signals from backgrounds, that include all

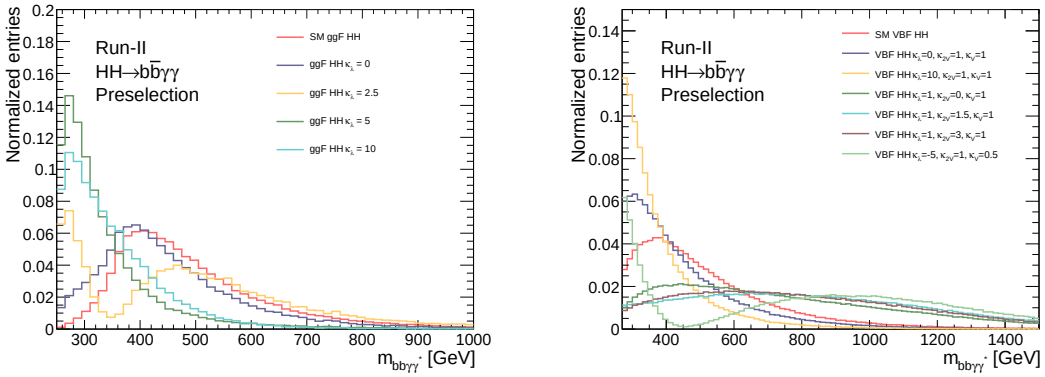

(a) (b)

Figure 6.1: Distribution of the reduced 4-body invariant mass $m^*_{b\bar{b}\gamma\gamma}$ for the (a) ggF and (b) VBF HH process in the SM case and different BSM scenarios.

single Higgs processes (ggH, VBF H, WH, ZH, $t\bar{t}H$, $tHjb$, tWH, $b\bar{b}H$), as well as $\gamma\gamma$ and $t\bar{t}\gamma\gamma$ continuum background samples.
In the high mass region, the BDT training comprises SM ggF and VBF HH events, as well as five non-SM VBF HH samples with different values for $(\kappa_\lambda, \kappa_{2V}, \kappa_V)$: (0, 1, 1), (10, 1, 1), (1, 1.5, 1), (1, 3, 1), and (-5, 1, 0.5), and the background. In the low mass region, the training signal samples consist of non-SM ggF HH events with $\kappa_\lambda = 10$ and $\kappa_\lambda = 5$, along with the same five non-SM VBF HH samples. All the samples used for training, along with the remaining ggF ($\kappa_\lambda = 0$) and VBF samples (Table (4.2)) generated alongside the data, are utilized as test samples.
During training, per-process weights are applied to training samples to balance signal and background contributions, avoiding to spoil the training performance and ensuring that the BDTs effectively target both SM-like and relevant BSM-like scenarios in each mass region. The application of the weights results in a normalization of the simulated events to a specific scale factor times their expected yields (Table (4.4)). The relative scale factors are obtained after a hyperparameter optimization, that is an important ingredient of the $HH \to b\bar{b}\gamma\gamma$ event selection. For each possible $m^*_{b\bar{b}\gamma\gamma}$ bin in the Low and High mass regions, the per-process scale factors and the hyperparameters of the BDT models are optimized simultaneously via a bayesian optimization algorithm [182], specifically the *Hyperopt* algorithm [183], to maximize the expected number-counting significance (Z_{tot}), defined as:

$$Z_{\text{bin}} = \sqrt{2 \cdot [(S+B) \cdot \log(1 + S/B) - S]}, \quad Z_{\text{tot}} = \sum_{\text{bin}} Z_{\text{bin}} \ , \tag{6.1}$$

where S is the signal from HH production, and B includes continuum background and single Higgs boson events. The sum is over all bins in all categories. The binning boundaries are exhaustively optimized to achieve the highest combined significance. To ensure optimal performance, the definition of signals are changed so that the counting significance targets different figures of merits:

- Low mass region: number counting significance $Z_{\text{target } \kappa_\lambda}$, using, as signals, ggF HH events with $\kappa_\lambda = 5$ and VBF HH events with $\kappa_\lambda = 10$, that is the only sample that is purely anomalous in κ_λ (as shown in Figure (6.1b)).

- High mass region: number counting significance $Z_{\text{target SM}}$, using, as signals, SM ggF HH plus SM VBF HH events.

For the hyperparameter optimization, a 5-fold cross-validation is employed to mitigate potential bias arising from data splitting during the training of the MVA model. Once the optimization process is complete, the selected hyperparameters are fixed within the model, and it is retrained using a 50% training, 25% validation, and 25% test split.
After 1000 trials, the best configuration of the per-process scale factors and the hyperparameters (defined in [184]) in each mass region are listed in Table (6.1).

Hyperparameter	Range	Value for Low Mass BDT	Value for High Mass BDT
min child weight	[0,100]	27	84
colsample bytree	[0.3, 1]	0.64	0.76
scale pos weight	[0.0, 9.0]	1.71	1.55
max delta step	[0.0, 20.0]	13.78	8.38
subsample	[0.5, 1.0]	1.0	0.82
eta	[0.01, 0.05]	0.01	0.01
alpha	[0.0, 1.0]	0.40	0.62
lambda	[0.0, 10.0]	9.70	6.76
max depth	[3, 20]	20	20
gamma	[0.0, 10.0]	0.0	3.13
max bin	[10, 512]	286	56
Scale factor	Range	Value for Low Mass BDT	Value for High Mass BDT
SM ggF HH	[1, 200]	-	128.06
SM VBF HH	[1, 200]	-	15.44
ggF HH $\kappa_\lambda = 10$	[1, 200]	83.74	-
ggF HH $\kappa_\lambda = 5$	[1, 200]	1.0	-
VBF HH $\kappa_\lambda = 0$, $\kappa_{2V} = 1$, $\kappa_V = 1$	[1, 200]	1.0	5.43
VBF HH $\kappa_\lambda = 1$, $\kappa_{2V} = 1.5$, $\kappa_V = 1$	[1, 200]	27.65	56.06
VBF HH $\kappa_\lambda = 1$, $\kappa_{2V} = 3$, $\kappa_V = 1$	[1, 200]	1.0	1.0
VBF HH $\kappa_\lambda = -5$, $\kappa_{2V} = 1$, $\kappa_V = 0.5$	[1, 200]	68.45	1.0
VBF HH $\kappa_\lambda = 10$, $\kappa_{2V} = 1$, $\kappa_V = 1$	[1, 200]	118.76	1.0
$\gamma\gamma$+jets	[1, 200]	183.72	194.15
$t\bar{t}\gamma\gamma$	[1,100]	35.29	11.41
$t\bar{t}H$	[1,100]	1.0	44.81
$ggH + b\bar{b}H$	[1,100]	1.0	38.65
$qq \to ZH + gg \to ZH$	[1,100]	1.0	3.61

Table 6.1: Best values of the XGBoost hyperparameters and the per-process scale factors for the High Mass and Low Mass BDTs after the hyperparameter optimization.

The *baseline* BDT input variables are listed in Table (6.2).
The same set of variables is used for both mass categories. The BDT merges several input variables that leverage distinct kinematic characteristics of signal and background events to distinguish them. It combines observables derived from the kinematic properties of the reconstructed photons, such as the angular information of the leading and subleading photons, and the transverse momentum of the diphoton system normalized by its invariant mass[1], with jet-based information. The *single topness* variable (χ_{Wt}) is also employed. It plays a critical role in mitigating contamination from the $t\bar{t}H$ production mode and can be understood as the likelihood of the event containing a top quark, defined as follows:

$$\chi_{Wt} = \min \sqrt{\left(\frac{m_{j_1 j_2} - m_W}{m_W}\right)^2 + \left(\frac{m_{j_1 j_2 j_3} - m_t}{m_t}\right)^2} \tag{6.2}$$

[1]This reduces the correlation between the input variables and the final discriminant, $m_{\gamma\gamma}$, ensuring unbiased $m_{\gamma\gamma}$ background distributions across the final categories.

Variable	Definition
Photon-related kinematic variables	
$p_T/m_{\gamma\gamma}$	Transverse momentum of each of the two photons divided by the diphoton invariant mass $m_{\gamma\gamma}$
η and ϕ	Pseudorapidity and azimuthal angle of the leading and subleading photon
Jet-related kinematic variables	
b-tag status	Tightest fixed b-tag working point (60%, 70%, or 77%) that the jet passes
p_T, η and ϕ	Transverse momentum, pseudorapidity and azimuthal angle of the two jets with the highest b-tagging score
$p_T^{b\bar{b}}$, $\eta_{b\bar{b}}$ and $\phi_{b\bar{b}}$	Transverse momentum, pseudorapidity and azimuthal angle of the b-tagged jets system
$m_{b\bar{b}}$	Invariant mass of the two jets with the highest b-tagging score
H_T	Scalar sum of the p_T of the jets in the event
Single topness	For the definition, see Eq. (6.2)
Missing transverse momentum variables	
E_T^{miss} and ϕ^{miss}	Missing transverse momentum and its azimuthal angle

Table 6.2: BDT baseline input variables used in the analysis.

where m_W and m_t are the masses of the W boson and the top quark, respectively, and the minimum is taken over all possible combinations of any three jets in the event, regardless of their b-tagging status.
For events with at least four jets, additional variables include the p_T, η, ϕ, and discrete b-tagging score of the third and fourth jets. Such events may originate from VBF HH production, in which case their invariant mass m_{jj} and the pseudorapidity difference $\Delta\eta(j_1, j_2)$ are used as input variables for the event classification BDTs.
Another set of variables for the event classification BDTs consists of event-level kinematic quantities such as $m^*_{b\bar{b}\gamma\gamma}$ and the angular separation $\Delta R(\gamma, \gamma)$ ($\Delta R(b, \bar{b})$) between the two photons ($b-$tagged jets). Lastly, three event-shape observables are used: the transverse sphericity $S_\perp$ [185], which captures global information about the event's full momentum tensor, the planar flow Pf [186], a two-dimensional jet shape contrasting the linear flow typical of QCD jets, and the transverse momentum balance defined as:

$$p_T^{\text{balance}} = \frac{|\vec{p}_T^{\,\gamma_1} + \vec{p}_T^{\,\gamma_2} + \vec{p}_T^{\,j_1} + \vec{p}_T^{\,j_2}|}{|\vec{p}_T^{\,\gamma_1}| + |\vec{p}_T^{\,\gamma_2}| + |\vec{p}_T^{\,j_1}| + |\vec{p}_T^{\,j_2}|}. \tag{6.3}$$

Model evaluation For assessing the performance of the BDT model, the commonly used evaluation metrics are utilized: the "LogLoss vs epochs" and the Receiver Operating Characteristic (ROC) curves. The first one tracks the logarithmic loss (a measure of the uncertainty in probabilistic classification) as a function of training epochs. This curve illustrates how the model's performance improves or stabilizes as the number of training iterations increases. The ROC curve graphically evaluates the performance of a binary classification model by plotting the True Positive Rate (sensitivity) against the False Positive Rate. These curves are presented in Fig. (6.2). The training process is designed to minimize the validation loss as much as possible. To achieve this, the maximum number of iterations is set to 3000, but early stopping is triggered if no improvement is observed

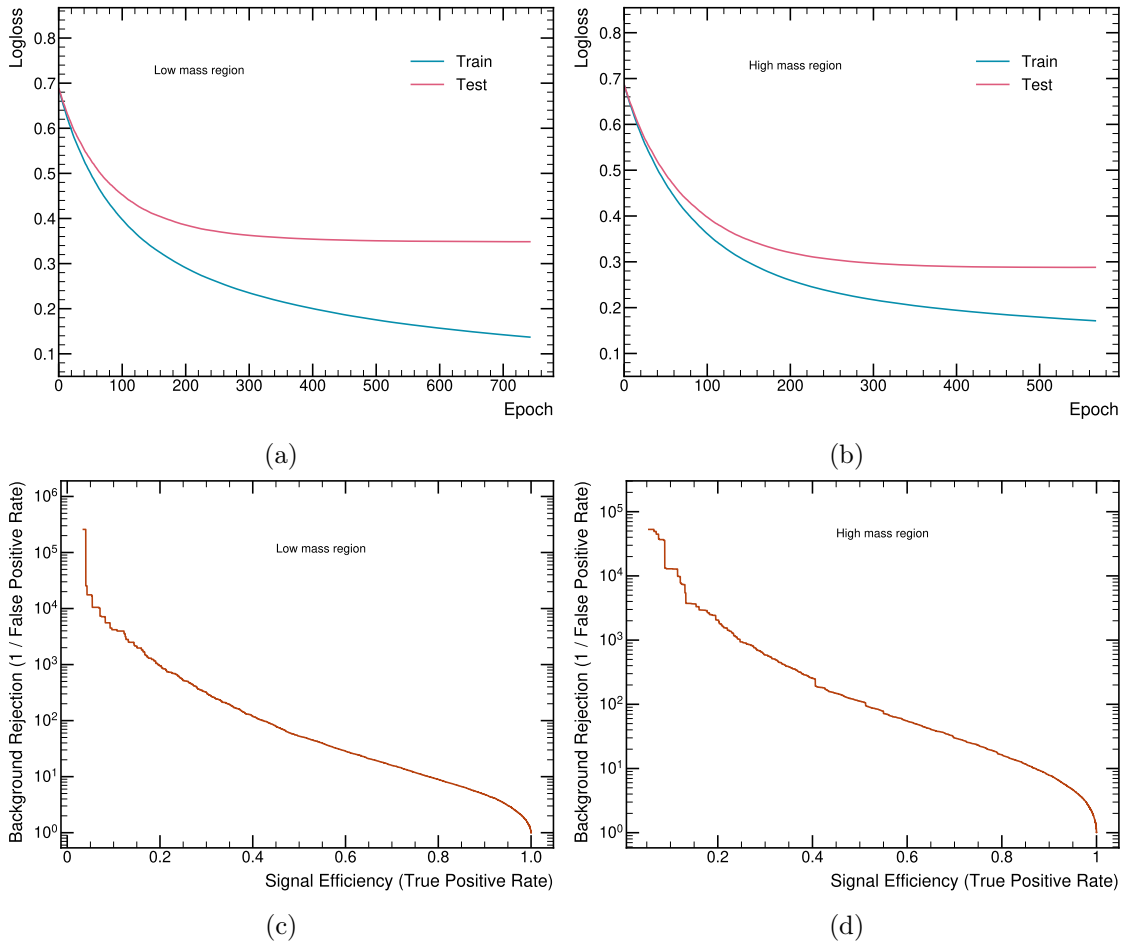

Figure 6.2: The "LogLoss vs epochs" and ROC curves for both BDT Low mass (Left) and High mass (Right) models.

over 20 consecutive iterations on metrics such as AUC (Area Under the Curve) and LogLoss. Despite the potential for overtraining in Low mass region -indicated by a larger gap between training and testing metrics in Fig. (6.2a)- this is not a concern here since the inference is performed on the test dataset, avoiding bias. Reducing the number of iterations would lead to an undertrained model. The BDT models for the High and Low Mass categories achieve AUC of 0.95 and 0.93, respectively, as evaluated on the validation dataset, indicating strong performance of the models (AUC equal to 1 represents the ideal model that correctly classifies).

Regarding the ROC curves, in the Low mass region, there is an initial sharp drop in background rejection as signal efficiency increases, a pattern not observed in the High mass region. This rapid decrease may arise from challenges in distinguishing signal from background, likely due to overlapping features between the two. In contrast, the high-mass region exhibits a more stable and gradual transition, suggesting that background rejection is less sensitive to changes in signal efficiency. In general, the two curves demonstrate good performance.

Lastly, the feature importances of the input variables used for training the BDTs in both the High Mass and Low Mass regions are presented in Figures (6.3).

Among the input variables, the invariant mass of the b-jet pair $m_{b\bar{b}}$ shows the highest signal-background discriminating power in both the SM and BSM regions.

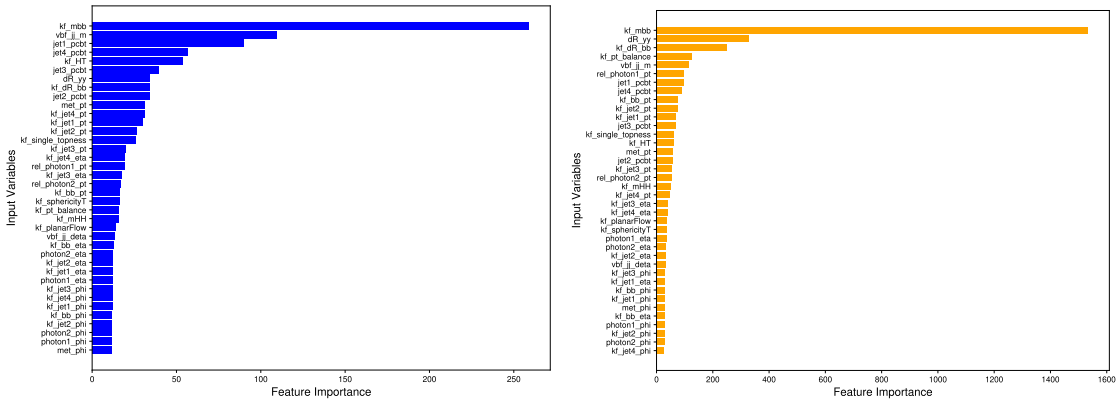

(a) (b)

Figure 6.3: Feature importances for BDTs trained in the Low Mass (Left) and High Mass (Right) regions. The x-axis values reflect the average contribution of a feature to the model's predictive power when it is selected for splitting a node in the decision tree within the model.

The distributions of the four most important discriminating variables (see Appendix C for the other quantities) for the two categories are shown in Figure (6.4):

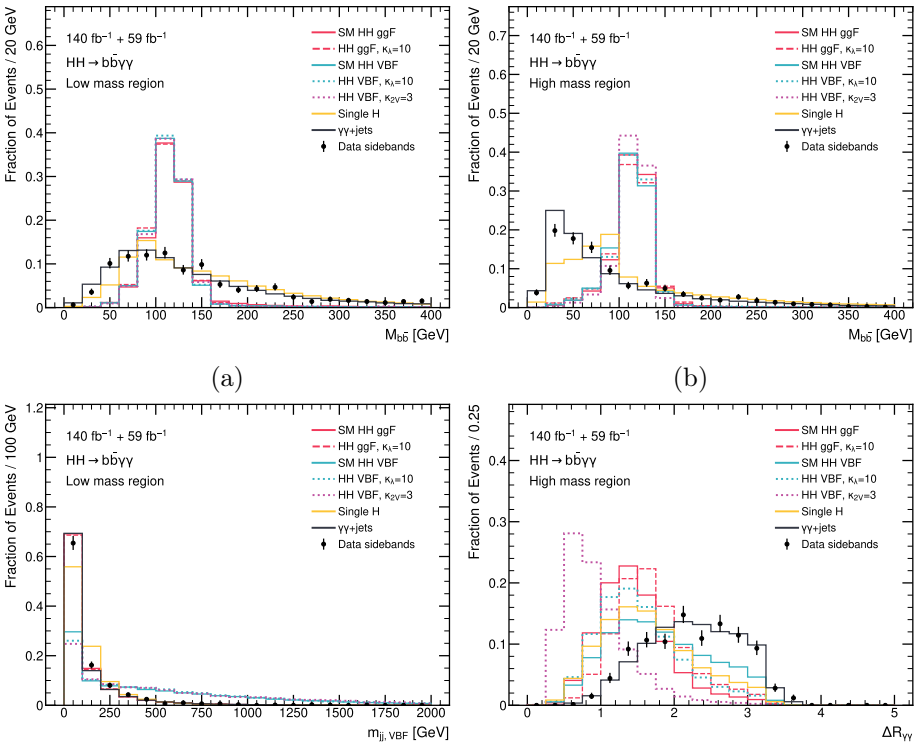

(a) (b)

(c) (d)

Figure 6.4: The $m_{b\bar{b}}$ mass exhibits the highest discriminative power for signal over background in both the Low mass (a) and High mass (b) regions, followed by the mass of the VBF jets (c) and the distance between the two photons (d) of the $H \to \gamma\gamma$ system, respectively. A comparison between data in the sideband region and MC simulation distributions is provided. The histograms are normalized to unit area, and the simulation distributions are not stacked.

After training, three categories (labeled *'High Mass i'*, with $i = 1..3$) are defined in the High mass region, and four categories (labeled *'Low Mass i'*, with $i = 1..4$) in the Low mass region. A higher category index i corresponds to higher BDT scores and more signal-like events. Events with a BDT score lower than the threshold for the lowest-index category in the respective mass region are discarded. The BDT score thresholds that define the categories are selected to maximize the expected di-Higgs significance Z_{tot} (Eq. (6.1)) in the diphoton invariant mass range 120 GeV $< m_{\gamma\gamma} <$ 130 GeV. The combined total significances $Z_{\text{tot } SM}$ and $Z_{\text{tot } \kappa_\lambda}$ (Eq. (6.1)), calculated by taking the square root of the sum of the squares of the individual significances of the categories (Table (6.3)), for the corresponding HM and LM regions, are 0.63 and 1.43, respectively, as also shown in the Plots (6.5). Each category must contain at least eleven expected continuum background events in the $m_{\gamma\gamma}$ sidebands, defined as 105–120 GeV and 130–160 GeV, to ensure sufficient events for constraining the shape of the diphoton invariant mass distribution of the continuum background when applied to the data.
The outputs of the BDT and the thresholds that define the categories in each mass region are shown in Figure (6.5) and Table (6.3).

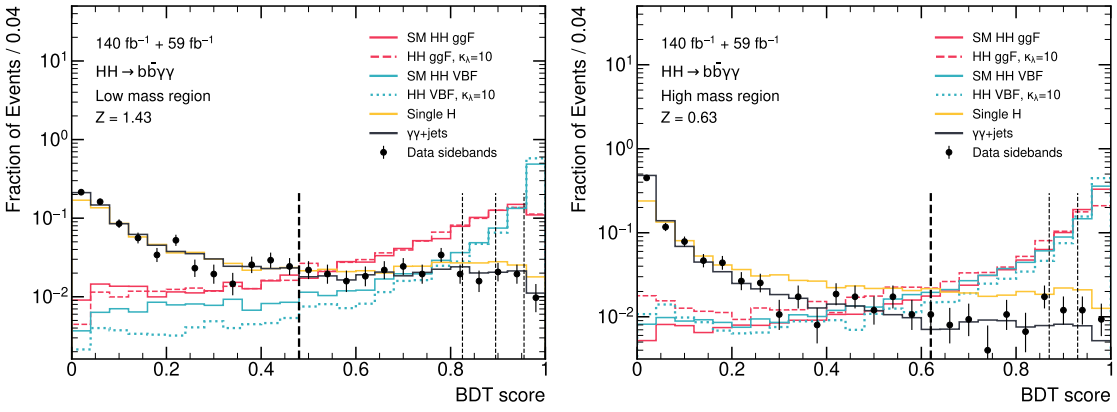

(a) (b)

Figure 6.5: BDT output distributions for the Low mass (a) and High mass (b) BDTs. The corresponding combined significance is also shown.

Category	**Selection criteria**	Significance
High Mass 1	$m^*_{bb\gamma\gamma} \geq 350$ GeV, BDT score $\in [0.620, 0.870]$	0.128
High Mass 2	$m^*_{bb\gamma\gamma} \geq 350$ GeV, BDT score $\in [0.870, 0.930]$	0.183
High Mass 3	$m^*_{bb\gamma\gamma} \geq 350$ GeV, BDT score $\in [0.930, 1.000]$	0.593
Low Mass 1	$m^*_{bb\gamma\gamma} < 350$ GeV, BDT score $\in [0.480, 0.825]$	0.279
Low Mass 2	$m^*_{bb\gamma\gamma} < 350$ GeV, BDT score $\in [0.825, 0.895]$	0.320
Low Mass 3	$m^*_{bb\gamma\gamma} < 350$ GeV, BDT score $\in [0.895, 0.955]$	0.486
Low Mass 4	$m^*_{bb\gamma\gamma} < 350$ GeV, BDT score $\in [0.955, 1.000]$	1.281

Table 6.3: The legacy analysis categories defined by the thresholds in $m^*_{bb\gamma\gamma}$ and the BDT output. The last column indicates the significance in each category, specifically $Z_{\text{target } SM}$ and $Z_{\text{target } \kappa_\lambda}$ (Eq. (6.1)) for HM and LM regions.

The expected yields of signal, background and data events in each category are summarized in Table (6.4).

	Yields						
Process	**HM1**	**HM2**	**HM3**	**LM1**	**LM2**	**LM3**	**LM4**
ggF HH SM	0.4398	0.3161	0.9994	0.0609	0.0347	0.0406	0.0242
ggF HH ($\kappa_\lambda = 0$)	0.8497	0.6035	1.6749	0.2918	0.1576	0.1854	0.1127
ggF HH ($\kappa_\lambda = 5$)	0.3742	0.2354	0.5296	1.1883	0.6084	0.6913	0.4223
ggF HH ($\kappa_\lambda = 10$)	3.6815	2.3055	5.0894	7.3089	3.7056	4.2424	2.6892
VBF HH SM	0.0137	0.0085	0.0306	0.0025	0.0015	0.0027	0.0086
VBF HH (0,1,1)	0.0308	0.0201	0.0843	0.0117	0.0074	0.0143	0.0504
VBF HH (1,1.5,1)	0.0201	0.0176	0.2435	0.0024	0.0016	0.0033	0.0124
VBF HH (1,3,1)	0.4364	0.3430	4.7503	0.0444	0.0305	0.0558	0.2423
VBF HH (10,1,1)	0.4196	0.2864	1.4824	0.3825	0.2562	0.5054	1.9602
VBF HH (-5,1,0.5)	0.0209	0.01721	0.3579	0.0152	0.0102	0.0201	0.0715
VBF HH (0,0,1)	0.2643	0.1958	1.8792	0.0483	0.0314	0.0574	0.2277
VBF HH (1,0,1)	0.1976	0.1465	1.5558	0.0212	0.0122	0.0272	0.1019
VBF HH (1,0.5,1)	0.0714	0.05256	0.4752	0.0086	0.0056	0.0091	0.0378
VBF HH (1,1,0.5)	0.0710	0.05753	0.7441	0.0092	0.0063	0.0121	0.0496
VBF HH (1,1,1.5)	0.4709	0.3486	3.1728	0.0784	0.0470	0.0997	0.3481
VBF HH (1,2,1)	0.0888	0.0772	1.1032	0.0094	0.0062	0.0118	0.0471
VBF HH (2,1,1)	0.0092	0.0058	0.0188	0.0035	0.0025	0.0054	0.0196
ggF H	0.4774	0.1769	0.1919	0.3502	0.0670	0.0809	0.0370
VBF H	0.0840	0.0225	0.0262	0.0458	0.0146	0.0113	0.0169
W^-H	0.0060	0.0007	0.0008	0.0036	0.0009	0.0005	0.0
W^+H	0.0024	0.0003	0.0	0.0076	0.0009	0.0	0.0006
bbH	0.0258	0.0078	0.0003	0.0857	0.0126	0.0657	0.0614
$gg \to ZH$	0.2611	0.0604	0.0509	0.0241	0.0065	0.0078	0.0032
$qq \to ZH$	0.4680	0.1140	0.0832	0.4798	0.1052	0.0687	0.0244
tHjb	0.0794	0.0199	0.0185	0.0480	0.0125	0.0142	0.0102
tWH	0.0041	0.0003	0.0005	0.0093	0.0008	0.0022	0.0003
ttH	0.3761	0.0773	0.0522	1.0976	0.2660	0.1899	0.0636
ttγγ (nonallhad)	0.0244	0.0059	0.0015	0.1405	0.0287	0.0192	0.0074
γγ-jets	28.3552	6.7692	6.1004	83.9242	18.8519	14.9856	6.9235
data sideband	43	17	11	152	30	21	11

Table 6.4: Expected yields for the analysis categories with 140+59 fb^{-1} for HH signals, for different values of κ_λ, and combinations of (κ_λ, κ_{2V}, κ_V) for the ggF and VBF production modes, H and continuum backgrounds, and observed data in the sideband region.

In order to investigate the coupling modifier κ_λ through double Higgs production, the cross sections for the ggF HH and VBF HH production modes are expressed as continuous functions of κ_λ, resulting in a parametric model dependent on κ_λ (as well as κ_{2V} and κ_V). Specifically, the parametrization of the ggF cross section in a quadratic form dependent on κ_λ and κ_t (set equal to 1) takes the form (see Eq. (3.4))

$$c_1 + c_2\kappa_\lambda + c_3\kappa_\lambda^2 \ , \tag{6.4}$$

while the parametrization for VBF production is (see Eq. (3.6))

$$a_1\kappa_{2V}^2 + a_2\kappa_V^4 + a_3\kappa_\lambda^2\kappa_V^2 + a_4\kappa_{2V}\kappa_V^2 + a_5\kappa_{2V}\kappa_\lambda\kappa_V + a_6\kappa_\lambda\kappa_V^3 \ . \tag{6.5}$$

Building a parametric model with respect to the coupling modifiers requires understanding how the double Higgs signals behave as a function of κ_λ and κ_{2V} in each category. For ggF production, starting from the available Monte Carlo samples, simulated with $\kappa_\lambda = 0, 1, 5$, and the corresponding yields for each category (Table (6.4)), a system of linear equations (Eq. (6.4)) is solved to extract the coefficients c_i. For VBF production, in order to obtain the six coefficients a_i, the basis consists of six samples: the Standard Model sample and five additional samples corresponding to different combinations of κ_λ, κ_{2V}, and κ_V: (1,1,1), (1, 1.5, 1), (0, 1, 1), (10, 1, 1), (1, 3, 1), and (-5, 1, 0.5). Using the coefficients obtained through this procedure, the combined ggF and VBF yield for each category can be calculated as a linear combination of the basis yields ($\text{yield}_{comb.} = c_1 \cdot \text{yield}_{basis_1} + ...$) and subsequently used in the statistical model (Eq. (6.11)).

6.2 Signal and background modeling

The presence of a di-photon resonance in the final state dictates the choice of the final discriminant variable. The di-photon invariant mass, $m_{\gamma\gamma}$, is particularly effective at distinguishing the double Higgs signal from the dominant continuum background. The signal appears as a narrow peak around $m_H \approx 125$ GeV, while the background exhibits a smooth, decreasing distribution without any peak. Consequently, signal extraction involves modeling both the signal and background processes within the $m_{\gamma\gamma}$ spectrum for each defined category.

The $m_{\gamma\gamma}$ distributions for signal events and resonant backgrounds from single Higgs boson decays to $\gamma\gamma$ are described by double-sided Crystal Ball (DSCB) function:

$$f_{\text{DSCB}}(x) = N \cdot \begin{cases} A_{\text{Lo}} \cdot \left(B_{\text{Lo}} - \frac{x-\mu_{\text{CB}}}{\sigma_{\text{CB}}}\right)^{-n_{\text{Lo}}} & \text{for } \frac{x-\mu_{\text{CB}}}{\sigma_{\text{CB}}} > -\alpha_{\text{Lo}} \\ A_{\text{Hi}} \cdot \left(B_{\text{Hi}} + \frac{x-\mu_{\text{CB}}}{\sigma_{\text{CB}}}\right)^{-n_{\text{Hi}}} & \text{for } \frac{x-\mu_{\text{CB}}}{\sigma_{\text{CB}}} > \alpha_{\text{Hi}} \\ \exp\left(-\frac{(x-\mu_{\text{CB}})^2}{2\sigma_{\text{CB}}^2}\right) & \text{for } \alpha_{\text{Hi}} < \frac{x-\mu_{\text{CB}}}{\sigma_{\text{CB}}} < -\alpha_{\text{Lo}} \end{cases} \tag{6.6}$$

where $A_{\text{Lo}}, B_{\text{Lo}}, A_{\text{Hi}}$, and B_{Hi} are normalization constants defined as follows:

$$A_k = \left(\frac{n_k}{|\alpha_k|}\right)^{n_k} \cdot \exp\left(-\frac{\alpha_k^2}{2}\right) \tag{6.7}$$

$$B_k = \frac{n_k}{|\alpha_k|} - |\alpha_k| \ . \tag{6.8}$$

The Gaussian core of the DSCB distribution is characterized by its mean μ_{CB} and width σ_{CB}, while α_{Lo} and n_{Lo} (α_{Hi} and n_{Hi}) describe the low (high) energy tail. The α_k parameters indicate the points, measured in units of σ_{CB}, where the Gaussian core transitions into the power-law tails, with the tail exponents defined by the n_k parameters. The Gaussian core is useful for modeling the mass of well-reconstructed $H \to \gamma\gamma$ candidates, although tails can emerge due to experimental factors such as photon energy miscalibration. The shape parameters of the DSCB distributions are determined in each category by performing an unbinned fit on the SM ggF and VBF HH Monte Carlo samples in the $m_{\gamma\gamma}$ range $[115, 135]$ GeV[2], as depicted in Fig. (6.6) for the two first analysis categories (see more in Appendix D) of the two mass regions ('Low Mass 1', 'High Mass 1').

[2]This selected interval is slightly larger than the signal region to capture most events while avoiding small fluctuations, thereby improving fit stability and overall fit quality.

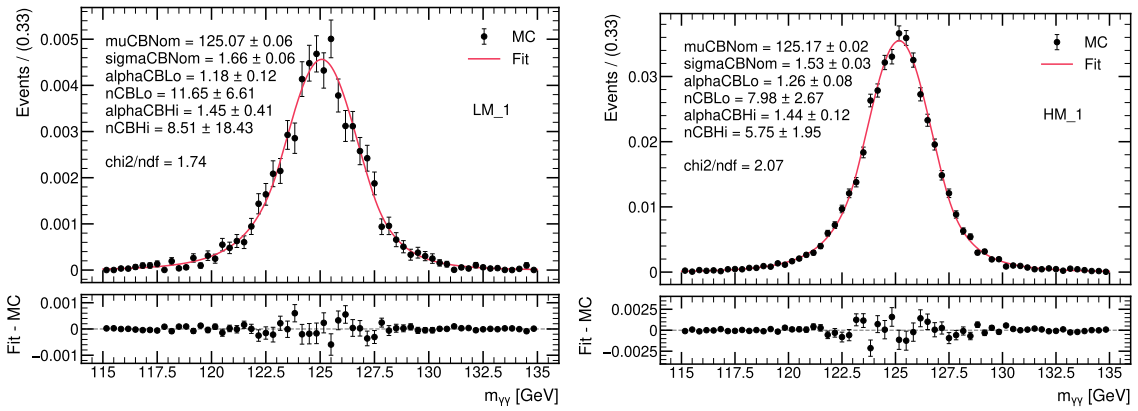

(a) (b)

Figure 6.6: Distributions of $m_{\gamma\gamma}$ for Standard Model ggF and VBF HH MC samples and for the first two (a) Low and (b) High mass categories. The double-sided Crystal Ball fit (red line) results are also present.

The $m_{\gamma\gamma}$ distributions for the continuum nonresonant diphoton background are modeled using exponential function, $exp(a \cdot m_{\gamma\gamma})$, with their normalization and shape parameters derived from data fits.
The exponential model accurately describes the data in the $m_{\gamma\gamma}$ sidebands, as well as the continuum background normalized to data in the $m_{\gamma\gamma}$ sidebands, and it is selected after the spurious signal studies carried out in the previous $b\bar{b}\gamma\gamma$ legacy analysis [103].
The potential bias from selecting a specific analytic function to model the continuum background is evaluated for each category. This bias is determined as the signal event yield extracted from a signal-plus-background fit to the background-only diphoton invariant mass distribution in the range 105 GeV $< m_{\gamma\gamma} <$ 160 GeV, commonly referred to as the *'spurious signal'* [187]. The number of fitted signal events is calculated for Higgs boson masses at 0.5 GeV intervals between 123 GeV and 127 GeV. The bias is defined as the maximum number of fitted spurious signal events within this 4 GeV mass window. Among the tested analytic functions, the exponential function is selected for having the fewest parameters and the lowest number of spurious signal events.

6.3 Systematic uncertainties

The sensitivity of the $HH \to b\bar{b}\gamma\gamma$ search is mainly constrained by statistical precision, which depends on to the amount of data collected by the ATLAS detector during Run-II. However, it is important to identify and evaluate each source of systematic uncertainty that could influence the final results.
Since certain analysis choices and strategies are still under investigation, including those related to systematics which involves the production of specific samples, the impact of these uncertainties on the statistical results has been approximately estimated by adopting the same values used in the legacy analysis. This approach is based on the assumption that the overall difference should not be significant, provided the same analysis strategy is maintained, including the same training variables, number of categories, signal modeling, and other relevant aspects.
The systematic uncertainties are categorized based on their source characteristics into two types: experimental and theoretical uncertainties.

Both experimental and theoretical systematic uncertainties are calculated separately for the ggF and VBF di-Higgs production modes and for the primarily single Higgs backgrounds.

6.3.1 Experimental systematic uncertainties

Experimental systematic uncertainties can affect either the yields of the double Higgs and single Higgs production processes in each category or their shape in the $m_{\gamma\gamma}$ spectrum.
This type of systematic uncertainties is related to the uncertainties of auxiliary measurements used to construct the model, as the dedicated measurements [62] of the total integrated luminosity collected by ATLAS during the Run-II and Run-III (a 0.83% and 2% associated uncertainty, respectively), or those related to the reconstruction of physics objects, and the impact of applying trigger requirements on events in the signal region.
Uncertainties associated to the diphoton system, such as vertex selection efficiency [188], trigger efficiency, photon energy scale and resolution, identification and isolation [89], are systematically evaluated using control samples from Z boson decays, photon+jet events, and J/ψ decays, and comparing data with simulation results, following the discussion presented in Section 2.3.2.
Jet energy scale and resolution uncertainties are determined using control samples of jets recoiling against well calibrated particles, such as photons [92] while uncertainties in the flavour-tagging efficiencies and misidentification rates are estimated by using $t\bar{t}$ and Z+jets events for $b-/c-$jets and light-flavour jets, respectively [102].

6.3.1.1 Yield uncertainties

The experimental systematic uncertainties affecting the event yields are evaluated using auxiliary MC samples, where systematic variations are applied upstream.
Asymmetric variations in category yields are obtained for each HH signal process or single Higgs production mode. The relative difference between these variations and the nominal results is quoted as the final systematic uncertainty.
For example, the upper ($+1\sigma$) and lower (-1σ) systematic uncertainties affecting the

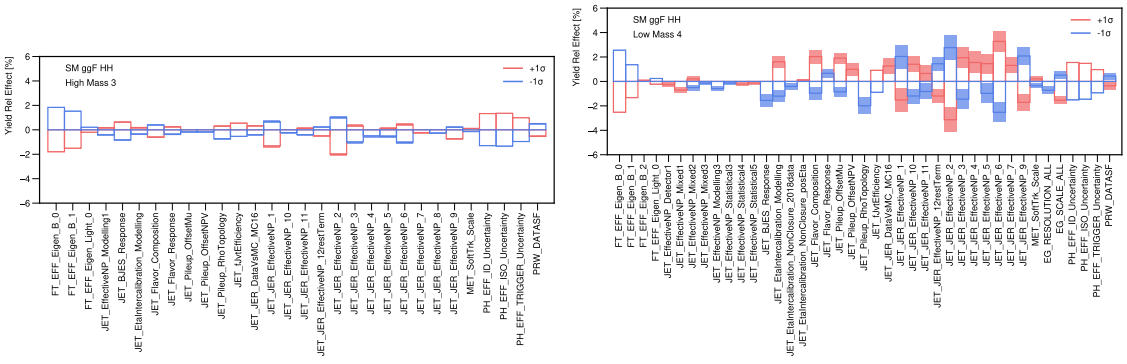

(a) High Mass 3 (b) Low Mass 4

Figure 6.7: $\pm 1\sigma$ experimental systematic uncertainties on expected yields for the High Mass ggF HH sample for the High Mass 3 (left) and Low Mass 4 (right) category. Only the significant and non-negligible contributions are shown. The shaded bands correspond to the statistical uncertainties of associated with the $\pm 1\sigma$ systematic uncertainties.

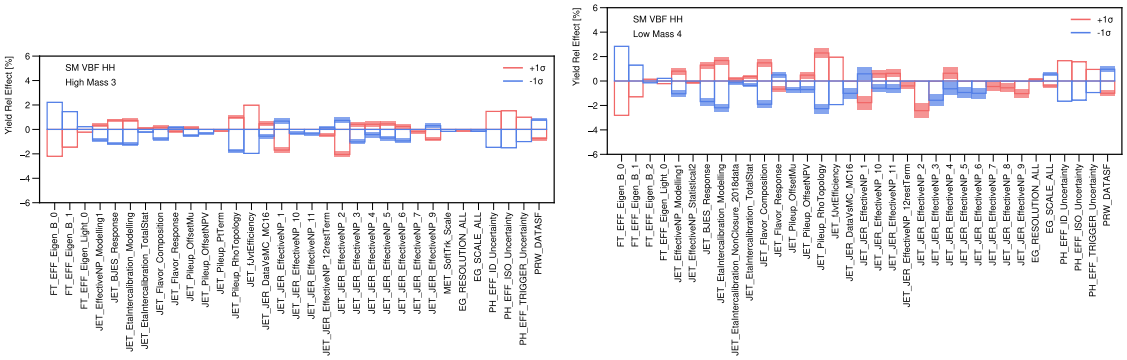

(a) High Mass 3 (b) Low Mass 4

Figure 6.8: $\pm 1\sigma$ experimental systematic uncertainties on expected yields for the High Mass VBF HH sample for the High Mass 3 (left) and Low Mass 4 (right) category. Only the significant and non-negligible contributions are shown. The shaded bands correspond to the statistical uncertainties of associated with the $\pm 1\sigma$ systematic uncertainties.

number of events for the i-th process in the c-th category are defined by

$$\delta N_c^i(\pm 1\sigma) = \frac{N_c^i(\pm 1\sigma)}{N_c^i} - 1 \ , \tag{6.9}$$

where N_c^i and $N_c^i(\pm 1\sigma)$ represent the nominal and varied yields, respectively.
Each systematic uncertainty has a statistical uncertainty, determined using the bootstrap method [189]. If a variation $\delta N_c^i(\pm 1\sigma)$ is smaller than 0.1%, it is deemed negligible, and its value is set to zero. It is considered to have no impact and then excluded from the statistical model.
Figures (6.7) and (6.8) show the experimental systematic uncertainties acting on yields for the High Mass ggF HH and High Mass VBF HH samples for the two most sensitive categories in the High mass region (High Mass 3) and Low mass region (Low Mass 4).
The experimental systematic uncertainties acting on yields were also evaluated for the ggF HH sample with $\kappa_\lambda = 10$, and for VBF HH samples with different Low Mass couplings, corresponding to $(\kappa_\lambda, \kappa_{2V}, \kappa_V) = (0, 1, 1), (10, 1, 1), (1, 1.5, 1), (1, 3, 1), (-5, 1, 0.5)$.

Syst. unc. on $m_{\gamma\gamma}$ peak position							
	High Mass 1	High Mass 2	High Mass 3	Low Mass 1	Low Mass 2	Low Mass 3	Low Mass 4
SM ggF HH	$^{+0.52}_{-0.52}$	$^{+0.52}_{-0.52}$	$^{+0.53}_{-0.53}$	$^{+0.45}_{-0.45}$	$^{+0.44}_{-0.44}$	$^{+0.45}_{-0.45}$	$^{+0.43}_{-0.45}$
SM VBF HH	$^{+0.55}_{-0.55}$	$^{+0.54}_{-0.55}$	$^{+0.55}_{-0.54}$	$^{+0.42}_{-0.43}$	$^{+0.44}_{-0.44}$	$^{+0.43}_{-0.45}$	$^{+0.44}_{-0.44}$
ggF H	$^{+0.54}_{-0.52}$	$^{+0.52}_{-0.56}$	$^{+0.52}_{-0.57}$	$^{+0.40}_{-0.41}$	$^{+0.48}_{-0.46}$	$^{+0.47}_{-0.38}$	$^{+0.36}_{-0.61}$
$t\bar{t}H$	$^{+0.52}_{-0.53}$	$^{+0.52}_{-0.52}$	$^{+0.52}_{-0.53}$	$^{+0.44}_{-0.44}$	$^{+0.44}_{-0.44}$	$^{+0.45}_{-0.45}$	$^{+0.44}_{-0.45}$
$qq \to ZH$	$^{+0.55}_{-0.55}$	$^{+0.56}_{-0.54}$	$^{+0.55}_{-0.55}$	$^{+0.44}_{-0.44}$	$^{+0.43}_{-0.44}$	$^{+0.46}_{-0.45}$	$^{+0.44}_{-0.43}$
$gg \to ZH$	$^{+0.51}_{-0.51}$	$^{+0.51}_{-0.51}$	$^{+0.53}_{-0.51}$	$^{+0.43}_{-0.43}$	$^{+0.47}_{-0.48}$	$^{+0.45}_{-0.35}$	$^{+0.28}_{-0.45}$

Table 6.5: Systematic uncertainties on $m_{\gamma\gamma}$ peak position (in %) extracted by applying the $\pm 1\sigma$ variations from the photon energy scale to the High Mass ggF HH and High Mass VBF HH signals and the ggH, ZH, and ttH production modes.

Syst. unc. on $m_{\gamma\gamma}$ peak width							
	High Mass 1	High Mass 2	High Mass 3	Low Mass 1	Low Mass 2	Low Mass 3	Low Mass 4
SM ggF HH	$^{+12.72}_{-9.60}$	$^{+14.00}_{-10.52}$	$^{+15.80}_{-10.71}$	$^{+10.21}_{-5.49}$	$^{+10.09}_{-9.03}$	$^{+13.12}_{-9.35}$	$^{+12.58}_{-9.40}$
SM VBF HH	$^{+12.04}_{-7.48}$	$^{+12.80}_{-8.57}$	$^{+14.02}_{-9.77}$	$^{+9.60}_{-7.04}$	$^{+8.13}_{-6.69}$	$^{+7.71}_{-11.69}$	$^{+9.99}_{-7.94}$
ggF H	$^{+18.91}_{-10.86}$	$^{+30.69}_{+0.00}$	$^{+12.32}_{-10.19}$	$^{+0.00}_{-5.42}$	$^{+0.00}_{+0.00}$	$^{+15.96}_{-29.42}$	$^{+0.00}_{+0.00}$
$t\bar{t}H$	$^{+14.42}_{-11.84}$	$^{+14.32}_{-12.94}$	$^{+16.24}_{-7.45}$	$^{+10.09}_{-7.89}$	$^{+8.80}_{-8.85}$	$^{+12.91}_{-5.81}$	$^{+11.88}_{-6.74}$
$qq \to ZH$	$^{+15.12}_{-10.59}$	$^{+16.00}_{-7.86}$	$^{+17.04}_{-11.17}$	$^{+9.36}_{-8.74}$	$^{+8.41}_{-5.12}$	$^{+11.11}_{-8.03}$	$^{+6.76}_{-7.12}$
$gg \to ZH$	$^{+14.04}_{-9.19}$	$^{+15.21}_{-11.48}$	$^{+16.80}_{-10.83}$	$^{+11.86}_{-10.40}$	$^{+12.92}_{-11.14}$	$^{+0.00}_{+0.00}$	$^{+0.00}_{+0.00}$

Table 6.6: Systematic uncertainties on $m_{\gamma\gamma}$ peak width (in %) extracted by applying the $\pm 1\sigma$ variations from the photon energy resolution to the High Mass ggF HH and High Mass VBF HH signals and the ggH, ZH, and ttH production modes.

6.3.1.2 Shape uncertainties

A procedure similar to that discussed for the yield uncertainties is applied to calculate the shape uncertainties for the mean μ_{CB} and width σ_{CB} of the Double-Sided Crystal Ball (DSCB) distributions (Eq. (6.6)) that model the $m_{\gamma\gamma}$ spectrum of resonant processes in different categories. These uncertainties arise from the photon energy scale and resolution. The impact of these two sources of systematic uncertainties are reported in Tables (6.5)-(6.6).

6.3.2 Theoretical systematic uncertainties

Theoretical uncertainties that impact the total expected yields of single Higgs boson and Higgs boson pair events and their contributions to each category, arise from several factors, such as missing higher-order terms in the perturbative expansion of the cross section, the PDF set, and the value of α_s. These uncertainties are assessed by considering different choices of factorization and renormalization scales, as well as alternative PDF sets and α_s values, and calculating the corresponding yields. The relative difference of the alternative yields with respect to the nominal value is then used to compute the corresponding theoretical uncertainty acting on the expected yields for the i-th process in the c-th category. The effect of the Scale and PDF $+ \alpha_S$ systematic uncertainties on the signal HH and main single Higgs processes are summarized in Tables (6.7), (6.8), and (6.9).

		ggF HH						
		High Mass 1	High Mass 2	High Mass 3	Low Mass 1	Low Mass 2	Low Mass 3	Low Mass 4
SM	QCD Scale	0.370	0.527	1.325	2.658	2.449	2.684	3.023
	PDF + α_S	0.509	0.471	0.449	1.318	1.308	1.347	1.395
$\kappa_\lambda = 0$	QCD Scale	0.291	0.975	1.738	2.629	2.116	2.145	2.677
	PDF + α_S	0.316	0.299	0.457	1.061	1.035	1.045	1.059
$\kappa_\lambda = 5$	QCD Scale	2.430	3.338	4.337	1.598	1.118	0.668	2.152
	PDF + α_S	0.873	0.950	1.371	0.508	0.479	0.482	0.479
$\kappa_\lambda = 10$	QCD Scale	1.39	1.11	1.21	0.94	0.87	0.87	0.32
	PDF + α_S	0.27	0.30	0.40	0.42	0.41	0.44	0.42
Envelope	QCD Scale	2.430	3.338	4.337	2.658	2.449	2.684	3.023
	PDF + α_S	0.873	0.950	1.371	1.318	1.308	1.347	1.395

Table 6.7: Systematic uncertainties on Scale and PDF $+ \alpha_S$ (in %) for the ggF HH signal, in the SM case and for different κ_λ values. The envelope across all the ggF HH samples is also quoted.

The impact of the Scale uncertainties on the signal SM ggF (VBF) HH sample is generally

		VBF HH						
		High Mass 1	High Mass 2	High Mass 3	Low Mass 1	Low Mass 2	Low Mass 3	Low Mass 4
SM	QCD Scale	0.992	0.690	1.567	5.125	4.675	3.989	1.534
	PDF + α_S	2.430	3.668	3.612	6.776	10.277	6.213	2.203
$\kappa_\lambda = 0$, $\kappa_{2V} = 1$, $\kappa_V = 1$	QCD Scale	0.365	0.058	2.042	4.089	3.365	2.980	0.819
	PDF + α_S	7.686	5.439	4.457	5.325	5.390	4.444	2.831
$\kappa_\lambda = 10$, $\kappa_{2V} = 1$, $\kappa_V = 1$	QCD Scale	0.318	0.705	2.727	2.862	2.875	2.561	0.202
	PDF + α_S	4.925	6.700	5.003	4.835	7.324	5.474	10.143
$\kappa_\lambda = 1$, $\kappa_{2V} = 1.5$, $\kappa_V = 1$	QCD Scale	3.414	2.657	0.614	7.951	7.899	7.770	4.491
	PDF + α_S	7.056	12.697	2.516	12.138	11.662	9.583	7.119
$\kappa_\lambda = 1$, $\kappa_{2V} = 3$, $\kappa_V = 1$	QCD Scale	3.161	2.567	0.578	7.349	7.095	7.094	4.218
	PDF + α_S	5.583	5.586	2.179	15.849	9.901	12.804	7.131
$\kappa_\lambda = -5$, $\kappa_{2V} = 1$, $\kappa_V = 0.5$	QCD Scale	1.008	0.643	2.299	7.720	7.453	7.547	4.908
	PDF + α_S	6.851	8.819	3.725	10.824	11.489	11.611	7.382
Envelope	QCD Scale	3.414	2.657	2.727	7.951	7.899	7.770	4.908
	PDF + α_S	7.686	12.697	5.003	15.849	11.662	12.804	10.143

Table 6.8: Systematic uncertainties on Scale and PDF + α_S (in %) for the VBF HH signal, in the SM case and for different BSM (κ_λ, κ_{2V}, κ_V) points. The envelope across all the VBF HH samples is also quoted.

		Single Higgs						
		High Mass 1	High Mass 2	High Mass 3	Low Mass 1	Low Mass 2	Low Mass 3	Low Mass 4
ggF	Scale	8.892	8.780	8.963	4.975	4.625	6.368	7.476
	PDF + α_S	2.026	2.116	2.106	1.613	1.907	1.823	1.846
VBF	Scale	1.560	2.562	2.336	3.117	3.878	4.714	2.772
	PDF + α_S	3.608	4.575	3.729	3.025	3.778	3.675	4.072

Table 6.9: Systematic uncertainties on Scale and PDF + α_S (in %) for the single Higgs production for ggF and VBF production mode.

below 3% (up to 5%) in all categories. The combined PDF+α_S is always less than 2% (of the order of 10% depending on the category and the (κ_λ, κ_{2V}, κ_V) configuration) for signal ggF (VBF) HH, in all categories and for all κ_λ.
The Scale and PDF+α_S uncertainties that affect the di-Higgs cross sections, as shown in Eq. (3.5), are included.
Uncertainties in the branching ratios of $H \to \gamma\gamma$ ($^{+2.90\%}_{-2.84\%}$), assigned to all the HH and H processes, and of $H \to b\bar{b}$ ($^{+1.70\%}_{-1.73\%}$), assigned to the ggF and VBF HH processes, are also included [119].
Additionally, the uncertainty affecting the expected yields related to the choice of parton shower model is evaluated by comparing the predictions of the nominal simulation using Pythia 8 with those from an alternative simulation where the same generator-level events are showered with Herwig v7.1.6 [190].

	Parton shower uncertainties						
	High Mass 1	High Mass 2	High Mass 3	Low Mass 1	Low Mass 2	Low Mass 3	Low Mass 4
SM ggF HH	2.119	-	−4.454	6.845	–	–	–
ggF HH $\kappa_\lambda = 10$	–	-	−8.260	–	–	−4.743	−7.973
SM VBF HH	–	-	−9.943	–	–	–	–
VBF HH $\kappa_\lambda = 10$, $\kappa_{2V} = 1$, $\kappa_V = 1$	−10.131	-	−5.940	–	–	–	−10.652
VBF HH $\kappa_\lambda = 1$, $\kappa_{2V} = 0$, $\kappa_V = 1$	7.269	-	−6.232	–	–	−15.516	−6.591
$qq \to ZH$	–	-	–	–	12.816	37.705	31.423
ttH	−3.217	-	–	−2.690	−6.757	–	–

Table 6.10: Systematic uncertainties on parton shower (in %) affecting the expected yields for the signal HH samples and the main single Higgs backgrounds. Only the significant contributions are quoted.

Table (6.10) shows the parton shower uncertainties for the available ggF HH samples (with either $\kappa_\lambda = 1$ or $\kappa_\lambda = 10$), for the available VBF HH samples, corresponding to the cou-

pling values $(\kappa_\lambda, \kappa_{2V}, \kappa_V) = (1,1,1), (1,0,1), (10,1,1)$, and for the $qq \to ZH$ and ttH backgrounds.
A further uncertainty is applied to the the yields of single Higgs boson ggF, VBF and WH production modes, based on studies of heavy-flavour production in association with top-quark pairs [191] and W boson production with $b-$jets [192].
Finally, Table (6.11) summarizes the results for the spurious signal, the sole source of systematic uncertainty associated with the continuum background, which is included as an additional uncertainty in the expected HH yield.

Category	Function	N_{sp}	max(N_{sp}/σ_{bkg}) [%]	Prob(χ^2) [%]
High Mass 3	Exponential	0.491	33.4	1.25
High Mass 2	Exponential	-0.511	-40.5	40.2
High Mass 1	Exponential	-0.707	-27	12
Low Mass 4	Exponential	0.168	16	63.7
Low Mass 3	Exponential	-0.179	-10.4	1.98
Low Mass 2	Exponential	-0.66	-24.2	9.54
Low Mass 1	Exponential	-1.04	-20.3	5.46

Table 6.11: Spurious signal results using the $\gamma\gamma$+jets template. For the exponential function and each category, the spurious signal N_{sp}, the N_{sp} relative to the expected background uncertainty (with and without 2σ deviations in the MC template), and the χ^2 probability from a background only fit (using MC statistical errors) are shown.

As reference, the impacts of the systematic uncertainties, that are typically quantified by propagating the uncertainty through the entire analysis and then expressed as the relative difference between the nominal and varied results, on the expected 95% Confidence Level upper limit on μ_{HH} and on the expected allowed κ_λ 95% CL range determined with the statistical interpretation described in the next section, that remains the same of the legacy analysis, are summarized in Tables (6.12)-(6.13).

Systematic uncertainty source	Type	**Relative impact [%]**
Experimental		
Photon energy resolution	Norm.+Shape	0.4
Photon energy scale	Norm+Shape	0.1
Jet energy scale and resolution	Normalization	0.1
Flavour tagging	Normalization	0.1
Theoretical		
Factorisation and renormalisation scale	Normalization	4.8
$\mathcal{B}(H \to \gamma\gamma, bb)$	Normalization	0.2
PDF set and α_S value	Normalization	0.1
Parton showering model	Normalization	0.2
Heavy-flavour content	Normalization	0.1
Background model (spurious signal)	Normalization	0.1

Table 6.12: Breakdown of the main systematic uncertainties in the expected μ_{HH} limit at 95% CL. Only systematic uncertainties with an impact of 0.1% or greater are included. Uncertainties of the "Norm. + Shape" type affect both the normalization and the parameters of the functional form. The rest of the uncertainties affect only the yields.

Systematic uncertainty source	Type	**Relative impact [%]**
Experimental		
Photon energy resolution	Norm.+Shape	0.3
Photon energy scale	Norm+Shape	0.02
Jet energy scale and resolution	Normalization	0.2
Flavour tagging	Normalization	0.1
Theoretical		
Factorisation and renormalisation scale	Normalization	1.2
$\mathcal{B}(H \to \gamma\gamma, bb)$	Normalization	0.1
PDF set and α_S value	Normalization	0.05
Parton showering model	Normalization	0.2
Heavy-flavour content	Normalization	0.2
Background model (spurious signal)	Normalization	0.1

Table 6.13: Breakdown of the main systematic uncertainties in the expected allowed κ_λ 95% CL range. Uncertainties of the "Norm. + Shape" type affect both the normalization and the parameters of the functional form. The rest of the uncertainties affect only the yields.

6.4 Statistical model and results

The results of the $HH \to b\bar{b}\gamma\gamma$ search are obtained via an unbinned maximum likelihood fit on the diphoton invariant mass distribution $m_{\gamma\gamma}$ in the window $105 < m_{\gamma\gamma} < 160$ GeV, excluding the blinded signal region ($120 < m_{\gamma\gamma} < 130$ GeV), performed simultaneously over all the analysis categories. The likelihood function is defined as:

$$\mathcal{L} = \prod_c \left(\text{Pois}(n_c | N_c(\boldsymbol{\theta})) \cdot \prod_{i=1}^{n_c} f_c(m^i_{\gamma\gamma}, \boldsymbol{\theta}) \cdot G(\boldsymbol{\theta}) \right) . \tag{6.10}$$

For each event i in a category c, n_c and N_c are the observed and the expected number of events, f_c is the value of the probability density function in the $m_{\gamma\gamma}$ spectrum, $\boldsymbol{\theta}$ are nuisance parameters (NPs), and $G(\boldsymbol{\theta})$ are constraint probability density functions for the nuisance parameters. The observed number of events n_c is modeled by a Poisson distribution with expectation value equal to $N_c(\boldsymbol{\theta})$, which is calculated as the sum of the expected event yields from the di-Higgs and single Higgs processes, the continuum $\gamma\gamma$ background, plus the contribution from the spurious signal (SS):

$$N_c(\boldsymbol{\theta}) = \mu \cdot N_{\text{c}}^{HH}(\boldsymbol{\theta}^{HH}_{\text{yield}}, \kappa_\lambda, \kappa_{2V}) + N_{\text{c}}^{\text{H}}(\boldsymbol{\theta}^{\text{H}}_{\text{yield}}) + N_{\text{c}}^{\text{SS}} \cdot \boldsymbol{\theta}_{\text{c}}^{\text{SS}} + N_{\text{c}}^{\gamma\gamma} . \tag{6.11}$$

As outlined in the previous section, the expected event yields of the HH and H processes are affected by various sources of systematic uncertainties, that are included in the statistical model via the nuisance parameters $\boldsymbol{\theta}$.
In the first term in Eq. (6.11) the signal strength μ is present, that depends on the coupling modifiers κ_λ, κ_{2V} affecting the expected HH yields. These quantities are the Parameters of Interests (POI) in the statistical model.
The probability density function f_c provides the shape information, represented by the sum of the signal and resonant background double-sided Crystal Ball functions and the continuum background exponential function.
The profile likelihood ratio test statistic [182] utilized for measuring the parameters of

interest, the signal strength μ or κ_λ and κ_{2V}, is given by:

$$\Lambda(\mu) = \frac{\mathcal{L}(\mu, \hat{\hat{\boldsymbol{\theta}}}(\mu))}{\mathcal{L}(\hat{\mu}, \hat{\boldsymbol{\theta}})} \ . \tag{6.12}$$

In this equation, μ is the general parameter of interest and $\boldsymbol{\theta}$ denotes always the nuisance parameters. In the denominator, the POI and NPs are set to the values $\hat{\mu}$ and $\hat{\boldsymbol{\theta}}$, which jointly maximize the likelihood, while in the numerator, the nuisance parameters are set to the values $\hat{\hat{\boldsymbol{\theta}}}$ which maximizes the likelihood for a fixed value of μ.
In absence of signal, upper limits on the signal strength μ and on the di-Higgs production cross-section at 95% CL are set, using the CL_s method [193] and the profile-likelihood-ratio test statistic $\tilde{q}_\mu$, defined as:

$$\tilde{q}_\mu = \begin{cases} -2\ln\frac{\Lambda(\mu,\hat{\hat{\boldsymbol{\theta}}}(\mu))}{\Lambda(0,\hat{\hat{\boldsymbol{\theta}}}(0))} & \hat{\mu} < 0, \\ -2\ln\frac{\Lambda(\mu,\hat{\hat{\boldsymbol{\theta}}}(\mu))}{\Lambda(\hat{\mu},\hat{\boldsymbol{\theta}}(\mu))} & 0 \le \hat{\mu} \le \mu, \\ 0 & \hat{\mu} > \mu. \end{cases} \tag{6.13}$$

The asymptotic approximation [182] is used for the test-statistic distribution.
The expected results are derived by performing the statistical analysis on Asimov datasets [182].

	Upper limits				
	-2σ	-1σ	Expected	$+1\sigma$	$+2\sigma$
di-Higgs signal strength	2.12	2.85	3.96	6.08	9.81

Table 6.14: Expected 95% CL upper limits on the di-Higgs signal strength $\mu^{HH}_{\text{ggF+VBF}}$.

Under the assumption of no di-Higgs production (the background-only Asimov dataset is generated using the model of Eq. (6.10) with $\mu = 0$), a 95% CL upper limit of 3.96 on the total HH production signal strength $\mu^{ggF+VBF}_{HH}$ is established. The expected limit with its $\pm1\sigma$ and $\pm2\sigma$ error bands is quoted in Table (6.14).

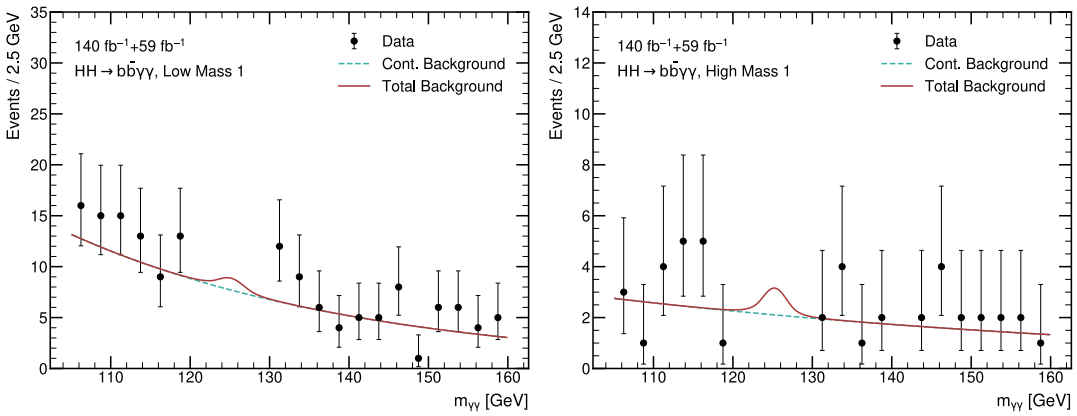

(a) (b)

Figure 6.9: Comparison between the distribution of $m_{\gamma\gamma}$ in data (points with error bars) sideband and the background-only fit (solid line), where the peak near 125 GeV is due to single Higgs production, for events in 'Low Mass 1' (a) and 'High Mass 1' (b) regions.

As an example, Figures (6.9) show the result of a background-only fit to the data sideband for the two 'Low Mass 1' and 'High Mass 1' analysis categories (see more in Appendix D). Evaluating the profile log-likelihood ratio $-2\ln(\Lambda)$ as a function of the coupling strength factor κ_λ, assuming SM HH production ($\mu_{HH} = 1$) and all other coupling modifiers equal to their SM predictions, allows to extract the corresponding 68% and 95% confidence intervals, as presented in Figures (6.10). In this case, the parametric model, i.e. the signals are parameterized in terms of the coupling parameters (Eq. (6.4)-(6.5)), is considered.

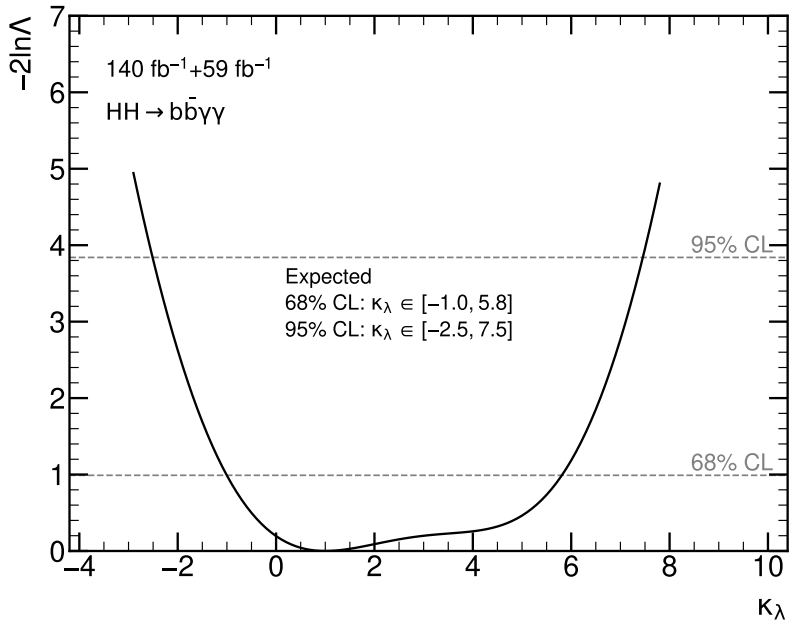

Figure 6.10: Expected value of $-2\ln(\Lambda)$ varying with (a) κ_λ. All other coupling modifiers are fixed to 1.

This analysis, which incorporates the systematic uncertainties discussed in Sect. 6.3, is performed after a statistics-only analysis (see Appendix E). The inclusion of systematics has a minor impact on the results, leading to a 7% increase in the upper limit on the signal strength and a widening of 3% (1.5%) in the 95% (68%) CL confidence intervals for the coupling modifiers, compared to cases where systematic uncertainties are neglected, as summarized in Table (6.15). This variation in the results is consistent with what was observed in the legacy analysis, confirming the validity of this approximate treatment of systematic uncertainties.

	Limit on μ	Allowed κ_λ 95% range	Length of κ_λ range	Allowed κ_λ 68% range	Length of κ_λ range
Stat-only	3.70[3]	[-2.4, 7.3]	9.7	[-0.9, 5.8]	6.7
Full-syst	3.96	[-2.5, 7.5]	10.0	[-1.0, 5.8]	6.8
Rel. Diff [%]	-7.0		-3.1		-1.5

Table 6.15: Expected upper limit on the di-Higgs signal strength (μ) and allowed κ_λ 95%-68% confidence intervals. The relative difference between the expected results emphasizes the impact of the systematics on the results.

[3]The corresponding error bands are: $+1\sigma : 5.44$, $-1\sigma : 2.66$ and $+2\sigma : 8.05$, $-2\sigma : 1.98$.

Conclusions

In this thesis, a search for Standard Model Higgs boson pair production in the $b\bar{b}\gamma\gamma$ channel is presented. The analysis uses the full Run-II pp collision dataset, corresponding to an integrated luminosity of 140 fb^{-1} at a center-of-mass energy of 13 TeV, recorded by the ATLAS experiment between 2015 and 2018, and partial Run-III data collected in 2022–2023 at 13.6 TeV, corresponding to 59 fb^{-1}. Since the $b\bar{b}\gamma\gamma$ group is targeting a combined Run-II and partial Run-III publication for mid-2025, the analysis is currently blinded, and only expected results are presented in this thesis. The statistical results are interpreted in terms of the expected upper limits on the signal strength and an exclusion interval for the trilinear Higgs boson self-coupling modifier $\kappa_\lambda = \lambda_{HHH}/\lambda^{SM}_{HHH}$. A 95% confidence level (CL) expected upper limit of 3.96 is set on the $HH \to b\bar{b}\gamma\gamma$ signal strength, assuming no di-Higgs production. Furthermore, a 95% (68%) CL expected allowed range for κ_λ is found to be $[-2.5, 7.5]$ ($[-1.0, 5.8]$), assuming SM HH production.
A direct comparison with the blinded results from the legacy analysis using the full Run-II dataset, which set a 95% CL upper limit of 5.21 on the signal strength and a 95% (68%) CI for κ_λ of $[-2.8, 7.7]$ ($[-1.2, 5.9]$), demonstrates a significant improvement. This improvement is largely due to the increased statistical power provided by the additional partial Run-III data. Additionally, as Run-III offers unique opportunities for HH searches, particularly with the full Run-III dataset, several aspects of the analysis have been explored to maximize the potential for an initial observation of HH production. Notable improvements are obtained and expected in the reconstruction, identification, and calibration of physics objects, as well as in the technical approaches across various stages of the analysis workflow. At the time of this thesis, the final analysis strategy is still being defined.
Among the improvements related to the $H \to b\bar{b}$ component of the channel, which already benefits from the use of a new b-tagging algorithm (GN2) compared to the full Run-II analysis, the Kinematic Fit technique, developed and implemented as part of this thesis, plays a significant role as an additional correction to the current b-jet calibration. This tool, by minimizing a per-event negative log-likelihood function, balances the HH system in the transverse plane and improves the invariant mass resolution of the $H \to b\bar{b}$ component, which typically suffers from a precision of about 15%, by leveraging the precise reconstruction of the $H \to \gamma\gamma$ component. After extensive testing and optimization, the Kinematic Fit improves the $m_{b\bar{b}}$ resolution (evaluated by fitting the distribution with a Bukin function) by approximately 13%, specifically on a Monte Carlo sample of SM ggF HH signal, relative to the current b-jet correction used in the analysis. This improvement is crucial, as the invariant mass of the two b-jets is the most discriminating variable among the inputs to the Boosted Decision Tree (BDT) used for separating signal from background, and ultimately for extracting the results on parameters of interest.
Furthermore, to improve the four-object reduced invariant mass distribution, $m^*_{b\bar{b}\gamma\gamma}$, which is used for event selection and in the BDT, and to bring it closer to its true value, the

Kinematic Fit is run independently a second time for each event, with a different configuration of constraints included in the likelihood function. In this case, the improvement in the resolution of the distribution constructed from the difference between the reconstructed $m^*_{b\bar{b}\gamma\gamma}$ and the true $m^*_{b\bar{b}\gamma\gamma}$ (fitted by a Double-Sided Crystal Ball function) is approximately 27% over the current b-jet calibration.

Finally, although the Kinematic Fit has been extensively studied and tested, ongoing exploration of its properties suggests that further improvements in its functionality and effectiveness may be possible, especially by leveraging the potential of the full Run-III dataset.

Appendix A

Bukin Distribution

Originally known as Novosibirsk A distribution, the Bukin distribution is a highly complex function able to fit a wide variety of asymmetric bell shaped curves and in this work it is largely used to characterize the variable of interest $m_{b\bar{b}}$ and in this way evaluate the performance of the Kinematic Fit Tool (Section 5).
Given its parameters (the peak position X_p, the peak width σ, the peak asymmetry χ, the left and right tails ρ_1 and ρ_2), the quantity r_2 is first evaluated in different ways depending on the side of the curve relative to the peak.

Left side:

$if\ x < \ x_1\ \&\&\ |\chi| > e^{-6}$:

$$r_2 = \frac{\rho_1(x-x_1)^2}{(X_{peak}-x_1)^2} - \log(2) + \sqrt{2\log(2)}\frac{x-x_1}{\sigma}\frac{\chi}{\log\left(\sqrt{\chi^2+1}+\chi\right)}... \\ ...\frac{\sqrt{\chi^2+1}}{\log\left(\sqrt{\chi^2+1}-\chi\right)}$$

$if\ x < \ x_1\ \&\&\ else$:

$$r_2 = \frac{\rho_1(x-x_1)^2}{(X_{peak}-x_1)^2} - \log(2) + \sqrt{2\log(2)}\frac{x-x_1}{\sigma}\frac{\sqrt{\chi^2+1}}{\log\left(\sqrt{\chi^2+1}-\chi\right)}$$

Centre:

$if\ \ x_1 \leq x < x_2\ \ \&\&\ \ |\chi| > e^{-6}$:

$$r_2 = -\log(2)\left(\frac{\log\left[1+4\cdot\chi\cdot\sqrt{\chi^2+1}\frac{(x-X_{peak})}{2\sigma\sqrt{2\log(2)}}\right]}{\log\left[1+2\cdot\chi\cdot(\chi-\sqrt{\chi^2+1})\right]}\right)^2$$

$if\ \ x < x_2\ \ \&\&\ \ else$:

$$r_2 = -\frac{(x-X_{peak})^2}{2\sigma^2}$$

Right side:

$if\ \ x \geq x_2\ \ \&\&\ \ |\chi| > e^{-6}$:

$$r_2 = \frac{\rho_2(x-x_2)^2}{(X_{peak}-x_2)^2} - \log(2) + \sqrt{2\log(2)}\frac{x-x_2}{\sigma}\frac{\chi}{\log\left(\sqrt{\chi^2+1}+\chi\right)}... \\ ...\frac{\sqrt{\chi^2+1}}{\log\left(\sqrt{\chi^2+1}-\chi\right)}$$

$if \quad x \geq x_2 \quad \&\& \quad else:$

$$r_2 = \frac{\rho_2(x - x_2)^2}{(X_{peak} - x_2)^2} - \log(2) + \sqrt{2\log(2)}\frac{x - x_2}{\sigma}\frac{\sqrt{\chi^2 + 1}}{\log\left(\sqrt{\chi^2 + 1} - \chi\right)}$$

where:

$$x_1 = X_{peak} + \sigma\sqrt{2\log(2)}\Big(\frac{\chi}{\sqrt{\chi^2 + 1}} - 1\Big)$$

and:

$$x_2 = X_{peak} + \sigma\sqrt{2\log(2)}\Big(\frac{\chi}{\sqrt{\chi^2 + 1}} + 1\Big)$$

Ultimately, the resulting function is expressed as:

$$Bukin(X_{peak}, \chi, \rho_1, \rho_2, \sigma) = e^{r_2} \tag{A.1}$$

It is clear from the condition-based nature of the function definition that its derivatives will most likely be discontinuous and consequently the function will not be analytical.

Appendix B

Kinematic Fit - Final Result Plots

In this Appendix, the plots of the distributions $m_{b\bar{b}}$ and $m^{*,Reco}_{b\bar{b}\gamma\gamma} - m^{*,True}_{b\bar{b}\gamma\gamma}$ obtained using the final Kinematic Fit configuration are presented for both the non-inclusive case of events with additional jets, Fig. (B.1)-(B.3), and the inclusive case, Fig. (B.2)-(B.4).

B.1 $m_{b\bar{b}}$ distributions

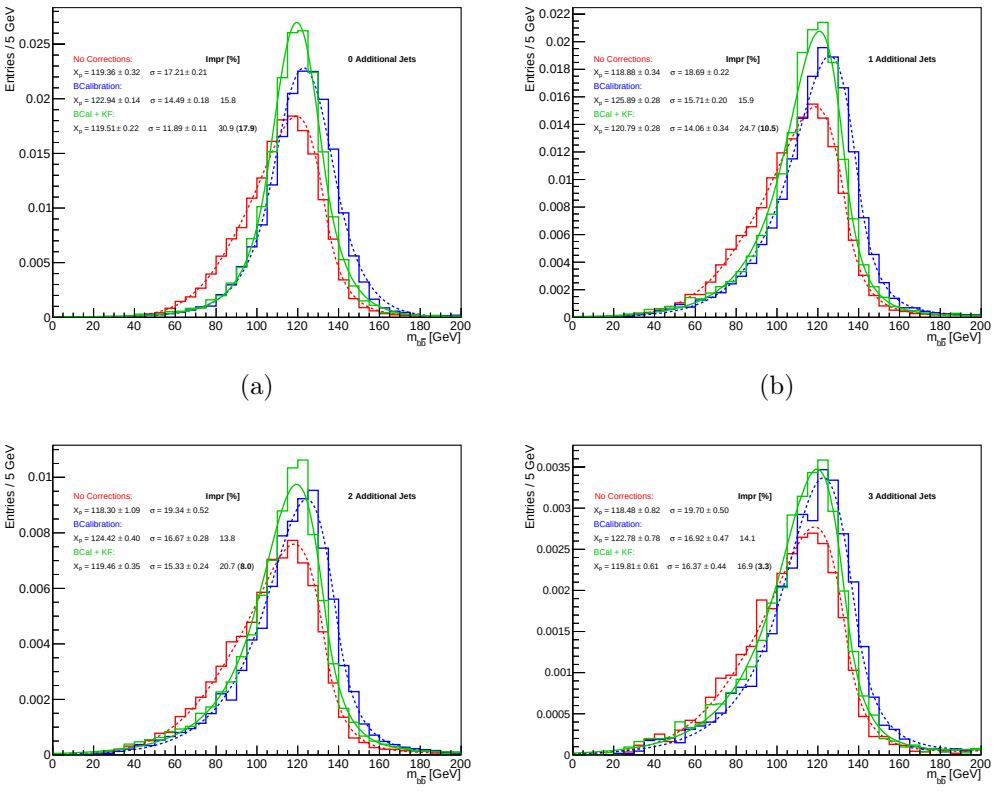

(a) (b)

(c) (d)

Figure B.1: Di-jet invariant mass plot in Run-III easyjet framework for events with 0 (a), 1 (b), 2 (c) or 3 (c) additional jets: red line indicates the nominal correction case, blue and green lines the BCal correction and the Kinematic Fit ones, respectively. Best-fit parameters: Roofit MLE method.

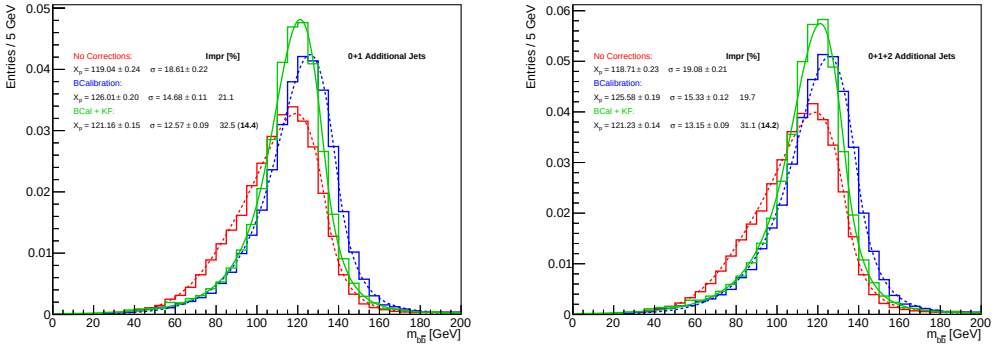

(a) (b)

Figure B.2: Di-jet invariant mass plot in Run-III easyjet framework for events with 0+1 (a) and 0+1+2 additional jets: red line indicates the nominal correction case, blue and green lines the BCal correction and the Kinematic Fit ones, respectively. Best-fit parameters: Roofit MLE method.

B.2 $m^{*,\ Reco}_{b\bar{b}\gamma\gamma} - m^{*,\ True}_{b\bar{b}\gamma\gamma}$ distributions

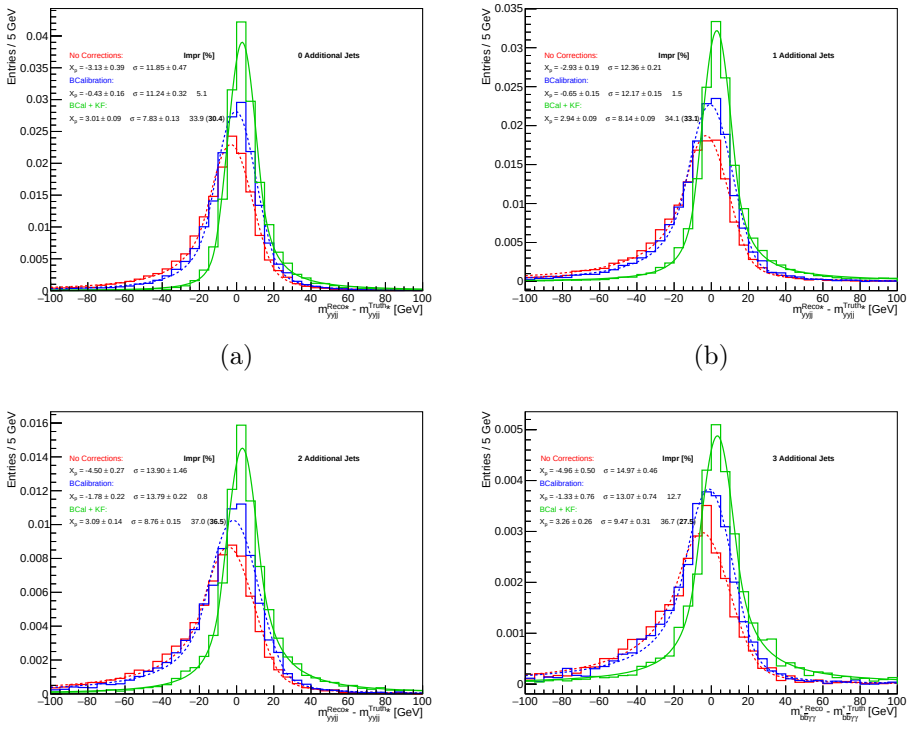

(a) (b)

(c) (d)

Figure B.3: Plot of the difference between $m^{*,Reco}_{b\bar{b}\gamma\gamma}$ and $m^{*,True}_{b\bar{b}\gamma\gamma}$ in Run-III easyjet framework for events with 0 (a), 1 (b), 2 (c) or 3 (c) additional jets: red line indicates the nominal correction case, blue and green lines the BCal correction and the Kinematic Fit ones, respectively. Best-fit parameters: Roofit MLE method.

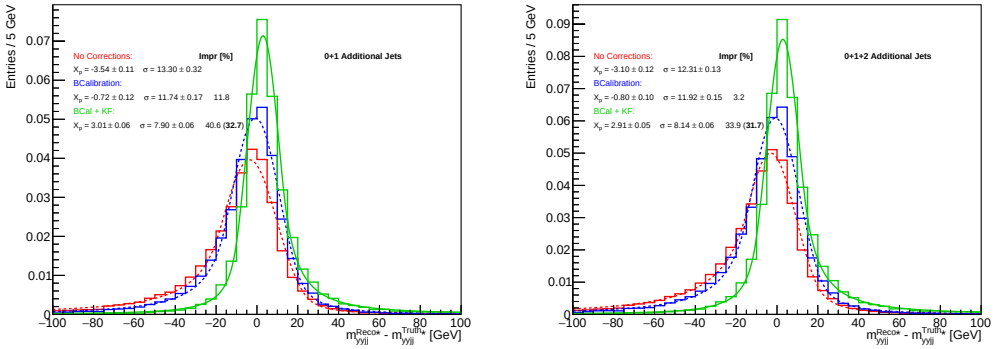

(a) (b)

Figure B.4: Plot of the difference between $m^{*,Reco}_{b\bar{b}\gamma\gamma}$ and $m^{*,True}_{b\bar{b}\gamma\gamma}$ in Run-III easyjet framework for events with 0+1 (a) and 0+1+2 (b) additional jets: red line indicates the nominal correction case, blue and green lines the BCal correction and the Kinematic Fit ones, respectively. Best-fit parameters: Roofit MLE method.

Appendix C

BDT Input Variables

In this Appendix, the distributions of the input variables for the High Mass and Low Mass BDTs in the $HH \to b\bar{b}\gamma\gamma$ analysis are presented.
The following convention is used for defining the training variables:

- All physics objects are rotated in the (x, y) plane such that the ϕ angle of the leading photon is always set to zero (i.e., the leading photon is always aligned along the x-axis in the transverse plane). Consequently, the ϕ variable of all physics objects in an event is calculated relative to the azimuthal direction of the leading photon.

A comparison between data in the sideband region and MC simulation distributions is also provided.
The histograms are normalized to unit area (except for the fourth jet pcbt), and the simulation distributions are shown unstacked.

C.1 High Mass Region

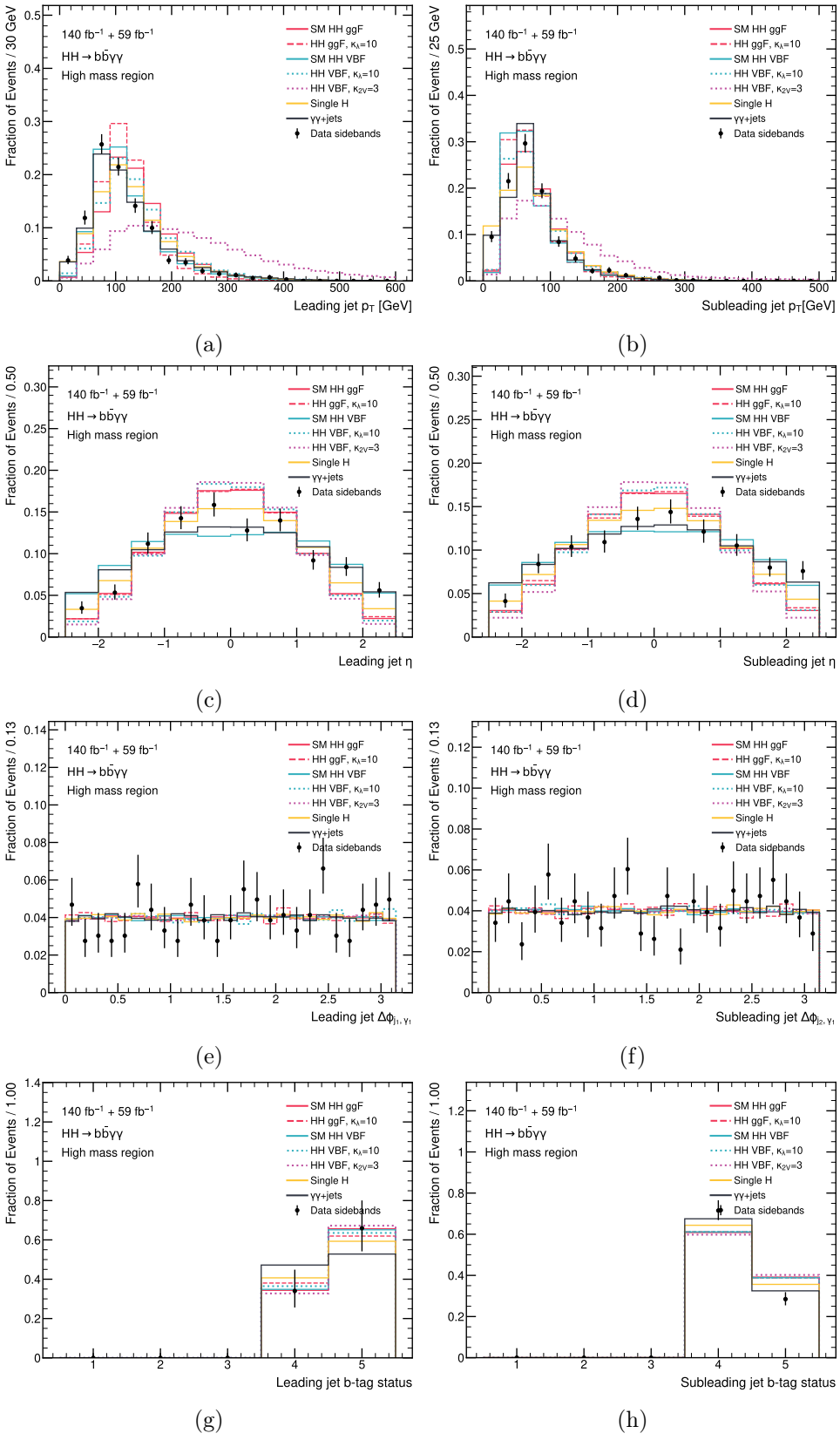

Figure C.1: Kinematic distributions for leading and subleading jets.

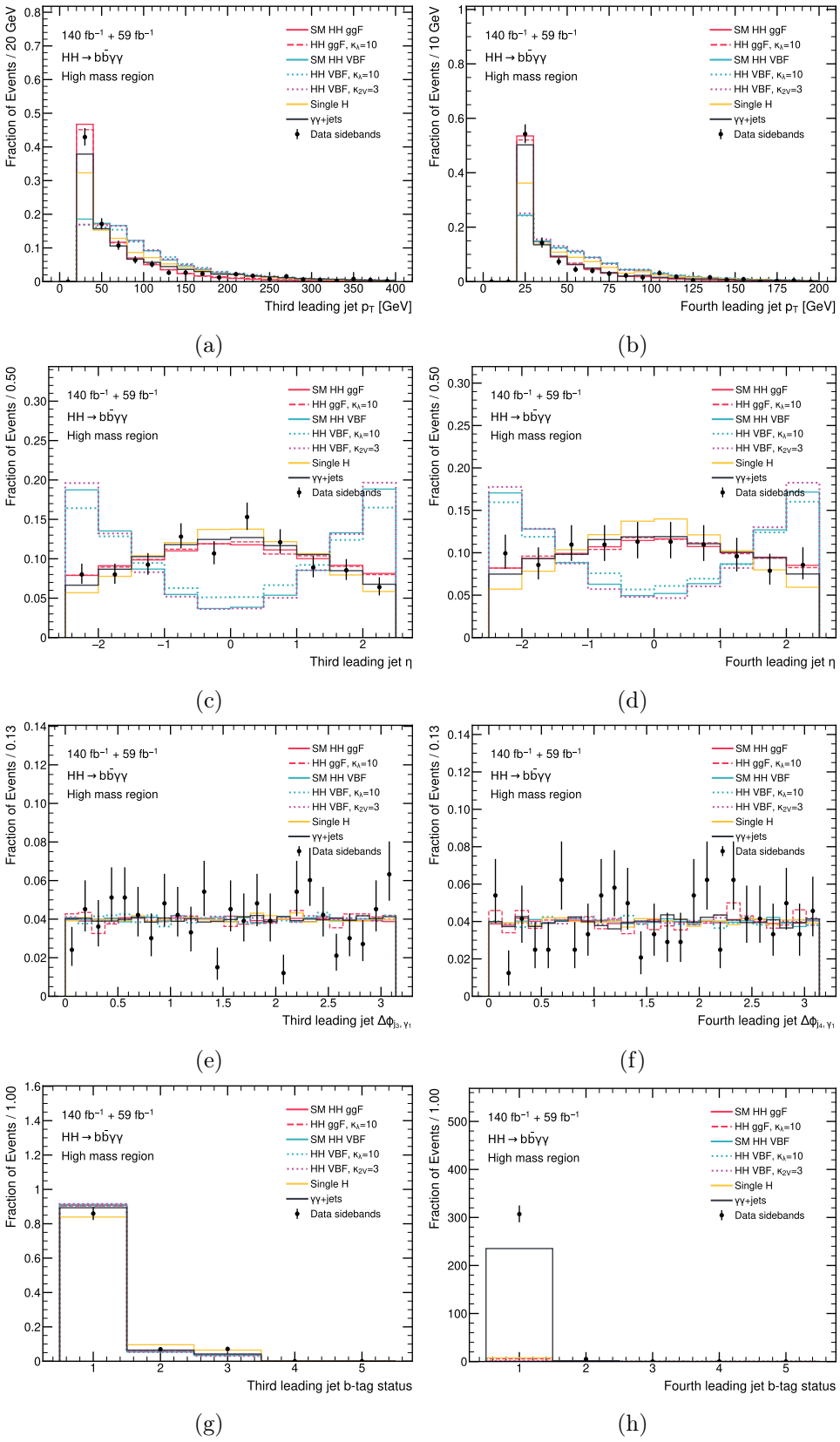

Figure C.2: Kinematic distributions for the third and fourth jets. The fourth jet pcbt histogram is not normalized in order to more clearly illustrate the signal-background differences.

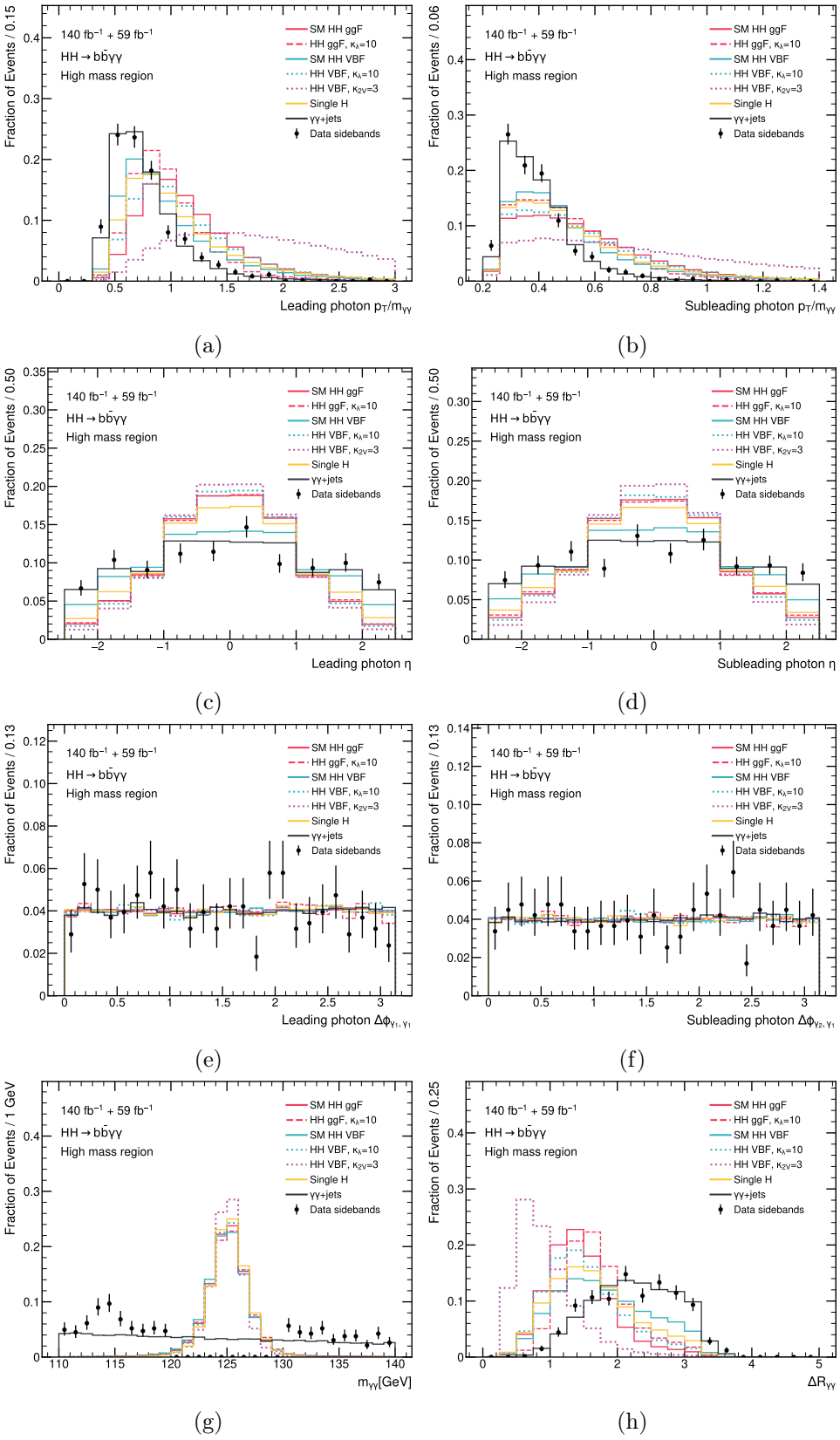

Figure C.3: Kinematic distributions of the $H \to \gamma\gamma$ system.

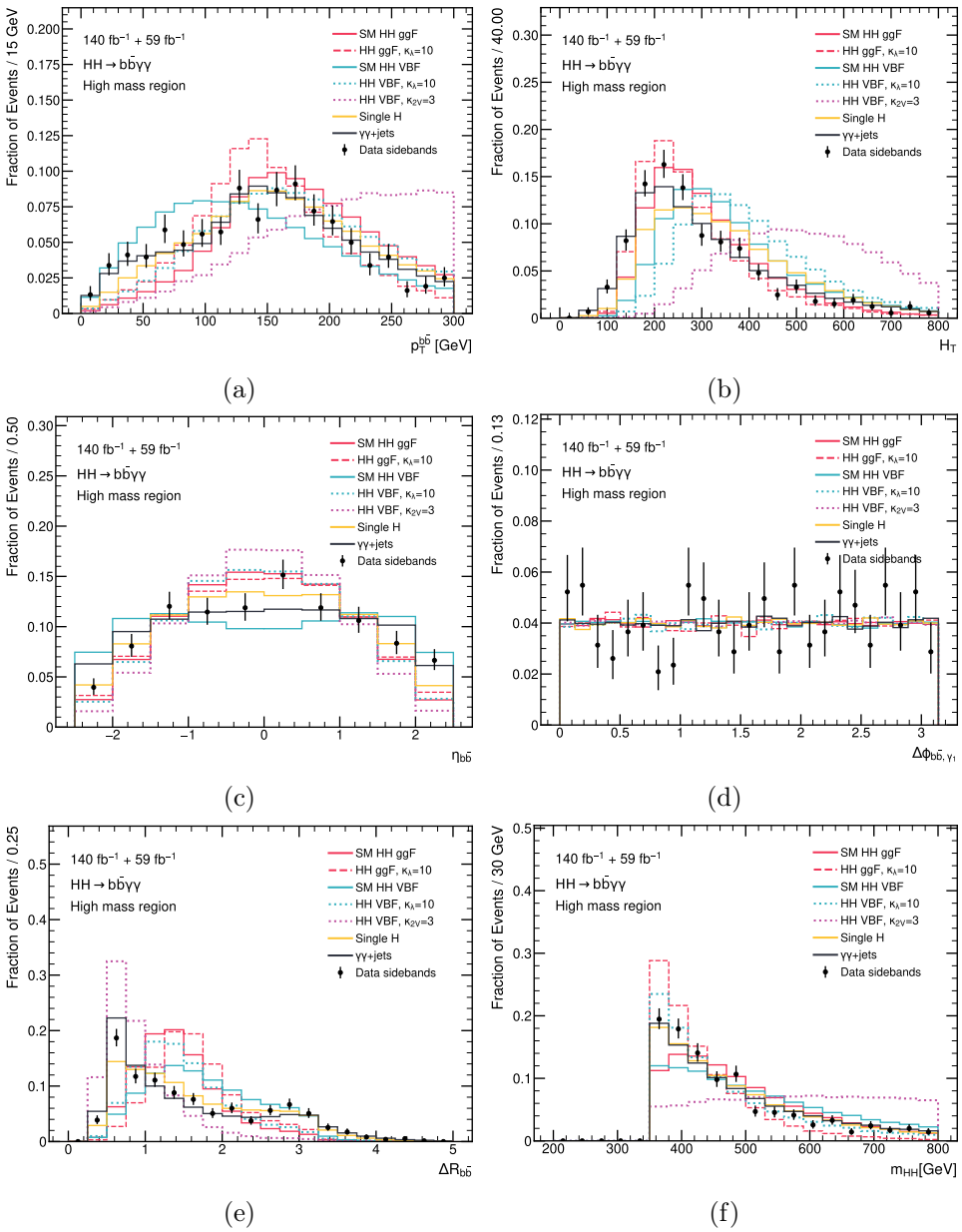

Figure C.4: Kinematic distributions of the $H \to b\bar{b}$ system and $m^{*}_{b\bar{b}\gamma\gamma}$.

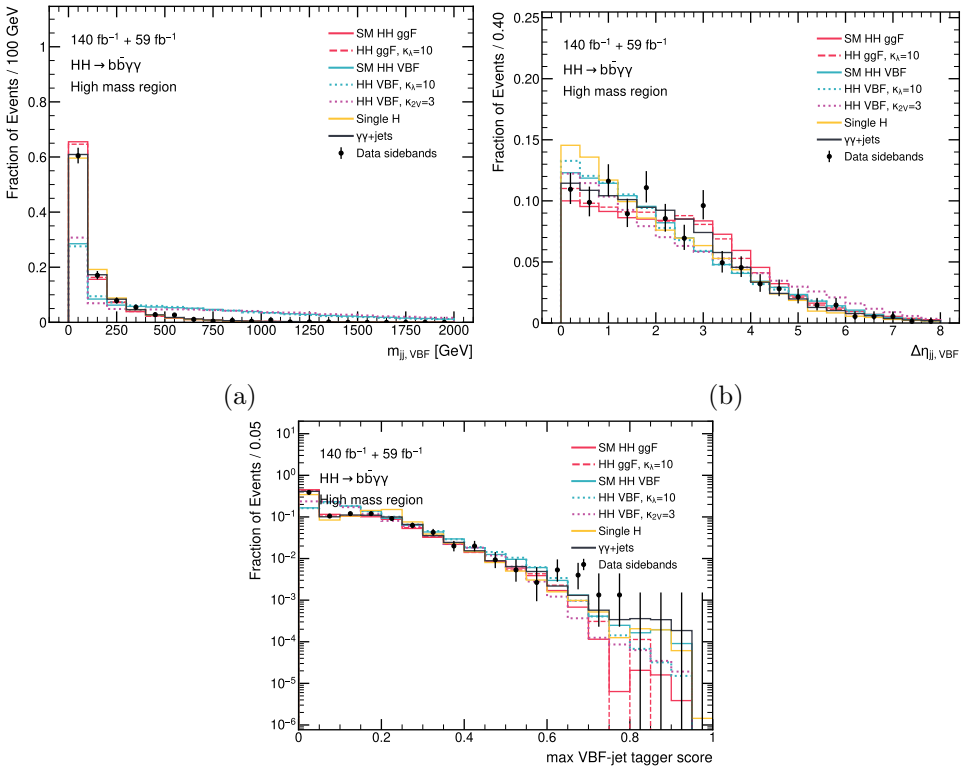

(a) (b)

(c)

Figure C.5: Kinematic distributions of the VBF system.

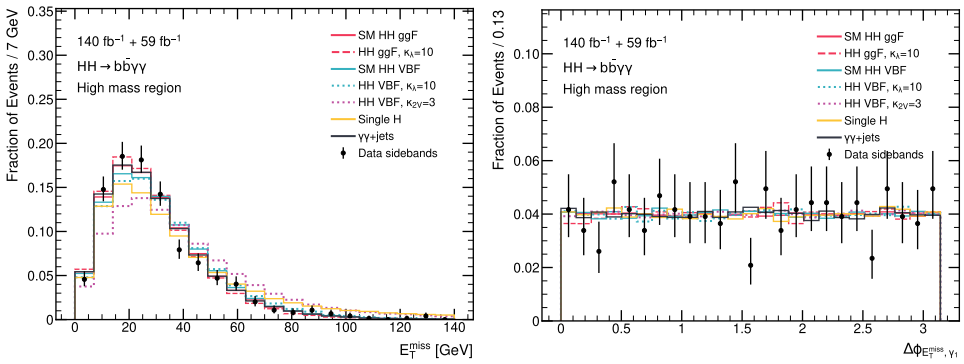

(a) (b)

Figure C.6: Distributions related to the Missing Transverse Energy variables.

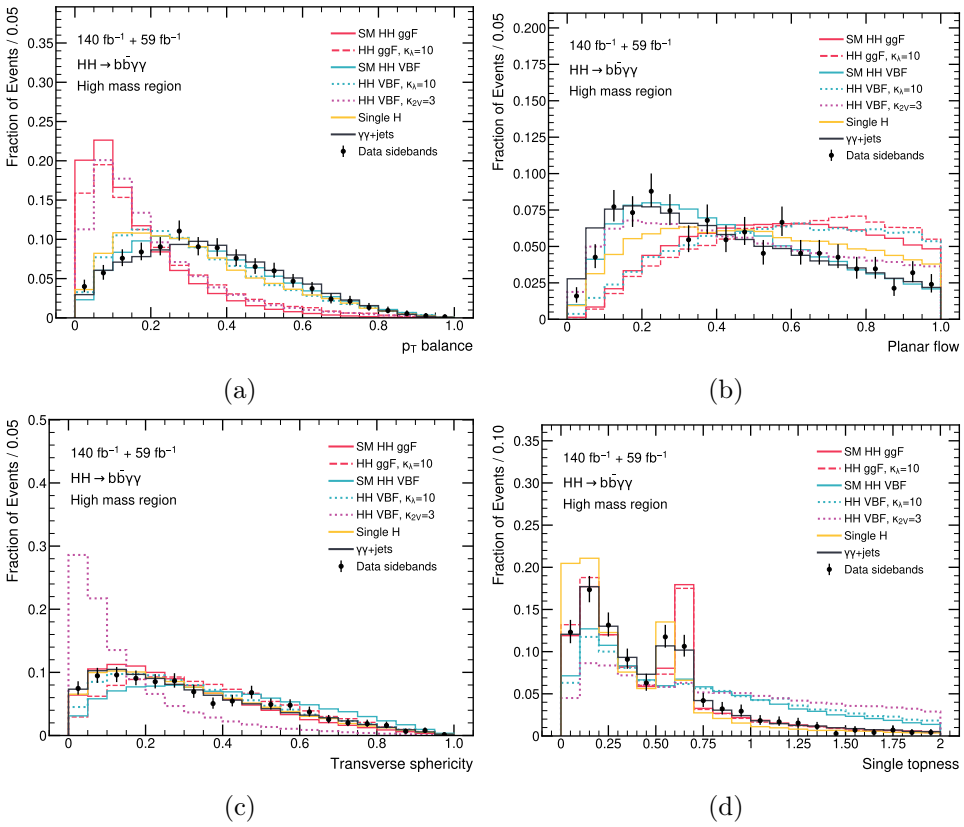

Figure C.7: Distributions of three event-shape observables and the single topness.

C.2 Low Mass Region

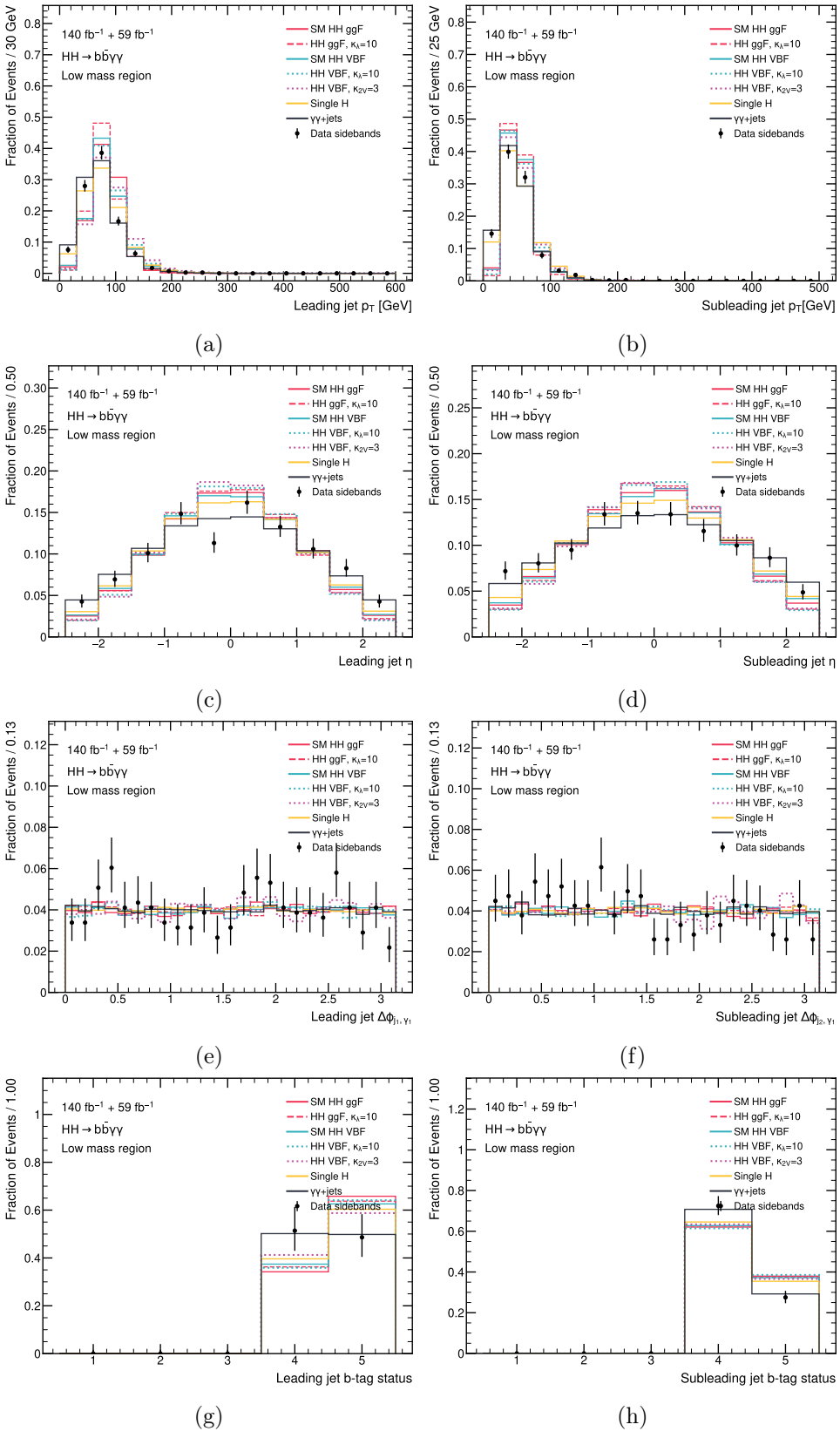

Figure C.8: Kinematic distributions for leading and subleading jets.

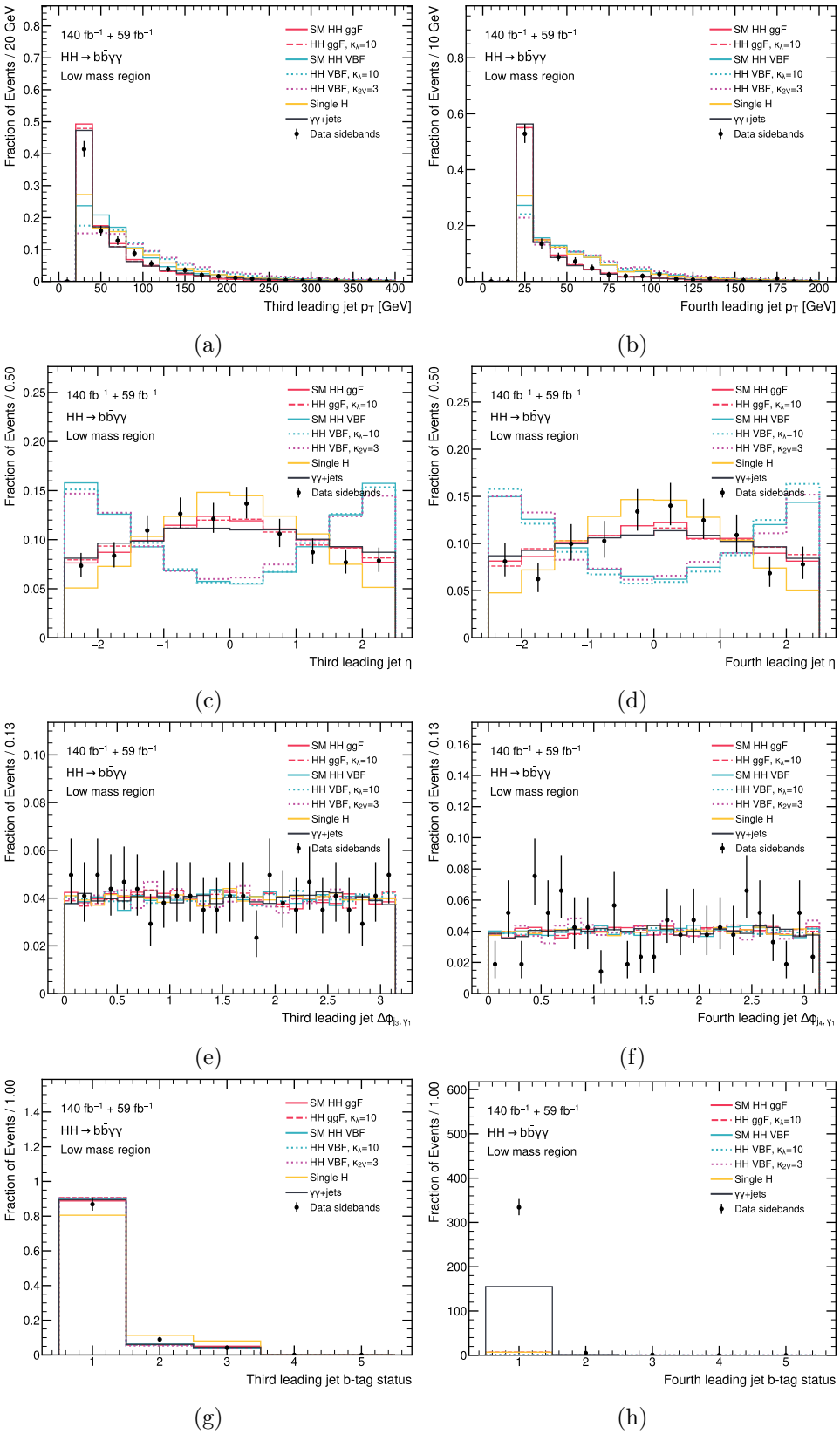

Figure C.9: Kinematic distributions for the third and fourth jets. The fourth jet pcbt histogram is not normalized in order to more clearly illustrate the signal-background differences.

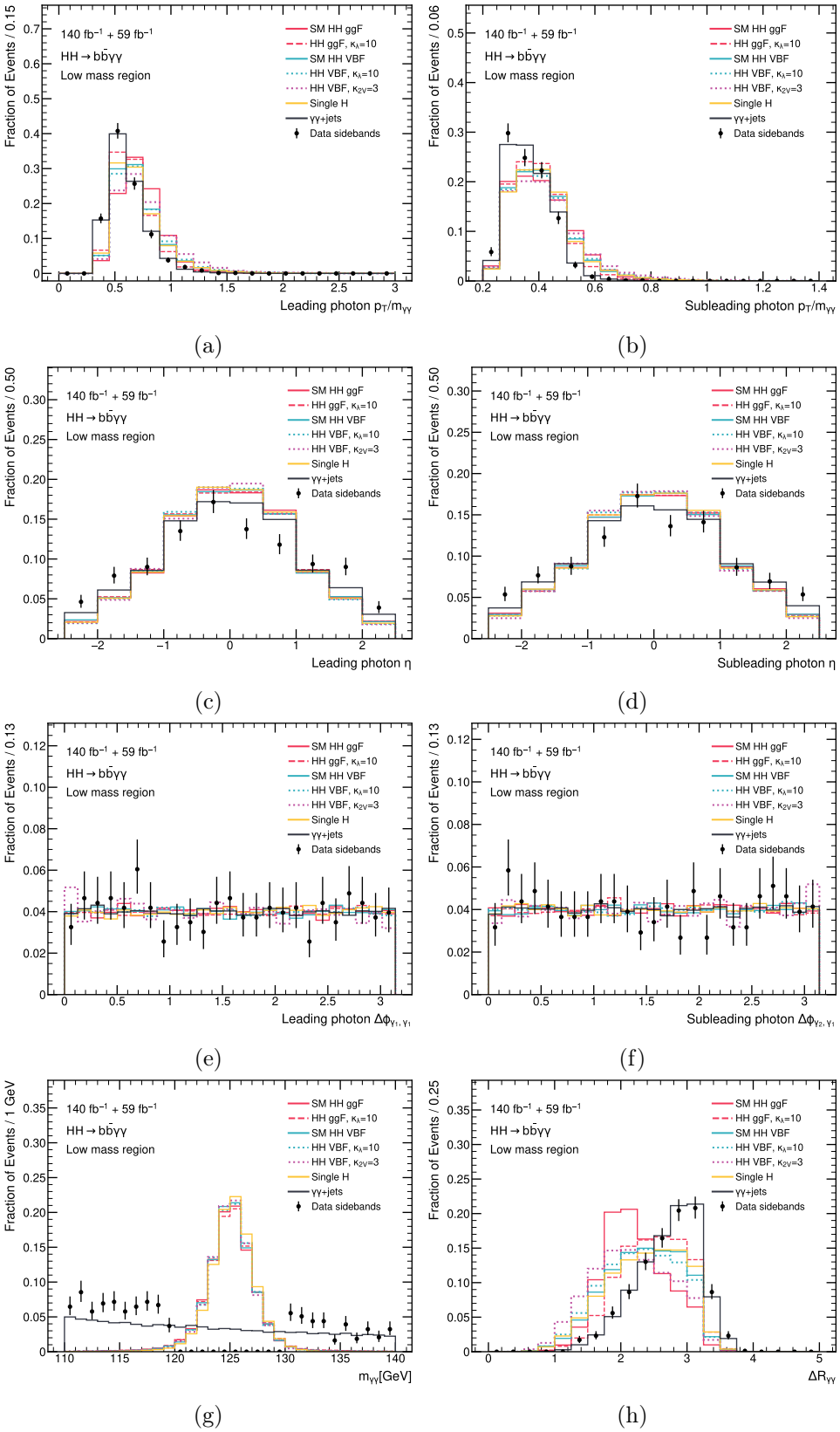

Figure C.10: Kinematic distributions of the $H \to \gamma\gamma$ system.

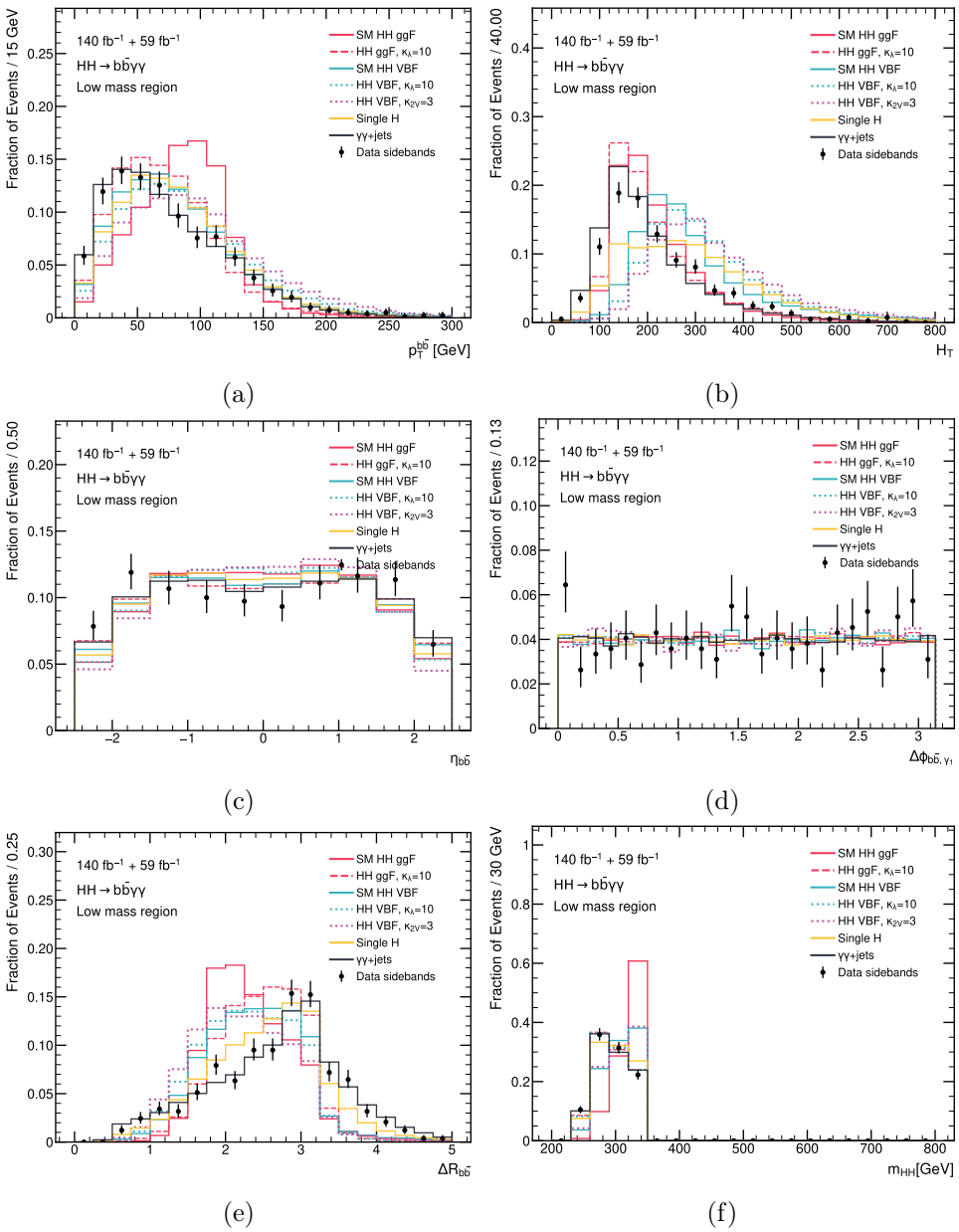

Figure C.11: Kinematic distributions of the $H \to b\bar{b}$ system and $m^*_{b\bar{b}\gamma\gamma}$.

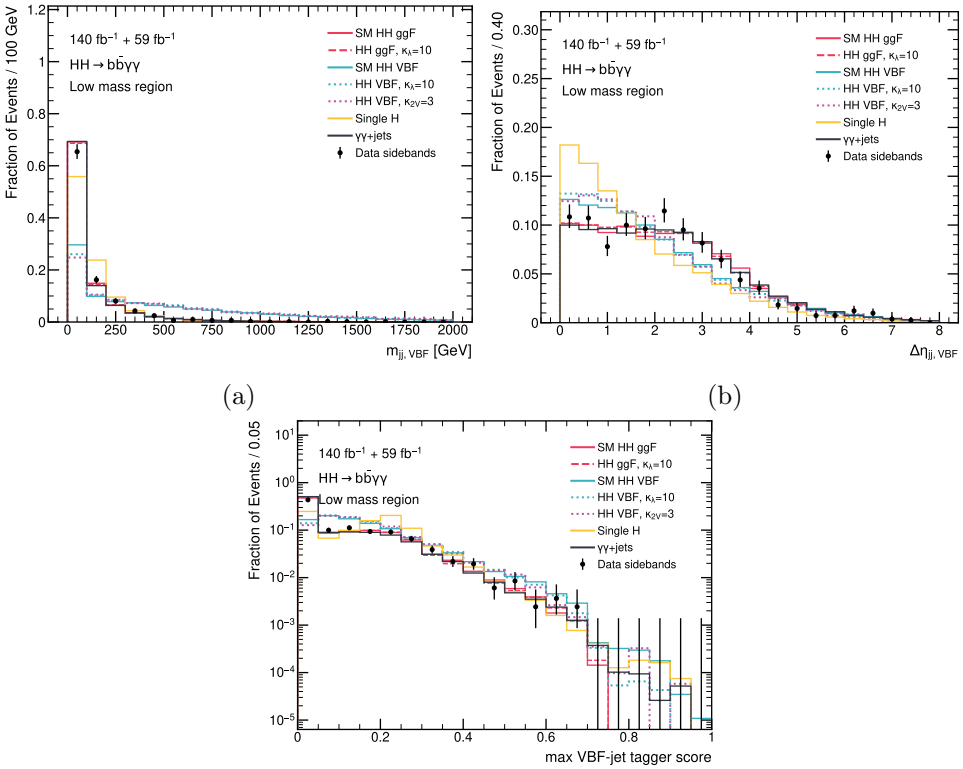

(a) (b)

(c)

Figure C.12: Kinematic distributions of the VBF system.

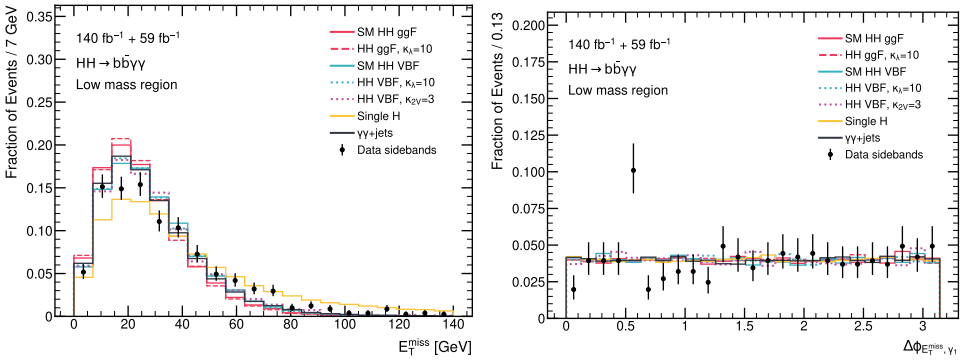

(a) (b)

Figure C.13: Distributions related to the Missing Transverse Energy variables.

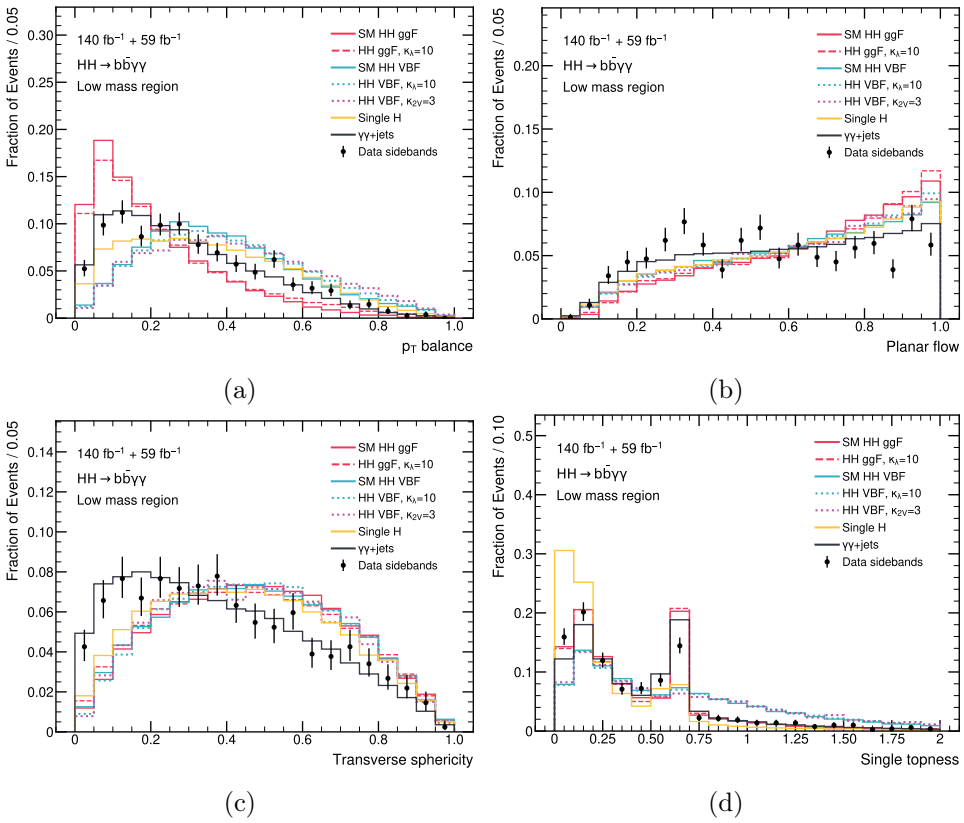

Figure C.14: Distributions of three event-shape observables and the single topness.

Appendix D

Analysis Fit Plots

In this appendix, the plots for the remaining event categories of the analysis of two fitting procedures used in the workflow are presented: the resonant signal-background modeling with the DSCB function, and the background-only fit to the data sideband. These fits are shown in the corresponding Sections 6.2-6.4 only for the first two analysis categories in the High and Low mass regions (Fig. (6.6)-(6.9)).

D.1 Signal and resonant background modelling

High Mass region

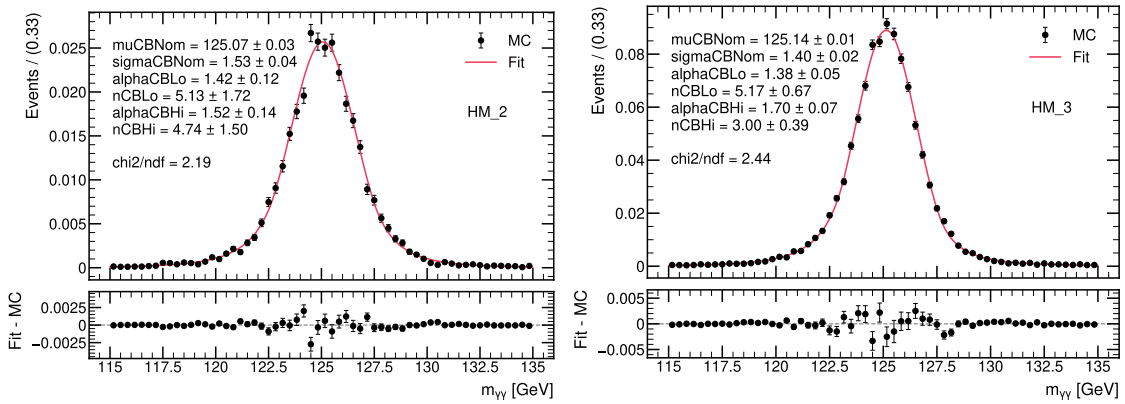

(a) (b)

Figure D.1: Distributions of $m_{\gamma\gamma}$ for Standard Model ggF and VBF HH MC samples and for the High Mass categories. The Double-Sided Crystal Ball fit (red line) results are present.

Low Mass region

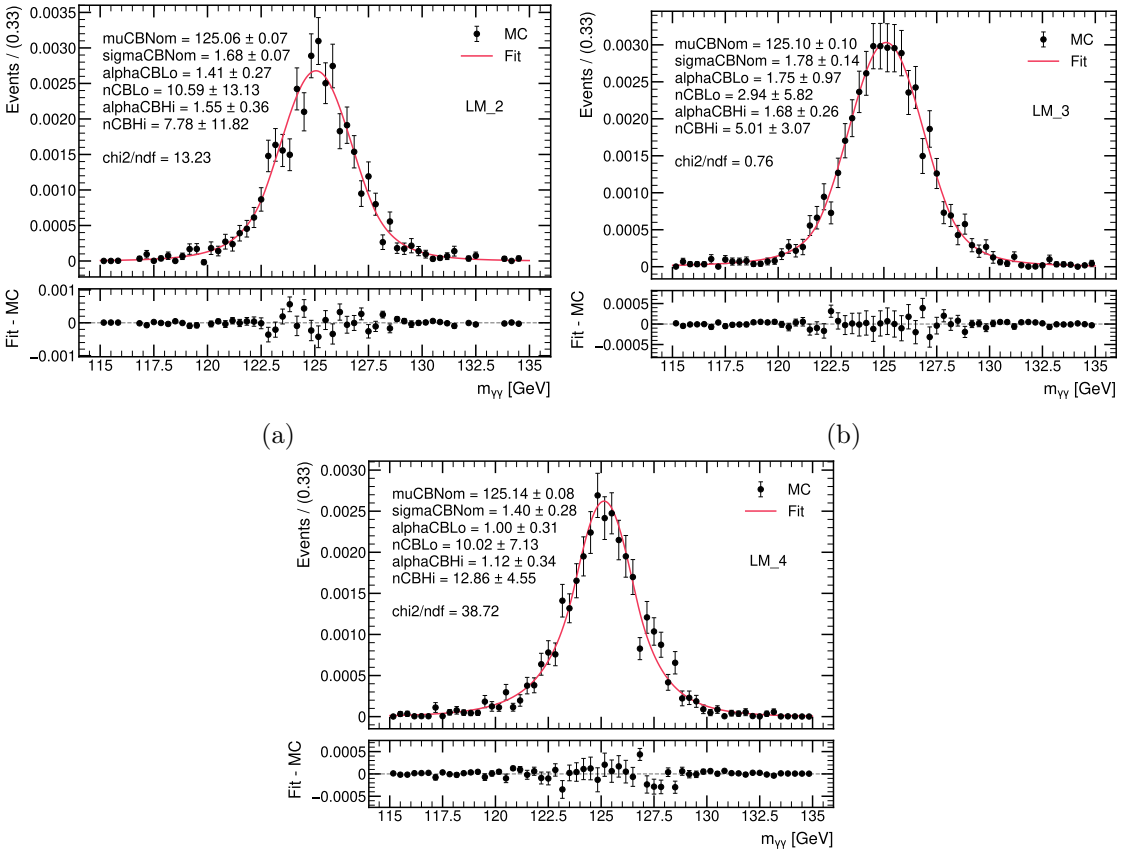

Figure D.2: Distributions of $m_{\gamma\gamma}$ for Standard Model ggF and VBF HH MC samples and for the Low Mass categories. The DSCB fit (red line) results are present.

D.2 Background-only fit to the data sideband

High Mass region

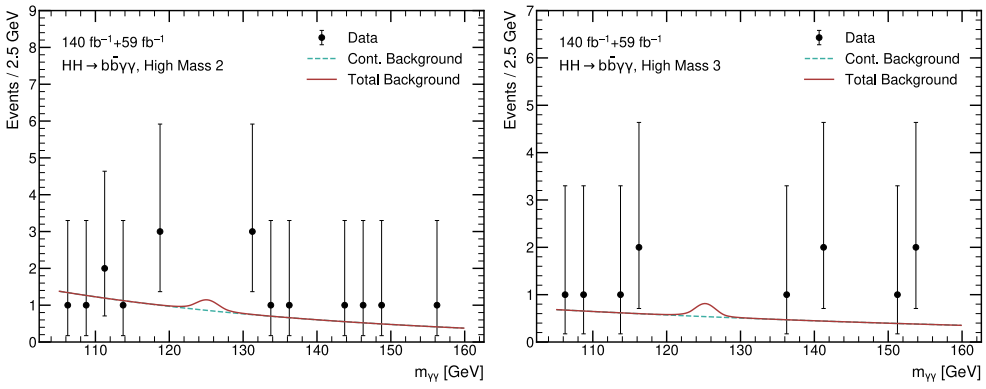

Figure D.3: Comparison between the distribution of $m_{\gamma\gamma}$ in data (points with error bars) sideband and the background-only fit (solid line), where the peak near 125 GeV is due to single Higgs production, for events in High Mass region categories.

Low Mass region

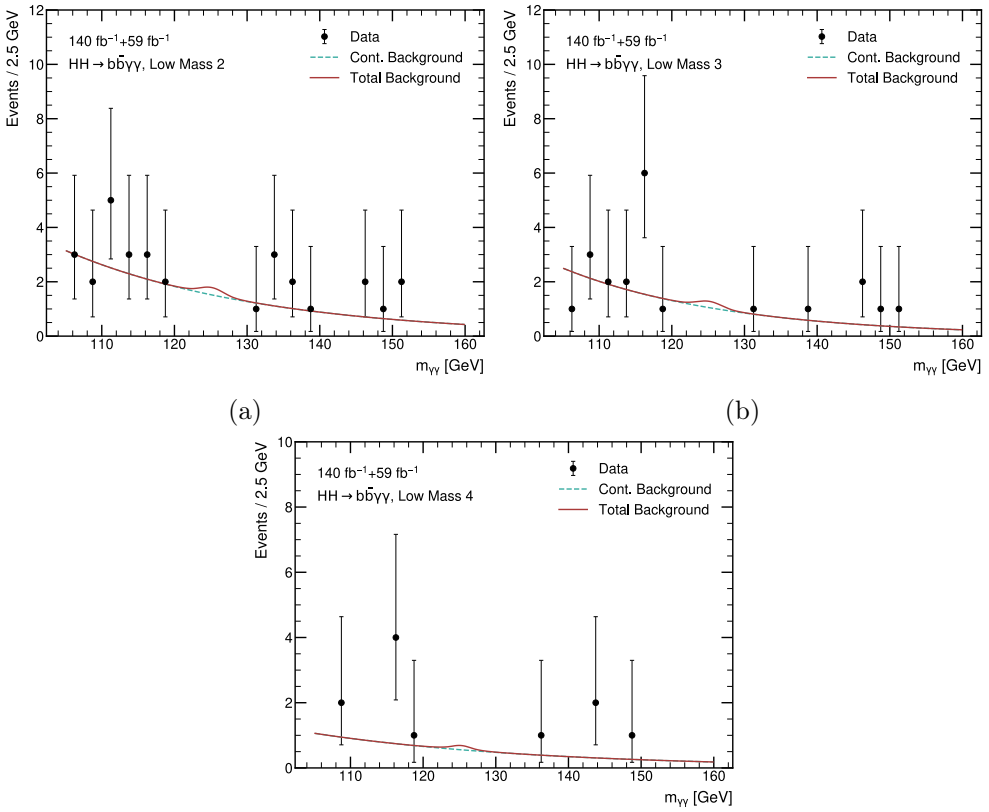

Figure D.4: Comparison between the distribution of $m_{\gamma\gamma}$ in data (points with error bars) sideband and the background-only fit (solid line), where the peak near 125 GeV is due to single Higgs production, for events in Low Mass region categories.

Appendix E

Statistical Results

This appendix presents the statistical results obtained during the initial stage of the analysis, excluding any systematic uncertainties.
The expected results are derived by performing the statistical analysis on Asimov datasets [182]. Under the assumption of no di-Higgs production, a 95% CL upper limit of 3.70 on the total HH production signal strength $\mu_{HH}^{ggF+VBF}$ is set. The expected limit with its $\pm 1\sigma$ and $\pm 2\sigma$ error bands is quoted in Table (E.1).

	Upper limits				
	-2σ	-1σ	Expected	$+1\sigma$	$+2\sigma$
di-Higgs signal strength	1.98	2.66	3.70	5.44	8.05

Table E.1: Expected 95% CL upper limits on the di-Higgs signal strength $\mu_{\text{ggF+VBF}}^{HH}$.

Evaluating the profile log-likelihood ratio $-2\ln(\Lambda)$ as a function of the coupling strength factor κ_λ, assuming SM HH production ($\mu_{HH} = 1$) and all other coupling modifiers equal to their SM predictions, allows to extract the corresponding 68% and 95% confidence intervals, as presented in Figures (E.1).

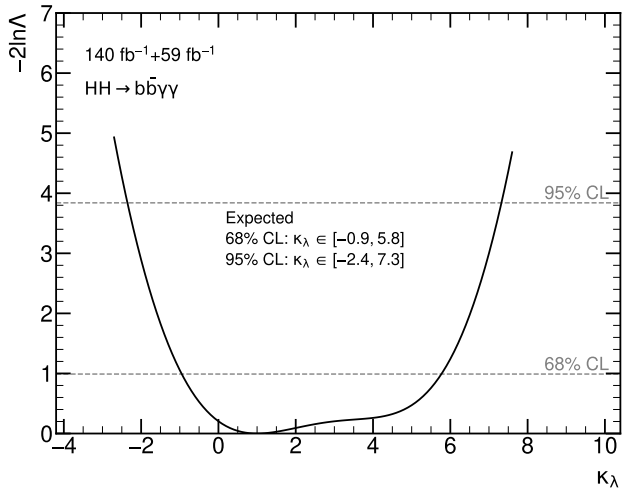

Figure E.1: Expected value of $-2\ln(\Lambda)$ varying with (a) κ_λ. All other coupling modifiers are fixed to 1.

Bibliography

[1] Steven Weinberg. The Making of the standard model. *Eur. Phys. J. C*, 34:5–13, 2004. doi:10.1140/epjc/s2004-01761-1.

[2] Gerard 't Hooft. *Under the spell of the gauge principle*, volume 19. 1994. doi:10.1142/1948.

[3] Gerard 't Hooft and M. J. G. Veltman. Regularization and Renormalization of Gauge Fields. *Nucl. Phys. B*, 44:189–213, 1972. doi:10.1016/0550-3213(72)90279-9.

[4] G. Aad et al. The ATLAS Experiment at the CERN Large Hadron Collider. *JINST*, 3:S08003, 2008. doi:10.1088/1748-0221/3/08/S08003.

[5] S. Chatrchyan et al. The CMS Experiment at the CERN LHC. *JINST*, 3:S08004, 2008. doi:10.1088/1748-0221/3/08/S08004.

[6] LHC Machine. *JINST*, 3:S08001, 2008. doi:10.1088/1748-0221/3/08/S08001.

[7] S. N. Bose. Wärmegleichgewicht im Strahlungsfeld bei Anwesenheit von Materie. *Zeitschrift für Physik*, 27:384–393, 1924. doi:10.1007/BF01328037.

[8] A. Einstein. Quantentheorie des einatomigen idealen Gases. *Sitzungsberichte der Preussischen Akademie der Wissenschaften (Berlin)*, 22:261–267, 1924. doi:10.1002/3527608958.ch27.

[9] Andrew Purcell. Go on a particle quest at the first CERN webfest. Le premier webfest du CERN se lance à la conquête des particules. (35/2012):10, 2012.

[10] W. Pauli. The connection between spin and statistics. *Phys. Rev.*, 58:716–722, Oct 1940. doi:10.1103/PhysRev.58.716.

[11] Gerhart Luders. Proof of the TCP theorem. *Annals Phys.*, 2:1–15, 1957. doi:10.1016/0003-4916(57)90032-5.

[12] E. Noether. Invariante Variationsprobleme. *Nachrichten von der Gesellschaft der Wissenschaften zu Göttingen, Mathematisch-Physikalische Klasse*, 1918:235–257, 1918.

[13] Nicola Cabibbo, Luciano Maiani, and Omar Benhar. *An Introduction to Gauge Theories*. CRC Press, 7 2017. ISBN 978-1-315-36972-3. doi:10.1201/9781315369723.

[14] E. Fermi. An attempt of a theory of beta radiation. 1. *Z. Phys.*, 88:161–177, 1934. doi:10.1007/BF01351864.

[15] T. D. Lee and C. N. Yang. Question of parity conservation in weak interactions. *Phys. Rev.*, 104:254–258, Oct 1956. doi:10.1103/PhysRev.104.254.

[16] C. S. Wu, E. Ambler, R. W. Hayward, D. D. Hoppes, and R. P. Hudson. Experimental test of parity conservation in beta decay. *Phys. Rev.*, 105:1413–1415, Feb 1957. doi:10.1103/PhysRev.105.1413.

[17] E. C. G. Sudarshan and R. E. Marshak. Chirality invariance and the universal fermi interaction. *Phys. Rev.*, 109:1860–1862, Mar 1958. doi:10.1103/PhysRev.109.1860.2.

[18] R. P. Feynman and M. Gell-Mann. Theory of the fermi interaction. *Phys. Rev.*, 109: 193–198, Jan 1958. doi:10.1103/PhysRev.109.193.

[19] J. J. Sakurai. Mass Reversal and Weak Interactions. *Nuovo Cim.*, 7:649–660, 1958. doi:10.1007/BF02781569.

[20] Steven Weinberg. A Model of Leptons. *Phys. Rev. Lett.*, 19:1264–1266, 1967. doi:10.1103/PhysRevLett.19.1264.

[21] Abdus Salam. Weak and Electromagnetic Interactions. *Conf. Proc. C*, 680519:367–377, 1968. doi:10.1142/9789812795915-0034.

[22] Sheldon L. Glashow. Partial-symmetries of weak interactions. *Nuclear Physics*, 22 (4):579–588, 1961. ISSN 0029-5582. doi:10.1016/0029-5582(61)90469-2.

[23] Nicola Cabibbo. Unitary symmetry and leptonic decays. *Phys. Rev. Lett.*, 10:531–533, Jun 1963. doi:10.1103/PhysRevLett.10.531.

[24] Makoto Kobayashi and Toshihide Maskawa. CP Violation in the Renormalizable Theory of Weak Interaction. *Prog. Theor. Phys.*, 49:652–657, 1973. doi:10.1143/PTP.49.652.

[25] W. Altmannshofer et al. The Belle II Physics Book. *PTEP*, 2019(12):123C01, 2019. doi:10.1093/ptep/ptz106.[Erratum: PTEP 2020, 029201 (2020)].

[26] Kazunori Akai, Kazuro Furukawa, and Haruyo Koiso. Superkekb collider. *Nuclear Instruments and Methods in Physics Research Section A: Accelerators, Spectrometers, Detectors and Associated Equipment*, 907:188–199, November 2018. ISSN 0168-9002. doi:10.1016/j.nima.2018.08.017.

[27] A. Augusto Alves, Jr. et al. The LHCb Detector at the LHC. *JINST*, 3:S08005, 2008. doi:10.1088/1748-0221/3/08/S08005.

[28] Murray Gell-Mann. The Eightfold Way: A Theory of strong interaction symmetry. 3 1961. doi:10.2172/4008239.

[29] David J. Gross and Frank Wilczek. Ultraviolet behavior of non-abelian gauge theories. *Phys. Rev. Lett.*, 30:1343–1346, Jun 1973. doi:10.1103/PhysRevLett.30.1343.

[30] H. David Politzer. Reliable perturbative results for strong interactions? *Phys. Rev. Lett.*, 30:1346–1349, Jun 1973. doi:10.1103/PhysRevLett.30.1346.

[31] Richard P. Feynman. Very high-energy collisions of hadrons. *Phys. Rev. Lett.*, 23: 1415–1417, 1969. doi:10.1103/PhysRevLett.23.1415.

[32] J. D. Bjorken. Asymptotic sum rules at infinite momentum. *Phys. Rev.*, 179:1547–1553, Mar 1969. doi:10.1103/PhysRev.179.1547.

[33] Richard D. Ball et al. Parton distributions from high-precision collider data. *Eur. Phys. J. C*, 77(10):663, 2017. doi:10.1140/epjc/s10052-017-5199-5.

[34] Yuri L. Dokshitzer. Calculation of the Structure Functions for Deep Inelastic Scattering and e+ e- Annihilation by Perturbation Theory in Quantum Chromodynamics. *Sov. Phys. JETP*, 46:641–653, 1977.

[35] V. N. Gribov and L. N. Lipatov. Deep inelastic e p scattering in perturbation theory. *Sov. J. Nucl. Phys.*, 15:438–450, 1972.

[36] Guido Altarelli and G. Parisi. Asymptotic Freedom in Parton Language. *Nucl. Phys. B*, 126:298–318, 1977. doi:10.1016/0550-3213(77)90384-4.

[37] M. Klein and R. Yoshida. Collider Physics at HERA. *Prog. Part. Nucl. Phys.*, 61: 343–393, 2008. doi:10.1016/j.ppnp.2008.05.002.

[38] T. Gleisberg, Stefan. Hoeche, F. Krauss, M. Schonherr, S. Schumann, F. Siegert, and J. Winter. Event generation with SHERPA 1.1. *JHEP*, 02:007, 2009. doi:10.1088/1126-6708/2009/02/007.

[39] Peter W. Higgs. Broken Symmetries and the Masses of Gauge Bosons. *Phys. Rev. Lett.*, 13:508–509, 1964. doi: 10.1103/PhysRevLett.13.508. doi:10.1103/PhysRevLett.13.508.

[40] F. Englert and R. Brout. Broken Symmetry and the Mass of Gauge Vector Mesons. *Phys. Rev. Lett.*, 13:321–323, 1964. doi:10.1103/PhysRevLett.13.321.

[41] Steven D. Bass, Albert De Roeck, and Marumi Kado. The higgs boson implications and prospects for future discoveries. *Nature Reviews Physics*, 3(9):608–624, July 2021. ISSN 2522-5820. doi:10.1038/s42254-021-00341-2.

[42] Heather E. Logan. TASI 2013 lectures on Higgs physics within and beyond the Standard Model. 6 2014.

[43] L. Maiani. *Electroweak Interactions*. CRC Press, 2015. ISBN 9781498722261.

[44] J R Andersen et al. Handbook of LHC Higgs Cross Sections: 3. Higgs Properties. 7 2013. doi:10.5170/CERN-2013-004.

[45] B. Pontecorvo. Mesonium and anti-mesonium. *Sov. Phys. JETP*, 6:429, 1957.

[46] Ziro Maki, Masami Nakagawa, and Shoichi Sakata. Remarks on the unified model of elementary particles. *Prog. Theor. Phys.*, 28:870–880, 1962. doi:10.1143/PTP.28.870.

[47] S. Di Vita, C. Grojean, G. Panico, M. Riembau, and T. Vantalon. A global view on the higgs self-coupling. *Journal of High Energy Physics*, 2017(9), 2017. ISSN 1029-8479. doi:10.1007/jhep09(2017)069.

[48] Andrei D. Linde. *Particle physics and inflationary cosmology*, volume 5. 1990.

[49] Fedor Bezrukov, Javier Rubio, and Mikhail Shaposhnikov. Living beyond the edge: Higgs inflation and vacuum metastability. *Phys. Rev. D*, 92(8):083512, 2015. doi:10.1103/PhysRevD.92.083512.

[50] Javier Rubio. Higgs inflation. *Front. Astron. Space Sci.*, 5:50, 2019. doi:10.3389/fspas.2018.00050.

[51] Roger Bailey, Cristoforo Benvenuti, Steve Myers, and Daniel Treille. The LEP collider. *Comptes Rendus. Physique*, 3(9):1107–1120, 2002. doi:10.1016/S1631-0705(02)01402-0.

[52] J. E. Augustin et al. Discovery of a Narrow Resonance in e^+e^- Annihilation. *Phys. Rev. Lett.*, 33:1406–1408, 1974. doi:10.1103/PhysRevLett.33.1406.

[53] J. J. Aubert et al. Experimental Observation of a Heavy Particle J. *Phys. Rev. Lett.*, 33:1404–1406, 1974. doi:10.1103/PhysRevLett.33.1404.

[54] Christiane Lefèvre. The CERN accelerator complex. Complexe des accélérateurs du CERN. 2008.

[55] P. Pugnat and A. Siemko. Review of quench performance of LHC main superconducting magnets. In *Applied Superconductivity Conference*, 2 2007.

[56] K. Aamodt et al. The ALICE experiment at the CERN LHC. *JINST*, 3:S08002, 2008. doi:10.1088/1748-0221/3/08/S08002.

[57] V. Berardi et al. TOTEM: Technical design report. Total cross section, elastic scattering and diffraction dissociation at the Large Hadron Collider at CERN. 1 2004.

[58] O. Adriani et al. Technical design report of the LHCf experiment: Measurement of photons and neutral pions in the very forward region of LHC. 2 2006.

[59] James Pinfold et al. Technical Design Report of the MoEDAL Experiment. 6 2009.

[60] Luca Bottura and Frank Zimmermann. High Energy LHC Machine Options in the LHC Tunnel. 2023. doi:10.1142/9789811280184-0026.

[61] William Barletta, Marco Battaglia, Markus Klute, Michelangelo Mangano, Soren Prestemon, Lucio Rossi, and Peter Skands. Working Group Report: Hadron Colliders. In *Snowmass 2013: Snowmass on the Mississippi*, 10 2013.

[62] Georges Aad et al. Luminosity determination in pp collisions at $\sqrt{s} = 13$ TeV using the ATLAS detector at the LHC. *Eur. Phys. J. C*, 83(10):982, 2023. doi:10.1140/epjc/s10052-023-11747-w.

[63] Georges Aad et al. ATLAS data quality operations and performance for 2015–2018 data-taking. *JINST*, 15(04):P04003, 2020. doi:10.1088/1748-0221/15/04/P04003.

[64] ATLAS Collaboration. ATLAS run-2 luminosity public results, 2020.

[65] G. Arduini et al. LHC Upgrades in preparation of Run 3. *JINST*, 19(05):P05061, 2024. doi:10.1088/1748-0221/19/05/P05061.

[66] L. Arnaudon et al. Linac4 technical design report. 12 2006.

[67] Expected performance of the ATLAS detector under different High-Luminosity LHC conditions. 2021.

[68] ATLAS Collaboration. ATLAS run-3 luminosity public results, 2024.

[69] Georges Aad et al. The ATLAS experiment at the CERN Large Hadron Collider: a description of the detector configuration for Run 3. *JINST*, 19(05):P05063, 2024. doi:10.1088/1748-0221/19/05/P05063.

[70] Izaak Neutelings. Coordinate system and Pseudorapidity, 2021.

[71] G. Aad et al. ATLAS pixel detector electronics and sensors. *JINST*, 3:P07007, 2008. doi:10.1088/1748-0221/3/07/P07007.

[72] Georges Aad et al. Operation and performance of the ATLAS semiconductor tracker. *JINST*, 9:P08009, 2014. doi:10.1088/1748-0221/9/08/P08009.

[73] B. Abbott et al. Production and Integration of the ATLAS Insertable B-Layer. *JINST*, 13(05):T05008, 2018. doi:10.1088/1748-0221/13/05/T05008.

[74] E. Abat et al. The ATLAS Transition Radiation Tracker (TRT) proportional drift tube: Design and performance. *JINST*, 3:P02013, 2008. doi:10.1088/1748-0221/3/02/P02013.

[75] A. Airapetian et al. ATLAS calorimeter performance Technical Design Report. 12 1996.

[76] hrefhttps://cds.cern.ch/record/331061ATLAS liquid argon calorimeter: Technical design report. 12 1996.

[77] ATLAS tile calorimeter: Technical design report. 12 1996.

[78] ATLAS muon spectrometer: Technical design report. 6 1997.

[79] Technical Design Report for the Phase-II Upgrade of the ATLAS Muon Spectrometer. Technical report, CERN, Geneva, 2017.

[80] T Kawamoto, S Vlachos, L Pontecorvo, J Dubbert, G Mikenberg, P Iengo, C Dallapiccola, C Amelung, L Levinson, R Richter, and D Lellouch. New Small Wheel Technical Design Report. Technical report, 2013.

[81] J Soukup. Lucid: technical design report. *CERN EDMS, ATL-UL-ES-0001*, 2006.

[82] S. Abdel Khalek et al. The ALFA Roman Pot Detectors of ATLAS. *JINST*, 11(11): P11013, 2016. doi:10.1088/1748-0221/11/11/P11013.

[83] L. Adamczyk et al. Technical Design Report for the ATLAS Forward Proton Detector. 5 2015.

[84] C. Adler, A. Denisov, E. Garcia, M. Murray, H. Strobele, and S. White. The RHIC zero-degree calorimeters. *Nucl. Instrum. Meth. A*, 499:433–436, 2003. doi:10.1016/j.nima.2003.08.112.

[85] Georges Aad et al. Operation of the ATLAS trigger system in Run 2. *JINST*, 15 (10):P10004, 2020. doi:10.1088/1748-0221/15/10/P10004.

[86] Performance of the ATLAS Inner Detector Track and Vertex Reconstruction in the High Pile-Up LHC Environment. Technical report, CERN, Geneva, 2012.

[87] R. Frühwirth. Application of Kalman filtering to track and vertex fitting. *Nuclear Instruments and Methods in Physics Research Section A: Accelerators, Spectrometers, Detectors and Associated Equipment*, 262(2):444–450, 1987. ISSN 0168-9002. doi:10.1016/0168-9002(87)90887-4.

[88] T G Cornelissen, M Elsing, I Gavrilenko, J F Laporte, W Liebig, M Limper, K Nikolopoulos, A Poppleton, and A Salzburger. The global χ^2 track fitter in ATLAS. *J. Phys.: Conf. Ser.*, 119:032013, 2008. doi:10.1088/1742-6596/119/3/032013.

[89] Georges Aad et al. Electron and photon performance measurements with the ATLAS detector using the 2015–2017 LHC proton-proton collision data. *JINST*, 14(12): P12006, 2019. doi:10.1088/1748-0221/14/12/P12006.

[90] Morad Aaboud et al. Jet reconstruction and performance using particle flow with the ATLAS Detector. *Eur. Phys. J. C*, 77(7):466, 2017. doi:10.1140/epjc/s10052-017-5031-2.

[91] Matteo Cacciari, Gavin P. Salam, and Gregory Soyez. The anti-k_t jet clustering algorithm. *JHEP*, 04:063, 2008. doi:10.1088/1126-6708/2008/04/063.

[92] Georges Aad et al. Jet energy scale and resolution measured in proton–proton collisions at $\sqrt{s} = 13$ TeV with the ATLAS detector. *Eur. Phys. J. C*, 81(8):689, 2021. doi:10.1140/epjc/s10052-021-09402-3.

[93] Tagging and suppression of pileup jets with the ATLAS detector. Technical report, CERN, Geneva, 2014.

[94] Morad Aaboud et al. Identification and rejection of pile-up jets at high pseudorapidity with the ATLAS detector. *Eur. Phys. J. C*, 77(9):580, 2017. doi:10.1140/epjc/s10052-017-5081-5.[Erratum: Eur.Phys.J.C 77, 712 (2017)].

[95] R.L. Workman et al. (Particle Data Group). Review of Particle Physics. *Progress of Theoretical and Experimental Physics*, 2022(8):083C01, 08 2022. ISSN 2050-3911. doi:10.1093/ptep/ptac097.

[96] Georges Aad et al. ATLAS b-jet identification performance and efficiency measurement with $t\bar{t}$ events in pp collisions at $\sqrt{s} = 13$ TeV. *Eur. Phys. J. C*, 79(11):970, 2019. doi:10.1140/epjc/s10052-019-7450-8.

[97] Optimisation and performance studies of the ATLAS b-tagging algorithms for the 2017-18 LHC run. Technical report, CERN, Geneva, 2017.

[98] Daniel Hay Guest. Identification of Jets Containing b-Hadrons with Recurrent Neural Networks at the ATLAS Experiment. IML Machine Learning Workshop. 2017.

[99] Alex Graves. *Supervised Sequence Labelling with Recurrent Neural Networks*. Studies in computational intelligence. Springer, Berlin, 2012. URL `https://cds.cern.ch/record/1503877`. doi:10.1007/978-3-642-24797-2.

[100] Secondary vertex finding for jet flavour identification with the ATLAS detector. Technical report, CERN, Geneva, 2017.

[101] Topological b-hadron decay reconstruction and identification of b-jets with the JetFitter package in the ATLAS experiment at the LHC. Technical report, CERN, Geneva, 2018.

[102] Georges Aad et al. ATLAS flavour-tagging algorithms for the LHC Run 2 pp collision dataset. *Eur. Phys. J. C*, 83(7):681, 2023. doi:10.1140/epjc/s10052-023-11699-1.

[103] Georges Aad et al. Studies of new Higgs boson interactions through nonresonant HH production in the $b\bar{b}\gamma\gamma$ final state in pp collisions at $\sqrt{s} = 13$ TeV with the ATLAS detector. *JHEP*, 01:066, 2024. doi:10.1007/JHEP01(2024)066.

[104] Neural Network Jet Flavour Tagging with the Upgraded ATLAS Inner Tracker Detector at the High-Luminosity LHC. 2022.

[105] Deep Sets based Neural Networks for Impact Parameter Flavour Tagging in ATLAS. 2020.

[106] Manzil Zaheer, Satwik Kottur, Siamak Ravanbakhsh, Barnabas Poczos, Ruslan Salakhutdinov, and Alexander Smola. Deep Sets, 2018.

[107] Graph Neural Network Jet Flavour Tagging with the ATLAS Detector. Technical report, CERN, Geneva, 2022.

[108] Jonathan Shlomi, Peter Battaglia, and Jean-Roch Vlimant. Graph Neural Networks in Particle Physics. 7 2020. doi:10.1088/2632-2153/abbf9a.

[109] ATLAS Collaboration. Jet Flavour Tagging With GN1 and DL1d. Generator dependence, Run 2 and Run 3 data agreement studies. 2023.

[110] Ashish Vaswani, Noam Shazeer, Niki Parmar, Jakob Uszkoreit, Llion Jones, Aidan N. Gomez, Lukasz Kaiser, and Illia Polosukhin. Attention Is All You Need, 2023.

[111] Georges Aad et al. Muon reconstruction and identification efficiency in ATLAS using the full Run 2 *pp* collision data set at $\sqrt{s} = 13$ TeV. *Eur. Phys. J. C*, 81(7):578, 2021. doi:10.1140/epjc/s10052-021-09233-2.

[112] Reconstruction, Energy Calibration, and Identification of Hadronically Decaying Tau Leptons in the ATLAS Experiment for Run-2 of the LHC. Technical report, CERN, Geneva, 2015.

[113] Morad Aaboud et al. Performance of missing transverse momentum reconstruction with the ATLAS detector using proton-proton collisions at $\sqrt{s} = 13$ TeV. *Eur. Phys. J. C*, 78(11):903, 2018. doi:10.1140/epjc/s10052-018-6288-9.

[114] H. T. Edwards. The Tevatron Energy Doubler: A Superconducting Accelerator. *Ann. Rev. Nucl. Part. Sci.*, 35:605–660, 1985. doi:10.1146/annurev.ns.35.120185.003133.

[115] Georges Aad et al. Observation of a new particle in the search for the Standard Model Higgs boson with the ATLAS detector at the LHC. *Phys. Lett. B*, 716:1–29, 2012. doi:10.1016/j.physletb.2012.08.020.

[116] Serguei Chatrchyan et al. Observation of a New Boson at a Mass of 125 GeV with the CMS Experiment at the LHC. *Phys. Lett. B*, 716:30–61, 2012. doi:10.1016/j.physletb.2012.08.021.

[117] Georges Aad et al. Study of the spin and parity of the Higgs boson in diboson decays with the ATLAS detector. *Eur. Phys. J. C*, 75(10):476, 2015. doi:10.1140/epjc/s10052-015-3685-1,[Erratum: Eur.Phys.J.C 76, 152 (2016)].

[118] Georges Aad et al. A detailed map of Higgs boson interactions by the ATLAS experiment ten years after the discovery. *Nature*, 607(7917):52–59, 2022. doi:10.1038/s41586-022-04893-w ,[Erratum: Nature 612, E24 (2022)].

[119] D. de Florian et al. Handbook of LHC Higgs Cross Sections: 4. Deciphering the Nature of the Higgs Sector. 2/2017, 10 2016. doi:10.23731/CYRM-2017-002.

[120] LHC Higgs Working Group. https://twiki.cern.ch/twiki/bin/view/LHCPhysics/HiggsXSBR.

[121] Georges Aad et al. Measurement of the Higgs boson mass with $H \to \gamma\gamma$ decays in 140 fb^{-1} of $\sqrt{s} = 13$ TeV pp collisions with the ATLAS detector. *Phys. Lett. B*, 847: 138315, 2023. doi:10.1016/j.physletb.2023.138315.

[122] Albert M Sirunyan et al. A measurement of the Higgs boson mass in the diphoton decay channel. *Phys. Lett. B*, 805:135425, 2020. doi:10.1016/j.physletb.2020.135425.

[123] Georges Aad et al. Measurement of the Higgs boson mass in the $H \to ZZ^* \to 4\ell$ decay channel using 139 fb^{-1} of $\sqrt{s} = 13$ TeV pp collisions recorded by the ATLAS detector at the LHC. *Phys. Lett. B*, 843:137880, 2023. doi:10.1016/j.physletb.2023.137880.

[124] https://cds.cern.ch/record/2871702. Technical report, CERN, Geneva, 2023.

[125] Georges Aad et al. Combined Measurement of the Higgs Boson Mass from the $H \to \gamma\gamma$ and $H \to ZZ^* \to 4l$ Decay Channels with the ATLAS Detector Using $\sqrt{s} = 7, 8$, and 13 TeV pp Collision Data. *Phys. Rev. Lett.*, 131(25):251802, 2023. doi:10.1103/PhysRevLett.131.251802.

[126] Georges Aad et al. Evidence of off-shell Higgs boson production from ZZ leptonic decay channels and constraints on its total width with the ATLAS detector. *Phys. Lett. B*, 846:138223, 2023. doi:10.1016/j.physletb.2023.138223.

[127] Georges Aad et al. Constraints on the Higgs boson self-coupling from single- and double-Higgs production with the ATLAS detector using pp collisions at s=13 TeV. *Phys. Lett. B*, 843:137745, 2023. doi:10.1016/j.physletb.2023.137745.

[128] J. Alison et al. Higgs boson potential at colliders: Status and perspectives. *Rev. Phys.*, 5:100045, 2020. doi:10.1016/j.revip.2020.100045.

[129] Georges Aad et al. Combination of searches for Higgs boson pairs in pp collisions at $\sqrt{s}$ =13 TeV with the ATLAS detector. *Phys. Lett. B*, 800:135103, 2020. doi:10.1016/j.physletb.2019.135103.

[130] J. Baglio, F. Campanario, S. Glaus, M. Mühlleitner, J. Ronca, and M. Spira. $gg \to hh$: Combined uncertainties. *Phys. Rev. D*, 103:056002, Mar 2021. doi:10.1103/PhysRevD.103.056002.

[131] Massimiliano Grazzini, Gudrun Heinrich, Stephen Jones, Stefan Kallweit, Matthias Kerner, Jonas M. Lindert, and Javier Mazzitelli. Higgs boson pair production at NNLO with top quark mass effects. *JHEP*, 05:059, 2018. doi:10.1007/JHEP05(2018)059.

[132] Frédéric A. Dreyer and Alexander Karlberg. Vector-Boson Fusion Higgs Pair Production at N^3LO. *Phys. Rev. D*, 98(11):114016, 2018. doi:10.1103/PhysRevD.98.114016.

[133] Frédéric A. Dreyer, Alexander Karlberg, Jean-Nicolas Lang, and Mathieu Pellen. Precise predictions for double-Higgs production via vector-boson fusion. *Eur. Phys. J. C*, 80(11):1037, 2020. doi:10.1140/epjc/s10052-020-08610-7.

[134] Aram Hayrapetyan et al. Search for Higgs boson pair production in the bbWW decay mode in proton-proton collisions at $\sqrt{s} = 13$ TeV. 3 2024.

[135] Armen Tumasyan et al. Search for nonresonant Higgs boson pair production in the four leptons plus twob jets final state in proton-proton collisions at $\sqrt{s} = 13$ TeV. *JHEP*, 06:130, 2023. doi:10.1007/JHEP06(2023)130.

[136] Georges Aad et al. Search for non-resonant Higgs boson pair production in the $2b + 2\ell + E_{\mathrm{T}}^{\mathrm{miss}}$ final state in pp collisions at $\sqrt{s} = 13$ TeV with the ATLAS detector. *JHEP*, 02:037, 2024. doi:10.1007/JHEP02(2024)037.

[137] Search for nonresonant Higgs boson pair production in the WW$\gamma\gamma$ channel in pp collisions at $\sqrt{s} = 13$ TeV. 2022.

[138] Georges Aad et al. Search for non-resonant Higgs boson pair production in final states with leptons, taus, and photons in *pp* collisions at $\sqrt{s} = 13$ TeV with the ATLAS detector. 5 2024.

[139] Armen Tumasyan et al. Search for Higgs boson pairs decaying to WW*WW*, WW*$\tau\tau$, and $\tau\tau\tau\tau$ in proton-proton collisions at $\sqrt{s} = 13$ TeV. *JHEP*, 07:095, 2023. doi:10.1007/JHEP07(2023)095.

[140] Emil Bols, Jan Kieseler, Mauro Verzetti, Markus Stoye, and Anna Stakia. Jet Flavour Classification Using DeepJet. *JINST*, 15(12):P12012, 2020. doi:10.1088/1748-0221/15/12/P12012.

[141] Georges Aad et al. Search for nonresonant pair production of Higgs bosons in the $\mathrm{bb^{-}bb^{-}}$ final state in pp collisions at s=13 TeV with the ATLAS detector. *Phys. Rev. D*, 108(5):052003, 2023. doi:10.1103/PhysRevD.108.052003.

[142] Armen Tumasyan et al. Search for Higgs Boson Pair Production in the Four b Quark Final State in Proton-Proton Collisions at s=13 TeV. *Phys. Rev. Lett.*, 129 (8):081802, 2022. doi:10.1103/PhysRevLett.129.081802.

[143] Armen Tumasyan et al. Search for Nonresonant Pair Production of Highly Energetic Higgs Bosons Decaying to Bottom Quarks. *Phys. Rev. Lett.*, 131(4):041803, 2023. doi:10.1103/PhysRevLett.131.041803.

[144] Georges Aad et al. Search for pair production of boosted Higgs bosons via vector-boson fusion in the $b\bar{b}b\bar{b}$ final state using *pp* collisions at $\sqrt{s} = 13$ TeV with the ATLAS detector. 4 2024.

[145] Huilin Qu and Loukas Gouskos. ParticleNet: Jet Tagging via Particle Clouds. *Phys. Rev. D*, 101(5):056019, 2020. doi:10.1103/PhysRevD.101.056019.

[146] Georges Aad et al. Identification of boosted Higgs bosons decaying into b-quark pairs with the ATLAS detector at 13 TeV. *Eur. Phys. J. C*, 79(10):836, 2019. doi:10.1140/epjc/s10052-019-7335-x.

[147] Georges Aad et al. Search for the non-resonant production of Higgs boson pairs via gluon fusion and vector-boson fusion in the $b\bar{b}\tau^+\tau^-$ final state in proton-proton collisions at $\sqrt{s} = 13$ TeV with the ATLAS detector. 4 2024.

[148] Armen Tumasyan et al. Search for nonresonant Higgs boson pair production in final state with two bottom quarks and two tau leptons in proton-proton collisions at s=13 TeV. *Phys. Lett. B*, 842:137531, 2023. doi:10.1016/j.physletb.2022.137531.

[149] Albert M Sirunyan et al. Search for nonresonant Higgs boson pair production in final states with two bottom quarks and two photons in proton-proton collisions at $\sqrt{s} =$ 13 TeV. *JHEP*, 03:257, 2021. doi:10.1007/JHEP03(2021)257.

[150] Georges Aad et al. Combination of searches for Higgs boson pair production in pp collisions at $\sqrt{s} = 13$ TeV with the ATLAS detector. 6 2024.

[151] Armen Tumasyan et al. A portrait of the Higgs boson by the CMS experiment ten years after the discovery. *Nature*, 607(7917):60–68, 2022. doi:10.1038/s41586-022-04892-x.[Erratum: Nature 623, (2023)].

[152] CMS Collaboration. CMS Higgs Physics Analysis Group Summary Plots, 2023.

[153] Georges Aad et al. Search for resonant pair production of Higgs bosons in the $b\bar{b}b\bar{b}$ final state using pp collisions at $\sqrt{s} = 13$ TeV with the ATLAS detector. *Phys. Rev. D*, 105(9):092002, 2022. doi:10.1103/PhysRevD.105.092002.

[154] Georges Aad et al. Combination of Searches for Resonant Higgs Boson Pair Production Using pp Collisions at s=13 TeV with the ATLAS Detector. *Phys. Rev. Lett.*, 132(23):231801, 2024. doi:10.1103/PhysRevLett.132.231801.

[155] Aram Hayrapetyan et al. Searches for Higgs Boson Production through Decays of Heavy Resonances. 3 2024.

[156] HL-LHC prospects for the measurement of Higgs boson pair production in the $b\bar{b}b\bar{b}$ final state and combination with the $b\bar{b}\gamma\gamma$ and $b\bar{b}\tau^+\tau^-$ final states at the ATLAS experiment. 2022.

[157] J. de Favereau, C. Delaere, P. Demin, A. Giammanco, V. Lemaître, A. Mertens, and M. Selvaggi. DELPHES 3, A modular framework for fast simulation of a generic collider experiment. *JHEP*, 02:057, 2014. doi:10.1007/JHEP02(2014)057.

[158] S. Agostinelli et al. GEANT4–a simulation toolkit. *Nucl. Instrum. Meth. A*, 506: 250–303, 2003. doi:10.1016/S0168-9002(03)01368-8.

[159] Paolo Nason. A New method for combining NLO QCD with shower Monte Carlo algorithms. *JHEP*, 11:040, 2004. doi:10.1088/1126-6708/2004/11/040.

[160] Simone Alioli, Paolo Nason, Carlo Oleari, and Emanuele Re. A general framework for implementing NLO calculations in shower Monte Carlo programs: the POWHEG BOX. *JHEP*, 06:043, 2010. doi:10.1007/JHEP06(2010)043.

[161] Richard D. Ball et al. The PDF4LHC21 combination of global PDF fits for the LHC Run III. *J. Phys. G*, 49(8):080501, 2022. doi:10.1088/1361-6471/ac7216.

[162] Christian Bierlich et al. A comprehensive guide to the physics and usage of PYTHIA 8.3. *SciPost Phys. Codeb.*, 2022:8, 2022. doi:10.21468/SciPostPhysCodeb.8.

[163] Andrew Buckley. ATLAS Pythia 8 tunes to 7 TeV data. In *6th International Workshop on Multiple Partonic Interactions at the LHC*, page 29, 12 2014.

[164] Georges Aad et al. Measurement of the Z/γ^* boson transverse momentum distribution in pp collisions at $\sqrt{s} = 7$ TeV with the ATLAS detector. *JHEP*, 09:145, 2014. doi:10.1007/JHEP09(2014)145.

[165] Keith Hamilton, Paolo Nason, and Giulia Zanderighi. MINLO: Multi-Scale Improved NLO. *JHEP*, 10:155, 2012. doi:10.1007/JHEP10(2012)155.

[166] J. Alwall, R. Frederix, S. Frixione, V. Hirschi, F. Maltoni, O. Mattelaer, H. S. Shao, T. Stelzer, P. Torrielli, and M. Zaro. The automated computation of tree-level and next-to-leading order differential cross sections, and their matching to parton shower simulations. *JHEP*, 07:079, 2014. doi:10.1007/JHEP07(2014)079.

[167] Richard D. Ball et al. Parton distributions for the LHC Run II. *JHEP*, 04:040, 2015. doi:10.1007/JHEP04(2015)040.

[168] Enrico Bothmann et al. Event Generation with Sherpa 2.2. *SciPost Phys.*, 7(3):034, 2019. doi:10.21468/SciPostPhys.7.3.034.

[169] ATLAS Collaboration. Athena, may 2021. URL `https://doi.org/10.5281/zenodo.4772550`.

[170] Georges Aad et al. Software and computing for Run 3 of the ATLAS experiment at the LHC. 4 2024.

[171] easyjet. URL `https://gitlab.cern.ch/easyjet/easyjet`.

[172] Georges Aad et al. Performance of electron and photon triggers in ATLAS during LHC Run 2. *Eur. Phys. J. C*, 80(1):47, 2020. doi:10.1140/epjc/s10052-019-7500-2.

[173] Eilam Gross and Ofer Vitells. Trial factors for the look elsewhere effect in high energy physics. *Eur. Phys. J. C*, 70:525–530, 2010. doi:10.1140/epjc/s10052-010-1470-8.

[174] L Carminati, M Delmastro, M Kataoka, M Kuna, R Lafaye, S Laplace, J Leveque, K Liu, G Marchiori, I Nikolic, J Ocariz, L Roos, J Schaarschmidt, M Schwoerer, and L Yuan. Measurement of the isolated di-photon cross section in 4.9 fb-1 of pp collisions at sqrt(s) = 7 TeV with the ATLAS detector. Technical report, CERN, Geneva, 2012.

[175] Hgamcore. URL `https://gitlab.cern.ch/atlas-hgam-sw/HGamCore`.

[176] R. A. Fisher. On the mathematical foundations of theoretical statistics. *Philosophical Transactions of the Royal Society of London (Series A)*, 222, 1922. doi:10.1098/rsta.1922.0009.

[177] Mohamed Belfkir. Search for Higgs pair production at LHC collider (CERN): The first measurement for Higgs potential and search for new physics. Recherche de production de paires de bosons de Higgs au collisionneur LHC (CERN): Premier test du potentiel de Higgs et recherche de nouvelle physique, 2021. URL `https://cds.cern.ch/record/2792268`. Presented 15 Sep 2021.

[178] R. Orlandini. Study of a kinematic fit algorithm for the $hh \to b\bar{b}\gamma\gamma$ channel reconstruction in the atlas experiment at the lhc. Master's thesis, University of Roma Tre, Rome, 2023.

[179] Peilong Wang. *Observation and Measurement of the Higgs Boson Produced in Association with a Vector Boson and Decaying to a Pair of Bottom Quarks with the ATLAS Detector at LHC*. PhD thesis, Southern Methodist U., 2020.

[180] Georges Aad et al. Search for Higgs boson pair production in the two bottom quarks plus two photons final state in pp collisions at $\sqrt{s} = 13$ TeV with the ATLAS detector. *Phys. Rev. D*, 106(5):052001, 2022. doi:10.1103/PhysRevD.106.052001.

[181] Tianqi Chen and Carlos Guestrin. Xgboost: A scalable tree boosting system. KDD '16, page 785–794, New York, NY, USA, 2016. Association for Computing Machinery. ISBN 9781450342322. doi:10.1145/2939672.2939785.

[182] Glen Cowan, Kyle Cranmer, Eilam Gross, and Ofer Vitells. Asymptotic formulae for likelihood-based tests of new physics. *Eur. Phys. J. C*, 71:1554, 2011. doi:10.1140/epjc/s10052-011-1554-0, [Erratum: Eur.Phys.J.C 73, 2501 (2013)].

[183] James Bergstra, Dan Yamins, and David D Cox. Making a science of model search. *arXiv preprint arXiv:1209.5111*, 2012. URL `https://arxiv.org/abs/1209.5111`.

[184] Xgboost parameters. URL `https://xgboost.readthedocs.io/en/stable/parameter.html`.

[185] Georges Aad et al. Measurement of event shapes at large momentum transfer with the ATLAS detector in pp collisions at $\sqrt{s} = 7$ TeV. *Eur. Phys. J. C*, 72:2211, 2012. doi:10.1140/epjc/s10052-012-2211-y.

[186] Leandro G. Almeida, Seung J. Lee, Gilad Perez, George F. Sterman, Ilmo Sung, and Joseph Virzi. Substructure of high-p_T Jets at the LHC. *Phys. Rev. D*, 79:074017, 2009. doi:10.1103/PhysRevD.79.074017.

[187] Recommendations for the Modeling of Smooth Backgrounds. Technical report, CERN, Geneva, 2020.

[188] Georges Aad et al. Measurement of the properties of Higgs boson production at $\sqrt{s} = 13$ TeV in the $H \to \gamma\gamma$ channel using 139 fb^{-1} of pp collision data with the ATLAS experiment. *JHEP*, 07:088, 2023. doi:10.1007/JHEP07(2023)088.

[189] B. Efron. Bootstrap methods: Another look at the jackknife. *Ann. Statist.*, 7(1): 1–26, 01 1979. doi: 10.1214/aos/1176344552. URL `https://doi.org/10.1214/aos/1176344552`.

[190] Johannes Bellm et al. Herwig 7.0/Herwig++ 3.0 release note. *Eur. Phys. J. C*, 76 (4):196, 2016. doi:10.1140/epjc/s10052-016-4018-8.

[191] Morad Aaboud et al. Measurements of inclusive and differential fiducial cross-sections of $t\bar{t}$ production with additional heavy-flavour jets in proton-proton collisions at $\sqrt{s} = 13$ TeV with the ATLAS detector. *JHEP*, 04:046, 2019. doi:10.1007/JHEP04(2019)046.

[192] Georges Aad et al. Measurement of the cross-section for W boson production in association with b-jets in pp collisions at $\sqrt{s} = 7$ TeV with the ATLAS detector. *JHEP*, 06:084, 2013. doi:10.1007/JHEP06(2013)084.

[193] Alexander L. Read. Presentation of search results: The CL_s technique. *J. Phys. G*, 28:2693–2704, 2002. doi:10.1088/0954-3899/28/10/313.